

**UCC Library and UCC researchers have made this item openly available.  
Please [let us know](#) how this has helped you. Thanks!**

<b>Title</b>	Development of on-farm diagnostic devices
<b>Author(s)</b>	Robinson, Caoimhe
<b>Publication date</b>	2020
<b>Original citation</b>	Robinson, C. 2020. Development of on-farm diagnostic devices. PhD Thesis, University College Cork.
<b>Type of publication</b>	Doctoral thesis
<b>Rights</b>	© 2020, Caoimhe Robinson. <a href="https://creativecommons.org/licenses/by-nc-nd/4.0/">https://creativecommons.org/licenses/by-nc-nd/4.0/</a>
<b>Item downloaded from</b>	<a href="http://hdl.handle.net/10468/10886">http://hdl.handle.net/10468/10886</a>

Downloaded on 2021-11-27T12:40:51Z



# UCC

**University College Cork, Ireland**  
Coláiste na hOllscoile Corcaigh

Ollscoil na hÉireann

**National University of Ireland**



**Development of On-Farm Diagnostic Devices**

Thesis presented by

**Caoimhe Robinson**

for the degree of

**Doctor of Philosophy**

**University College Cork**

**Dept. of Chemistry**

**&**

**Tyndall National Institute**



Head of School/Department: Dr Humphrey Moynihan

Supervisors: Dr Alan O’Riordan, Dr Riona Sayers and Dr Emer Kennedy

2020

## Table of Contents

<b>Chapter 1 Introduction</b> .....	<b>1</b>
1.1 Effect of Disease in Livestock.....	2
1.2 Point-of-Care (POC) Sensors .....	5
1.3 Fundamentals of Electrochemistry .....	7
1.3.1 Electron Transfer.....	7
1.3.2 Faradaic and Non-Faradaic Responses .....	8
1.3.3 Factors Affecting Faradaic Responses .....	10
1.3.4 Electrochemical Cell .....	11
1.4 Electrochemical Techniques.....	14
1.4.1 Chronoamperometry .....	14
1.4.2 Cyclic Voltammetry .....	15
1.4.3 Electrochemical Impedance Spectroscopy.....	16
1.5 Macroelectrodes vs. Ultramicroelectrodes .....	27
1.6 Fabrication of UMEs .....	30
1.7 Impedimetric Biosensors .....	36
1.7.1 Antibodies and Antigens .....	36
1.7.2 Electrode Modifications .....	38
1.7.3 Immobilisation Technique .....	54
1.7.4 Faradaic vs Non-Faradaic Sensors .....	56
1.8 Scope of Thesis .....	58
1.9 References .....	60
<b>Chapter 2 Detection of Bovine Immunoglobulin G to Determine Passive Transfer in Calves</b> .....	<b>76</b>
2.1 Introduction .....	77
2.2 Experimental .....	81

2.2.1	Materials and Buffer Preparation .....	81
2.2.2	ELISA .....	81
2.2.3	Electrochemical Immunoassay .....	82
2.3	Results and Discussion .....	88
2.3.1	ELISA .....	88
2.3.2	Structural Characterisation of Microband Electrodes .....	88
2.3.3	Electrochemical Characterisation of Microband Electrodes.....	90
2.3.4	Characterisation of the Biocompatible Polymer .....	92
2.3.5	Detection of Bovine IgG in Buffer.....	96
2.3.6	Detection of Bovine IgG in Serum.....	98
2.4	Conclusion.....	103
2.5	References .....	104
<b>Chapter 3</b>	<b>Fabrication of Polymer Microneedle Arrays.....</b>	<b>108</b>
3.1	Introduction .....	109
3.2	Experimental .....	113
3.2.1	Materials and Reagents .....	113
3.2.2	Fabrication of Epoxy Microneedle Arrays.....	113
3.2.3	Passivation of Microneedle Arrays .....	116
3.2.4	Characterisation of Structures .....	118
3.3	Results and Discussion .....	119
3.3.1	Polymer Replication of Silicon MN Arrays.....	119
3.3.2	Selective Passivation of Array Surface .....	124
3.4	Conclusion.....	132
3.5	References .....	133
<b>Chapter 4</b>	<b>Fabrication of Octagonal Nanoring Arrays.....</b>	<b>137</b>
4.1	Introduction .....	138
4.2	Experimental .....	142

4.2.1	Materials and Reagents .....	142
4.2.2	Fabrication of Octagonal Nanoring Arrays.....	142
4.2.3	Characterisation of Structures .....	145
4.3	Results and Discussion .....	146
4.3.1	Electrochemical Characterisation of Nanoring Devices .....	146
4.3.2	Structural Characterisation of Nanoring Devices .....	151
4.3.3	Three-Electrode System .....	152
4.3.4	Optimisation of Cutting Method .....	154
4.4	Conclusion.....	157
4.5	References .....	159
<b>Chapter 5</b>	<b>Summary and Future Work.....</b>	<b>163</b>
5.1	Summary .....	164
5.2	Future Work .....	167
5.2.1	Silicon Based Electrochemical Device .....	167
5.2.2	Epoxy Based Electrochemical Device .....	170
<b>Appendices</b>	<b>.....</b>	<b>173</b>
A.1	Abbreviations and Acronyms .....	174
A.2	Peer Reviewed Publications .....	176
A.3	Conference Attended .....	177
A.4	Award .....	178

## **Declaration**

This is to certify that the work I am submitting is my own and has not been submitted for another degree, either at University College Cork or elsewhere. All external references and sources are clearly acknowledged and identified within the contents. I have read and understood the regulations of University College Cork concerning plagiarism.

---

Caoimhe Robinson

June 2020

## Abstract

The global population, currently 7.7 billion, is expected to grow to 9.7 billion by 2050. This is expected to lead to a 70% increase in demand for animal-based protein. Irish beef and dairy products account for over 50% of our agricultural output and DAFM's Food Wise 2025 strategy aims to position Ireland as a world leader in sustainable agri-food production. However, the high percentage of livestock that are lost due to infectious diseases (20%), poses a challenge to achieving this sustainability, in addition to more sustainable use of antimicrobials, smarter livestock diagnostics and treatments are therefore required. The goal of this thesis was to develop a low-cost disposable biosensor that would permit point-of-care (POC) detection of diseases in bovines, through cost-effective, scalable microfabrication techniques. Such devices could enable real-time determination of the health status of animals on farm and contribute to more informed therapeutic interventions. Electrochemistry presents a viable option for POC devices in this regard and allows easy integration with portable electronics.

Electrochemical Impedance Spectroscopy (EIS) is a surface sensitive technique that measures the resistive and capacitive behaviour of an electrochemical system. It lends itself to serological immunosensor development as it allows label-free detection. For the purposes of this research, silicon devices were fabricated with six microband working electrodes, gold counter, and platinum pseudo-reference electrodes. The microband working electrodes were modified with a biocompatible co-polymer. This co-polymer supported the cross-linking of a bioreceptor (e.g., anti-bovine IgG) to electrode surface, which selectively bound to the target biomolecule (bovine IgG) in serum. This EIS device could distinguish between seronegative and seropositive samples in 15 minutes making it suitable for POC applications. Additionally, the presence of six working electrodes allowed for testing of multiple samples at a time. Often, however, only a single test is required. As such, silicon presents an expensive option for disposable sensors. Hence, polymer replication methods were also investigated in this thesis. This process allowed a single silicon wafer to be repeatedly used to produce polymer structures. A microneedle format was chosen to eliminate the need for taking samples on-farm and provide a pain-free method of *in vivo* measurements in interstitial fluid in interstitial fluid. The fabrication method used a double-sided micro-moulding process to move towards mass manufacturing. COMSOL simulations were performed to explore the active layer on the

microneedle tip surface, ensuring no diffusional overlap between electrodes and providing the most effective tip design.

The microneedle structures also presented the opportunity for novel fabrication of nanoring arrays, by removing part of the protruding structure and exposing underlying nanorings. These have the potential to be highly sensitive electrochemical devices due to enhanced mass transport and high current densities, while maintaining the scalable cost-effective fabrication process of the microneedles. Devices produced steady-state CVs in a known redox molecule, with currents in the nA range.



## Acknowledgements

I wish to thank my supervisors, Dr Alan O’Riordan, Dr Riona Sayers and Dr Emer Kennedy, for your support and guidance throughout my PhD. Riona’s veterinarian expertise was invaluable to someone like me who barely knows what a cow looks like. Emer’s positive attitude helped me believe writing this thesis was possible. And although a great deal of my discussions with Alan turned to arguments, or talks about his polytunnel, he remained cheerfully patient. Through his guidance I have grown as a scientist and his slightly forceful encouragement has helped me get over my fear of public speaking. However, I must apologise for being a disappointment and not finding my future spouse during my time in Tyndall.

I would also like to thank all the other supervisors in the Nanotechnology group, Dr. Aidan Quinn, Dr. Micheal Burke, Dr. Daniela Iacopino, and Dr Mary Manning for all their help and advice. A special thanks to Pierre for showing confidence in me and recommending me for the position. Also, for always being available with advice and terrible jokes. I have many fond memories including “Barcelona Day”, and your performance at the Student vs Staff soccer match (you know the year I mean). To Amelie, Sean, Colm, Daniel, Baby Dan, Micki, Ethel, Roxane, Keith, and Carola for welcoming me into the group and to everyone else who joined after. Thanks to Luiza, Shane and Fernando for making Friday’s “JT Day”. Aidan thanks for being the equivalent of a lab puppy. Benjy thanks for double checking my calculation on days I was too tired for simple addition. And Rob brightened up the lab every Christmas by being a walking decoration.

In the extended Tyndall community, I am especially grateful to Donal O’Sullivan, Richard Murphy, Krimo Khalfi, Dan O’Connell, Alan Blake, Conor O’Mahony, and Eileen O’Leary for their collaboration throughout my project. Also, thanks to Michael Diskin in Teagasc.

Thank you to Niamh, Colm, and Sofia for being my unofficial Post-docs and answering my incessive questions. Niamh took time to teach me everything I know about impedance, while we ate jellies. I will forever think of you when I hear Zombie. Colm taught me that anything is fixable with a bit of blu tack and parafilm. Sofia thanks for sharing all your sensor knowledge and thanks for being the only person as loud as me. Andrea thanks for

all the help with the microneedle fabrication. No matter how busy you were you always made time to help.

I would like to give a special mention to the friends who kept me sane with tea breaks, pints, cinema trips, hikes and strolls for ice-cream. Louise thank you for giving my water bottle a safe place to live. Fiona thanks for being my Green Team buddy. My “work wife” Julia, thank you for all the movie nights. Ian thank you for being my encyclopaedia on everything electrochemistry, but more importantly, thanks for being my tall friend and reaching high shelves for me.

I also must mention a couple of friends outside Tyndall who also supported me. Megan and Harney, thanks for never asking when I will be finished. Anytime spent with either of you has ended up with me doubled over with laughter, even on day three of a music festival when we were completely sleep deprived. Also, to everyone else from college who I have had so many great nights out with. Amy thanks for always being proud, though completely clueless about what I do. Phil you remain the most genuine person I know, and always show interest in everyone’s life. To all the staff in Cavanagh’s and later Impala, thank you for creating a safe place for us to relax after a bad day of work. And where else would we have gone when there was something to celebrate!

Finally, I would like to thank my family for their endless love and support, and admirably tolerating me when I was stressed. My grandparents, Mary and Willie have always let me know how proud they are (even if they couldn’t remember what I was studying). Alec even across the Atlantic Ocean I know you are celebrating my wins. Tracy thanks for the endless number of gigs, trips away and walks with Penny, you’re always up for a bit of craic. Mum you have always made everything seem possible. I inherited your stubbornness which undoubtedly got me here today. Thank you for giving me so many opportunities and encouraging me to follow any and all dreams.

*To my family*

*Chapter 1*      **Introduction**

## **1.1 Effect of Disease in Livestock**

The agri-food sector is one of Ireland's most important indigenous manufacturing sectors, employing 8.4% of the working population. It was valued at €13 billion in 2018, which was a 67% increase since 2010.<sup>1</sup> This sector accounted for 10% of the value of Irish merchandise exported in 2018.<sup>2</sup> Ireland's beef and dairy products account for over 52% of our agricultural output,<sup>3</sup> we produce 12% of the world's infant formula<sup>4</sup> and butter exports are worth €1.2 billion.<sup>5</sup> These statistics place Ireland as the fifth largest beef exporter in the world and the largest in the EU.<sup>6, 7</sup> Further growth projections for the industry are identified in DAFM's Food Wise 2025 strategy, which aims to position Ireland as a world leader in sustainable agri-food production. Within 10 years, the strategy plans to deliver a 65% increase in the value of primary production amounting to €10 billion, and an 85% increase in the value of exports to €19 billion.<sup>4, 8</sup> On a global scale, the population is currently 7.7 billion and is expected to reach 9.7 billion by 2050. In addition to this, the demand for animal-based protein is projected to increase by 70%. One of the major challenges facing global agriculture is how to cost-effectively and sustainably meet this production demand, while competing with a changing climate, limited farmland, water scarcity, soil depletion, weather extremes and loss of livestock to diseases.<sup>9, 10</sup>

Disease outbreaks can impact the agricultural economy greatly. Bovine spongiform encephalopathy (BSE) was first detected in the UK in 1986. Once a link between BSE and Creutzfeldt-Jakob disease (CJD), which infects the human population, was established, global beef consumption declined drastically. The EU implemented an international ban on trade of beef products with the UK (Commission Decision 96/239/EC), until 2005, with a partial lift in 1999. Similarly, the US banned beef imports from Canada in 2003, when a case of BSE was discovered in a Canadian herd. Trading between the US and Canada resumed in 2005 with strict regulations imposed.<sup>11</sup> Another notable disease outbreak was the foot and mouth (FMD) epidemic of 2001 which was estimated to cost the UK losses equivalent to £3.1 billion.<sup>12</sup> More common diseases of cattle may not seem as conspicuous but with the World Organisation for Animal Health (OIE) estimating that one livestock animal out of five is lost to disease cattle health remains a major concern. The OIE updated their list of notifiable diseases in 2020 and

now contains 117 animal diseases, including infections and parasitic infestations.<sup>13</sup> These diseases are of international concern and thirteen of these pertain to cattle. Animal disease surveillance mechanisms are therefore of vital importance and these are most useful if they enable early detection and rapid response to reduce and eliminate the spread of disease.<sup>14</sup> For this to be possible better disease diagnostics devices are required.<sup>15</sup>

The inappropriate overuse of antibiotics is a growing concern. In the US, it is estimated that 70% of the antibiotics sold are for use in livestock farming.<sup>16</sup> Antibiotics are often administered in feeds as a preventative measure against infections and to marginally improve growth rates.<sup>17</sup> Though these practices are being abolished in the US and EU, antibiotics are still being inappropriately used due to poor disease diagnostic methods. It remains commonplace for a veterinarian to administer broad-spectrum antibiotics to an animal presenting with viral clinical signs before a diagnosis is established. The remainder of the herd may also be treated prophylactically.<sup>18</sup> Although such interventions may be appropriate in some cases (e.g. pneumonia in young calves), many are not. These misuses of antibiotics are leading to increasing cases of antimicrobial resistance in animals, which are contaminating human food supplies. Resistant bacteria have several routes into the human system including (i) direct contact with the animal, (ii) exposure to manure, (iii) contact with uncooked meat or surfaces the meat has been in contact with, and, (iv) consumption of undercooked meat.<sup>19</sup> The US Food and Drug Administration (FDA) has already prohibited the use of cephalosporin antibiotics in cattle, pigs, chicken and turkeys.<sup>20</sup> Similarly, Denmark has banned avoparcin, an antibiotic similar to vancomycin, which has shown a decrease in vancomycin-resistant enterococci in both livestock and humans.<sup>16</sup>

To address this issue on a farm-level, smart treatment plans for livestock need to be implemented. Also, preventative blanket treatments of naive herds, before infection is confirmed, need to be curtailed. Many of the diseases being treated on-farm are asymptomatic, highly contagious, and exacerbated by stress. With diagnostic methods being slow and costly on a per animal basis, it is understandable that these pre-emptive measures are hard to avoid. Quarantining the symptomatic animal could be an alternative to unnecessary antibiotic administration. Unfortunately, drawbacks to this include cost, availability of suitable facilities, and increased workload. Furthermore, the expected increase in herd size and stocking density caused by demand-driven food production will

intensify this high stress environment, increasing the risk of contracting infectious disease within a herd. To this end, there is an urgent need for new point-of-care diagnostic devices, which deliver rapid and economical identification of animal disease states.<sup>21</sup>

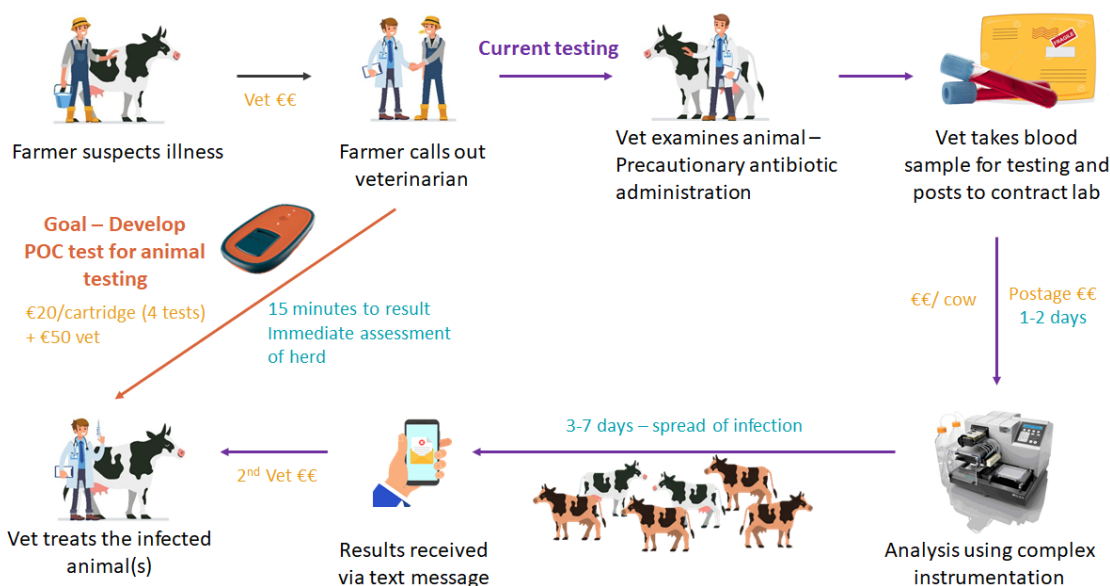


**Figure 1.1:** Timeline and costs involved in current farm animal diagnosis vs projected time and cost involved in point-of-care testing.

Screening for pathogenic exposure in live animals on-farm will support the use of targeted, appropriate treatment interventions, eliminating the need for precautionary antibiotic administrations. Additionally, the further spread of disease will be prevented by faster analysis. This will ultimately lead to reduced therapeutic costs, improved herd performance, implementation of targeted vaccination strategies, and enable proactive herd health management. To this end, new point-of-care diagnostic devices are required, that will provide rapid, real-time data of animal disease status thereby providing informed decision-making capability to veterinarians and farmers on-farm.

## 1.2 Point-of-Care (POC) Sensors

The development of veterinary POC devices is often driven by common concerns between human and animal health with existing human biosensors being modified for use in animals. For instance, Becton–Dickenson’s automated cell counter has been adapted to yield several relatively small benchtop systems for veterinarians, such as IDEXX’s LaserCyte Dx Hematology Analyzer.<sup>22</sup> Similarly, the Lactate Scout was originally designed to assess performance of athletes during training. This handheld device, which requires only a finger prick of blood has recently been tested on cattle for lactic acid measurement. Lactate measurements in cattle indicates the severity of various conditions including respiratory disease, displacement of the abomasum (a ruminant’s fourth stomach) and neonatal diarrhoea, as well as determining if a cow is fit enough for calving.<sup>23</sup> Many POC devices target companion animals, as diagnosis most often occurs in the controlled environment of a veterinary clinic. Additionally, there is a willingness of owners to spend money on their pets’ health.<sup>22</sup> Zoetis are the leading providers of POC animal diagnostics, manufacturing the AlphaTRAK®, Witness® diagnostic kits, VETSCAN® and i-STAT® analysers.<sup>24,25</sup> Fewer commercial on-farm products exist due to obstacles such as an uncontrolled environment which exposes devices to weather that may compromise its function including temperature fluctuations, light, moisture and dirt.<sup>26</sup> Some devices have successfully met these challenges and have been applied to cattle, such as the previously mentioned i-STAT® which is a portable analyser for blood gases and electrolytes. The i-STAT® performs an assay in 2 mins and can be used in small and large animals, making it suitable for on-farm applications. Additionally, Biomed Diagnostics developed a simple strip progesterone test, P4 Rapid, which will give information on whether a cow is in heat in 15 mins from a milk sample, allowing for accurately timed artificial insemination.<sup>27</sup>

Mastitis is the inflammation of the udder caused by bacterial infection, resulting in reduced milk production. This disease accounts for the vast majority of antibiotic usage and associated veterinary costs on a dairy farm.<sup>28</sup> To that end, Virbac has developed the Speed Mam Color™ which identifies eight mastitis causing bacteria from a milk sample and fourteen types of antibiotics in 24 to 48 hours.<sup>29</sup> Mastaplex is also developing a new mastitis test. Mastest® is a colorimetric assay which identifies four of the main mastitis bacteria from a milk sample.<sup>30</sup> These kits require 22 hr incubation in the benchtop



LapBox™, which automatically emails results to the end-user. Virbac also supply the Speed V-Diar™ which identifies pathogenic causes of diarrhoea in calves. This assay detects coronavirus, rotavirus, *Cryptosporidium parvum*, *Escherichia coli* F5 and CS31A antigens in faeces in 15 mins.<sup>31</sup> IDEXX use serum or ear notch samples in their SNAP® test for bovine viral diarrhoea (BVD), which determines virus presence in 20 mins.<sup>32</sup> *C. parvum* is also detectable in faeces using the 10 min assay Bio K 403 from BioX Diagnostics.<sup>33</sup>

Other emerging technologies are aimed toward on-farm diagnostics such as the BovAlert. DIT Hothouse and ITT MiCRA are collaborating on this electrochemical sensor for the detection of liver fluke in milk and serum samples. The sensor consists of a disposable cartridge and a custom reader which takes 15 mins to produce a result.<sup>34</sup> This method has also successfully detected the presence of parasitic stomach worms.<sup>35</sup> Moduleic Sensing™ VET will generate same day results from a blood sample using a cartridge inserted into a hub. This device will remotely report BVD and contagious bovine pleuropneumonia results and is expected on the market shortly.<sup>36</sup> STIGAField is an assay which looks to integrate with existing glucometers by providing disposable test strips which can detect biomarkers from a single drop of blood or milk. These test strips aim to detect bovine immunoglobulin (Ig) G, lactoferrin, a mastitis biomarker, and blood calcium to assess milk fever.<sup>37</sup>

Growing consumer concerns regarding antibiotics tainting food supplies and the contraction of transmissible diseases from food sources such as milk, eggs and meat will drive the market for livestock POC devices. Electrochemical immunosensors constitute a promising technology for development of sensing devices. These would offer the potential to fulfil the criteria for rapid, adaptable, and economical on-farm diagnosis through the use of microfabrication and biochemistry methods.

## 1.3 Fundamentals of Electrochemistry

Electrochemistry is the branch of chemistry that is concerned with the processes at an electrode/electrolyte interface, primarily the transfer of electrons.

### 1.3.1 Electron Transfer

A simple electrochemical reaction is represented in Equation 1.1:



This is a redox reaction which is driven by the application of a suitable potential to the electrode. The oxidised species O, will gain  $n$  number of electrons,  $e^-$ , from the reduced species, R.<sup>38</sup> For this transfer of electrons to occur, the energy level of the electrode needs to match the energy level of the electrolyte. Applying a negative potential to the electrode raises the energy of the electron. If this is sufficient to reach the lowest unoccupied molecular orbital (LUMO) of the electrolyte, then the electron will be transferred to the electrolyte, as seen in Figure 1.2 (a). Alternatively, in Figure 1.2 (b) the electrode can be driven to a positive potential, reducing the energy of the electrode. If the energy of the electrode is reduced enough to match the highest occupied molecular orbital (HOMO), then an electron will transfer from the electrolyte to the electrode.

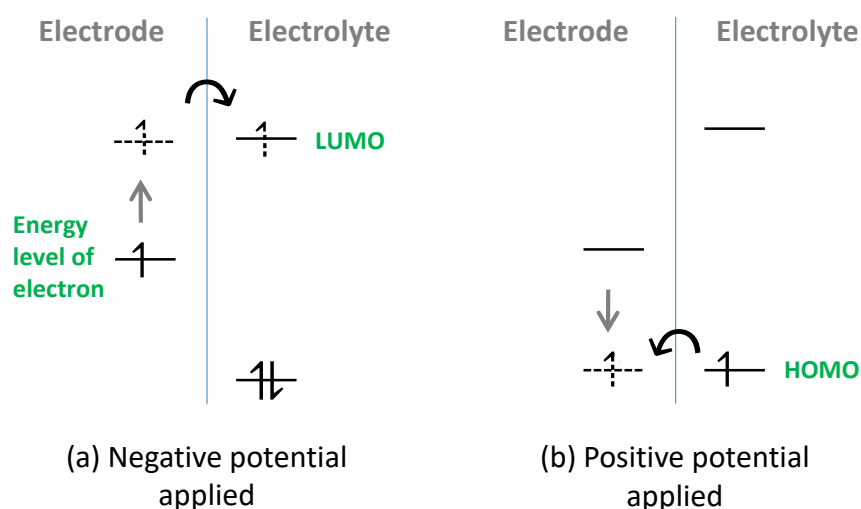


**Figure 1.2:** Representation of (a) a reduction of a species in solution where an electron moves into the LUMO of the electrolyte and (b) an oxidation of a species where it gains an electron from the HOMO of the electrolyte.

The loss of an electrons from the electroactive species in the solution is referred to as oxidation and its gain of an electron is referred to as reduction. This transfer of electrons causes the flow of current.

A mediator is an electrochemically active species that has a rapid electron transfer rate. It will undergo an oxidation or a reduction reaction at the electrode surface once an appropriate voltage is applied, thus producing a faradaic current. The ferrocene/ferrocenium (Fc/Fc<sup>+</sup>) couple is commonly adopted as a redox mediator. This couple is soluble and stable in many solvents, with the standard potential, E<sup>0</sup>, known for a variety of solvents. The E<sup>0</sup> is the potential at which the energy level of the electrode is suitable to allow flow between electrode and the active species in the electrolyte, in this case the iron at the centre of the Fc molecule. When a positive potential exceeding the E<sup>0</sup> is applied oxidation of the Fe<sup>2+</sup> to Fe<sup>3+</sup> will occur. As this is a reversible reaction, on the reverse sweep the Fe<sup>3+</sup> will be reduced back to Fe<sup>2+</sup>. This couple shows Nernstian behaviour as it is electrochemically reversible and is described using the Nernst equation:

$$E_{eq} = E^0 + \frac{RT}{nF} \ln \frac{C_O}{C_R} \quad 1.2$$

This can be used to calculate the potential of an electrode at the reaction equilibrium, E<sub>eq</sub>. E<sup>0</sup> is the standard potential, R is the universal gas constant, T is temperature (K), n is number of electrons of electrodes transferred, F is Faraday's constant and C is the concentration of the oxidised and reduced species (mol L<sup>-1</sup>).

### 1.3.2 Faradaic and Non-Faradaic Responses

The electron transfer that occurs across the electrode/electrolyte interface during oxidation or reduction produces a faradaic current. These reactions are governed by Faraday's Law:

$$Q = nFN \quad 1.3$$

where *Q* is the total charge, *n* is the number of electrons transferred per mole, *F* is Faraday's constant and *N* is the amount of product. For these faradaic reactions, the amount of material produced at the electrode/electrolyte interface is directly proportional to the total conducted charge. However, there are usually a range of potentials where no

charge-transfer occurs depending on the electrochemically active species in the electrolyte. At these potentials, reactions are either thermodynamically or kinetically unfavourable. However, other processes such as adsorption or desorption, can occur which structurally changes the electrode/electrolyte interface. These are non-faradaic processes. Although no charge crosses the interface, external currents can flow. During an electrochemical reaction, faradaic processes are the principle concern. Nonetheless, non-faradaic processes are still taking place. Any current attributing to these processes is referred to as a charging current, as the ions accumulating on the electrode is similar to a capacitor charging.

Even when an electrode is immersed in an inert electrolyte, the act of changing the potential will cause a charge imbalance across the electrode/electrolyte interface. Charged species near the interface will rearrange themselves to neutralise this imbalance, thus creating a double layer at an electrode surface. The solution portion of the double layer has two regions, illustrated in Figure 1.3.<sup>39,40</sup> The first is the inner Helmholtz plane (IHP), which consists of solvent molecules and specifically adsorbed ions, which are not solvated. The second region consists of solvated ions (non-specifically adsorbed). As these ions are completely surrounded by solvent molecules, they cannot approach as close to the electrode surface, thus they make up the outer Helmholtz plane (OHP). Beyond this is the diffusion layer, which will be discussed in Section 1.4.1.

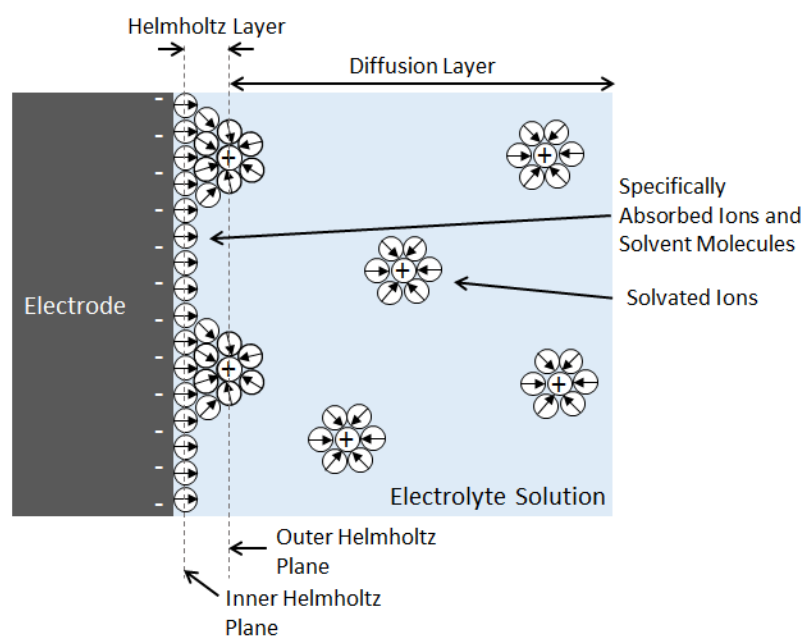


**Figure 1.3:** Schematic of Helmholtz's proposed model for the double layer at an electrode/electrolyte interface.

### 1.3.3 Factors Affecting Faradaic Responses

#### 1.3.3.1 Kinetics

The rate of an electrochemical reaction is affected by the kinetics of the reaction and mass transport. The slowest process will be the rate determining step. The Butler-Volmer Model accounts for the kinetics in the system and can be used to calculate the current resulting from an overpotential when mass-transport limitations are inconsequential.<sup>41</sup> The overpotential is the potential difference between the standard potential and the potential applied to create the reaction.

$$i = i_0 [e^{-\alpha f \eta} - e^{(1-\alpha) f \eta}] \quad 1.4$$

where  $i_0$  is the exchange current (A) and  $\alpha$  is the transfer coefficient, typically estimated to be 0.5, a dimensionless value between 0 and 1. The  $\eta$  is the overpotential (V) and  $f = F/RT$ , where  $F$  is Faraday's constant (C),  $R$  is the gas constant ( $\text{J mol}^{-1} \text{K}^{-1}$ ) and  $T$  is temperature (K).

#### 1.3.3.2 Mass Transport

Mass transport is how species moves in the bulk solution towards the electrode. It is a combination of three different effects; (i) diffusion, (ii) migration, and (iii) convection.<sup>41</sup> Diffusion is the spontaneous movement of molecules from regions of high concentration to regions of lower concentration. Migration is the movement of charged particles in an electric field. Convection is the movement of molecules in a stirred solution or thermal motion. The unidirectional ( $x$ ) flux of a species,  $j$ , in relation to diffusion, migration and convection is described by the Nernst-Planck equation:

$$J_j(x) = \underbrace{-D_j \frac{\partial C_j(x)}{\partial x}}_{\text{Diffusion}} - \underbrace{\frac{z_j F}{RT} D_j C_j \frac{\partial \phi(x)}{\partial x}}_{\text{Migration}} + \underbrace{C_j v(x)}_{\text{Convection}} \quad 1.5$$

$\underbrace{\hspace{10em}}_{\text{Total Flux}}$

where  $J_i(x)$  is a one-dimensional flux for species  $j$  at distance  $x$  (cm) from the electrode ( $\text{mol cm}^{-2} \text{sec}^{-1}$ );  $D_j$  ( $\text{cm}^2 \text{sec}^{-1}$ ) is the diffusion coefficient,  $z_j$  is the charge and  $C_j$  ( $\text{mol cm}^{-3}$ ) is the concentration for the species  $j$ ;  $v(x)$  is the rate with which a volume element moves in solution;  $\partial C_j(x)/\partial x$  is the concentration gradient and  $\partial \phi(x)/\partial x$  is the potential gradient along the  $x$ -axis. The first term in Equation 1.5 describes Fick's first law which accounts for diffusion. It describes diffusional movement as a function of the change in

its concentration with distance from an electrode. The second term represents migration and the final term details convection.

It is beneficial to minimise some of the effects of mass transport for experimental scenarios. Although, it is not possible to completely eliminate mass transport, nor is it desirable as it is required to deliver analyte to the electrode surface, some of the effects can be eliminated. For instance, if the solution is constantly stirred at a sufficient speed, the mass transport becomes a function of convection only. Alternatively, by eliminating stirring and leaving the solution static, convection would be eradicated. Adding a supporting electrolyte greatly reduces migration. This supporting electrolyte should be inert and present in high concentrations so to minimise the solution resistance,  $R_s$  and the potential gradient. With the addition of the supporting electrolyte in a static solution, the only contribution to mass transfer would be diffusion. In this case Cottrell's equation can be used to calculate the current with respect to time at a controlled potential:

$$i(t) = \frac{nFAD^{1/2}C^*}{\pi^{1/2}t^{1/2}} \quad 1.6$$

where,  $t$  is the time,  $A$  ( $\text{cm}^2$ ) is the area of the electrode and  $C^*$  is the bulk concentration. The rate-determining step can vary with potential. When the applied potential is low and charge transfer is slow, the effects of mass transport become negligible. However, at higher potentials, charge transfer has become fast and mass transport reverts to being the rate-determining step.

### 1.3.4 Electrochemical Cell

It is not possible to measure the potential difference at a single interface. However, by adding a second electrode to the system, an electrochemical cell is created. This second electrode is the reference electrode (RE) and must have a constant potential. Since its potential is fixed, any changes in the system are attributed to the working electrode (WE). This change of potential is reported as the potential difference between the WE and the RE. Any potential measured from, or applied to, an electrochemical cell is the potential of the WE with respect to the RE. This is a two-electrode system. A more commonly adopted system is the three-electrode cell, which introduces the counter electrode (CE). The presence of large current densities may cause the reference electrode to lose its 'ideal'

non-polarizable behaviour, causing a change in potential and inaccurate measurement of the system's potential difference. The CE acts as a current sink to prevent damage occurring to the RE.

All three electrodes are submerged in the electrolyte solution. The electrodes are electrically connected to a potentiostat which allows for the control of the applied potential and the measurement of the current generated by electrochemical reactions occurring at the electrode/electrolyte interface. The potentiostat is connected to a computer to acquire data. The electrochemical cell may be placed in a Faraday cage to minimise electromagnetic noise interferences facilitating lower detection limits.

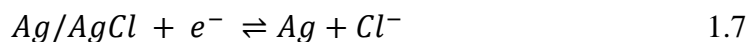
#### ***1.3.4.1 Working Electrode***

The WE is the electrode where the reaction(s) of interest occur(s). A WEs need to be conductive and they are commonly made of noble metals, carbon, liquid metals, and semiconductors. The electrode material and dimensions are selected depending on its application. The electrode surface may be modified to increase its affinity for specific analytes and to reduce reactions with interfering species.

#### ***1.3.4.2 Reference Electrode***

The RE must maintain a stable potential as its purpose is to regulate the WE. The RE should be an ideal non-polarisable electrode, meaning the potential will not change regardless of the current passing through it. The reaction occurring at the RE should be reversible, permitting a potential to be calculated from the Nernst equation. It must also have the capability to recover its potential after a current stress.

The Standard Hydrogen Electrode (SHE) is the standard reference point for standard electrochemical reduction potentials and has a standard potential,  $E^0$ , of 0 V at all temperatures and 1 atm pressure.<sup>42</sup> Maintaining this pressure is often not feasible. Other reference electrodes are therefore employed, such as the silver-silver chloride electrode (Ag/AgCl).<sup>43, 44</sup> This is an inexpensive electrode and its non-toxic components make it favourable over other mercury containing electrodes, such as the Saturated Calomel Electrode (SCE). The Ag/AgCl consists of a silver wire, coated with silver chloride and immersed in a solution containing chloride ions, usually potassium chloride (KCl). The controlling redox reaction is:



Ag/AgCl, KCl (saturated) has a potential of 0.197 V versus SHE.

To prevent contamination of the test solution with unwanted solvent molecules or ions, an inert wire such as platinum or silver can be utilised as a pseudo-reference electrode.<sup>45</sup> They are not ideally non-polarisable electrodes but they do behave predictably under specific conditions, such as a range of pH or temperatures. However, they can be subject to potential drift and need to be calibrated regularly. Their standard potential versus the standard potential of a true reference electrode is known. Therefore, they can be calibrated against a true reference, or alternatively using a well know redox couple.<sup>42</sup> These pseudo-reference electrodes allow for smaller dimensions and are more compatible with emerging POC devices.

#### **1.3.4.3 Counter Electrode**

The CE is generally made from electrochemically inert metals such as platinum, gold or carbon. It is inactive in the reaction conditions and its function is to stabilise the RE. A potentiostat adjusts the voltage to maintain a potential difference between the WE and the RE, whereas it is the current that passes between the WE and the CE that is measured.

#### **1.3.4.4 Supporting Electrolyte**

The supporting electrolyte is employed to reduce the solution resistance and ensure conductivity. An ionic solution containing species such as H<sup>+</sup>, Na<sup>+</sup>, K<sup>+</sup>, Cl<sup>-</sup> in water or a nonaqueous solvent are often adopted. This solution does not undergo a redox reaction and, therefore the ions are spectator ions. They help to reduce the migration effects on the system.



## 1.4 Electrochemical Techniques

### 1.4.1 Chronoamperometry

Chronoamperometry is a technique which applies a potential to an electrode and records the current as a function of time. If the potential is chosen at a region where the kinetics are rapid for the electroactive species causing it to be reduced (or oxidised), and mass transfer is the limiting factor, the net concentration at the electrode surface will be nearly zero. The electroactive species will be promptly reduced (or oxidised) and cause current to flow. This reduction (oxidation) will cause a concentration gradient, which will result in a continual flow of oxidant to the electrode surface through diffusion. As the oxidant (reductant) reaches the electrode surface from the bulk material, this too is reduced (or oxidised) and maintains the flow of Faradaic current. At the same time, the reduced (or oxidised) species diffuses back into the bulk. The current over time can be calculated using Equation 1.6.

As the potential is maintained over time, the region of depleted reactant species near the electrode surface grows out from the electrode. The electroactive species must diffuse across this depleted zone, known as the diffusion layer, to reach the electrode surface. As the diffusion layer increases and the rate of diffusion falls, the current also falls as fewer molecules are available to be reduced/oxidised. The Cottrell equation predicts this current to reach zero over long periods of time. However, experimentally for a Nernstian electron-transfer, this is not observed, rather a steady-state current is reached. The diffusion layer will not grow indefinitely. At a critical dimension from the electrode surface, the bulk solution will maintain a constant concentration of the reactant species, due to the occurrence of natural convection.<sup>46</sup> Fick's first law, Equation 1.5, can be used to calculate the diffusion limited current and determine the changes linearly in the diffusion layer and the diffusive flux.

The current measured is a combination of the faradaic current and the charging current. The faradaic current is of interest as it is typically directly proportional to the concentration of the analyte of interest. At the start of a potential step experiment, the majority of the current flowing is associated with the double layer charging and is thus charging current. Its magnitude depends on the solution resistance,  $R_s$ , and the double

layer capacitance,  $C_{dl}$ , which is directly proportional to the electrode surface area. This decays exponentially with time, however, and leaves the mainly faradaic current attributing to the measured current. Nonetheless, the charging current will always be residually present, though it can be accounted for by performing the experiment in the supporting electrolyte where no charge transfer will occur.

### 1.4.2 Cyclic Voltammetry

Voltammetry is a potential sweep method where the current produced by the electrode is measured as the potential is changed linearly from an initial potential,  $E_i$  to a final potential,  $E_f$ , see Figure 1.4 (a). In the case of cyclic voltammetry (CV), once the final potential is reached, the direction of the sweep is reversed back to the initial potential. This completes one cycle of a CV and multiple cycles can be recorded. The initial potential should be one at which no reaction occurs, and only non-faradaic currents are flowing. As the potential is swept more positively/negatively and passes the formal potential,  $E^{0'}$ , oxidation/reduction occurs producing a faradaic current. In a diffusion-dependent scenario a peak current will be reached. The current then begins to drop off as the concentration of the electroactive species depletes at the electrode surface due to the growth of the diffusion layer. On the reverse sweep, if the molecule is reversible, reduction of the oxidised species will occur. Each peak in a CV coincides with an electrochemical process, with the peak height pertaining to the concentration of the analyte in solution.

Consider a reversible reaction such as the  $Fc/Fc^+$  redox couple mentioned in Section 1.3.1. On the forward sweep,  $Fc$  loses electrons to the electrode becoming  $Fc^+$  and produces an increase in current as seen in Figure 1.4 (b). The  $Fc^+$  is then reduced back to  $Fc$  on the reverse sweep, creating a second peak.

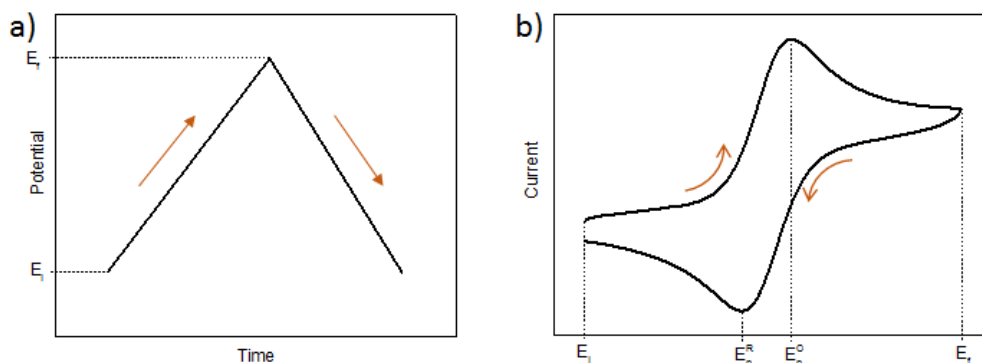


**Figure 1.4:** (a) Waveform for a single cycle CV and (b) the typical current response for a reversible redox couple.

As the peak current,  $i_p$ , is due to a faradaic response, it will be dependent on the bulk concentration of the reactant, according to the Randles-Sevcik equation:

$$i_p = 0.4463 \frac{n^{3/2} F^{3/2}}{R^{1/2} T^{1/2}} A D_0^{1/2} C_0^* \nu^{1/2} \quad 1.8$$

This equation also predicts that the  $i_p$  is proportional to the square root of the scan rate,  $\nu$ . The faster the scan rate the larger the  $i_p$ . This can be explained by the formation of the diffusion layer. The diffusion layer grows with time, thus at a slower scan rate it will have more time to grow. Therefore, the flux of reactants towards the electrode surface reduces at slower scan rates. The magnitude of the current is proportional to the flux of species to the electrode surface.

### 1.4.3 Electrochemical Impedance Spectroscopy

Electrochemical Impedance Spectroscopy (EIS) examines the impedance of an electrochemical cell over a range of frequencies. It is a surface sensitive technique and can detect changes at the electrode surface which may go unnoticed when employing other techniques, such as CV. For this reason, it is often adopted in the field of analytical electrochemistry.

#### 1.4.3.1 Ohm's Law

Ohm's law was established to describe the resistance ( $R$ ) in an electrical circuit:

$$R = E/I \quad 1.9$$

where  $E$  is the circuit potential, and  $I$  is the current. Ohm's law can be considered for direct current (DC) and alternating current (AC) circuits. However, this relationship only applies to an ideal resistor, which has the following properties:

- The circuit follows Ohm's law for all current and potential values.
- The resistance is independent of frequency.
- AC current and voltage signals through the resistor are in phase with each other.

An electrochemical system does not possess these properties. Instead impedance, rather than resistance, is adopted to resolve a circuit's resistance to the flow of current in a complex system.

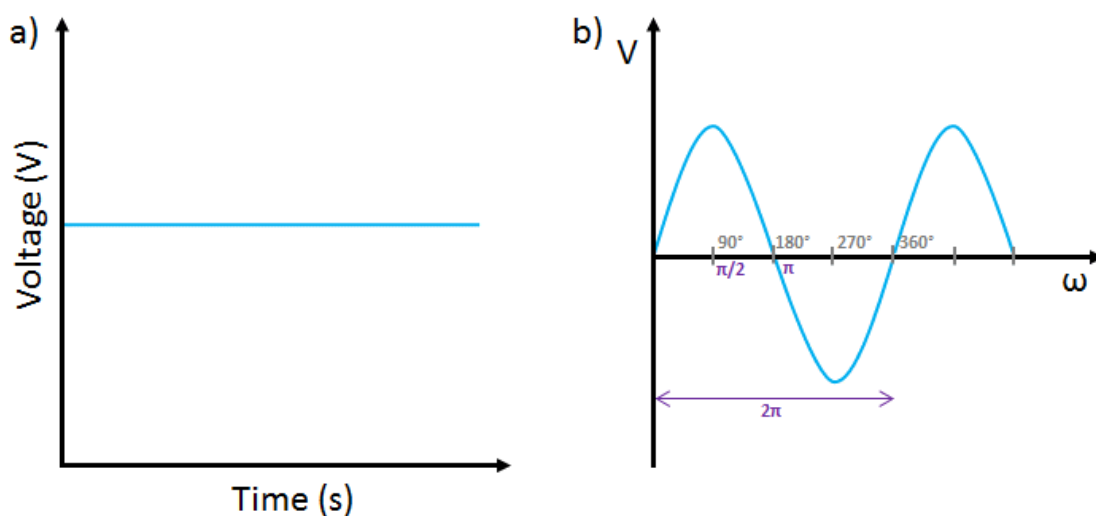


**Figure 1.5:** Plots of voltage vs time for (a) DC and (b) AC.

EIS investigates the AC current response to an AC potential in respect to frequency,  $f$ . A sinusoidal potential is applied to the system and the responding sinusoidal current is measured over a range of frequencies. These sinusoidal responses are at the same frequency but out of phase ( $\phi$ ) with each other. The impedance,  $Z$ , is the relationship between the potential and the current of the system.

$$Z_{\omega} = E_{\omega}/I_{\omega} \quad 1.10$$

where  $Z_{\omega}$  is the frequency-dependent impedance,  $E_{\omega}$  is the frequency-dependent potential and  $I_{\omega}$  is the frequency-dependent current and  $\omega$  is the angular frequency. The excitation voltage can be expressed as a function of time:

$$E_t = E_0 \sin(\omega t) \quad 1.11$$

where  $E_t$  is the potential at time  $t$ ,  $E_0$  is the signal amplitude and  $\omega$  is the angular frequency. The relationship between frequencies  $\omega$  ( $\text{rad s}^{-1}$ ) and  $f$  (Hz) is:

$$\omega = 2\pi f \quad 1.12$$

The responding current can also be expressed as a function of time:

$$I_t = I_0 \sin(\omega t + \varphi) \quad 1.13$$

where  $I_t$  is the current at time  $t$ ,  $I_0$  is the signal amplitude and  $\varphi$  is the phase shift.

A corresponding version of Ohm's law, therefore, can be used to describe AC impedance:

$$Z = Z_0 \frac{\sin(\omega t)}{\sin(\omega t + \varphi)} \quad 1.14$$

This frequency-dependent impedance is expressed in terms of a magnitude,  $Z_0$ , and phase shift.

### 1.4.3.2 Impedance as a Complex Function

It is possible to describe impedance as a complex function, giving it real,  $Z'$ , and imaginary,  $Z''$ , components. To express impedance as a complex function Euler's relationship can be used:

$$e^{j\varphi} = \cos\varphi + j\sin\varphi \quad 1.15$$

where  $j$  is the imaginary component. Similar to equations 1.11 and 1.13, which express the excitation voltage and resulting current as a function of time, the imaginary component can be included:

$$E_t = E_0 e^{j\omega t} \quad 1.16$$

and for the resulting current:

$$I_t = I_0 e^{(j\omega t - \varphi)} \quad 1.17$$

The impedance can therefore be expressed in terms of complex number:

$$Z(\omega) = \frac{E_0 e^{j\omega t}}{I_0 e^{(j\omega t - \varphi)}} = Z_0 e^{j\varphi} = Z_0 (\cos\varphi + j\sin\varphi) \quad 1.18$$

### 1.4.3.3 Reactance

A resistor is an electrical component that hinders the flow of current. Reactance ( $X$ ) is the opposition that an electrical element presents to the flow of AC current, due to its capacitance or inductance. As with resistance, reactance is measured in Ohms.

#### Capacitor

A capacitor consists of two conductive plates which store energy in the form of electric charge and are separated by an insulating medium. It will charge when a voltage is applied to it, causing current to flow into the capacitor. Once "fully-charged" the capacitor will oppose the flow of electrons as its plate becomes saturated. If a DC voltage is then

applied, it will maintain its charge indefinitely until the voltage is removed. When an AC current is applied, it is alternatively charging and discharging as the voltage is continually increased and decreased. The rate of charge and discharge is determined by frequency.

$$X_C = \frac{1}{\omega C} = \frac{1}{2\pi fC} \quad 1.19$$

### **Inductor**

An inductor is a wire coil that stores energy in the form of a magnetic field, which is created when a voltage is applied. Current is initially obstructed from flowing through the inductor, due to a self-induced electromotive force (emf). As this emf decays, the flow of current grows until it reaches a steady state where the emf is zero. However, in an AC circuit, the magnetic field is constantly changing and the opposition to current flow through the coils depends on the frequency of the applied voltage.

$$X_L = \omega L = 2\pi fL \quad 1.20$$

Instead of the current reaching a steady state as is would with a DC circuit, the voltage changes polarity causing the current to change direction. This induces the emf to obstruct the flow of current again.

#### **1.4.3.4 Phase**

As mentioned in Section 1.4.3.1, an ideal resistor has no phase change between the AC current and potential (Figure 1.6 (a)), and can be described as being “in-phase”. For a purely capacitive circuit, the phase shift would be  $-90^\circ$ , as seen in Figure 1.6 (b). A purely inductive impedance would have a phase angle of  $90^\circ$ . All circuits with capacitor or inductor components are “out-of-phase”.

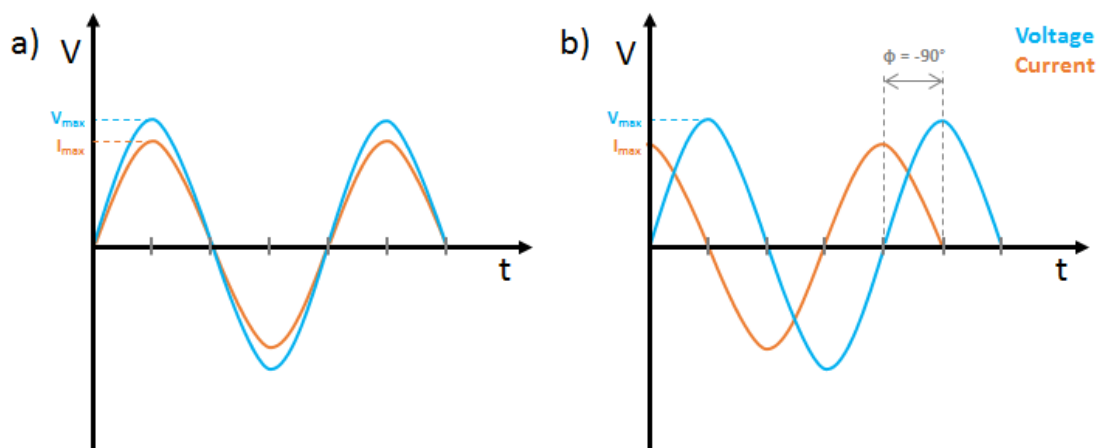


**Figure 1.6:** Sinusoidal wave form of applied voltage and measure current for (a) an ideal resistor and (b) an ideal capacitor.

The sine waves in Figure 1.6 have the same frequency but different amplitudes (i.e.  $V_{max} \neq I_{max}$ ). There is a negative shift in Figure 1.6 (b) as the charge in a capacitor must build up preventing current flow. When the voltage is at its maximum, the capacitor is charging and there is no current flowing. Current will begin to flow as the voltage decreases and vice versa when the current reaches maximum amplitude the voltage is at zero. The capacitor current leads the voltage and will have a negative impedance value for all frequencies. Alternatively, the current lags the voltage for an inductor and its impedance value will be positive for all frequencies.

#### 1.4.3.5 Linearity

Impedance is conveyed for a linear system. Electrochemical cells, however, are not linear as seen in Figure 1.7. Although, if you take a small enough window (1-10 mV), it becomes pseudo-linear. For EIS, the AC signal applied to the cell, referred to as a perturbation, is within this small voltage window to mimic linearity and remove harmonics from the current response wave.

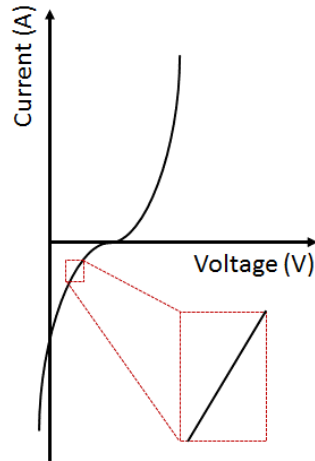


**Figure 1.7:** Current vs voltage for an electrochemical cell.

#### 1.4.3.6 Electrical Circuit Elements

As with the ideal resistor, an electrochemical system will also not possess the properties of an ideal capacitor or inductor. Instead, the electrical circuit is made up of a mixture of these components connected together, in series or in parallel. In this thesis, inductance does not have an effect on the electrochemical systems being investigated and will therefore not be discussed further. As the system is composed of resistors and capacitors, the phase angle will lie between  $0^\circ$  and  $-90^\circ$ .

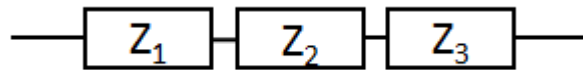


**Figure 1.8:** Impedance components connected in series.

For components in series, the same current is running through each component. The sum of impedance components in series is:

$$Z = Z_1 + Z_2 + Z_3 \quad 1.21$$

The impedance of a resistor is independent of frequency and has no imaginary component to its impedance. Therefore, to calculate the impedance of two resistors in series would be:

$$Z = R_1 + R_2 \quad 1.22$$

Capacitors are inversely proportional to frequency i.e. as the frequency is increased, the capacitor's impedance decreases. The impedance of two capacitors in series would be calculated as:

$$Z = \frac{1}{j\omega C_1} + \frac{1}{j\omega C_2} \quad 1.23$$



where  $j$  is the imaginary component of impedance and  $C$  is the capacitance. Capacitors only have imaginary components to their impedance.

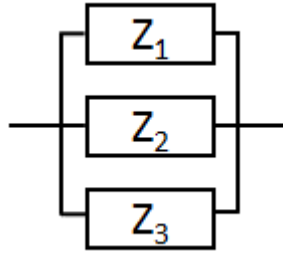


**Figure 1.9:** Impedance components connected in parallel.

For components in parallel, the current is split through the components. The sum of impedance components in parallel is:

$$Z = \frac{1}{Z_1} + \frac{1}{Z_2} + \frac{1}{Z_3} \quad 1.24$$

#### 1.4.3.7 Equivalent Circuit Modelling

Equivalent circuits are constructed in EIS using typical electronic components, such as resistors and capacitors. This circuit accounts for interactions at the electrode/electrolyte interface, such as the formation of the double layer or the occurrence of charge-transfer. The most commonly used circuit is the Randles circuit.<sup>47</sup> It consists of solution resistance ( $R_s$ ), charge-transfer resistance ( $R_{ct}$ ), double layer capacitance ( $C_{dl}$ ) and a Warburg element ( $W$ ) as shown in Figure 1.10. A modified version of this circuit is used in all the modelling in this thesis.

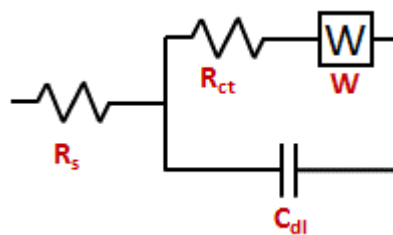


**Figure 1.10:** Randles circuit.

#### Solution Resistance ( $R_s$ )

A cell experiences resistance as a voltage is passed from the working electrode, through an ionic solution, to the reference electrode. The resistance is affected by the solution properties such as ionic concentration, ion type, temperature, and the cell's geometry. For a fixed current carrying area  $A$  and length,  $l$ , the resistance is described as:

$$R = \rho \frac{l}{A} \quad 1.25$$

where  $\rho$  is the cell resistivity. Conductivity,  $\kappa$ , is often used as a reciprocal for resistivity, giving the resistance as:

$$R = \frac{l}{\kappa A} \quad 1.26$$

### **Double Layer Capacitance ( $C_{dl}$ )**

As discussed in Section 1.3.3, changing the voltage of an electrode causes a double layer to form at the electrode/electrolyte interface. This double layer acts as an insulator, separating the charged electrode from the charged ions, causing the electrode to act as a capacitor.

### **Charge Transfer Resistance ( $R_{ct}$ )**

Faradaic processes cause electrons to be transferred between the electrode to and from the species in solution.  $R_{ct}$  is the resistance to this transfer of electrons. The kinetics of the electrochemical reaction will factor into the magnitude of the  $R_{ct}$ .

### **Warburg Element (W)**

Warburg impedance is caused by diffusion and depends on the frequency of the potential perturbation. At high frequencies, the diffusing species have a small distance to cover and the Warburg impedance is small. At low frequencies, the species have to diffuse much further, and the Warburg impedance is large.

### **Constant Phase Element (CPE)**

Other components, such as CPEs, may have to be added to the Randles circuit to account for the overall impedance of a system. CPE is the circuit component for an imperfect capacitor. There are several factors which induce imperfect capacitive behaviour in electrodes, such as the roughness of the surface.<sup>48</sup> The crystal structure of the electrode can also come into play. Polycrystalline metals have an inhomogeneous distribution of active sites causing varying rates of reaction across the electrode.<sup>49</sup> Additionally, electrode coatings often have varying thicknesses and, if the bulk conductivity of a coating changes with thickness, the impedance will also be affected.<sup>50</sup> Current is often distributed non-uniformly across an electrode. Homogeneous distribution is experienced at the centre of the electrode but becomes perturbed at the edge. A CPE is used to account for the heterogeneous characteristics of the electrode surface.

### 1.4.3.8 Data Presentation

#### Nyquist Plot

A Nyquist plot shows the relationship between the real and the imaginary components of impedance. The imaginary axis ( $-Z''$ ) has a negative value as capacitance, its contributing component, always has a negative phase shift. Two distinctive features are seen in Figure 1.11, which coincides with Randles cell. Firstly, a semicircle forms which then transforms into a diagonal line. The semicircle data is produced by the kinetically controlled process. Here charge transfer is occurring which has a resistive element yielding a real impedance component. This coincides with the charging of the double layer, generating an imaginary impedance, hence the resulting semicircle shape. The diagonal line shows the effects of diffusion on the system which causes Warburg impedance as previously mentioned.

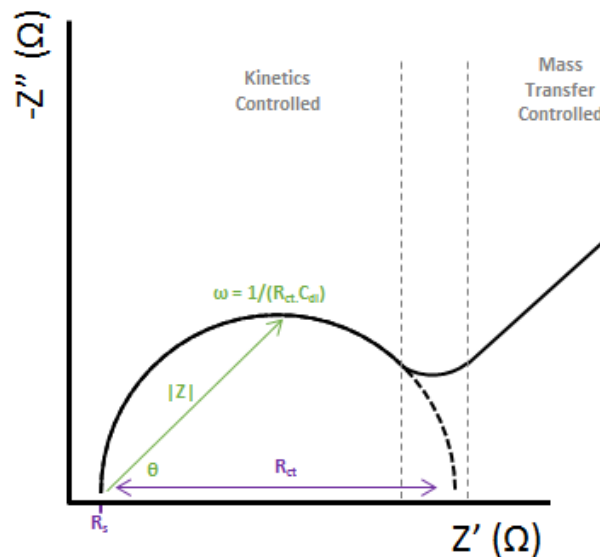


**Figure 1.11:** Nyquist plot as expected from a Randles equivalent circuit.

The plot moves from high frequency to low frequency. The high frequency intercept of the x-axis ( $Z'$ ) gives the value for the  $R_s$  and the low frequency intercept is the sum of  $R_s$  and  $R_{ct}$ . Therefore, the diameter of the semicircle corresponds to the  $R_{ct}$ . The modulus impedance,  $|Z|$ , can be represented as a vector going from the start of the semicircle to the maximum  $-Z''$  value within the circle. The angle between this vector and the x-axis is the phase angle.

### Nyquist Plot for Ultramicroelectrodes

Ultramicroelectrodes have a critical dimension of  $\leq 25\mu\text{m}$ <sup>51</sup> and are discussed in detail Section 1.5. At these dimensions, the effects of diffusion are no longer seen and a Simplified Randle circuit (Figure 1.12 inset) can be used to model these systems. The Warburg element is no longer needed as the Nyquist plot only contains its semicircle feature.<sup>52</sup>

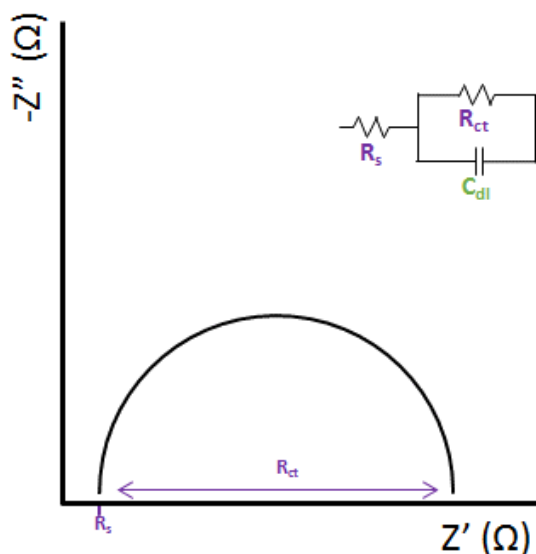


**Figure 1.12:** Nyquist plot for UME with equivalent circuit model inset.

The semicircle is characteristic of a single time constant. A plot can contain several time constants, though sometimes a semicircle is only partially visible. These tell us about the timescale at which different processes occur with smaller time constants appearing at higher frequencies. The time constant is inversely proportional to the  $\omega$ .

### Bode Plot

The main disadvantage of the Nyquist plot is it doesn't show the frequency-dependency of impedance. For this information the Bode plot can be considered. This plot actually consists of two plots; the bode modulus represents the frequency-dependency of the overall impedance, and the bode phase represents the frequency-dependency of the phase shift. Both are plotted against the logarithm of the excitation frequency and can share an x-axis, as seen in Figure 1.13.

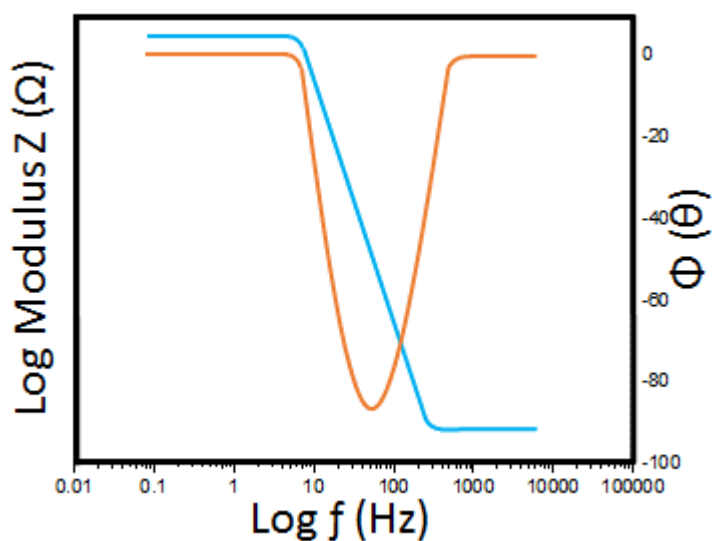


**Figure 1.13:** Bode plot with the impedance modulus (blue) and the phase angle (orange) vs log of the frequency.

Bode plots can be especially beneficial for studying high frequencies as the data on a Nyquist plot becomes densely packed as  $\omega \rightarrow \infty$ . The logarithmic scale of the x-axis for the bode modulus gives the impedance equal weight at high frequencies along the plot as at low frequencies. However, the logarithmic scale does not allow for clear analysis of diffusion, which is better studied using the Nyquist plot. The capacitive behaviour is seen in the bode phase at low frequencies as the angle approaches  $-90^\circ$ . If the response does not reach this limiting angle, then the behaviour is not purely capacitive. This deviation from ideal behaviour can be modelled using a CPE.

## 1.5 Macroelectrodes vs. Ultramicroelectrodes

A macroelectrode is a relatively large electrode, typically in the millimetre range. A microelectrode is an electrode with a critical dimension in the micrometre range, and a nanoelectrode is an electrode with a critical dimension  $\leq 100$  nm.<sup>53, 54</sup> Ultramicroelectrodes (UME) can have dimensions in the micrometre or sub-micrometre range ( $\leq 25$   $\mu\text{m}$ ), but generally are smaller than the diffusion layer formed during electrochemical processes.<sup>51</sup> Effectively, ultramicroelectrodes and nanoelectrodes display enhanced mass transport, over microelectrodes, due to their small critical dimension.<sup>55, 56</sup>

At short times, i.e. fast scan rates, the diffusion layer is relatively small compared to the critical dimension of the electrode. In this case, the electrode current follows Cottrell's equation (Equation 1.6) and planar diffusion dominates (Figure 1.14 (a)). At slow scan rates, the diffusion layer has time to exceed the critical electrode dimension, thus a radial diffusion prevails. With radial diffusion (Figure 1.14 (c)), the diffusion layer moves further out into the bulk solution and more of the solution contributes to the flux at the electrode.<sup>57</sup> This produces a steady-state response, where the rate of electron-transfer equals the rate at which the electroactive species diffuse to the electrode surface. As seen in Figure 1.14 (d), the CV no longer has a drop off in current after the peak current is reached. Instead a sigmoidal response is produced due to the radial diffusion.

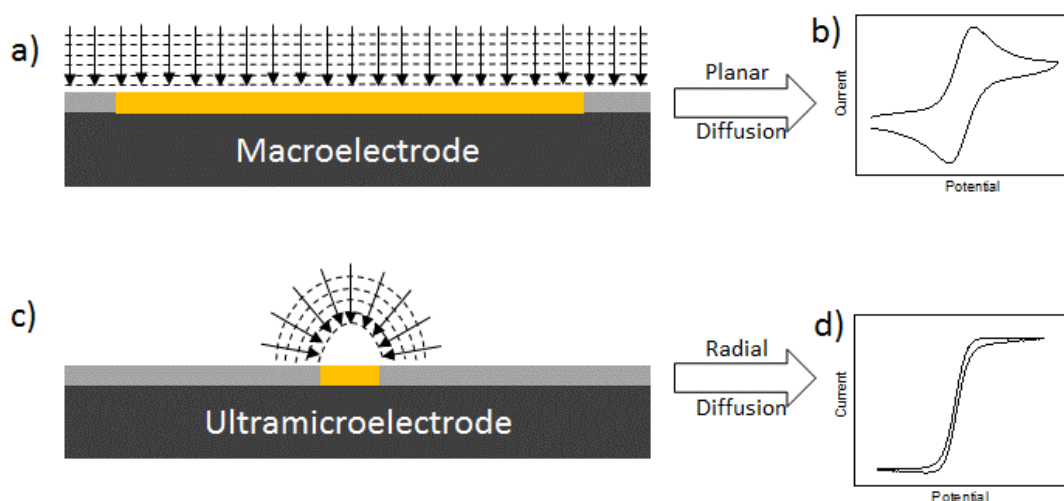


**Figure 1.14:** (a) Planar diffusion at a gold microelectrode and (b) its diffusion limited CV response for to a  $\text{Fc}/\text{Fc}^+$  redox couple. (c) Radial diffusion at a gold UME and (d) its steady-state CV response to a  $\text{Fc}/\text{Fc}^+$  redox couple.

Although it is possible to see steady-state behaviour at a macroelectrode, the time scale would be experimentally impractical. For an UME electrode, the time it takes for the diffusion layer to become larger than the critical dimension is extremely fast. Therefore steady-state behaviour is seen for general experimental set-ups. The steady-state current,  $i_{ss}$ , can be calculated using the following equation:

$$i_{ss} = nFAm_oC_0^* \quad 1.27$$

where  $m_o$  is the mass transfer coefficient, which depends on the geometry of the electrode. Typical UME geometries include hemispherical electrodes, disk electrodes, band electrodes, and cylindrical electrodes. For band and cylindrical UMEs, the non-critical dimension (the length) can be much larger. Unlike diffusion limited peak currents, the steady-state current is independent of scan rate. Additionally, the double layer charging current reduces with electrode area, resulting in less capacitance in an UME set-up. Overall, UMEs have enhanced mass transport resulting in high current densities; they have fast response times which allows study of faster kinetics; excellent signal-to noise ratio, and require small sample volumes due to their diminished sizes.<sup>54, 58</sup>

Arrays of ultramicroelectrodes are often employed as they can achieve steady-state with higher current outputs allowing for lower detection limits.<sup>59, 60</sup> For an array to have the benefits of a single UME, they must not interact with each other as electrochemical processes are occurring, i.e. are diffusionally independent, Figure 1.15 (a). If their diffusion profiles overlap, as in Figure 1.15 (b) the electrodes behave as a single macroelectrode and exhibit planar diffusion, therefore limiting the current measured. When fabricating UME arrays the distance between each electrode must be carefully considered, to ensure steady-state performance.

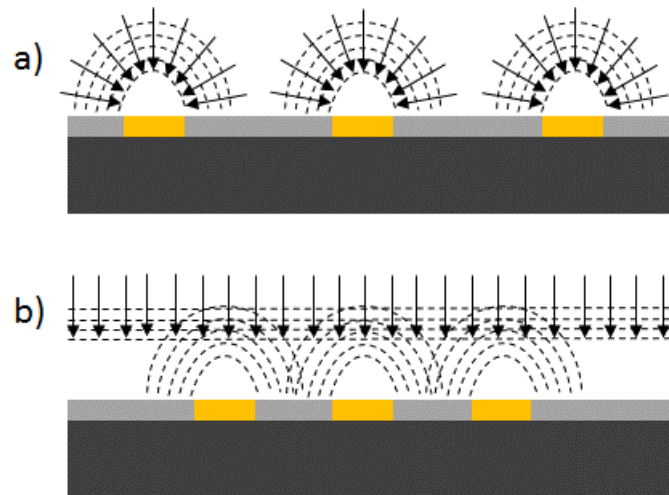


**Figure 1.15:** Schematic of UME arrays where (a) the individual electrodes are sufficiently separated to exhibit radial diffusion and (b) where the diffusion profiles of the individual electrode overlap and combine to exhibit planar diffusion.



## 1.6 Fabrication of UMEs

Disk shaped UMEs can be fabricated by encapsulating fine wires into glass capillaries and sealing them with a Bunsen burner. Pipette pullers can be used to taper the glass around the wire, thus decreasing the disk diameter.<sup>51</sup> This simple fabrication method is ideal for lab-based experiments. However, it is limited to single UMEs and is not compatible with mass production. Hence, other methods are employed for UME arrays and developing electrodes for commercialisation.

Microelectrodes are commonly fabricated on a silicon substrate,<sup>59, 61</sup> but substrates such as glass and quartz can also be used.<sup>62-64</sup> A standard silicon wafer with a thermally grown oxide layer is compatible with lithography masks and evaporation techniques as well as providing a platform for mass production. UV lithography can produce features as small as 100 nm.<sup>65</sup> Thin metal films can be deposited by chemical vapour deposition (CVD), electron beam evaporation or sputtering of a target.<sup>59, 61</sup> A photoresist layer can be spin coated onto the silicon wafer and patterned using UV lithography, along with a photomask. Depending on whether the photoresist is positive or negative, areas irradiated with the UV source will either become soluble and are removed from the substrate or will become insoluble and remain on the substrate, respectively. Figure 1.16 (a) outlines using a positive photoresist spin coated directly onto the substrate surface. Once the photoresist is developed, the metal layer is then deposited on top of the patterned resist. Gaps in the resist layer allow for the metal layer to form the desired pattern on the substrate surface. The sacrificial resist layer is then dissolved in an appropriate solvent, “lifting-off” the metal that is not in direct contact with the substrate. Alternatively, the metal can be deposited prior to the photoresist, as outlined in Figure 1.16 (b). The same method is used to pattern the resist and after development, the remaining resist protects the underlying resist during subsequent etching processes. Wet-etching or dry-etching can be used for further processing of the structures. Wet etching uses potassium hydroxide (KOH), ethylene diamine pyrochatechol (EDP), and tetramethyl ammonium hydroxide (TMAH) which have high material selectivity.<sup>66</sup> Dry etching uses techniques such as plasma etching, reactive ion etching (RIE), and ion milling, which can produce smaller pattern lines.<sup>66</sup> After etching the resist can be removed with the appropriate solvent. Finally, the wafer is coated with an insulating layer. This is generally deposited plasma enhanced

chemical vapor deposition (PECVD) and RIE is used to define the electroactive areas of the UMEs.<sup>59, 67</sup>

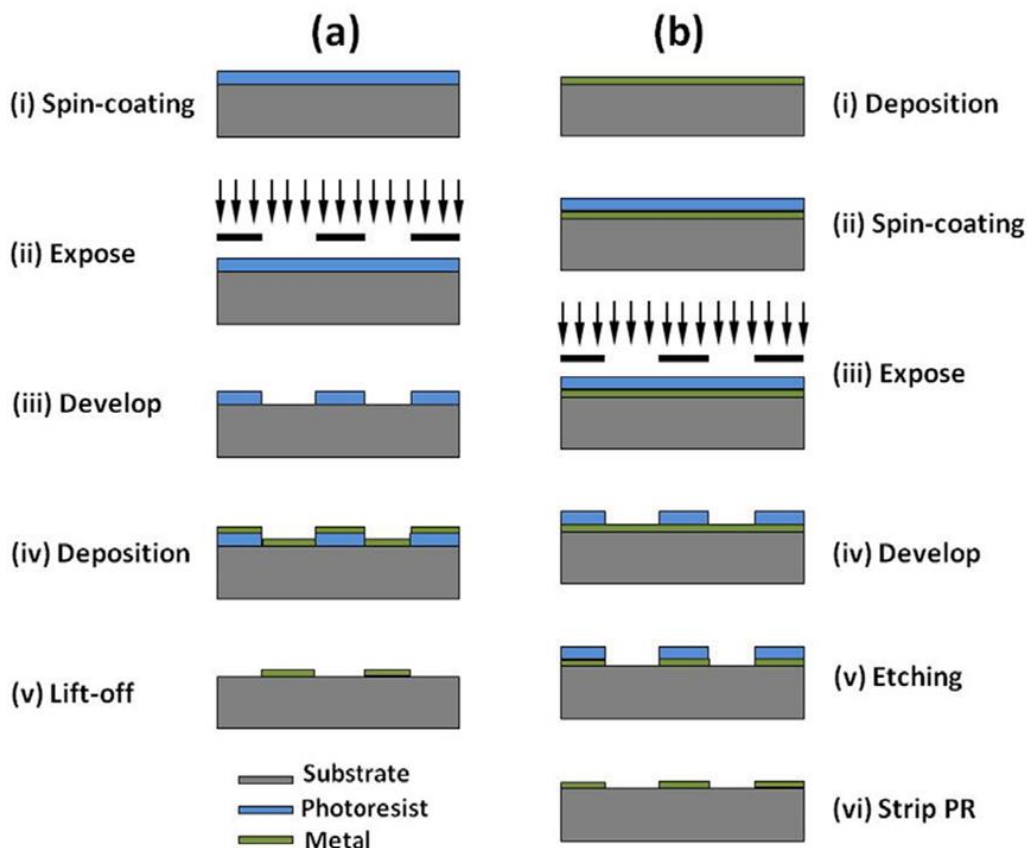


**Figure 1.16:** Fabrication process for developing electrodes using UV lithography. (Taken from <sup>66</sup>)

Aside from UV lithography, other patterning methods include electron beam lithography (EBL),<sup>68</sup> focused ion beam (FIB),<sup>69</sup> and laser ablation<sup>70</sup> which can directly write the pattern into the resist layer without a mask. These methods are costly but have higher resolution (2.5 – 10 nm) than a mask can offer.<sup>71-73</sup>

Printing techniques provide a route to fabricating UMEs on flexible surfaces. These can either be contact (microcontact printing, transfer printing and nanoimprinting) or non-contact (screen printing and inkjet printing) methods. Microcontact printing uses a long alkyl chain thiol to form a SAM layer on Au and act as an etchant resist. As seen in Figure 1.17, an elastomer, typical polydimethylsiloxane (PDMS), which is cast from a master, is used as a stamp to generate patterned SAM on the Au surface. Once the sample is wet etched, the inverse of the master structures is formed. The master can be repeatedly replicated and the PDMS stamp is durable to multiple uses making this an economic

method, however, it does have limitations.<sup>74</sup> The SAM layer may contain pinholes which allow covered areas to be etched. An excess of SAM “ink” on the PDMS stamp will cause the SAM to diffuse into areas not in contact with the stamp. Additionally, stamp deformation may occur during removal from the master or during contact with the substrate.

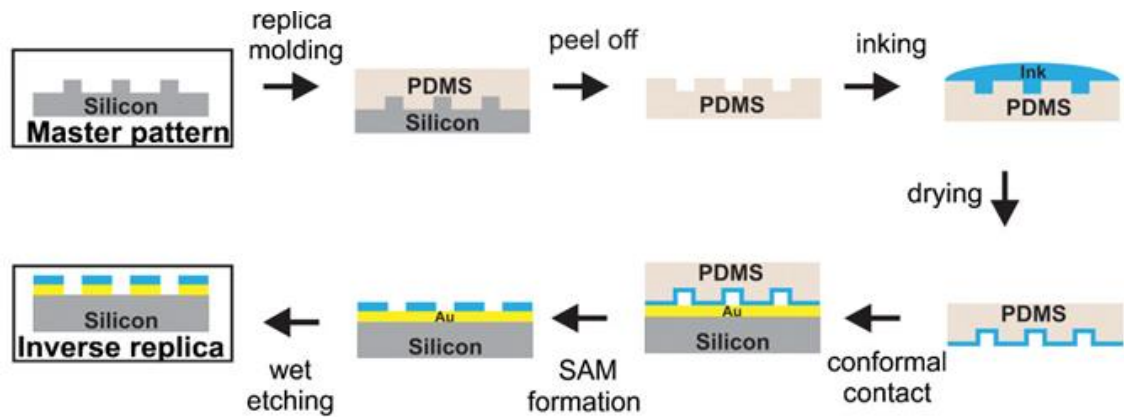


**Figure 1.17:** Fabrication process for developing electrodes using microcontact printing. (Adapted from<sup>74</sup>)

Transfer printing also utilises a PDMS stamp cast and cured from a master. An additive (Figure 1.18 (a)) or subtractive (Figure 1.18 (b)) transfer method can be used. For the additive method, the “ink” is deposited onto the patterned stamp. The stamp and receiving substrate are pressed together. By slowly peeling the PDMS stamp, the printable ink is transferred onto the substrate surface. This process relies on receiving substrate having higher adhesion to the ink compared to the PDMS stamp.<sup>75</sup> Alternatively, the ink can be deposited directly onto the substrate. Once the PDMS stamp is pressed into the ink and peeled away it removes areas of ink from the substrate with it. Both methods of transfer can be aided by chemical modification of the receiver, heat, or thin intermediate polymeric adhesion promoting layers between the stamp and ink.<sup>76</sup> Additionally transfer printing has been successfully used to transfer silicon microwires from one substrate to another.<sup>77</sup> A smooth PDMS stamp was used to pick up free standing silicon microstructures from on top of an Si wafer and transferred to a flexible substrate with controlled orientation.

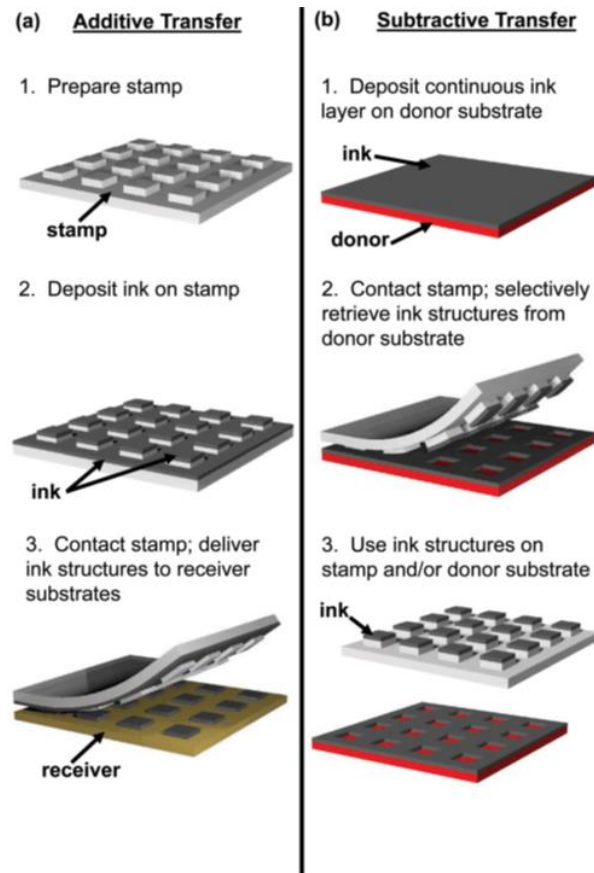


**Figure 1.18:** Fabrication process for developing electrodes using transfer printing. (Adapted from <sup>76</sup>)

Nanoimprinting lithography (NIL) patterns a wet resist layer using either a hard or soft stamp. The stamp is pressed into the resist layer coating the substrate to create a thickness contrast as in Figure 1.19. A thin residual layer of resist remains to prevent direct impact with the underlying surface which may damage the stamp's features.<sup>78</sup> This residual layer is first etched to complete the pattern definition, followed by the etching of the substrate. This technique has high patterning resolution of 3D structures over a large area with high throughput and low cost.<sup>77</sup> However, mechanical damage can be sustained by both the stamp and moulded structures during the moulding and demoulding steps if the critical force is exceeded.<sup>79</sup>

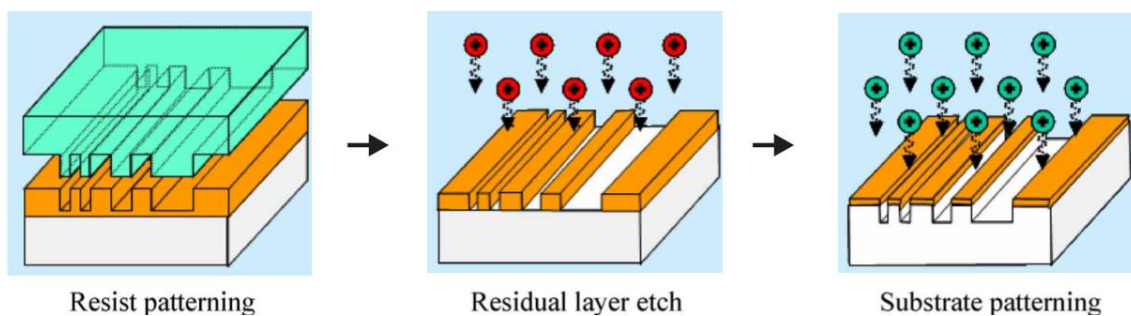


**Figure 1.19:** Fabrication process for developing electrodes using NIL. (Adapted from <sup>79</sup>)

Screen printing is becoming increasingly popular for fabricating disposable electrochemical sensors as planar electrodes can be printed on cheap plastic or ceramic supports and a wide variety of these devices are commercially available.<sup>80</sup> Ink is squeegeed through openings in the stencil to create the desired pattern and heat treated. Using various stencils a layer-by-layer assembly can produce a three-electrode system as presented by Chang and Zen.<sup>81</sup>

Inkjet printing allows for direct patterning onto the substrate surface. Ink is ejected through a nozzle via piezoelectric action. The ink droplets fall onto the surface under gravity and air resistance. Once on the surface it spreads under momentum, aided by the surface tension along the surface before drying through solvent evaporation.<sup>82</sup> Therefore, the final print shape will depend on the drop height and ink viscosity. Inkjet printing can also be used for 3D printing, which builds three-dimensional objects by stacking 2D layers. This technique has generally been restricted to fabricating electrochemical cells, microfluidics, and supercapacitors.<sup>83</sup> However, due to low cost, direct writing, and fast turnover for prototypes, work has branched out to include electrode fabrication as well. 3D printers can employ different fabrication techniques, which includes but is not limited to the following techniques.<sup>84</sup> Inkjet printing, as previously mentioned, which uses solid particles bonded layer by layer *via* adhesion or UV light has a resolution of 68 x 68 x 32  $\mu\text{m}$ .<sup>84</sup> Polyjet printing which uses liquid material which requires curing with UV light between each layer has a resolution of 1.7 x 1.7 x 16  $\mu\text{m}$ .<sup>85</sup> Stereolithography which also cures each layer with UV light and the has the substrate placed in a resin bath has a resolution of 30 x 30 x 5  $\mu\text{m}$ .<sup>86, 87</sup> All these techniques require support material, unlike fused deposition modelling. This technique lays out layers of semi molten thermoplastic filaments and has a resolution of 125 x 125 x 100  $\mu\text{m}$ .<sup>84, 88</sup> To create the conductive electrode either stainless-steel electrodes are printed and electroplated with a suitable

metal coating or carbon based electrodes are printed from materials such as carbon nanotubes (CNTs), graphene or carbon black mixed with a thermoplastic.<sup>89</sup> Zhu et al.<sup>90</sup> have printed 3D graphene aerogels microlattices which had large surface areas and good electrical conductivity. Stainless-steel is often chosen to create helix shaped electrodes for DNA detection<sup>91</sup> heavy metals,<sup>92</sup> nitroaromatic explosives,<sup>93</sup> and acetaminophen and dopamine.<sup>94</sup> Printing techniques generally have low fabrication costs, reduced material waste and offer simple patterning techniques on wafer-scale. However, they would not have the same the same resolution as UV lithography.

Micro-injection moulding is commonly used for polymer-based electrodes as it can produce 3D structures at high rates, relatively low costs and has mass-production capabilities, with the potential for full-automation.<sup>95, 96</sup> It involves the heating of a thermoplastic so it becomes molten and can be injected into a mould cavity. It is subjected to pressure to compensate for material shrinkage and cooled to solidify in the shape of the mould. A wide range of thermoplastics are available and accurate shape replication and dimension control is found.<sup>95</sup> Literature shows inconsistencies on parameters including the mould temperature, the polymer temperature and the injection rate. For instance, a high injection rate can improve the filling of microstructures but may result in poor edge definition.<sup>97</sup>

## 1.7 Impedimetric Biosensors

A biosensor is an analytical device which combines a biological component with a transducer to convert a biological response into a detectable electronic signal.<sup>98</sup> It has three components, (i) the bio-recognition site, (ii) the transducer; and (iii) the reader. The bio-recognition site or bioreceptor is the biological component that will interact with the analyte. This must selectively recognise the analyte of interest. Common bioreceptors include microorganisms, antibodies, enzymes, cells, and DNA. The transducer converts the event at the bio-recognition site into a measurable signal, which is proportional to the analyte/bioreceptor interactions. Examples of transducers include optical, electrochemical, piezoelectric and electrochemiluminescent devices. Their signal is processed by the reader and displayed in a user-friendly format.

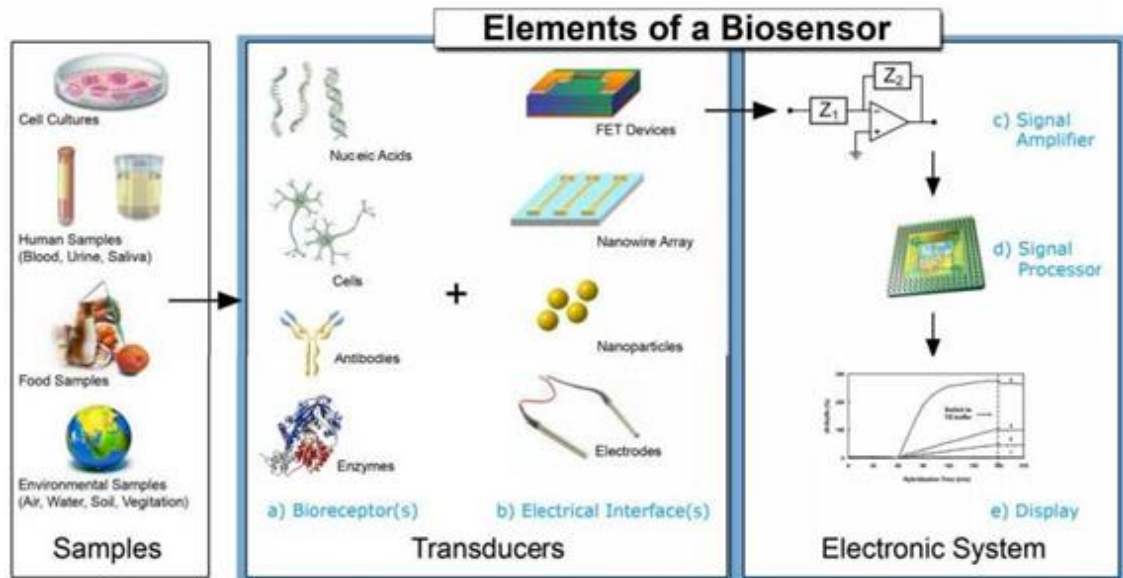


**Figure 1.20:** Elements of a biosensor. (Taken from <sup>98</sup>).

### 1.7.1 Antibodies and Antigens

An immunosensor is a biosensor which exploits the highly specific antibody/antigen interaction. Either an antigen is immobilised onto the transducer surface and detects the antibody, or the antibody is the bioreceptor immobilised on the transducer and it detects the antigen. The interaction between the antigen and antibody cause a variation in electric charge, mass, optical or temperature properties detectable by the transducer.<sup>99, 100</sup> This thesis focuses on electrochemical immunosensors which exploit EIS as the transduction signal.

Antibodies, or immunoglobins (Ig), are glycoproteins produced by mammalian white blood cells, more specifically B-lymphocytes, to elicit an immune response.<sup>101</sup> They bind to proteins (antigens) on the surface of pathogenic organisms e.g. bacteria, viruses, fungi, parasites, targeting them for destruction by the immune system.<sup>102</sup> Antibodies recognise specific epitopes on the surface of the pathogen allowing the antibodies to either neutralise the foreign entity or facilitate further immune responses.

Antibodies are composed of one or more Y-like units (monomer).<sup>103</sup> Each unit contains four polypeptide chains: two identical heavy chains (H) and two identical light chains (L), which are held together by disulfide bonds.<sup>104</sup> Each polypeptide chain has a constant (C) and a variable (V) region. The H chain consists on one variable region  $V_H$ , and three constant regions  $C_{H1}$ ,  $C_{H2}$ , and  $C_{H3}$ . The light chains consist of one variable  $V_L$ , and one constant  $C_L$  region. The variable domains of the heavy and light chains form two antigen-binding sites (paratopes), creating a bivalent unit. The immunoglobulin monomer structure is additionally classified by its fragments. Primarily the structure is isolated into two groups, the Fc and Fab regions.<sup>105</sup> The constant domain containing Fc region is the class defining region which has no antigen binding capabilities. It is in the Fab fragment that binds the antigen to the structure. The Fab comprises of one constant and one variable region from each heavy and light chain. The variable region of the antibody can also be referred to as Fv, which constitutes the paratope.



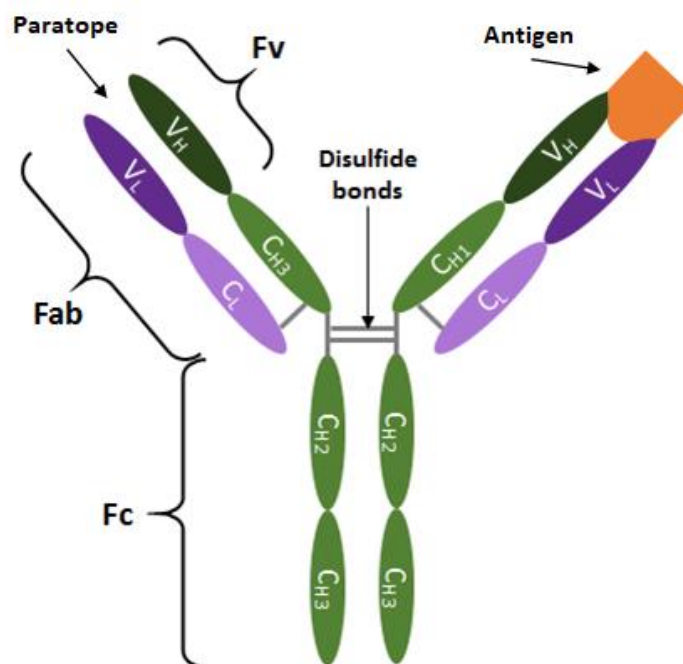


**Figure 1.21:** Structure of antibody monomer and paratope-epitope interaction.

An impedimetric sensor may be based on the EIS technique discussed in Section 1.4.3. It measures the resistive or capacitive behaviour of an electrochemical system. By immobilising the bioreceptor to the electrode surface, the antibody-antigen binding event will create a change at the interfacial region and elicit an impedimetric response. Since EIS is sensitive to fluctuations on the electrode surface, it facilitates label-free detection. This is highly advantageous as biosensors typically require a label such as a fluorophore, enzyme, or nanostructure to enable detection. Labelling techniques can change binding properties of biomolecules, increase costs, increase assay time, and requires extra sample handling making them unsuitable for POC devices.<sup>106</sup> In order to create a label-free impedimetric immunosensor, the bioreceptor must first be immobilised onto the electrode surface. This immobilisation requires electrode surface to be modified first.

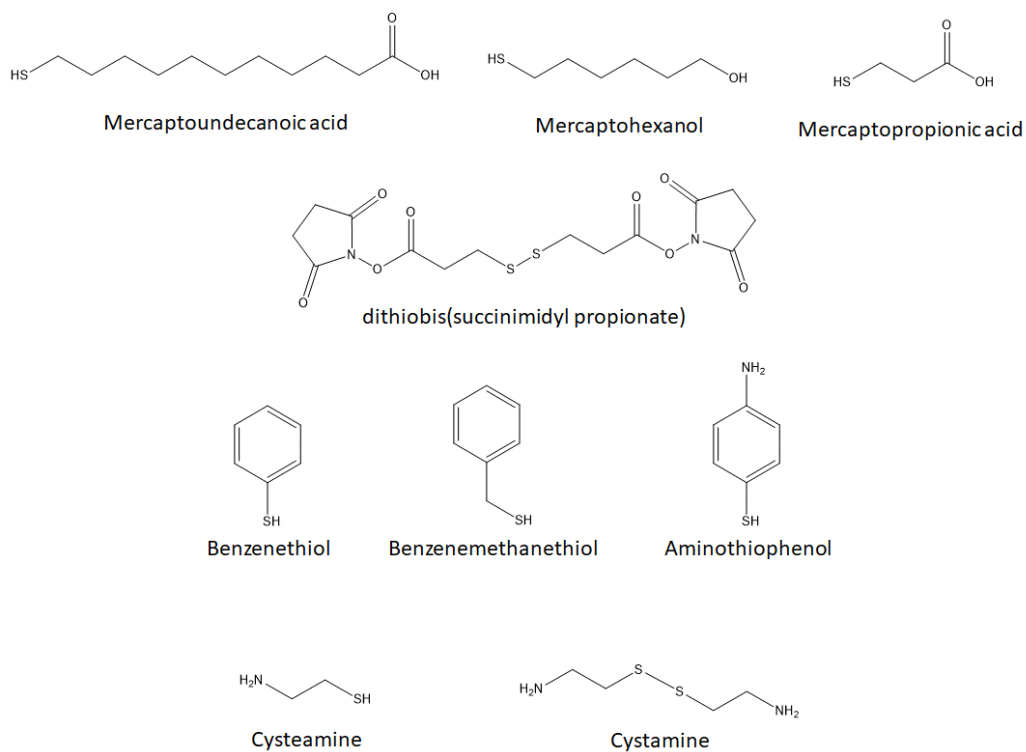
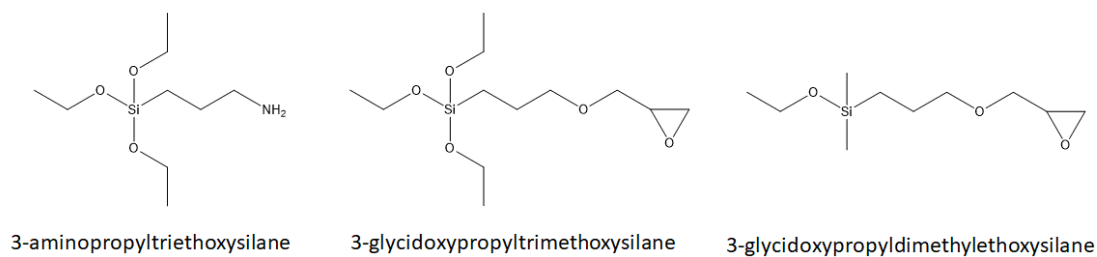
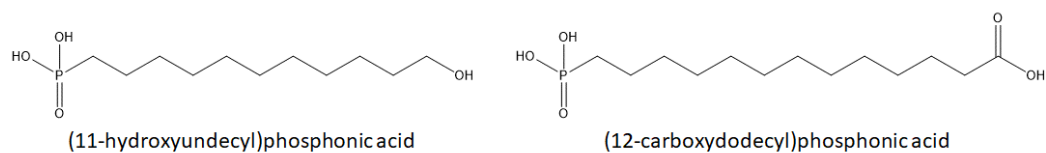
## 1.7.2 Electrode Modifications

Biomolecules, such as antibodies, can physically adsorb directly onto an electrode to form the bioreceptor. This adsorption process leads to a variation in antibody orientation, strength of the surface binding, and antigen accessibility, all of which will affect the sensor's response. Fab' fragments, which consist of the Fab region with a free sulfhydryl group, alone can chemisorb directly onto gold electrodes as they can form a thiolate bond with the gold substrate. This has the advantage of favourably orientating the antigen

recognition site.<sup>107-109</sup> In order to produce the Fab' fragment, the Fc region must first be cleaved with an enzyme, leaving a F(ab')<sub>2</sub> fragment. The disulfide bond (Figure 1.21) can then be reduced to separate the two Fab' fragments. This does present an issue however, in that additional disulphide bonds i.e. those that connect heavy and light chains, may also be reduced, resulting in damage to the antigen recognition site<sup>108</sup> To allow use of the entire antibodies structure in the correct orientation and with satisfactory antigen accessibility, electrode modifications are undertaken to immobilise the antibody bioreceptor to the electrode. This can also lead to increased surface binding strength compared to physisorption. Surface modifications must have available functional groups for linking to the bioreceptor and be stable in storage. Examples of such modifications include self-assembled monolayers, polymers and nanostructures.

#### ***1.7.2.1 Self-Assembled Monolayers***

Self-assembled monolayers (SAM) consist of molecules which will spontaneously adsorb onto a surface, forming a film with relatively uniform molecular orientation and conformation, and close-packed adsorbate molecules.<sup>110, 111</sup> One end of the SAM molecule is designed to have a favourable interaction with the transducer surface, creating a stable monolayer.

**Thiols and Sulphides****Silanes****Phosponates**

**Figure 1.22:** Molecular structure of self-assembled monolayers.

## Thiols and Sulphides

Thiols are organic compounds which are terminated by an -SH group. It is this terminal group that favourably interacts with the electrode surface. The other terminal generally consists of a carboxyl or amine group which allow for the immobilisation of biomolecules. The formation of a thiol-based SAM consists of a two-step process; the first step is the fast, physical adsorption of the thiol molecules onto the surface, with some of the molecules orientated perpendicular to the surface. The second step is much slower and involves the physisorbed layer being converted to a chemisorbed monolayer and reordered to be parallel to the surface.<sup>110</sup>

Alkanethiols are the most established SAMs used for biosensors. Long alkyl chain thiols display a higher degree of order due to the attractive van der Waals forces between adjacent chains,<sup>112, 113</sup> and exhibits a tilt of  $\sim 30^\circ$  in the direction of its nearest neighbour,<sup>114, 115</sup> suggesting longer alkanethiols ( $\geq 10$  alkyl carbons) would be advantageous for an electrode modification. However, long chains produce a densely packed monolayer which restricts access to the underlying electrode surface, inhibiting electrochemical processes. Conversely, short chains have a large tilt angle and low coverage but do not restrict access to the electrode surface. For electrochemical sensing applications, therefore, mixed thiols are often employed using a short chain thiol to disrupt the long chain SAM.<sup>116-119</sup> Mixed monolayers also allow for large bioreceptors to be sufficiently spaced apart, reducing steric hindrance, as well as allowing access for mediator molecules to the electrode surface.

Alkanethiol SAMs are stable at potentials between approximately 0.8 and 1.4 V versus SCE,<sup>120, 121</sup> which is compatible with most electrochemical applications. Outside of this potential window, the thiol may be oxidised or reduced, causing them to desorb from the surface.<sup>120, 122, 123</sup> The exact potential at which this desorption occurs is dependent on the alkanethiol's structure including the length of the alkyl chain. This can be used to control the formation of the SAM, as demonstrated by Satjapipat et al.<sup>124</sup> Their mixed SAM consisted of 3-mercaptopropionic acid (MPA) and mercaptohexanol (MCH). MPA was selectively removed by reduction desorption, resulting in bare regions on the substrate. The electrode was then placed in a solution of thiolated DNA (the bioreceptor), before the remaining adsorbed MCH could diffuse across the surface to cover the bare regions.

Instead, the thiolated DNA filled these bare regions. A similar protocol could be adopted to create an immunosensor using thiolated antibodies. For the absorption of a mixture of two alkanethiols, the mole fraction of each thiol in solution reflects, but is not equal to the mole fraction of it as an absorbate in the SAM. Experimental conditions influence the ratio of absorbates in the SAM formed on the substrate surface. Again, the length of the alkyl chain is significant, with a bias towards the longer alkanethiol which increases over time.<sup>125</sup> The choice of solvent can also be a factor if the SAM is formed from a mixture of polar and non-polar molecules.<sup>125-127</sup>

Asymmetric disulfides (RSSR') pose an alternative for forming mixed SAMs, though they have lower solubility. Their S-S bond cleaves to form a bond between the metal of the electrode surface and the sulphur molecule (M-S), as with thiols. As with a mixed SAM using two different alkanethiols, asymmetric disulfides do not present a 1:1 ratio of absorbates in the SAM due to shorter chains being substituted with longer chains. This is again due to the thermodynamically favourable van der Waals interactions between the longer hydrocarbon chains.<sup>128</sup> Symmetrical disulfides, such as dithiobis(succinimidyl propionate), DSP, can also be employed for the attachment of proteins to an electrode surface. This presents an attractive surface modification alternative due to the N-hydroxysuccinimide ester terminal groups, which facilitate binding to a bioreceptor without an intermediate step or cross-linker molecule.<sup>129, 130</sup>

Other popular thiols include aromatic thiols, cysteamine, and cystamine. SAMs formed with the aromatic thiol, benzenethiol (BT), has been shown to be disordered, with inconsistent tilts of the phenyl ring, as both sp and sp<sup>3</sup> hybridised sulphur atoms existing in the monolayer.<sup>131</sup> As with alkanethiols, if a long chain is substituted in the para-position, interchain interactions will increase leading to a more densely packed monolayer. Alternatively, benzenemethanethiol (BMT) which has an alkyl spacer group between the sulphur and phenyl group, forms a stable, orientated monolayer, similar to that of an alkanethiol.<sup>131, 132</sup> This is due to the favourable sp<sup>3</sup> hybridisation of the sulphur atom in BMT, causing a 104° angle with the surface to the S-C bond and allowing a more stable, densely packed monolayer.<sup>133</sup> Another common derivative of BT is aminothiophenol (ATP), which has an amine group, allowing attachment to a bioreceptor, as demonstrated by Billah et al.<sup>134</sup> They demonstrated that this can also form a densely packed layer, while still allowing for a Faradaic EIS response. Despite their short carbon

chains, which yields insufficient interchain stabilisation, cysteamine and cystamine are still popular. Wirde et al.<sup>135</sup> found cystamine had an approximate 80% surface coverage of that for a C<sub>18</sub> thiol monolayer after 5 mins. With longer adsorption times this coverage increased to approach that of the long chain thiol. Due to its short carbon chain cystamine has successfully been utilised in biosensors in a mixed SAM and in conjunction with nanoparticles.<sup>136</sup>

## Silanes

“Silanes” refer to a group of compounds with four substituents on a silicon atom, customarily in the form of RSiX<sub>3</sub>. Though these are often described with regard to a silicon surface, they have been successfully bound to several electrode surfaces in construction of electrochemical biosensors.<sup>137-142</sup> The three most commonly used silanes for SAM formation are 3-aminopropyltrimethoxysilane (APTES), 3-glycidoxypropyltrimethoxysilane (GPMS) and 3-glycidoxypropyldimethylethoxysilane (GPMES), all which contain methoxy groups to facilitate binding to the surface. The growth of a silane SAMs includes an irreversible covalent cross-linking step. The silicon forms bonds with the hydroxyl groups on the hydrolysed surface. Silanes are popular monolayers for silicon which can oxidise in the atmospheric environment, providing hydroxyl groups for attachment of the silane. However, these monolayers have also successfully been assembled onto electrode surfaces.<sup>143-145</sup> If there are adsorbed water molecules in the system the remaining Si-X bonds are hydrolysed resulting in the Si-O-Si linkage between adjacent silanes and the formation of silanols (SiOH), stabilising the layer. Without the presence of water cross-linking will not occur and the silicon will form three bonds (or however many X groups it has) to the hydroxyl groups at the surface.<sup>146</sup> The most commonly used solvents are hexadecane, Isopar™ G and bicyclohexyl; sometimes with the inclusion of small volumes of either chloroform or carbontetrachloride to the solution to control agglomeration caused by the predominance of the cross-linking.<sup>147</sup>

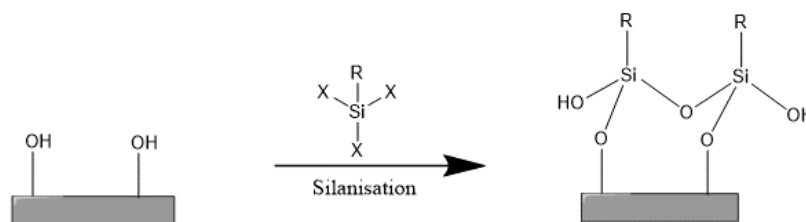


**Figure 1.23:** Schematic representation of possible mode of covalent attachment of a  $RSiX_3$  to a hydroxyl-terminated surface, with cross-linking between adjacent silane molecules.

The film growth of APTES is also temperature dependent. At  $10^\circ\text{C}$ , dendritic islands grow and fuse to cover the surface at  $10^\circ\text{C}$ , whereas at  $40^\circ\text{C}$  a homogeneous uniform film forms.<sup>110, 148</sup> Further elevated incubation temperatures ( $\sim 70^\circ\text{C}$ ) leads to denser, stronger and better orientated films, without compromising the self-termination of the deposition.<sup>149</sup> The position of the amine group in APTES has a strong effect on its chemistry in aqueous solution compared to silanes that lack the amine or have the amine in a different position. It has a catalytic effect on the hydrolysis of the methoxy groups and can cause the formation of a six membered hydrogen bonded ring.<sup>150, 151</sup> Howarter and Youngblood's<sup>152</sup> work focused on optimising the reaction conditions - temperature, concentration and time - to establish a uniform thin film. They found that the concentration of APTES solution and the temperature of the incubation governed the surface roughness and receding contact angle, whereas they had minimal effect on the film thickness. It was the incubation time that controlled this characteristic. For low concentrations (1%) good films were produced when incubation time was limited to 1 hour and these did not appear to be temperature sensitive. To produce smooth thick films at higher concentrations (10-33%) incubation required 25 – 72 hours at  $75^\circ\text{C}$ .

GPMS and GPMES being epoxy silanes have the advantage of being able to directly immobilise the bioreceptor unlike APTES, which requires a cross-linking step. The terminal epoxide group can react with amines through a ring opening mechanism (Figure 1.24), as proposed in Sales et al<sup>153</sup>. The non-bonded electron pair on the nitrogen atom of the amine group interacts with the carbon in the epoxy ring and the electrons from the carbon-oxygen bond are transferred to the oxygen thereby driving the ring opening. The excess charge on the oxygen atom attracts a hydrogen atom from the nearby nitrogen. This rearrangement of electrons produces a neutral product where the biomolecule is now immobilised to the surface through its amine group.<sup>138, 154</sup>

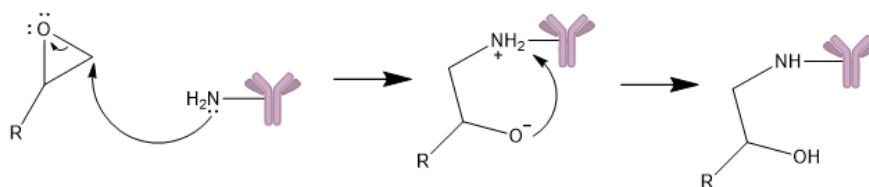


**Figure 1.24:** Epoxy ring opening mechanism.

## Phosphonates

Phosphonates, also referred to as phosphonic acids (PA), have the typical molecular formula of  $\text{RCPO}(\text{OR})_2$ . These can be deprotonated to form two anions,  $\text{RPO}_2(\text{OH})^-$  and  $\text{RPO}_3^{2-}$ , which can bind to a variety of metals from monovalent cations to tetravalent cations with an assortment of connectivity modes.<sup>155</sup>

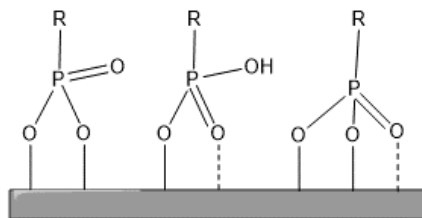


**Figure 1.25:** Schematic representation of PAs interaction with an oxide surface.

PAs are not typically suited to SAM formation on silicon substrates as the Si-O-P bonds are easily cleaved by nucleophiles such as water or alcohols. The T-BAG method was established to allow the chemisorption of PAs onto a silicon surface. This method forms a densely packed layer of organic groups which prohibits the diffusion of water to the interface causing the SAM to be stable against hydrolysis.<sup>155, 156</sup> Whereas, silane groups may be more suited to silicon substrates, PAs appear to be superiorly anchored to metal oxide substrates, at pHs 1-10.<sup>157, 158</sup> Both the pH and solvent of the phosphonate solution play an important role in the formation of a stable layer. Varying the pH and using an organic solvent has been shown to stimulate the monolayer grafting and prevent a precipitation process.<sup>159</sup> Another possible issue is that the solubility will depend on the hydrophilic/hydrophobic nature of the organic backbone, though phosphonate ester analogues are often employed as they usually show no solubility issue.<sup>160</sup>

As they are not as well characterised as thiols and silanes, PAs are not as often adopted as a SAM for the immobilisation of antibodies. However, both (11-hydroxyundecyl)phosphonic acid and (12-carboxydodecyl)phosphonic acid have been



assembled on a titanium substrate and cross-linked to a protein's amino group. The hydroxyl-terminated PA was determined to form a more ordered SAM than that of the carboxyl-terminated SAM.<sup>161</sup> This hydroxyl-terminated layer could be utilised for the immobilisation of antibodies or antigens to an electrode surface.

### 1.7.2.2 Polymers

Polymer coatings can be applied to a variety of electrode materials including graphite, glassy carbon, Au, Ag and Pt. Unlike alkanethiols, the absorption mechanism for polymer layers is not well understood.<sup>162</sup> They can be formed on the electrode surface using two methods: solution casting of preformed polymers, or electropolymerisation of monomers. Using preformed polymers allows easy control of the particle sizes, but poor adhesion to the electrode surface.<sup>163</sup> Electropolymerisation overcomes this obstacle; it involves the application of an appropriate potential to the working electrode, immersed in an aqueous solution of the monomer. This allows better control over the deposition thickness than the casting method. Another advantage of electrodeposition is that it concentrates the deposition of the polymer to the electrode area and can coat complicated geometries and 3D structures.<sup>164, 165</sup>

A one-step immobilisation process can be used by including the biological component in the solution, which will be homogeneously incorporated into the growing polymer during the electropolymerisation.<sup>166</sup> This entrapment of the bioreceptor is popular in enzyme-based biosensors but generally is not suitable for an immunosensor. Entrapment of an antibody or antigen can diminish its biological activity due to steric hindrance as the surrounding polymer reduces accessibility to immobilised molecule. Additionally, the conditions required for the polymerisation may be too harsh for biomolecules causing denaturing. Instead this section will focus on two-step immobilisation where the polymer is first deposited onto the electrode surface, and then the antibody or antigen is attached to the polymer layer. A two-step procedure permits the polymer to be deposited in harsher conditions for an optimal layer, while the bioreceptor can still be immobilised in mild conditions to prevent denaturing.<sup>162</sup> The polymer layer requires to available functional groups for binding to the bioreceptor and must not impede electrochemical activity by completely insulating the electrode if monitoring Faradaic processes.

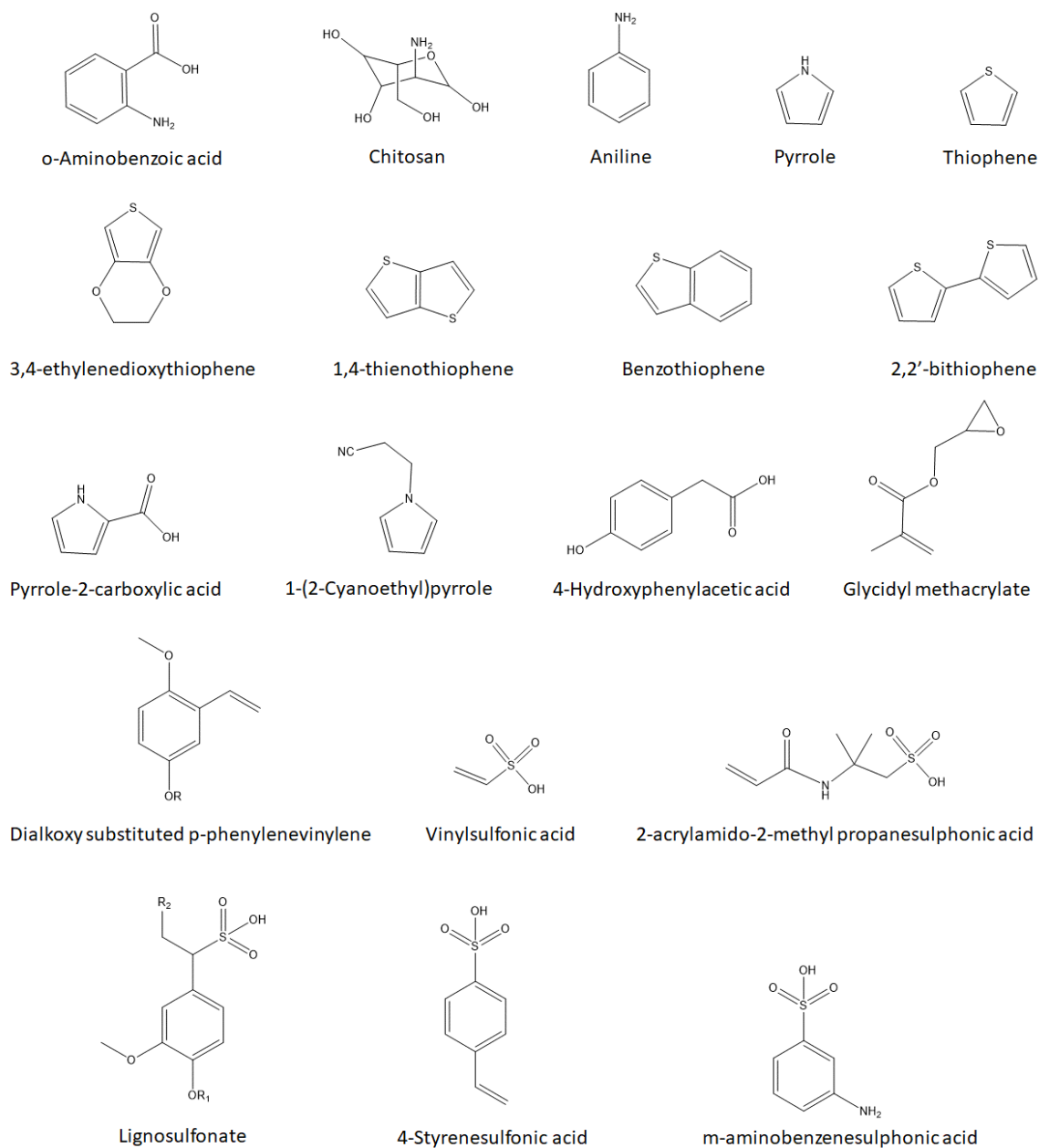


**Figure 1.26:** Molecular structure of monomer units for polymers.

### Insulative Polymers

Non-conductive polymers are generally used for the entrapment of enzymes onto an electrode surface. However, they may also be used in immunosensors despite their insulating properties due to their permselectivity enhancing sensitivity and anti-fouling abilities.<sup>166</sup> Polymers such as *o*-aminobenzoic acid (*o*-ABA) have been electrodeposited onto electrodes resulting in the partial insulation of the electrodes while still allowing for

impedimetric response and reducing non-specific absorption onto the electrode surface.<sup>167, 168</sup> Additionally, o-ABA has a carboxylic acid functional group through which proteins can be immobilised onto the surface.

Chitosan is popular for electrode modifications due to its available amino groups, good adhesion and biocompatibility.<sup>169</sup> As with o-ABA, a porous film is formed allowing reagents to reach the electrode surface, though the electrochemical response is reduced compared to the bare electrode. Non-conducting polymers are limited to thin layers to ensure it is sufficiently permeable to the mediator molecule. Often conductive nanoparticles are incorporated into the chitosan matrix to reduce the insulative behaviour of the coating. Luo et al.<sup>170</sup> demonstrated that an electrode coated with a chitosan film containing multi-wall carbon nanotubes (MWCNT) exhibited a larger current response in 5 mM  $\text{Fe}(\text{CN})_6^{3-/4-}$  than when the electrode was modified with a chitosan film without the MWCNT. Similarly, Zang et al.<sup>171</sup> used a chitosan layer containing single-wall carbon nanotubes (SWCNT) to immobilise anti-aflatoxin B<sub>1</sub> onto the electrode surface, as chitosan enhanced the dispersion of the SWCNTs. Other groups have adopted gold nanoparticles (AuNPs),<sup>172</sup> reduced graphene oxide (rGO),<sup>173</sup> magnetic nanoparticles<sup>174</sup> and other nanoparticles<sup>175</sup> in conjunction with chitosan for biosensors. Electrode modification with nanostructures is discussed further in Section 1.7.2.3.

### Conductive Polymers

Conductive polymers owe their unusual electronic properties such as electrical conductivity, and high electron affinity to the conjugated  $\pi$ -electron backbone in their polymer chain.<sup>176</sup> This chain has alternating single and double bonds, with  $sp^2$  hybridised carbon atoms which generate a wide charge delocalisation. This allows charge mobility along the polymer backbone and results in metal-like semiconductor properties.<sup>177</sup> Literature describes the current generated at an electrode modified with a conducting polymer and antibodies immobilised on the surface to have four steps:<sup>178, 179</sup>

- (i) Charge transfer at the polymer/electrode interface.
- (ii) Diffusion of ions from the solution to the electrode.
- (iii) Migration of ions through the polymer membrane for balance of charge.
- (iv) Adsorption/desorption of antigen at the polymer/solution interface.

Common conducting polymers used in impedimetric biosensors include polypyrrole, polyaniline and polythiophene. Polypyrrole (PPy) has an advantage over other conducting polymers as it can be electropolymerised from an aqueous solution at neutral pH, whereas aniline is only soluble in acidic solutions and thiophene in organic solvents.<sup>180</sup> Although thiophene is not water soluble, its derivatives can be, such as poly(3,4-ethylenedioxythiophene) (PEDOT).<sup>181</sup>

The electrochemical properties of a polymer layer can be influenced by the electropolymerisation process. For instance, at positive potentials PPy is overoxidised, reducing its conductivity. The potential at which this overoxidation will occur depends on the environment during polymerisation. Water and/or oxygen containing solutions will experience overoxidation at lower potentials, and partially deconstruct the polymer backbone generating oxygen containing carboxyl, carbonyl, and hydroxyl groups.<sup>163</sup> Although, this process reduces the conductivity of the PPy, these layers are still utilised in biosensors due to the enhanced permselectivity non-conducting polymers provide<sup>182</sup> and functional groups for antibody immobilisation. Similarly, polyaniline (PANI) has multiple oxidation states; leucoemeraldine, emeraldine, and pernigraniline. Leucoemeraldine, the fully reduced state and pernigraniline, the fully oxidised form, are poor conductors, even when doped with acid.<sup>183</sup> Emeraldine, the half-oxidised form is considered the most useful form as it is highly stable at room temperature.<sup>183</sup> It comes in two configurations: the emeraldine base and the emeraldine salt. The salt form which is doped with acid and the imine's nitrogen is protonated making it highly conductive.<sup>184</sup><sup>185</sup> The structure of the PANI layer can be converted between oxidation states during electrodeposition by using potentiodynamic cycling. Chen et al.<sup>185</sup> also produced a benzoquinone biproduct due to their potential range which induced inductive behaviour in the electrical circuit.

A dopant is an impurity introduced into a semiconductor's structure to improve the electrical properties. During electropolymerisation, a polymer can be doped with counter ions, which will induce polymer conductivity. The  $\pi$ -electron backbone is either oxidised (p-doping) or reduced (n-doping) and the counter anion or cation produce a neutral polymer. Some sections of the chain, referred to as polarons and bipolarons, consist of radical cations or dications and act as charge carriers.<sup>177</sup> The doping percentage and type of dopant will influence the level of conductivity. Possible doping ions include

camphorsulphonate, tosylate, tetrafluoroborate chloride, perchlorate, sulphate and phosphate.<sup>186</sup> Aniline is typically polymerised using an acid, however buffer solutions with an acidic pH have also proven to be suitable media. Moraes et al.<sup>187</sup> using phosphate buffers with pH between 1.7 and 2.2 found some phosphate species to be effective dopants. Hexacyano-ferrate ( $\text{Fe}(\text{CN})_6$ ) ions and ferrocene derivatives have successfully been incorporated into polymer layers.<sup>188, 189</sup> This is an attractive dopant due to excellent electrochemical behaviour of the iron molecule which can undergo reversible electrochemical oxidation. Nanoparticles (NPs) constructed from conductive materials can also be adopted as dopants.

Derivatives of the three common conducting polymers have additional functional groups for cross-linking to the bioreceptor. Cross-linking will be discussed in detail in Section 1.7.3.1. Examples of such modified structures include aminobenzoic acids which are anilines with a carboxylic acid in the ortho, meta or para position of the benzene ring. Similarly, nitroanilines contain a nitro group in one of these three positions. Carboxylic acids may be added to a pyrrole ring. Indole is a bicyclic structure with a pyrrole ring fused to a benzene ring. Pyrrole may also undergo N-substitution with methyl and cyano groups, which will also facilitate cross-linking protocols. Thiophene derivatives other than PEDOT include thienothiophenes which consist of two thiophenes rings fused together; benzothiophene which has a benzene ring fused to a thiophene ring; and bithiophenes which has two thiophenes linked by a C-C bond. These are just some examples of possible derivatives of common conducting polymers and many other polymers exist which can be utilised in immunosensors such as: hydroxyphenylacetic acids which have free carboxyl functional groups once polymerised;<sup>190</sup> Poly(p-phenylenevinylene) (PPV) can have a dialkoxy substitution;<sup>191</sup> and poly(glycidyl methacrylate) (PGMA) has an epoxy group,<sup>192</sup>

### **Co-Polymers**

An alternative dopant method to counter-ions is to use a second polymer, forming a copolymer. The film properties can be regulated by adjusting the monomer concentrations. PANI co-deposited with poly(vinyl sulfonate) (PVS) has recorded improved electrode surface morphology and electrical conductivity of the polymer at non-acidic pH.<sup>193</sup> Poly(2-acrylamido-2-methyl propanesulphonic acid) (PAMPS) is used as a dopant to make PANI soluble in water.<sup>194</sup> Lignosulfonate (LGS) was shown to increase

the conductivity of PANI by more than two-fold as well as improving the thermal stability.<sup>195</sup> PANI polymers containing aniline derivatives, such as o-ABA or m-aminobenzenesulphonic acid, have displayed electrochemical activity over a wide pH range,<sup>196, 197</sup> while the additional aniline increases the rate of polymerisation.<sup>198</sup> Such polymers are often referred to as self-doped PANI. PPy can similarly be self-doped and be co-polymerised with pyrrole-2-carboxylic acid.<sup>199</sup> As previously mentioned, these additional functional groups on the self-doped polymer films can serve as a linker for covalent attachment to a biomolecule. Polystyrene sulphonic acid (PSSA) has also successfully been incorporated into polymer layers such as PANI and PEDOT.<sup>200, 201</sup> These molecules have a higher molecular weight than counter ions and thus have a larger impact on the polymer's morphology. Additionally, they are unlikely leach out or de-dope as they are partially entrapped in the layer.<sup>177</sup>

### 1.7.2.3 Nanostructures

Nanostructures used in impedimetric immunosensors include metallic nanoparticles (NPs) or nanorods such as Au, Ag and Pt, as well as metal oxide NPs; and carbon-based nanostructures, such as CNTs, carbon nanodots and graphene. As well as being used as dopants for conducting polymers, nanostructures can also be utilised to amplify the electrochemical signal by acting as a label for the target biomolecule.<sup>202</sup> This thesis focuses on label-free detection. This section will, therefore, focus on nanostructures used for electrode modifications prior to biomolecule immobilisation. Nanoparticles provide a larger surface-to-volume ratio, often leading to an increase in sensitivity, as it will increase the amount of the bioreceptor on the electrode surface.

As with polymers, nanostructures can be absorbed onto the surface of the transducer from solution or electrodeposition onto the surface. NPs to be adsorbed onto the electrode surface are prepared by the reduction of metal salts in the presence of a protecting agent such as polyvinylpyrrolidone (PVP) to prevent agglomeration.<sup>203</sup> The adsorption time for such NPs could be minutes to days. Electrodeposition presents a faster option for modifying an electrode. This is undertaken at a reducing potential and, as with electropolymerisation, the chosen parameters will affect the resulting layer. Varying the applied potential, the current density, or deposition time will allow control of the nanoparticle size.<sup>204</sup> Alternatively, NPs can be attached to the surface through a molecular

linker.<sup>205</sup> There are four options for this linkage as depicted in Figure 1.27, all of which require the NP to have a preformed ligand shell.

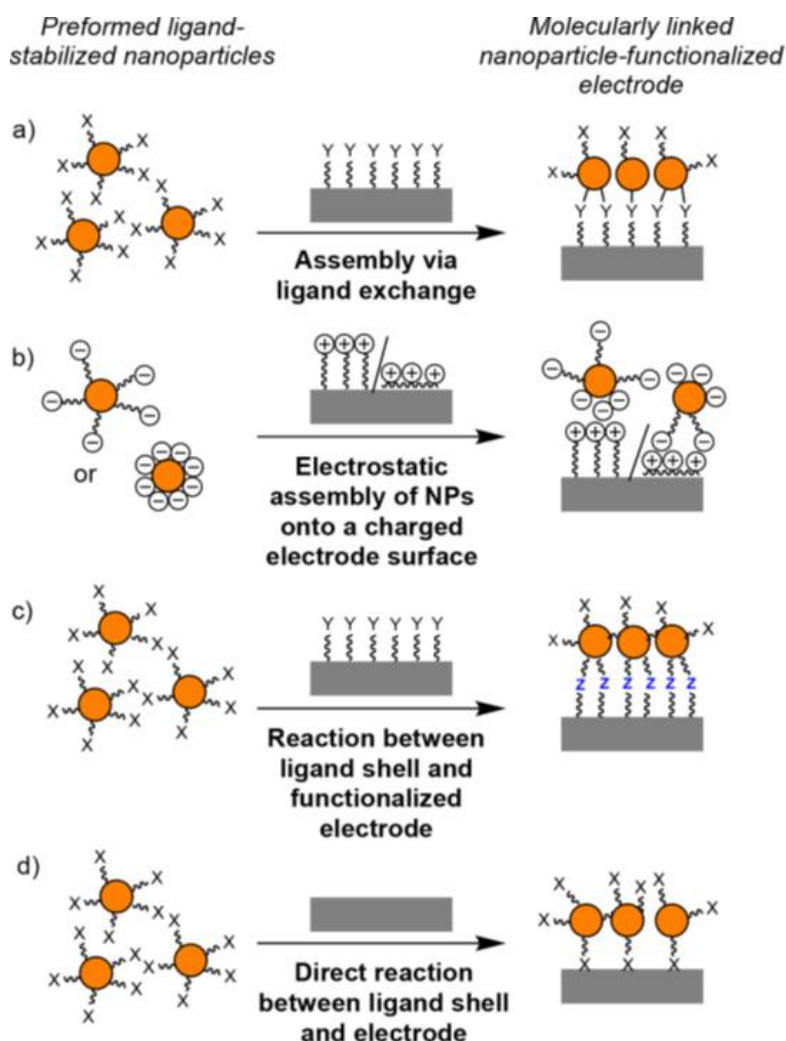


**Figure 1.27:** Strategies to functionalise electrodes with nanoparticles through molecular linkers. (Taken from <sup>205</sup>)

The first method (Figure 1.27 (a)) requires the electrode to be pre-functionalised with a SAM which will act as the molecular linker. The terminal functional group will bind to the NP's ligand shell either through ligand exchange or electrostatic interactions. Long chain SAMs can act as an insulative layer on the electrode, but the attachment of metallic NPs can facilitate charge transfer.<sup>206</sup> The second method (Figure 1.27 (b)) pre-functionalises the electrode surface with an ionically charged polymer. The NP's shell electrostatically interacts with this charged layer. The third method (Figure 1.27 (c)) uses "click chemistry" to couple the functional group on the electrode surface to the functional

group on the NP ligand. The fourth method (Figure 1.27 (d)) directly binds the NP ligand to the electrode surface.

Graphene is a single layer of carbon atoms organised in a  $sp^2$  hybridised honeycomb lattice. Graphene oxide (GO) is popular for electrode modifications as it overcomes obstacles presented by graphene, i.e. poor production yield, requirement for surface support, and uncontrollable thickness.<sup>207</sup> GO is rich in oxygen containing functional groups such as hydroxyl, epoxide, carbonyl, and carboxyl groups, which can facilitate antibody immobilisation. Alternatively, a reduction process can remove these functional groups yielding reduced GO (rGO). This reduction process can be chemical, electrochemical, or thermal. There is evidence that reduction by electrochemical methods produces defects in the GO which contributes to its augmented electroactivity as the defects consequently become active sites for electroactivity.<sup>208</sup> Thermal reduction has demonstrated even greater electroactivity. The morphology of the rGO, however, will depend on the reduction strategy<sup>209, 210</sup> and this needs to be considered when selecting a reduction method.

CNTs are seamless, hollow tubes formed from graphene sheets. As with nanoparticles they offer a high surface-to-volume ratio and promote electron transfer. Due to the  $\pi$ - $\pi$  stacking and van der Waals interactions between CNTs in aqueous solution, aggregation occurs causing non-homogenous and unstable coatings for electrodes.<sup>211</sup> For this reason, dispersal of CNTs through a suitable polymer has become a popular method of functionalising the electrode surface. Molecular linkers, as proposed for NPs, can also be used. Unlike typical NPs, CNTs have structural heterogeneity due to the diversity between the properties of the wall and the edges, making the orientation imperative. The rate of electron transfer will be affected by the orientation of the CNTs on the electrode surface. Vertically aligned structures result in better electrochemical performance, as the edge of the tubes have faster electron transfer kinetics than the wall.<sup>212</sup> The length of the CNT governs the rate of electron transport.<sup>213</sup> Additionally, producing oxygenated carbon species at the tips of the tubes is beneficial to electrochemical behaviour.<sup>214</sup>

The forms of electrode modifications that have been discussed in Section 1.7.2 can be combined resulting in a huge range of possible electrode modifications for the immobilisation of a bioreceptor. As mentioned in the previous section polymers are often



deposited onto the electrode surface in conjunction with nanostructures, incorporating them into the polymers coating. However, nanostructures are also deposited onto electrodes that have already been modified with a polymer layer and form a second separate layer on top of the polymer. For instance, Narang et al.<sup>215</sup> coated their impedimetric sensor with chitosan and then decorated it with Au nanorods. Similarly, Amouzadeh Tabrizi et al.<sup>216</sup> decorated an overoxidised pyrrole layer with Au NPs. Other groups layer several different types of electrode modifications. For instance, some groups have decorated polymers with NPs and then coated the NPs with thiols.<sup>217, 218</sup> Lu et al.<sup>219</sup> coated a carbon electrode with PPy and GO and then reduced the graphene oxide before depositing Au NPs. Finally, they added an MPA layer to facilitate immobilisation of anti-fumonisin B<sub>1</sub> or anti-deoxynivalenol for the detection of mycotoxins.

### 1.7.3 Immobilisation Technique

Once the electrode has been modified the bioreceptor, i.e. antibody or antigen, can be immobilised onto the surface. As previously mentioned, bioreceptors such as enzymes can be immobilised onto the surface during the electrode modification step, usually within a polymer layer. Although this technique is generally not adopted for immunosensors due to steric hinderance, some groups have successfully detected analytes through entrapped antibodies or antigens. John et al.<sup>220</sup> deposited PPy on a platinum electrode with anti-human serum albumin (HSA). Huang et al.<sup>221</sup> formed a semi-insulating layer on Au with insulative polymer o-phenylenediamine and antibodies for a hepatic fibrosis biomarker.

Other electrode modifications require the bioreceptor to be immobilised after the electrode has been modified. The bioreceptor may be physisorbed onto the modified surface,<sup>216, 222</sup> though this is not common due to dissociation from the surface. If the modification layer is charged it can electrostatically interact with the bioreceptor once an appropriate pH assures that the bioreceptor is also charged. This method has drawbacks as the conformation of the protein can be changed by altering the pH causing denaturation. Additionally, there is no control of the packing density and there is a possibility that the biomolecules can leach off the electrode surface.<sup>111</sup> Instead, as mentioned in Section 1.7.2.1, GPMS and GPMES can directly covalently bind to the bioreceptor. Other surfaces not equipped to directly bind to the bioreceptor opt for an additional step to ensure a stable immunosensor surface but in most other surfaces require a covalent linker.

### 1.7.3.1 Cross-linking

A cross-linker can covalently bond the amine or carboxylic acid group on a bioreceptor to the functional group on the surface modification, typically a carboxylic acid group, aldehyde, or amine.<sup>111</sup> These functional groups commonly terminate SAMs or are found on side chains on a polymer backbone or are present as ligands on nanostructures. N-hydroxysuccinimide (NHS) can activate a carboxylic acid functional group via the formation of NHS-ester. However, NHS-esters are vulnerable to hydrolysis, thus EDC/NHS (1-ethyl-3-(3-dimethylaminopropyl)-carbodiimide) coupling is generally used instead.<sup>111</sup> As seen in Figure 1.28 the EDC reacts with the carboxylic acid to form an O-acylisourea intermediate. Though this intermediate can react directly with a primary amine, it is unstable and prone to hydrolysis. As hydrolysis is largely dependent on pH, an acidic buffer is used for this step.<sup>223</sup> NHS or its water-soluble derivative (Sulfo-NHS) couples to the carboxylate to form a more stable ester which can react with a primary amine at physiological pH. EDC can also be used to covalently link phosphates to amines.<sup>223</sup>

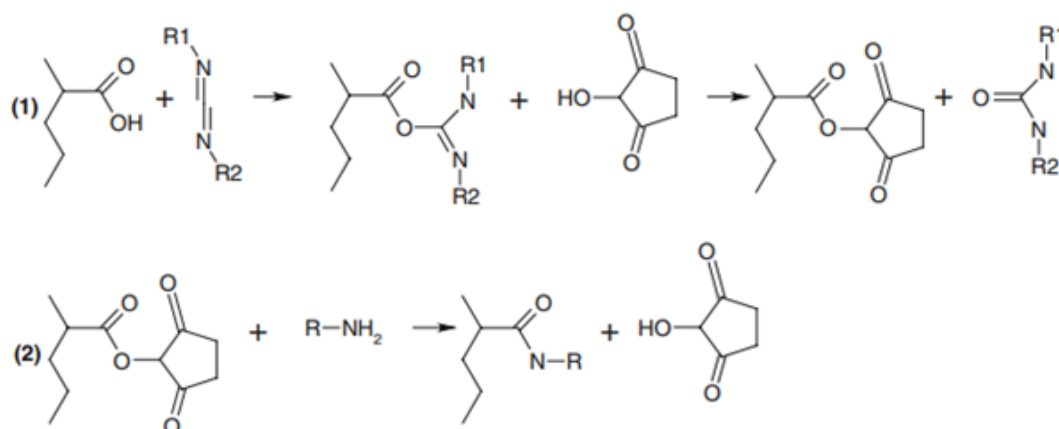


**Figure 1.28:** Chemical reaction scheme of EDC/NHS coupling of a carboxyl group on the electrode surface to a primary amine on the bioreceptor. First the EDC/NHS activates the surface (step 1) then the amine covalently attaches to the surface (step 2). (Adapted from<sup>224</sup>)

Aldehyde functional groups form imine with an amine, which can be reduced to a more stable secondary amine using NaBH<sub>3</sub>CN to form an irreversible bond.<sup>225</sup> Glutaraldehyde is a dialdehyde used to cross-link two primary amines. One aldehyde end reacts with the first amine forming an imine. The second aldehyde end is free to form an imine with the second amine, linking an amine on the surface to an amine on the bioreceptor.<sup>226</sup>

### 1.7.3.2 Affinity Binding

A non-covalent method of immobilisation exploits proteins such as avidin, streptavidin and neutravidin which have high natural affinity for biotin. This strong, rapidly forming non-covalent interaction is typically unaffected by pH, temperature or organic solvents.<sup>111</sup> Biotin is bicyclic with a carboxylic acid group which can be functionalised to graft to the modified electrode surface. By functionalising the carboxyl group the bicyclic ring remains intact for affinity binding. Typical biotin functionalisation methods involve NHS ester,<sup>227, 228</sup> hydrazine,<sup>229</sup> dicyclohexylcarbodiimide,<sup>230</sup> or maleimide.<sup>231</sup> As avidin, streptavidin and neutravidin can each bind four biotin molecules, a second biotin molecule can be conjugated to the bioreceptor. Immobilisation then occurs through a biotin-avidin-biotin interaction.

### 1.7.3.3 Controlled Orientation

Protein G and protein A are bacterial proteins from *Streptococci* and *Staphylococcus aureus*, respectively. They can be immobilised onto the modified electrode surface using cross-linking protocols discussed in Section 1.7.3.1. These proteins selectively bind to the Fc region of antibodies controlling the orientation of the bioreceptor and leaving the Fab paratope containing regions free and accessible to the antigens. Once the antibody is bound to either protein A or protein G it can be further stabilised by cross-linking the antibody to the protein A/protein G support.<sup>232</sup>

## 1.7.4 Faradaic vs Non-Faradaic Sensors

By modifying the electrode and immobilising biomolecules to the surface, the electrode/electrolyte interface has been altered thus changing the impedimetric response of the electrode. Furthermore, formation of the antibody-antigen complex will result in a change of capacitance and electron transfer resistance at the interface.

Faradaic impedance spectroscopy monitors the change in insulation of the electrode surface in relation to a redox probe added to the electrolyte which provides a Faradaic current.<sup>233</sup> The binding of the target (e.g. antigen) to the probe (e.g. antibody) partially inhibits charge transfer and is observed by an increase in the real component of the impedance data i.e.  $R_{ct}$ .

Non-Faradaic impedance spectroscopy is performed in the absence of a redox probe. Without the redox probe to provide charge transfer, the capacitance effects of the antibody-antigen binding are monitored. Capacitance based immunosensors typically have an insulating layer on the electrode surface, which pushes the solvated ions in the Helmholtz plane (Section 1.3.2) away from the electrode surface. Once the target binds to the bioreceptor the solvated ions and water molecules are pushed further back towards the diffusion layer generating a change in capacitance.<sup>234</sup> This technique is attractive for POC devices as no redox reagent is required. Pinhole defects in the insulating layer, however, can decrease the sensitivity of the device.<sup>106, 234</sup> Due to this drawback this thesis focuses on Faradaic impedance.

## 1.8 Scope of Thesis

Electrochemical biosensors offer promising solutions to address the adverse and costly veterinary issues, through cost effective, scalable microfabrication techniques and easy integration with portable electronics. The aim of this work is to exploit the enhanced electrochemical behaviour observed with UMEs and utilise the surface sensitive EIS technique to develop a label-free sensor for POC applications in bovine diagnostics.

Chapter 2 describes the fabrication of silicon devices containing six microband electrodes, gold counter and platinum pseudo-reference electrodes. I developed a surface modification for immobilising antibodies to a gold microband electrode and present a proof-of-concept immunosensor for the detection of bovine IgG. The surface modification consisted of a co-polymer which supported the cross-linking of a bioreceptor to electrode surface, which selectively bound to the target biomolecule in bovine serum. The sensor could discriminate between seronegative and seropositive serum samples with minimal sample preparation in a short analysis time (15 mins), enabling the creation of a POC biosensors. However, silicon is an expensive substrate, and would not be cost-effective for use as a single test, disposable device. Therefore, in Chapter 3, polymer replication methods were investigated as alternatives to silicon devices as a lower-cost fabrication of electrochemical sensors.

The polymer replication fabrication process allowed for a single silicon wafer to be repeatedly used as a mould, to create reproducible polymer structures. The selected design was a microneedle structure, which was chosen to eliminate the need for taking blood samples on-farm, providing a pain-free method of *in vivo* measurement in bovine interstitial fluid. The fabrication method used a double-sided micro-moulding process to enable future scale-up and mass manufacturing of these devices. The microneedle mechanism of action is via an exposed tip, to permit electrical contact with the solution of interest. COMSOL simulation were performed to explore the active layer on the microneedle tip surface, providing the most effective tip design. However, issues with the surface passivation required development of a new tip exposure, which is addressed in Chapter 4.

The microneedle structures presented the opportunity for novel fabrication of nanoring arrays by removing part of the protruding structure and exposing underlying nanorings.

These have the potential to be highly sensitive electrochemical devices due to enhanced mass transport and high current densities. Devices produced steady-state CVs in a known redox molecule. This chapter addresses the surface passivation issue, while maintaining the scalable cost-effective fabrication process discussed previously. Due to COVID-19 work was stopped at the proof-of-concept stage and optimisation of the electrode fabrication was not performed.

This electrochemical technology can provide label-free and cost-efficient sensing capability in a compact size. This work demonstrates the potential development of immunoassay-based point-of-use devices for on-farm diagnosis or therapeutic monitoring in animal health applications. Chapter 5 summarises the key results of this thesis and explores how the electrodes presented could be further developed towards achieving a POC device.

## 1.9 References

1. Bia, B. Export Performance and Prospects 2019-2020. <https://www.bordbia.ie/globalassets/bordbia.ie/industry/performance-and-prospects/2019-pdf/performance-and-prospects-2019-2020.pdf> (accessed 02/03/2020).
2. Agriculture, D. o. F. a. Annual Report 2018. <https://www.agriculture.gov.ie/media/migration/publications/2019/AnnualReport2018120819.pdf> (accessed 02/03/2020).
3. Department of Agriculture, F. a. t. M. Fact Sheet on Irish Agriculture <https://www.agriculture.gov.ie/media/migration/publications/2018/January2018Factsheet120118.pdf> (accessed 14/02/2020).
4. Ireland, S. F. S. AGRICULTURE AND FOOD IN IRELAND. <http://www.sfsi.ie/agriculture-food-ireland/> (accessed 14/02/2020).
5. Bia, B. Ireland's food, drink and horticulture industry as exports reach €13bn in 2019. <https://www.bordbia.ie/press-releases/irelands-food-drink-and-horticulture-industry-as-exports-reaches-13bn-in-2019/> (accessed 14/02/2020).
6. Department of Agriculture, F. a. t. M. Meat. <http://www.marketaccess.agriculture.gov.ie/meat/> (accessed 14/02/2020).
7. Ireland, E. Meat and Livestock. <https://www.enterprise-ireland.com/en/Start-a-Business-in-Ireland/Food-Investment-from-Outside-Ireland/Key-Sectors/Meat-and-Livestock/> (accessed 14/02/2020).
8. 2025, F. W. A 10-year vision for the Irish agri-food industry. <https://www.agriculture.gov.ie/media/migration/foodindustrydevelopmenttrademarkets/agri-foodandtheeconomy/foodwise2025/report/FoodWise2025.pdf> (accessed 02/03/2020).
9. Nations, F. a. A. O. o. t. U. The future of food and agriculture trends and challenges. <http://www.fao.org/3/a-i6583e.pdf> (accessed 14/02/2020).
10. Teagasc Situation and Outlook For Irish Agriculture July 2019. <https://www.teagasc.ie/media/website/publications/2019/Situation-and-Outlook-for-Irish-Agriculture-July-2019.pdf> (accessed 14/02/2019).
11. Marsh, J. M.; Brester, G. W.; Smith, V. H., Effects of North American BSE Events on U.S. Cattle Prices. *Review of Agricultural Economics* **2008**, *30* (1), 136-150.
12. Feng, S.; Patton, M.; Davis, J., Market Impact of Foot-and-Mouth Disease Control Strategies: A UK Case Study. *Frontiers in Veterinary Science* **2017**, *4* (129).
13. Health, T. W. O. f. A. OIE-Listed diseases, infections and infestations in force in 2020. <https://www.oie.int/animal-health-in-the-world/oie-listed-diseases-2020/> (accessed 02/03/2020).
14. Dehove, A.; Commault, J.; Petitclerc, M.; Teissier, M.; Mace, J., Economic analysis and costing of animal health: a literature review of methods and importance. *Rev Sci Tech* **2012**, *31* (2), 605-17, 591-604.

15. Tomley, F. M.; Shirley, M. W., Livestock infectious diseases and zoonoses. *Philos Trans R Soc Lond B Biol Sci* **2009**, *364* (1530), 2637-2642.
16. Martin, M. J.; Thottathil, S. E.; Newman, T. B., Antibiotics Overuse in Animal Agriculture: A Call to Action for Health Care Providers. *Am J Public Health* **2015**, *105* (12), 2409-2410.
17. Van Boeckel, T. P.; Brower, C.; Gilbert, M.; Grenfell, B. T.; Levin, S. A.; Robinson, T. P.; Teillant, A.; Laxminarayan, R., Global trends in antimicrobial use in food animals. *Proceedings of the National Academy of Sciences* **2015**, *112* (18), 5649-5654.
18. Gustafson, R. H.; Bowen, R. E., Antibiotic use in animal agriculture. *Journal of Applied Microbiology* **1997**, *83* (5), 531-541.
19. Marshall, B. M.; Levy, S. B., Food Animals and Antimicrobials: Impacts on Human Health. *Clinical Microbiology Reviews* **2011**, *24* (4), 718-733.
20. Gilbert, N., Rules tighten on use of antibiotics on farms: clampdown aims to stop spread of drug-resistant microbes. *Nature* **2012**, *481*, 125.
21. Gunn, G. J.; Saatkamp, H. W.; Humphry, R. W.; Stott, A. W., Assessing economic and social pressure for the control of bovine viral diarrhoea virus. *Preventive Veterinary Medicine* **2005**, *72* (1), 149-162.
22. Cummins, B. M.; Ligler, F. S.; Walker, G. M., Point-of-care diagnostics for niche applications. *Biotechnology advances* **2016**, *34* (3), 161-176.
23. Burfeind, O.; Heuwieser, W., Validation of handheld meters to measure blood l-lactate concentration in dairy cows and calves. *Journal of Dairy Science* **2012**, *95* (11), 6449-6456.
24. Zoetis Animal Diagnostics. <https://www.zoetis.mu/diagnostics.aspx> (accessed 06/03/2020).
25. Abaxis Veterinary. <https://www.abaxis.com/veterinary> (accessed 06/03/2020).
26. Nichols, J. H., Point of Care Testing. *Clinics in Laboratory Medicine* **2007**, *27* (4), 893-908.
27. Diagnostics, B. P4. <https://biomeddiagnostics.com/l/p4> (accessed 06/03/2020).
28. Halasa, T.; Huijps, K.; Østerås, O.; Hogeveen, H., Economic effects of bovine mastitis and mastitis management: A review. *Veterinary Quarterly* **2007**, *29* (1), 18-31.
29. BVT, V. Speed Mam Color. <https://bvt.virbac.com/en/home/diagnostic-solutions/pour-le-veterinaire-praticien/produit-1/main/produits/speed-mam-color-1.html> (accessed 06/03/2020).
30. Mastaplex Mastatest. <https://www.mastaplex.com/mastatest> (accessed 06/03/2020).
31. BVT, V. Speed V-Diar 4 & Speed V-Diar 5. <https://bvt.virbac.com/en/home/diagnostic-solutions/pour-le-veterinaire-praticien/produit-1/main/produits/speed-v-diar-4--v-diar-1.html> (accessed 06/03/2020).
32. IDEXX IDEXX SNAP BVDV Antigen Test. <https://www.idexx.com/en/livestock/livestock-tests/ruminant-tests/idexx-snap-bvdv-antigen-test/> (accessed 06/03/2020).



33. BioX BIO K 403 - SmartStrips *Cryptosporidium* sp. <https://www.biox.com/en/bio-k-403-smartstrips-cryptosporidium-sp-p-442/> (accessed 03/06/2020).
34. Hothouse BovAlert Priority Animal Health Testing. <https://www.dit.ie/hothouse/media/dithothouse/BovAlert%20Technology%20Information%20Sheet-2.pdf> (accessed 06/03/2020).
35. MiCRA Immunotouch. <http://micra.ie/micra-technologies/immunotouch/> (accessed 06/03/2020).
36. Biotangents Moduleic Sensing™ VET <https://www.biotangents.co.uk/veterinarians> (accessed 06/03/2020).
37. Solutions, C. P. Point-of-Care Tests. <https://creativeproteinsolutions.com/point-of-care-tests> (accessed 06/03/2020).
38. Marcus, R. A., Electron transfer reactions in chemistry theory and experiment. *Journal of Electroanalytical Chemistry* **1997**, 438 (1), 251-259.
39. Helmholtz, P., XLII.—On the modern development of Faraday's conception of electricity. *Journal of the Chemical Society, Transactions* **1881**, 39 (0), 277-304.
40. Conway, B. E.; Bockris, J. O. M.; Ammar, I. A., The dielectric constant of the solution in the diffuse and Helmholtz double layers at a charged interface in aqueous solution. *Transactions of the Faraday Society* **1951**, 47 (0), 756-766.
41. Bard, A. J.; Faulkner, L. R., *Electrochemical Methods: Fundamentals and Applications, 2nd Edition*. Wiley Textbooks: 2000.
42. Smith, T. J.; Stevenson, K. J., Reference electrodes. In *Handbook of Electrochemistry*, 2007; pp 73-110.
43. Pedrotti, J. J.; Angnes, L.; Gutz, I. G. R., Miniaturized reference electrodes with microporous polymer junctions. *Electroanalysis* **1996**, 8 (7), 673-675.
44. Zhou, J.; Ren, K.; Zheng, Y.; Su, J.; Zhao, Y.; Ryan, D.; Wu, H., Fabrication of a microfluidic Ag/AgCl reference electrode and its application for portable and disposable electrochemical microchips. *Electrophoresis* **2010**, 31 (18), 3083-9.
45. Inzelt, G., Pseudo-reference Electrodes. In *Handbook of Reference Electrodes*, Inzelt, G.; Lewenstam, A.; Scholz, F., Eds. Springer Berlin Heidelberg: Berlin, Heidelberg, 2013; pp 331-332.
46. Wagner, C., The role of natural convection in electrolytic processes. *Journal of the Electrochemical Society* **1949**, 95 (4), 161-173.
47. Randles, J. E. B., Kinetics of rapid electrode reactions. *Discussions of the Faraday Society* **1947**, 1 (0), 11-19.
48. Jorcin, J.-B.; Orazem, M.; Pébère, N.; Tribollet, B., CPE Analysis by Local Electrochemical Impedance Spectroscopy. *Electrochim. Acta* **2006**, 51.
49. Kim, C.-H.; Pyun, S.-I.; Kim, J.-H., An investigation of the capacitance dispersion on the fractal carbon electrode with edge and basal orientations. *Electrochim. Acta* **2003**, 48 (23), 3455-3463.

50. Schiller, C. A.; Strunz, W., The evaluation of experimental dielectric data of barrier coatings by means of different models. *Electrochim. Acta* **2001**, *46* (24), 3619-3625.
51. Zoski, C. G., Ultramicroelectrodes: Design, Fabrication, and Characterization. *Electroanalysis* **2002**, *14* (15-16), 1041-1051.
52. Kiran, R.; Rousseau, L.; Lissorgues, G.; Scorsone, E.; Bongrain, A.; Yvert, B.; Picaud, S.; Mailley, P.; Bergonzo, P., Multichannel boron doped nanocrystalline diamond ultramicroelectrode arrays: design, fabrication and characterization. *Sensors (Basel)* **2012**, *12* (6), 7669-81.
53. Menon, V. P.; Martin, C. R., Fabrication and Evaluation of Nanoelectrode Ensembles. *Anal. Chem.* **1995**, *67* (13), 1920-1928.
54. Arrigan, D. W. M., Nanoelectrodes, nanoelectrode arrays and their applications. *Analyst* **2004**, *129* (12), 1157-1165.
55. Aoki, K., Theory of ultramicroelectrodes. *Electroanalysis* **1993**, *5* (8), 627-639.
56. Heinze, J., Ultramicroelectrodes in Electrochemistry. *Angewandte Chemie International Edition in English* **1993**, *32* (9), 1268-1288.
57. Forster, R. J.; Keyes, T. E., 6 - Ultramicroelectrodes. In *Handbook of Electrochemistry*, Zoski, C. G., Ed. Elsevier: Amsterdam, 2007; pp 155-171.
58. Henstridge, M. C.; Compton, R. G., Mass Transport to micro- and nanoelectrodes and their arrays: a review. *The Chemical Record* **2012**, *12* (1), 63-71.
59. Feeney, R.; Kounaves, S. P., Microfabricated Ultramicroelectrode Arrays: Developments, Advances, and Applications in Environmental Analysis. *Electroanalysis* **2000**, *12* (9), 677-684.
60. Orozco, J.; Fernández-Sánchez, C.; Jiménez-Jorquera, C., Ultramicroelectrode array based sensors: a promising analytical tool for environmental monitoring. *Sensors (Basel)* **2010**, *10* (1), 475-90.
61. Hierlemann, A.; Brand, O.; Hagleitner, C.; Baltes, H., Microfabrication techniques for chemical/biosensors. *Proceedings of the IEEE* **2003**, *91* (6), 839-863.
62. Lee, G.-Y.; Park, J.-H.; Chang, Y. W.; Cho, S.; Kang, M.-J.; Pyun, J.-C., Chronoamperometry-Based Redox Cycling for Application to Immunoassays. *ACS Sensors* **2018**, *3* (1), 106-112.
63. Lee, G.-Y.; Park, J.-H.; Chang, Y. W.; Cho, S.; Kang, M.-J.; Pyun, J.-C., Redox cycling-based immunoassay for detection of carcinogenic embryonic antigen. *Analytica Chimica Acta* **2017**, *971*, 33-39.
64. Ueno, Y.; Furukawa, K.; Hayashi, K.; Takamura, M.; Hibino, H.; Tamechika, E., Graphene-modified Interdigitated Array Electrode: Fabrication, Characterization, and Electrochemical Immunoassay Application. *Anal. Sci.* **2013**, *29* (1), 55-60.
65. Ashby, M. F.; Ferreira, P. J.; Schodek, D. L., Chapter 8 - Nanomaterials: Synthesis and Characterization. In *Nanomaterials, Nanotechnologies and Design*, Ashby, M. F.; Ferreira, P. J.; Schodek, D. L., Eds. Butterworth-Heinemann: Boston, 2009; pp 257-290.

66. Li, M.; Li, W. H.; Zhang, J.; Alici, G.; Wen, W., A review of microfabrication techniques and dielectrophoretic microdevices for particle manipulation and separation. *Journal of Physics D: Applied Physics* **2014**, *47* (6), 063001.
67. Wang, J.; Wu, C.; Hu, N.; Zhou, J.; Du, L.; Wang, P., Microfabricated electrochemical cell-based biosensors for analysis of living cells in vitro. *Biosensors* **2012**, *2* (2), 127-170.
68. Virgilio, F.; Prasciolu, M.; Ugo, P.; Tormen, M., Development of electrochemical biosensors by e-beam lithography for medical diagnostics. *Microelectronic Engineering* **2013**, *111*, 320-324.
69. Lanyon, Y. H.; Arrigan, D. W. M., Recessed nanoband electrodes fabricated by focused ion beam milling. *Sensors and Actuators B: Chemical* **2007**, *121* (1), 341-347.
70. Cugnet, C.; Zaouak, O.; René, A.; Pécheyran, C.; Potin-Gautier, M.; Authier, L., A novel microelectrode array combining screen-printing and femtosecond laser ablation technologies: Development, characterization and application to cadmium detection. *Sensors and Actuators B: Chemical* **2009**, *143* (1), 158-163.
71. Groves, T. R.; Pickard, D.; Rafferty, B.; Crosland, N.; Adam, D.; Schubert, G., Maskless electron beam lithography: prospects, progress, and challenges. *Microelectronic Engineering* **2002**, *61-62*, 285-293.
72. Ocola, L. E.; Rue, C.; Maas, D., High-resolution direct-write patterning using focused ion beams. *MRS Bulletin* **2014**, *39* (4), 336-341.
73. Bucella, S. G.; Nava, G.; Vishunubhatla, K. C.; Caironi, M., High-resolution direct-writing of metallic electrodes on flexible substrates for high performance organic field effect transistors. *Organic Electronics* **2013**, *14* (9), 2249-2256.
74. Perl, A.; Reinhoudt, D.; Huskens, J., Microcontact Printing: Limitations and Achievements. *Advanced Materials* **2009**, *21*, 2257-2268.
75. Schmid, H.; Wolf, H.; Allenspach, R.; Riel, H.; Karg, S.; Michel, B.; Delamarche, E., Preparation of Metallic Films on Elastomeric Stamps and Their Application for Contact Processing and Contact Printing. *Advanced Functional Materials* **2003**, *13* (2), 145-153.
76. Carlson, A.; Bowen, A. M.; Huang, Y.; Nuzzo, R. G.; Rogers, J. A., Transfer Printing Techniques for Materials Assembly and Micro/Nanodevice Fabrication. *Advanced Materials* **2012**, *24* (39), 5284-5318.
77. Khan, S.; Lorenzelli, L.; Dahiya, R. S., Technologies for Printing Sensors and Electronics Over Large Flexible Substrates: A Review. *IEEE Sensors Journal* **2015**, *15* (6), 3164-3185.
78. Guo, L., Nanoimprint Lithography: Methods and Material Requirements. *Advanced Materials* **2007**, *19*, 495-513.
79. Schiff, H., Nanoimprint lithography: An old story in modern times? A review. *Journal of Vacuum Science & Technology B: Microelectronics and Nanometer Structures Processing, Measurement, and Phenomena* **2008**, *26* (2), 458-480.
80. Renedo, O. D.; Alonso-Lomillo, M. A.; Martínez, M. J. A., Recent developments in the field of screen-printed electrodes and their related applications. *Talanta* **2007**, *73* (2), 202-219.

81. Chang, J.-L.; Zen, J.-M., Fabrication of disposable ultramicroelectrodes: Characterization and applications. *Electrochemistry Communications* **2006**, *8* (4), 571-576.
82. Singh, M.; Haverinen, H.; Dhagat, P.; Jabbour, G., Inkjet Printing-Process and Its Applications. *Advanced materials (Deerfield Beach, Fla.)* **2010**, *22*, 673-85.
83. Arenas, L. F.; Ponce de León, C.; Walsh, F. C., 3D-printed porous electrodes for advanced electrochemical flow reactors: A Ni/stainless steel electrode and its mass transport characteristics. *Electrochemistry Communications* **2017**, *77*, 133-137.
84. Chen, C.; Mehl, B. T.; Munshi, A. S.; Townsend, A. D.; Spence, D. M.; Martin, R. S., 3D-printed microfluidic devices: fabrication, advantages and limitations—a mini review. *Analytical Methods* **2016**, *8* (31), 6005-6012.
85. Proto3000 <https://proto3000.com/> (accessed 25 June 2020).
86. MIICRAFT <https://miicraft.com/> (accessed 25 June 2020).
87. B9Creator® <https://www.b9c.com/> (accessed 25 June 2020).
88. Makerbot <https://www.makerbot.com/> (accessed 25 June 2020).
89. Hamzah, H. H.; Shafiee, S. A.; Abdalla, A.; Patel, B. A., 3D printable conductive materials for the fabrication of electrochemical sensors: A mini review. *Electrochemistry Communications* **2018**, *96*, 27-31.
90. Zhu, C.; Han, T. Y.-J.; Duoss, E. B.; Golobic, A. M.; Kuntz, J. D.; Spadaccini, C. M.; Worsley, M. A., Highly compressible 3D periodic graphene aerogel microlattices. *Nat Commun* **2015**, *6*, 6962-6962.
91. Loo, A. H.; Chua, C. K.; Pumera, M., DNA biosensing with 3D printing technology. *Analyst* **2017**, *142* (2), 279-283.
92. Lee, K. Y.; Ambrosi, A.; Pumera, M., 3D-printed Metal Electrodes for Heavy Metals Detection by Anodic Stripping Voltammetry. *Electroanalysis* **2017**, *29* (11), 2444-2453.
93. Tan, C.; Nasir, M. Z. M.; Ambrosi, A.; Pumera, M., 3D Printed Electrodes for Detection of Nitroaromatic Explosives and Nerve Agents. *Anal. Chem.* **2017**, *89* (17), 8995-9001.
94. Liyarita, B. R.; Ambrosi, A.; Pumera, M., 3D-printed Electrodes for Sensing of Biologically Active Molecules. *Electroanalysis* **2018**, *30* (7), 1319-1326.
95. Attia, U. M.; Marson, S.; Alcock, J. R., Micro-injection moulding of polymer microfluidic devices. *Microfluidics and Nanofluidics* **2009**, *7* (1), 1.
96. Dimla, D. E.; Camilotto, M.; Miani, F., Design and optimisation of conformal cooling channels in injection moulding tools. *Journal of Materials Processing Technology* **2005**, *164-165*, 1294-1300.
97. Sha, B.; Dimov, S.; Griffiths, C.; Packianather, M. S., Investigation of micro-injection moulding: Factors affecting the replication quality. *Journal of Materials Processing Technology* **2007**, *183* (2), 284-296.
98. Grieshaber, D.; MacKenzie, R.; Vörös, J.; Reimhult, E., Electrochemical biosensors - Sensor principles and architectures. *Sensors* **2008**, *8* (3), 1400-1458.

99. Lippa, P. B.; Sokoll, L. J.; Chan, D. W., Immunosensors—principles and applications to clinical chemistry. *Clinica Chimica Acta* **2001**, *314* (1), 1-26.
100. Lin, J.; Ju, H., Electrochemical and chemiluminescent immunosensors for tumor markers. *Biosensors and Bioelectronics* **2005**, *20* (8), 1461-1470.
101. Edelman, G. M., Antibody Structure and Molecular Immunology. *Science* **1973**, *180* (4088), 830-840.
102. Forthal, D. N., Functions of Antibodies. *Microbiol Spectr* **2014**, *2* (4), 1-17.
103. Davies, D. R.; Chacko, S., Antibody structure. *Accounts of Chemical Research* **1993**, *26* (8), 421-427.
104. Wang, W.; Singh, S.; Zeng, D. L.; King, K.; Nema, S., Antibody structure, instability, and formulation. *Journal of pharmaceutical sciences* **2007**, *96* (1), 1-26.
105. Goding, J. W., 2 - The Antibody Response. In *Monoclonal Antibodies (Third Edition)*, Goding, J. W., Ed. Academic Press: London, 1996; pp 7-25.
106. Daniels, J. S.; Pourmand, N., Label-Free Impedance Biosensors: Opportunities and Challenges. *Electroanalysis* **2007**, *19* (12), 1239-1257.
107. O'Brien, J. C.; Jones, V. W.; Porter, M. D.; Mosher, C. L.; Henderson, E., Immunosensing Platforms Using Spontaneously Adsorbed Antibody Fragments on Gold. *Anal. Chem.* **2000**, *72* (4), 703-710.
108. Lee, W.; Oh, B.-K.; Lee, W. H.; Choi, J.-W., Immobilization of antibody fragment for immunosensor application based on surface plasmon resonance. *Colloids and Surfaces B: Biointerfaces* **2005**, *40* (3), 143-148.
109. Vikholm, I., Self-assembly of antibody fragments and polymers onto gold for immunosensing. *Sensors and Actuators B: Chemical* **2005**, *106* (1), 311-316.
110. Schwartz, D. K., Mechanisms and kinetics of self-assembled monolayer formation. *Annu Rev Phys Chem* **2001**, *52*, 107-37.
111. Samanta, D.; Sarkar, A., Immobilization of bio-macromolecules on self-assembled monolayers: methods and sensor applications. *Chemical Society Reviews* **2011**, *40* (5), 2567-2592.
112. Gooding, J. J.; Mearns, F.; Yang, W.; Liu, J., Self-Assembled Monolayers into the 21st Century: Recent Advances and Applications. *Electroanalysis* **2003**, *15* (2), 81-96.
113. Porter, M. D.; Bright, T. B.; Allara, D. L.; Chidsey, C. E. D., Spontaneously organized molecular assemblies. 4. Structural characterization of n-alkyl thiol monolayers on gold by optical ellipsometry, infrared spectroscopy, and electrochemistry. *Journal of the American Chemical Society* **1987**, *109* (12), 3559-3568.
114. Vemparala, S.; Karki, B. B.; Kalia, R. K.; Nakano, A.; Vashishta, P., Large-scale molecular dynamics simulations of alkanethiol self-assembled monolayers. *The Journal of Chemical Physics* **2004**, *121* (9), 4323-4330.
115. Franzen, S., Density functional calculation of a potential energy surface for alkane thiols on Au(111) as function of alkane chain length. *Chemical Physics Letters* **2003**, *381* (3), 315-321.

116. Wan, J.; Ai, J.; Zhang, Y.; Geng, X.; Gao, Q.; Cheng, Z., Signal-off impedimetric immunosensor for the detection of Escherichia coli O157:H7. *Sci Rep* **2016**, *6*, 19806-19806.
117. Soler, M.; Estevez, M. C.; Alvarez, M.; Otte, M. A.; Sepulveda, B.; Lechuga, L. M., Direct detection of protein biomarkers in human fluids using site-specific antibody immobilization strategies. *Sensors (Basel, Switzerland)* **2014**, *14* (2), 2239-2258.
118. Briand, E.; Salmain, M.; Herry, J.-M.; Perrot, H.; Compère, C.; Pradier, C.-M., Building of an immunosensor: How can the composition and structure of the thiol attachment layer affect the immunosensor efficiency? *Biosensors and Bioelectronics* **2006**, *22* (3), 440-448.
119. Briand, E.; Gu, C.; Boujday, S.; Salmain, M.; Herry, J. M.; Pradier, C. M., Functionalisation of gold surfaces with thiolate SAMs: Topography/bioactivity relationship – A combined FT-RAIRS, AFM and QCM investigation. *Surface Science* **2007**, *601* (18), 3850-3855.
120. Everett, W. R.; Welch, T. L.; Reed, L.; Fritsch-Faules, I., Potential-Dependent Stability of Self-Assembled Organothiols on Gold Electrodes in Methylene Chloride. *Anal. Chem.* **1995**, *67* (2), 292-298.
121. Finklea, H. O.; Avery, S.; Lynch, M.; Furtch, T., Blocking oriented monolayers of alkyl mercaptans on gold electrodes. *Langmuir* **1987**, *3* (3), 409-413.
122. Widrig, C. A.; Chung, C.; Porter, M. D., The electrochemical desorption of n-alkanethiol monolayers from polycrystalline Au and Ag electrodes. *Journal of Electroanalytical Chemistry and Interfacial Electrochemistry* **1991**, *310* (1), 335-359.
123. Walczak, M. M.; Popenoe, D. D.; Deinhammer, R. S.; Lamp, B. D.; Chung, C.; Porter, M. D., Reductive desorption of alkanethiolate monolayers at gold: a measure of surface coverage. *Langmuir* **1991**, *7* (11), 2687-2693.
124. Satjapipat, M.; Sanedrin, R.; Zhou, F., Selective Desorption of Alkanethiols in Mixed Self-Assembled Monolayers for Subsequent Oligonucleotide Attachment and DNA Hybridization. *Langmuir* **2001**, *17* (24), 7637-7644.
125. Love, J. C.; Estroff, L. A.; Kriebel, J. K.; Nuzzo, R. G.; Whitesides, G. M., Self-Assembled Monolayers of Thiolates on Metals as a Form of Nanotechnology. *Chemical Reviews* **2005**, *105* (4), 1103-1170.
126. Kang, J. F.; Liao, S.; Jordan, R.; Ulman, A., Mixed Self-assembled Monolayers of Rigid Biphenyl Thiols: Impact of Solvent and Dipole Moment. *Journal of the American Chemical Society* **1998**, *120* (37), 9662-9667.
127. Laibinis, P. E.; Fox, M. A.; Folkers, J. P.; Whitesides, G. M., Comparisons of self-assembled monolayers on silver and gold: mixed monolayers derived from HS(CH<sub>2</sub>)<sub>21</sub>X and HS(CH<sub>2</sub>)<sub>10</sub>Y (X, Y = CH<sub>3</sub>, CH<sub>2</sub>OH) have similar properties. *Langmuir* **1991**, *7* (12), 3167-3173.
128. Heister, K.; Allara, D. L.; Bahnck, K.; Frey, S.; Zharnikov, M.; Grunze, M., Deviations from 1:1 Compositions in Self-Assembled Monolayers Formed from Adsorption of Asymmetric Dialkyl Disulfides on Gold. *Langmuir* **1999**, *15* (17), 5440-5443.
129. Park, M.-K.; Park, J. W.; Oh, J.-H., Optimization and application of a dithiobis-succinimidyl propionate-modified immunosensor platform to detect *Listeria monocytogenes* in chicken skin. *Sensors and Actuators B: Chemical* **2012**, *171-172*, 323-331.

130. Arya, S. K.; Chornokur, G.; Venugopal, M.; Bhansali, S., Dithiobis(succinimidyl propionate) modified gold microarray electrode based electrochemical immunosensor for ultrasensitive detection of cortisol. *Biosensors and Bioelectronics* **2010**, *25* (10), 2296-2301.
131. Tao, Y.-T.; Wu, C.-C.; Eu, J.-Y.; Lin, W.-L.; Wu, K.-C.; Chen, C.-h., Structure Evolution of Aromatic-Derivatized Thiol Monolayers on Evaporated Gold. *Langmuir* **1997**, *13* (15), 4018-4023.
132. Noh, J.; Ito, E.; Hara, M., Self-assembled monolayers of benzenethiol and benzenemethanethiol on Au(111): Influence of an alkyl spacer on the structure and thermal desorption behavior. *J Colloid Interface Sci* **2010**, *342* (2), 513-7.
133. Sellers, H.; Ulman, A.; Shnidman, Y.; Eilers, J. E., Structure and binding of alkanethiolates on gold and silver surfaces: implications for self-assembled monolayers. *Journal of the American Chemical Society* **1993**, *115* (21), 9389-9401.
134. Billah, M. M.; Hodges, C. S.; Hays, H. C. W.; Millner, P. A., Directed immobilization of reduced antibody fragments onto a novel SAM on gold for myoglobin impedance immunosensing. *Bioelectrochemistry* **2010**, *80* (1), 49-54.
135. Wirde, M.; Gelius, U.; Nyholm, L., Self-Assembled Monolayers of Cystamine and Cysteamine on Gold Studied by XPS and Voltammetry. *Langmuir* **1999**, *15* (19), 6370-6378.
136. Carneiro, P.; Loureiro, J.; Delerue-Matos, C.; Morais, S.; do Carmo Pereira, M., Alzheimer's disease: Development of a sensitive label-free electrochemical immunosensor for detection of amyloid beta peptide. *Sensors and Actuators B: Chemical* **2017**, *239*, 157-165.
137. Teixeira, S.; Burwell, G.; Castaing, A.; Gonzalez, D.; Conlan, R. S.; Guy, O. J., Epitaxial graphene immunosensor for human chorionic gonadotropin. *Sensors and Actuators B: Chemical* **2014**, *190*, 723-729.
138. Yang, L.; Li, Y., AFM and impedance spectroscopy characterization of the immobilization of antibodies on indium-tin oxide electrode through self-assembled monolayer of epoxysilane and their capture of Escherichia coli O157:H7. *Biosensors and Bioelectronics* **2005**, *20* (7), 1407-1416.
139. de la Escosura-Muñiz, A.; Merkoçi, A., Label-free voltammetric immunosensor using a nanoporous membrane based platform. *Electrochemistry Communications* **2010**, *12* (6), 859-863.
140. Zhang, G.-J.; Luo, Z. H. H.; Huang, M. J.; Ang, J. A. J.; Kang, T. G.; Ji, H., An integrated chip for rapid, sensitive, and multiplexed detection of cardiac biomarkers from fingerprick blood. *Biosensors and Bioelectronics* **2011**, *28* (1), 459-463.
141. Arya, S. K.; Prusty, A. K.; Singh, S. P.; Solanki, P. R.; Pandey, M. K.; Datta, M.; Malhotra, B. D., Cholesterol biosensor based on N-(2-aminoethyl)-3-aminopropyltrimethoxysilane self-assembled monolayer. *Analytical Biochemistry* **2007**, *363* (2), 210-218.
142. Ahuja, T.; Rajesh; Kumar, D.; Tanwar, V. K.; Sharma, V.; Singh, N.; Biradar, A. M., An amperometric uric acid biosensor based on Bis[sulfosuccinimidyl] suberate crosslinker/3-aminopropyltriethoxysilane surface modified ITO glass electrode. *Thin Solid Films* **2010**, *519* (3), 1128-1134.
143. Hatton, R. A.; Day, S. R.; Chesters, M. A.; Willis, M. R., Organic electroluminescent devices: enhanced carrier injection using an organosilane self assembled monolayer (SAM) derivatized ITO electrode. *Thin Solid Films* **2001**, *394* (1), 291-296.

144. Snell, K. D.; Keenan, A. G., Surface modified electrodes. *Chemical Society Reviews* **1979**, 8 (2), 259-282.
145. Sewvandi, G. A.; Tao, Z.; Kusunose, T.; Tanaka, Y.; Nakanishi, S.; Feng, Q., Modification of TiO<sub>2</sub> Electrode with Organic Silane Interposed Layer for High-Performance of Dye-Sensitized Solar Cells. *ACS Applied Materials & Interfaces* **2014**, 6 (8), 5818-5826.
146. Wasserman, S. R.; Tao, Y. T.; Whitesides, G. M., Structure and reactivity of alkylsiloxane monolayers formed by reaction of alkyltrichlorosilanes on silicon substrates. *Langmuir* **1989**, 5 (4), 1074-1087.
147. Lessel, M.; Bäumchen, O.; Klos, M.; Hähl, H.; Fetzer, R.; Paulus, M.; Seemann, R.; Jacobs, K., Self-assembled silane monolayers: an efficient step-by-step recipe for high-quality, low energy surfaces. *Surface and Interface Analysis* **2015**, 47 (5), 557-564.
148. Carraro, C.; Yauw, O. W.; Sung, M. M.; Maboudian, R., Observation of Three Growth Mechanisms in Self-Assembled Monolayers. *The Journal of Physical Chemistry B* **1998**, 102 (23), 4441-4445.
149. Pasternack, R. M.; Rivillon Amy, S.; Chabal, Y. J., Attachment of 3-(Aminopropyl)triethoxysilane on Silicon Oxide Surfaces: Dependence on Solution Temperature. *Langmuir* **2008**, 24 (22), 12963-12971.
150. Ishida, H.; Naviroj, S.; Tripathy, S. K.; Fitzgerald, J. J.; Koenig, J. L., The structure of an aminosilane coupling agent in aqueous solutions and partially cured solids. *Journal of Polymer Science: Polymer Physics Edition* **1982**, 20 (4), 701-718.
151. Kurth, D. G.; Bein, T., Thin Films of (3-Aminopropyl)triethoxysilane on Aluminum Oxide and Gold Substrates. *Langmuir* **1995**, 11 (8), 3061-3067.
152. Howarter, J. A.; Youngblood, J. P., Optimization of Silica Silanization by 3-Aminopropyltriethoxysilane. *Langmuir* **2006**, 22 (26), 11142-11147.
153. Sales, J. A. A.; Prado, A. G. S.; Airoidi, C., The incorporation of propane-1,3-diamine into silylant epoxide group through homogeneous and heterogeneous routes. *Polyhedron* **2002**, 21 (25-26), 2647-2651.
154. Nam, Y.; Branch, D. W.; Wheeler, B. C., Epoxy-silane linking of biomolecules is simple and effective for patterning neuronal cultures. *Biosensors and Bioelectronics* **2006**, 22 (5), 589-597.
155. Guerrero, G.; Alauzun, J. G.; Granier, M.; Laurencin, D.; Mutin, P. H., Phosphonate coupling molecules for the control of surface/interface properties and the synthesis of nanomaterials. *Dalton Transactions* **2013**, 42 (35), 12569-12585.
156. Hanson, E. L.; Schwartz, J.; Nickel, B.; Koch, N.; Danisman, M. F., Bonding Self-Assembled, Compact Organophosphonate Monolayers to the Native Oxide Surface of Silicon. *Journal of the American Chemical Society* **2003**, 125 (51), 16074-16080.
157. Silverman, B. M.; Wieghaus, K. A.; Schwartz, J., Comparative Properties of Siloxane vs Phosphonate Monolayers on A Key Titanium Alloy. *Langmuir* **2005**, 21 (1), 225-228.
158. Marcinko, S.; Fadeev, A. Y., Hydrolytic Stability of Organic Monolayers Supported on TiO<sub>2</sub> and ZrO<sub>2</sub>. *Langmuir* **2004**, 20 (6), 2270-2273.



159. Queffelec, C.; Petit, M.; Janvier, P.; Knight, D. A.; Bujoli, B., Surface Modification Using Phosphonic Acids and Esters. *Chemical Reviews* **2012**, *112* (7), 3777-3807.
160. Guerrero, G.; Mutin, P. H.; Vioux, A., Organically modified aluminas by grafting and sol-gel processes involving phosphonate derivatives. *Journal of Materials Chemistry* **2001**, *11* (12), 3161-3165.
161. Adden, N.; Gamble, L. J.; Castner, D. G.; Hoffmann, A.; Gross, G.; Menzel, H., Phosphonic Acid Monolayers for Binding of Bioactive Molecules to Titanium Surfaces. *Langmuir* **2006**, *22* (19), 8197-8204.
162. Teles, F. R. R.; Fonseca, L. P., Applications of polymers for biomolecule immobilization in electrochemical biosensors. *Materials Science and Engineering: C* **2008**, *28* (8), 1530-1543.
163. Ramanavičius, A.; Ramanavičienė, A.; Malinauskas, A., Electrochemical sensors based on conducting polymer—polypyrrole. *Electrochim. Acta* **2006**, *51* (27), 6025-6037.
164. Sassin, M. B.; Long, J. W.; Wallace, J. M.; Rolison, D. R., Routes to 3D conformal solid-state dielectric polymers: electrodeposition versus initiated chemical vapor deposition. *Materials Horizons* **2015**, *2* (5), 502-508.
165. Zeeshan, M. A.; Grisch, R.; Pellicer, E.; Sivaraman, K. M.; Peyer, K. E.; Sort, J.; Özkale, B.; Sakar, M. S.; Nelson, B. J.; Pané, S., Hybrid Helical Magnetic Microrobots Obtained by 3D Template-Assisted Electrodeposition. *Small* **2014**, *10* (7), 1284-1288.
166. Cosnier, S., Biosensors based on electropolymerized films: new trends. *Analytical and Bioanalytical Chemistry* **2003**, *377* (3), 507-520.
167. Creedon, N.; Robinson, C.; Kennedy, E.; Riordan, A. O. In *Agriculture 4.0: Development of Seriological on-Farm Immunosensor for Animal Health Applications*, 2019 IEEE SENSORS, 27-30 Oct. 2019; 2019; pp 1-4.
168. Mattos, A. B.; Freitas, T. A.; Kubota, L. T.; Dutra, R. F., An o-aminobenzoic acid film-based immunoelectrode for detection of the cardiac troponin T in human serum. *Biochemical Engineering Journal* **2013**, *71*, 97-104.
169. Liu, X.; Zheng, S.; Hu, Y.; Li, Z.; Luo, F.; He, Z., Electrochemical Immunosensor Based on the Chitosan-Magnetic Nanoparticles for Detection of Tetracycline. *Food Analytical Methods* **2016**, *9*.
170. Luo, X.-L.; Xu, J.-J.; Wang, J.-L.; Chen, H.-Y., Electrochemically deposited nanocomposite of chitosan and carbon nanotubes for biosensor application. *Chemical Communications* **2005**, (16), 2169-2171.
171. Zhang, X.; Li, C.-R.; Wang, W.-C.; Xue, J.; Huang, Y.-L.; Yang, X.-X.; Tan, B.; Zhou, X.-P.; Shao, C.; Ding, S.-J.; Qiu, J.-F., A novel electrochemical immunosensor for highly sensitive detection of aflatoxin B1 in corn using single-walled carbon nanotubes/chitosan. *Food Chemistry* **2016**, *192*, 197-202.
172. Jin, W.-J.; Yang, G.-J.; Shao, H.-X.; Qin, A.-J., A novel label-free impedimetric immunosensor for detection of semicarbazide residue based on gold nanoparticles-functional chitosan composite membrane. *Sensors and Actuators B: Chemical* **2013**, *188*, 271-279.

173. Chen, X.; Qin, P.; Li, J.; Yang, Z.; Wen, Z.; Jian, Z.; Zhao, J.; Hu, X.; Jiao, X. a., Impedance immunosensor for bovine interleukin-4 using an electrode modified with reduced graphene oxide and chitosan. *Microchim. Acta* **2015**, *182* (1), 369-376.
174. Kaushik, A.; Solanki, P. R.; Ansari, A. A.; Ahmad, S.; Malhotra, B. D., Chitosan–iron oxide nanobiocomposite based immunosensor for ochratoxin-A. *Electrochemistry Communications* **2008**, *10* (9), 1364-1368.
175. Wang, Z.; Yang, Y.; Li, J.; Gong, j.; Shen, G.; Yu, R., Organic–inorganic matrix for electrochemical immunoassay: Detection of human IgG based on ZnO/chitosan composite. *Talanta* **2006**, *69* (3), 686-690.
176. Gerard, M.; Chaubey, A.; Malhotra, B. D., Application of conducting polymers to biosensors. *Biosensors and Bioelectronics* **2002**, *17* (5), 345-359.
177. Guimard, N. K.; Gomez, N.; Schmidt, C. E., Conducting polymers in biomedical engineering. *Progress in Polymer Science* **2007**, *32* (8), 876-921.
178. Guan, J.-G.; Miao, Y.-Q.; Zhang, Q.-J., Impedimetric biosensors. *Journal of Bioscience and Bioengineering* **2004**, *97* (4), 219-226.
179. Gooding, J. J.; Wasiowych, C.; Barnett, D.; Hibbert, D. B.; Barisci, J. N.; Wallace, G. G., Electrochemical modulation of antigen–antibody binding. *Biosensors and Bioelectronics* **2004**, *20* (2), 260-268.
180. Adeloju, S. B.; Wallace, G. G., Conducting polymers and the bioanalytical sciences: new tools for biomolecular communication. A review. *Analyst* **1996**, *121* (6), 699-703.
181. Vedrine, C.; Fabiano, S.; Tran-Minh, C., Amperometric tyrosinase based biosensor using an electrogenerated polythiophene film as an entrapment support. *Talanta* **2003**, *59* (3), 535-44.
182. Geise, R. J.; Adams, J. M.; Barone, N. J.; Yacynych, A. M., Electropolymerized films to prevent interferences and electrode fouling in biosensors. *Biosensors and Bioelectronics* **1991**, *6* (2), 151-160.
183. Dhand, C.; Das, M.; Datta, M.; Malhotra, B. D., Recent advances in polyaniline based biosensors. *Biosensors and Bioelectronics* **2011**, *26* (6), 2811-2821.
184. MacDiarmid, A. G., “Synthetic Metals”: A Novel Role for Organic Polymers (Nobel Lecture). *Angewandte Chemie International Edition* **2001**, *40* (14), 2581-2590.
185. Chen, W. C.; Wen, T. C.; Hu, C. C.; Gopalan, A., Identification of inductive behavior for polyaniline via electrochemical impedance spectroscopy. *Electrochim. Acta* **2002**, *47* (8), 1305-1315.
186. Sethumadhavan, V.; Rudd, S.; Switalska, E.; Zuber, K.; Teasdale, P.; Evans, D., Recent advances in ion sensing with conducting polymers. *BMC Materials* **2019**, *1*, 4.
187. Moraes, S. R.; Huerta-Vilca, D.; Motheo, A. J., Characteristics of polyaniline synthesized in phosphate buffer solution. *European Polymer Journal* **2004**, *40* (9), 2033-2041.
188. Janáky, C.; Visy, C., Conducting polymer-based hybrid assemblies for electrochemical sensing: a materials science perspective. *Analytical and Bioanalytical Chemistry* **2013**, *405* (11), 3489-3511.

189. Vidal, J.; Garcia-Ruiz, E.; Castillo, J.-R., Recent Advances in Electropolymerized Conducting Polymers in Amperometric Biosensors. *Microchim. Acta* **2003**, *143*, 93-111.
190. Rodrigues, L. P.; Ferreira, D. C.; Sonoda, M. T.; Madurro, A. G. B.; Abrahão Jr, O.; Madurro, J. M., Electropolymerization mechanisms of hydroxyphenylacetic acid isomers. *Journal of Molecular Structure* **2014**, *1072* (1), 298-306.
191. Cooreman, P.; Thoelen, R.; Manca, J.; vandeVen, M.; Vermeeren, V.; Michiels, L.; Ameloot, M.; Wagner, P., Impedimetric immunosensors based on the conjugated polymer PPV. *Biosensors and Bioelectronics* **2005**, *20* (10), 2151-2156.
192. Ko, S.; Jang, J., Protein Immobilization on Aminated Poly(glycidyl methacrylate) Nanofibers as Polymeric Carriers. *Biomacromolecules* **2007**, *8* (5), 1400-1403.
193. Mistry, K. K.; Layek, K.; Mahapatra, A.; RoyChaudhuri, C.; Saha, H., A review on amperometric-type immunosensors based on screen-printed electrodes. *Analyst* **2014**, *139* (10), 2289-2311.
194. Shao, L.; Qiu, J.; Liu, M.; Feng, H.; Lei, L.; Zhang, G.; Zhao, Y.; Gao, C.; Qin, L., Synthesis and characterization of water-soluble polyaniline films. *Synth. Met.* **2011**, *161* (9-10), 806-811.
195. Shao, L.; Qiu, J. H.; Feng, H. X.; Liu, M. Z.; Zhang, G. H.; An, J. B.; Gao, C. M.; Liu, H. L., Structural investigation of lignosulfonate doped polyaniline. *Synth. Met.* **2009**, *159* (17-18), 1761-1766.
196. Karyakin, A. A.; Strakhova, A. K.; Yatsimirsky, A. K., Self-doped polyanilines electrochemically active in neutral and basic aqueous solutions.: Electropolymerization of substituted anilines. *Journal of Electroanalytical Chemistry* **1994**, *371* (1), 259-265.
197. Fusco, G.; Gallo, F.; Tortolini, C.; Bollella, P.; Ietto, F.; De Mico, A.; D'Annibale, A.; Antiochia, R.; Favero, G.; Mazzei, F., AuNPs-functionalized PANABA-MWCNTs nanocomposite-based impedimetric immunosensor for 2,4-dichlorophenoxy acetic acid detection. *Biosensors and Bioelectronics* **2017**, *93*, 52-56.
198. Benyoucef, A.; Boussalem, S.; Ferrahi, M. I.; Belbachir, M., Electrochemical polymerization and in situ FTIRS study of conducting polymers obtained from o-aminobenzoic with aniline at platinum electrodes. *Synth. Met.* **2010**, *160* (15-16), 1591-1597.
199. Truong, L. T. N.; Chikae, M.; Ukita, Y.; Takamura, Y., Labelless impedance immunosensor based on polypyrrole-pyrolecarboxylic acid copolymer for hCG detection. *Talanta* **2011**, *85* (5), 2576-2580.
200. Owino, J. H. O.; Ignaszak, A.; Al-Ahmed, A.; Baker, P. G. L.; Alemu, H.; Ngila, J. C.; Iwuoha, E. I., Modelling of the impedimetric responses of an aflatoxin B1 immunosensor prepared on an electrosynthetic polyaniline platform. *Analytical and Bioanalytical Chemistry* **2007**, *388* (5-6), 1069-1074.
201. Rozlosnik, N., New directions in medical biosensors employing poly(3,4-ethylenedioxy thiophene) derivative-based electrodes. *Analytical and Bioanalytical Chemistry* **2009**, *395* (3), 637-645.
202. Lim, S. A.; Ahmed, M. U., Electrochemical immunosensors and their recent nanomaterial-based signal amplification strategies: a review. *RSC Adv.* **2016**, *6* (30), 24995-25014.

203. Caschera, D.; Federici, F.; Zane, D.; Focanti, F.; Curulli, A.; Padeletti, G., Gold nanoparticles modified GC electrodes: electrochemical behaviour dependence of different neurotransmitters and molecules of biological interest on the particles size and shape. *Journal of Nanoparticle Research* **2008**, *11* (8), 1925.
204. Rodríguez-Sánchez, L.; Blanco, M. C.; López-Quintela, M. A., Electrochemical Synthesis of Silver Nanoparticles. *The Journal of Physical Chemistry B* **2000**, *104* (41), 9683-9688.
205. Kellon, J. E.; Young, S. L.; Hutchison, J. E., Engineering the Nanoparticle–Electrode Interface. *Chemistry of Materials* **2019**, *31* (8), 2685-2701.
206. Shein, J. B.; Lai, L. M. H.; Eggers, P. K.; Paddon-Row, M. N.; Gooding, J. J., Formation of Efficient Electron Transfer Pathways by Adsorbing Gold Nanoparticles to Self-Assembled Monolayer Modified Electrodes. *Langmuir* **2009**, *25* (18), 11121-11128.
207. Wongkaew, N.; Simsek, M.; Griesche, C.; Baeumner, A. J., Functional Nanomaterials and Nanostructures Enhancing Electrochemical Biosensors and Lab-on-a-Chip Performances: Recent Progress, Applications, and Future Perspective. *Chemical Reviews* **2019**, *119* (1), 120-194.
208. Wang, J.; Yang, S.; Guo, D.; Yu, P.; Li, D.; Ye, J.; Mao, L., Comparative studies on electrochemical activity of graphene nanosheets and carbon nanotubes. *Electrochemistry Communications* **2009**, *11* (10), 1892-1895.
209. Pei, S.; Cheng, H.-M., The reduction of graphene oxide. *Carbon* **2012**, *50* (9), 3210-3228.
210. Shang, Y. U.; Zhang, D.; Liu, Y.; Guo, C., Preliminary comparison of different reduction methods of graphene oxide. *Bulletin of Materials Science* **2015**, *38* (1), 7-12.
211. Vasilescu, A.; Hayat, A.; Gáspár, S.; Marty, J.-L., Advantages of Carbon Nanomaterials in Electrochemical Aptasensors for Food Analysis. *Electroanalysis* **2018**, *30* (1), 2-19.
212. Liu, J.; Chou, A.; Rahmat, W.; Paddon-Row, M. N.; Gooding, J. J., Achieving Direct Electrical Connection to Glucose Oxidase Using Aligned Single Walled Carbon Nanotube Arrays. *Electroanalysis* **2005**, *17* (1), 38-46.
213. Patolsky, F.; Weizmann, Y.; Willner, I., Long-Range Electrical Contacting of Redox Enzymes by SWCNT Connectors. *Angewandte Chemie International Edition* **2004**, *43* (16), 2113-2117.
214. Chou, A.; Böcking, T.; Singh, N. K.; Gooding, J. J., Demonstration of the importance of oxygenated species at the ends of carbon nanotubes for their favourable electrochemical properties. *Chemical Communications* **2005**, (7), 842-844.
215. Narang, J.; Malhotra, N.; Singh, G.; Pundir, C. S., Electrochemical impedimetric detection of anti-HIV drug taking gold nanorods as a sensing interface. *Biosensors & bioelectronics* **2015**, *66*, 332-7.
216. Amouzadeh Tabrizi, M.; Shamsipur, M.; Mostafaie, A., A high sensitive label-free immunosensor for the determination of human serum IgG using overoxidized polypyrrole decorated with gold nanoparticle modified electrode. *Mater Sci Eng C Mater Biol Appl* **2016**, *59*, 965-969.

217. Ferreira, V. C.; Melato, A. I.; Silva, A. F.; Abrantes, L. M., Attachment of noble metal nanoparticles to conducting polymers containing sulphur – preparation conditions for enhanced electrocatalytic activity. *Electrochim. Acta* **2011**, *56* (10), 3567-3574.
218. Ferreira, V. C.; Melato, A. I.; Silva, A. F.; Abrantes, L. M., Conducting polymers with attached platinum nanoparticles towards the development of DNA biosensors. *Electrochemistry Communications* **2011**, *13* (9), 993-996.
219. Lu, L.; Seenivasan, R.; Wang, Y.-C.; Yu, J.-H.; Gunasekaran, S., An Electrochemical Immunosensor for Rapid and Sensitive Detection of Mycotoxins Fumonisin B1 and Deoxynivalenol. *Electrochim. Acta* **2016**, *213*, 89-97.
220. John, R.; Spencer, M.; Wallace, G. G.; Smyth, M. R., Development of a polypyrrole-based human serum albumin sensor. *Analytica Chimica Acta* **1991**, *249* (2), 381-385.
221. Huang, H. H.; Zhou, J.; Huang, Y. P.; Kong, J. L., Impedimetric immunosensor with on-chip integrated electrodes for high-throughput screening of liver fibrosis markers. *Journal of Analytical Chemistry* **2008**, *63* (5), 492-498.
222. Loo, A. H.; Bonanni, A.; Ambrosi, A.; Poh, H. L.; Pumera, M., Impedimetric immunoglobulin G immunosensor based on chemically modified graphenes. *Nanoscale* **2012**, *4* (3), 921-5.
223. Conde, J.; Dias, J. T.; Grazú, V.; Moros, M.; Baptista, P. V.; de la Fuente, J. M., Revisiting 30 years of biofunctionalization and surface chemistry of inorganic nanoparticles for nanomedicine. *Frontiers in Chemistry* **2014**, *2* (48).
224. Fischer, M. J., Amine coupling through EDC/NHS: a practical approach. *Methods Mol Biol* **2010**, *627*, 55-73.
225. Peelen, D.; Kodoyianni, V.; Lee, J.; Zheng, T.; Shortreed, M. R.; Smith, L. M., Specific capture of mammalian cells by cell surface receptor binding to ligand immobilized on gold thin films. *J Proteome Res* **2006**, *5* (7), 1580-5.
226. Yuan, H.; Mullett, W.; Pawliszyn, J., Biological sample analysis with immunoaffinity solid-phase microextraction. *The Analyst* **2001**, *126*, 1456-61.
227. Lasseter, T. L.; Cai, W.; Hamers, R. J., Frequency-dependent electrical detection of protein binding events. *Analyst* **2004**, *129* (1), 3-8.
228. Hays, H. C. W.; Millner, P. A.; Prodromidis, M. I., Development of capacitance based immunosensors on mixed self-assembled monolayers. *Sensors and Actuators B: Chemical* **2006**, *114* (2), 1064-1070.
229. McKnight, T. E.; Peeraphatdit, C.; Jones, S. W.; Fowlkes, J. D.; Fletcher, B. L.; Klein, K. L.; Melechko, A. V.; Doktycz, M. J.; Simpson, M. L., Site-Specific Biochemical Functionalization along the Height of Vertically Aligned Carbon Nanofiber Arrays. *Chemistry of Materials* **2006**, *18* (14), 3203-3211.
230. Mouffouk, F.; Higgins, S. J.; Brown, S. J.; Sedghi, N.; Eccleston, B.; Reeman, S., A regioregular polyalkylthiophene bearing covalently-linked biotin, and its interaction with avidin in solution and in thin films. *Chemical Communications* **2004**, (20), 2314-2315.

231. Nieves, D. J.; Azmi, N. S.; Xu, R.; Lévy, R.; Yates, E. A.; Fernig, D. G., Monovalent maleimide functionalization of gold nanoparticles via copper-free click chemistry. *Chemical Communications* **2014**, 50 (86), 13157-13160.
232. Rao, S. V.; Anderson, K. W.; Bachas, L. G., Oriented immobilization of proteins. *Microchim. Acta* **1998**, 128 (3), 127-143.
233. Katz, E.; Willner, I., Probing Biomolecular Interactions at Conductive and Semiconductive Surfaces by Impedance Spectroscopy: Routes to Impedimetric Immunosensors, DNA-Sensors, and Enzyme Biosensors. *Electroanalysis* **2003**, 15 (11), 913-947.
234. Berggren, C.; Bjarnason, B.; Johansson, G., Capacitive Biosensors. *Electroanalysis* **2001**, 13, 173-180.

***Chapter 2*      **Detection of Bovine Immunoglobulin G to  
Determine Passive Transfer in Calves****

## 2.1 Introduction

The bovine placenta prevents antibodies, such as immunoglobulin G (IgG) from being transferred from the dam to the foetus.<sup>1</sup> New-born calves are therefore hypogammaglobulinemic and rely on the first maternal feed of milk as a source of antibodies. The milk a dam produces immediately after calving is referred to as colostrum and has a substantially higher concentration of antibodies and nutrients than ordinary milk. The ingestion of colostrum presents a route by which the new-born calf can absorb IgG into their system. Uptake of antibodies in this way is called passive transfer and is crucial for the new-born calf to fight pathogens until they can actively produce their own antibodies. Calves suffering from Failure of Passive Transfer (FPT) are at greater risk from infectious diseases and mortality. In Ireland, almost 40% of all calf mortality recorded annually can be attributed to FPT.<sup>2</sup> Monitoring of new-born calves for successful passive transfer is therefore essential to their early health and survival, and to their long term productivity. Passive transfer of macromolecules into the calf's blood stream occurs via an apical tubular system in the intestinal absorptive cells. This route of absorption is only present for a limited period after birth.<sup>3</sup> Feeding of colostrum to a calf within the first 6 hrs after birth is crucial as the potential for IgG absorption is at its highest. Cessation of antibody absorption occurs at an increasing rate from 12 hrs after birth, with complete gut closure occurring by 48 hrs postpartum.<sup>3-5</sup> Currently, determination of successful passive transfer is assessed from 18 to 48 hrs after birth,<sup>6</sup> outside of the critical absorption window. However, if sub-optimal IgG uptake can be identified earlier, while IgG gut absorption is still possible further colostrum can be given to the calf to prevent FPT and improve calf vitality and viability.

Factors that affect the transfer of IgG from dam to calf include colostrum quality, timing of ingestion, method of feeding, volume of colostrum consumed, parity, presence of dam, breed of dam, and pooling of colostrum from multiple dams.<sup>1</sup> Current methods for measuring passive transfer include radial immunodiffusion,<sup>7-10</sup> enzyme-linked immunosorbent assay (ELISA),<sup>2, 9, 10</sup> serum total solid concentration by refractometer,<sup>2, 11-13</sup> sodium sulfite turbidity test,<sup>10, 11, 13</sup> zinc sulfate turbidity test,<sup>2, 8, 9, 11, 13</sup>  $\gamma$ -glutamyl transferase (GGT) activity<sup>2, 13-15</sup> and whole-blood glutaraldehyde coagulation test.<sup>16</sup>



Radial immunodiffusion is the “gold standard” for identification of FPT.<sup>10</sup> Antisera specific to IgG are incorporated onto an agarose plate. Serum samples are then dispensed into wells in the gel. The target antigen diffuses into the gel, binding to the antisera and forming antibody-antigen complexes which produce a visible precipitate in the gel. Although this technique is more sensitive than ELISA, it has a lengthier time to result.<sup>10</sup> Thus ELISA is often favoured as a detection method. Disadvantages of ELISA include its greater cost compared to the other techniques listed and it is also more technically demanding. Other standard detection methods are indirect. Although these tests are often more economical and are approaching point-of-care technology, they often lack either sensitivity or specificity, resulting in a high number of false-negatives or -positives, respectively.

Serum total solid concentration is easily performed by refractometer and has the potential to be used on-farm.<sup>2</sup> However, no standard threshold for a determination of FPT exists and the test cut-off point remains a subject of debate across researchers. It has also been suggested that non-immunoglobulin components of the serum’s globulin may lead to misclassifications using this assay. The sodium sulphite turbidity test and zinc sulphate turbidity test are semi-quantitative tests which cause the precipitation of high molecular weight proteins out of solution producing a visible turbidity.<sup>2</sup> They are simple and cheap and have the potential to be developed as pen-side diagnostic devices. However, these indirect methods lack sensitivity.<sup>2, 11</sup> Moreover, the solutions can be unstable when exposed to atmospheric CO<sub>2</sub>.<sup>2, 8</sup>

The GGT enzyme is produced by ductile cells in the mammary gland. Consequently, this is ingested by the calf through colostrum feeding. GGT levels can be monitored to determine successful passive transfer as an alternative to IgG levels.<sup>2</sup> This is ideal for large scale analysis as automated analysers exist for inexpensive and fast sample turnover. However, standard cut off points have again not been agreed for this method and calf age at testing would appear to impact results. Additionally, some studies have argued that the correlation between GGT activity and IgG concentration is low,<sup>17-20</sup> discouraging the use of this method to assess passive transfer.<sup>1</sup> The basis for the white blood glutaraldehyde coagulation test is that uncharged amino groups on proteins will form cross-linkages with aldehyde groups forming a visible clot. If the clot forms in less than 5 mins, passive transfer is deemed to have occurred. This provides limited information, giving no insight

to the actual IgG levels which are needed to determine if further interventions may be required.<sup>16</sup>

To meet the demand for IgG measurements on farm, the following devices are commercially available; FASTest Bovine IgG,<sup>21</sup> ZAPvet Bovine IgG<sup>22</sup> and DVM Rapid Test™ II.<sup>23</sup> Several more tests are aimed at equine IgG determination, such as Gamma Check® E,<sup>24</sup> FOALCHEK®<sup>25</sup> and SNAP Foal IgG Test (IDEXX).<sup>24</sup> These are all semiquantitative tests based on indirect IgG detection. None are routinely used on dairy farms (personal communication from Irish private veterinary practitioners) due to complex sample preparation procedures and cost. Additionally, they reportedly record a low specificity leading to an over prediction of FTP which in turn leads to unnecessary and potentially costly interventions. Electrochemical transducers have been a favoured option for point of care immunosensors due to their low cost of production, their straightforward operation, and the rapid turnaround time to result.<sup>26-29</sup> Electrochemical devices can also be designed to allow for simultaneous measurement of different analytes;<sup>30</sup> to allow label-free detection, and be readily compatible with integrated circuits<sup>31</sup> and microfluidics.<sup>32</sup> They also have the ability to be modified into low-cost portable devices which are user friendly negating the need for trained technicians. Most importantly, these benefits can be achieved without compromising diagnostic sensitivity or specificity. EIS, in particular, can sensitively monitor the changes in capacitance or charge-transfer resistance associated with material binding at specifically prepared receptive electrode surfaces, and requires no prior labelling.<sup>33</sup>

Failure of passive transfer predisposes calves to increased morbidity and mortality. This immunodeficiency, however, can be corrected by administering immediate treatments such as plasma transfusions and/or administration of antibiotics. Rapid and accurate diagnosis is required to allow such interventions. Current IgG detection methods are flawed and do not allow farmers to routinely check their newborn livestock for successful passive transfer. Our aim was to develop and evaluate an immunosensor which could rapidly and accurately measure levels of IgG in calf serum. In this chapter, the development of an impedimetric immunosensor device on a silicon substrate is described and its capability as a bovine IgG sensor for newborn calves is established. The fully integrated device comprised of six individual gold microband sensors, a platinum pseudo-reference electrode and gold counter electrode. Contact pads were designed to connect to

a PCB through a MicroSD edge connector for future integration into portable electronics for pen-side diagnostics. The ultramicroelectrode characteristics of these sensors, compared to larger electrodes, leads to steady-state behaviour, low charge transfer resistance, high current density due to enhanced mass transport, low depletion of target molecules, low supporting electrolyte concentrations, and faster response times.<sup>34</sup> In this work, I developed a customised electrode surface coating for the immobilisation of biomolecules to allow the development of a functioning immunosensor. The functionality of the immunosensor was then confirmed over a range of IgG concentrations in buffer, followed by evaluation in newborn calf serum pre- and post-colostrum feeding.

## 2.2 Experimental

### 2.2.1 Materials and Buffer Preparation

Bovine purified IgG (PBP002) was purchased from Bio-Rad Laboratories, Oxford, UK, along with anti-bovine IgG polyclonal antibody (AAI23) and biotinylated anti-Bovine IgG polyclonal antibody (AAI23B), both produced in sheep. Streptavidin conjugated with HRP (STAR5B) was also purchased from Bio-Rad. Anti-Bovine IgG produced in mouse (B6901) was purchased from Sigma Aldrich. Calf serum samples were provided by Teagasc, Moorepark, Cork, Ireland. NANNYcare® goat-based milk was purchased from the local supermarket. All other reagents were purchased from Sigma Aldrich unless stated.

HBS-EP buffer was prepared by mixing 10 mM HEPES, 150 mM NaCl, 3 mM EDTA and 0.005% Tween-20 in DI water and adjusted to pH to 7.4 with 5% sodium hydroxide solution. Deionised water (resistance 18.2 M $\Omega$  cm<sup>-1</sup>) was obtained using an ELGA Pure Lab Ultra system purchased from Alpha Diagnostic International.

### 2.2.2 ELISA

An in-house ELISA was set up for the purposes of selecting a suitable capture molecule for the detection bovine IgG (Bo IgG). Two capture antibodies were employed for this work, mouse anti-bovine IgG and sheep anti-bovine IgG. These antibodies were diluted to 1  $\mu$ g/ml in PBS and 100  $\mu$ L was incubated in each well of an ELISA plate (Nunc-Immuno™ MicroWell™ 96 well solid plates) at 4°C overnight. The plate was then rinsed three times with washing buffer (PBS + 0.05% Tween20) with a plate washer (DiaSource). Each well was blocked with 200  $\mu$ L of 5% skimmed milk in PBS to prevent other biomolecules absorbing onto the well surface and prevent non-specific binding. Following incubation for one hour, the plate was rinsed three times as before. The target, Bo IgG was diluted into working solutions of varying concentrations (4 ng/ml – 300 ng/ml) in PBS. Each of these solutions was incubated in triplicate in the ELISA plate for one hour. PBS was also incubated in three wells to allow correction for background noise. The plate was rinsed and a dilution of biotinylated sheep anti-Bo IgG (1:5000 in PBS) was aliquoted into each well. After one hour this solution was rinsed from and replaced

with diluted Streptavidin – HRP (1:4000 in PBS) for 15 mins. The plate was rinsed three times with PBS + Tween20 for a final time. A volume of 100  $\mu\text{L}$  of TMB with 12 mM hydrogen peroxide in 50 mM phosphate citrate buffer, pH 5, was pipetted into each well. After 5 mins, 50  $\mu\text{L}$  of 1 M sulphuric acid was pipetted into each well to stop further reaction. The absorbance of each well was measured at 450 nm using an ELISA plate reader (DiaSource).

## 2.2.3 Electrochemical Immunoassay

### 2.2.3.1 Device Fabrication

Devices containing gold microband electrodes, parallel gold counter and platinum pseudo-reference electrodes, interconnection tracks and peripheral contact pad were fabricated on a 4-inch wafer scale, similar to those described in Dawson.<sup>35</sup> These devices were designed to facilitate an electrical connection to external electronics through a PCB mounted microSD port.<sup>36</sup> thereby facilitating development of a point-of-care application. A 4-inch wafer allowed for the simultaneous production of 28 devices (9.78 x 17.52 mm) on silicon substrates bearing a ~300 nm layer of thermally grown silicon dioxide. A blank metal evaporation (Ti 10 nm /Au 50 nm Temescal FC-2000 E-beam evaporator) and lift-off techniques yielded microband (55  $\mu\text{m}$  x 1  $\mu\text{m}$  x 60 nm) structures. A second Au metal deposition and lift-off technique protocol was performed to create interconnection tracks and the counter (90  $\mu\text{m}$  x 7 mm) electrode. A final platinum deposition and lift-off technique protocol was performed to create a pseudo-reference electrode. To impede unwanted electrochemical reactions occurring at the metallic interconnection tracks, a passivation layer of thick insulating layer silicon nitride ( $\text{Si}_3\text{N}_4$ ) was blanket deposited by plasma-enhanced chemical vapour deposition. Photolithography and dry etching were utilised to selectively open a window (45  $\mu\text{m}$  x 100  $\mu\text{m}$ ) in the insulating SiN layer over the microband electrodes, allowing electrical contact between the electrode and the electrolyte. Openings were also created over the counter and pseudo-reference electrodes and the contact pads. Each device contained six microbands (sensors) which were 0.94 mm apart. Once the wafer was completed, it was diced into individual devices.

To facilitate the connection of these devices to electronic equipment, a custom-made cell was fabricated to allow small electrolyte volumes (~50  $\mu\text{L}$  – 8 mls) to come in contact with the working, counter and pseudo-reference electrodes. The cell was constructed from

an aluminium base and a Teflon lid. Spring loaded pins (Coda Systems Ltd. PM4J Plain Radius Microprobes) were inserted into the lid in position above the peripheral contact pads on both sides of the device. The base was milled to mount the chip. The cell was assembled using a series of screws and with a Viton O-ring secured in place in the lid to prevent leaking of analyte solution. Viton O-rings were chosen as they are chemical resistant. A 7 mm inner diameter x 1.6 mm cross-section O-ring was selected to generate an opening large enough to cover all six sensors on the device with solution. A well was milled across the rest of the lid to allow for a larger reservoir of solution if needed. An alternative holder was also designed that did not cover the microSD contact pads. These contact pads were left to protrude from the cell to be accessible to a PCB mounted microSD port.

### **2.2.3.2 Sensor Characterisation**

#### **Optical Characterisation**

After fabrication, the structural integrity of the device was characterised optically and electrochemically. For optical inspection, devices were viewed using a calibrated microscope (Olympus, Tokyo, Japan) furnished with a charge-coupled detector camera. This ensured there was no visual damage to any feature on the device.

#### **Electrochemical Characterisation**

All electrochemical studies were performed using an Autolab Potentiostat/ Galvanostat PGSTAT128N (Metrohm Ltd, Utrecht, The Netherlands) controlled by Autolab NOVA software. All experiments were performed at room temperature in a Faraday cage. The custom-made cell was used for all electrochemical experiments. A three-electrode cell was adopted, using a single gold microband as a working electrode, the on-chip gold counter and platinum pseudo-reference electrodes. Each of the six microbands on the device were characterised in 1 mM FcCOOH in 10 mM PBS (pH 7.4) using CV and EIS. The CV measurements were performed at a potential window of -150 mV to 450 mV at 50 mV s<sup>-1</sup>. The EIS measurements were performed at a frequency range of 100 mHz to 10 kHz at a potential of 200 mV. The amplitude of the alternating voltage was set at 5 mV.

### **Atomic Force Microscopy (AFM)**

AFM images of the bare gold electrodes across a range of wafers were acquired with a Veeco Dimension 3100 AFM (New York, USA) in tapping mode using commercial Olympus probes (Oxford Instruments Asylum Research, High Wycombe, UK). This technique was used to illustrate the structural integrity of the microbands following cleaning and modification. An area of  $5\ \mu\text{m} \times 5\ \mu\text{m}$  was investigated at a scan rate of 0.7 Hz. Background plane subtraction was applied to the images.

### **Scanning Electron Microscopy (SEM)**

SEM images of the microband electrodes were acquired by Dr. Colm Barrett using a field emission SEM (JSM – 7500F, JEOL UK Ltd.) operating at beam voltages between 5 and 10 kV. SEM analysis was undertaken to structurally characterise the fabricated microbands.

#### **2.2.3.3 Electrode Modification**

##### **Surface Modification with Electropolymer**

Poly *o*-aminobenzoic acid (*o*-ABA) and polyaniline (PANI) are both biocompatible polymers which can be electrodeposited onto electrodes. Both molecules consist of an amine group attached to a benzene ring. By cycling the potential of an electrode these molecules polymerise through their amine group and coat the electrode. *o*-ABA has a carboxylic acid group in the ortho position that can be used for attachment of biomolecules to the electrode surface.

Prior to use the device was cleaned by immersing in acetone and sonicating for 10 mins. This was repeated in deionised water prior to drying with  $\text{N}_2$ . Stock solutions of 50 mM *o*-ABA in 0.5 M  $\text{H}_2\text{SO}_4$  and 100 mM aniline in deionised water were prepared. The copolymerisation of *o*-ABA and PANI was achieved by cycling the potential between 150 mV and 1200 mV *vs* Ag/AgCl at  $50\text{mV s}^{-1}$  at different ratios and different numbers of cycles. Following electrodeposition, the surface was characterised using CV and EIS in 1 mM FcCOOH in 10 mM PBS. A second set of stock solutions was also used containing 50 mM *o*-ABA in 1 M  $\text{H}_2\text{SO}_4$  and 100 mM aniline in 1 M  $\text{H}_2\text{SO}_4$ .

### **Sensor Functionalisation with Capture Molecule**

Prior to use devices were cleaned as described above. The co-polymer consisting of o-ABA and PANI was electrodeposited using CV at a ratio of 9:1 in 1 M H<sub>2</sub>SO<sub>4</sub> for 20 cycles. The device was gently rinsed with DI water and dried with N<sub>2</sub>. A fresh 1:1 mixture of EDC/NHS (150 mM of EDC and 30 mM of NHS) was incubated on the working electrodes for 30 mins to activate the carboxylic acid for antibody binding. The capture protein was covalently attached to the activated polymer-coated working electrode by incubating at room temperature for 2 hrs. Once the capture molecule was immobilised onto the surface, the device was rinsed in acetate buffer pH 4 with 0.05% Tween20 to remove unbound molecules, then rinsed with deionised water and dried with N<sub>2</sub>. Any remaining active binding sites were capped by submerging working electrodes in 1 M ethanolamine HCl for 10 mins, followed by rinsing in DI water. Voltammetric and impedimetric scans were performed to establish a baseline measurement for the sensor. To use this sensor for the detection of the target biomolecule, an aliquot of the target must be incubated on the electrode in use for 10 mins. The device must be thoroughly cleaned in HBS-EP buffer and deionised water, before CV and EIS measurements are taken. All data were fitted using an equivalent circuit and experimental data were background subtracted using the values for the blocking baseline as defined.

### **Target Detection in Buffer**

Electrodes were modified as above with 1 µg/ml (acetate buffer, pH 4) using sheep anti-Bo IgG as the capture protein. After, active sites were capped with ethanolamine as previously described. The target Bo IgG was prepared in varying concentrations in HBS-EP buffer. Each concentration, starting with the lowest, was incubated on the device for 10 mins. The device was thoroughly rinsed with HBS-EP buffer and CV and EIS measurements were taken before the next concentration was incubated.

### **Target Detection in Serum**

Blood samples were collected at the Animal & Grassland Research and Innovation Centre, Teagasc, Moorepark, Fermoy, Co. Cork, Ireland between January and April 2016. Ethical approval was received from the Teagasc Animal Ethics Committee (TAEC) (TAEC101/2015) and procedure authorisation was granted by the Irish Health Products Regulatory Authority (HPRA) (AE19132/P044). Experiments were undertaken in accordance with the Cruelty to Animals Act (Ireland 1876, as amended by European



Communities regulations 2002 and 2005) and the European Community Directive 86/609/EC.

Within one hour of birth, and prior to colostrum feeding, one 10 ml blood sample was taken from each calf via the jugular vein using a plain vacutainer (BD, Belliver Industrial Estate, Plymouth PL6 7BP, United Kingdom). A second blood sample was taken from each calf 24 hrs post colostrum feeding. Blood samples were refrigerated at 4°C for 24 hrs prior to serum separation by centrifugation (3,000 g × 30 min) at 4°C. Following centrifugation, serum was collected, aliquoted into microtubes, and frozen at -20°C until IgG concentration determination assays were undertaken. Samples taken immediately after birth, and prior to consumption of colostrum, were classified as seronegative as no antibodies are present in the calf's bloodstream until they receive colostrum. Samples taken at later stages are classified as seropositive as the calf has received colostrum and has started to absorb the dam's antibodies. All post-colostrum samples were confirmed to have successively absorbed enough antibodies to be considered healthy before transport to Tyndall

The detection of varying concentrations of Bo IgG was repeated using serum as the diluent to establish a calibration curve in a complex matrix. Serum was pooled from seven individual pre-colostral samples. As serum is a complex biological sample matrix an additional blocking step was required to ensure assay specificity. After the capping of the unbound EDC/NHS sites by ethanolamine, 0.5% NANNYcare® powder in 10 mM PBS deposited on the sensor surface for 20 mins to achieve the necessary blocking. The device was rinsed well with PBS buffer with 0.05% Tween20, PBS buffer and DI water to remove any unbound molecules. Each concentration, again starting with the lowest, was incubated on the device for 10 mins, followed by thorough rinsing with HBS-EP buffer. CV and EIS measurements in FcCOOH were taken before the next concentration was incubated.

Undiluted and diluted (in 10 mM PBS) serum samples were tested to assess on-farm application of this sensor. The sensor surface was prepared as above. A spotting technique was employed to deposit both seropositive and seronegative samples on the same device. A 0 hr serum (taken just after birth) was spotted (~5 µL) on electrode #2, and the

corresponding 24 hr serum (taken from the same calf a day later) was spotted on electrode #4. Both serum samples were incubated for 10 mins on the device.

## 2.3 Results and Discussion

### 2.3.1 ELISA

ELISA is often carried out establish suitable parameters for immunoassays. It can be used to determine the relevant buffers and blocking agent. In this work, it also evaluated the antibodies available to act as the capture. Both antibodies (mouse and sheep anti-IgG) proved to be suitable capture proteins for Bo IgG to develop this sensor. The anti-Bo IgG raised in mouse had a linear detection range from 60 – 200 ng/ml and the protein raised in sheep had a linear portion at 60 – 100 ng/ml, as seen in Figure 2.1.

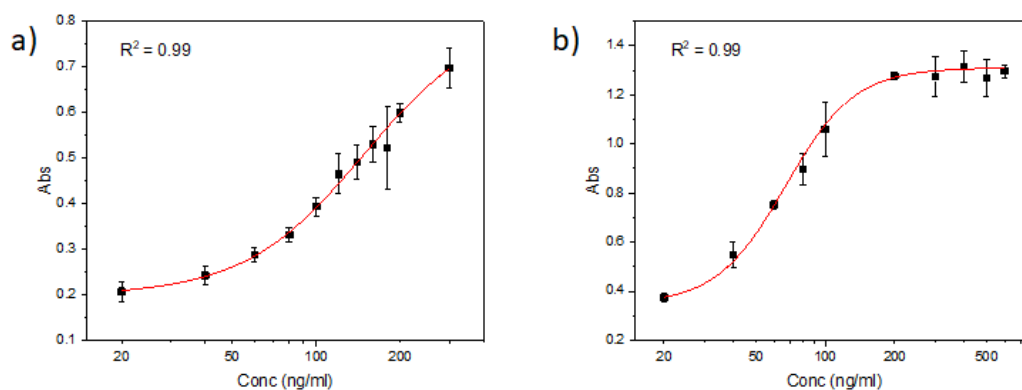


**Figure 2.1:** ELISA calibration curves for the detection of Bo IgG using (a) Mouse anti-Bo IgG capture molecule at a concentration 20 – 300 ng/ml of Bo IgG and (b) Sheep anti-Bo IgG capture molecule at a concentration 20 – 600 ng/ml of Bo IgG. Both were fitted using a four-parameter logistic fit in Origin. Errors bars are the standard deviations of the mean for three well replicants.

For development of the sensor the sheep anti-Bo IgG was selected as it was more compatible with the blocking step required for incubation with serum. This biomolecule showed lower non-selective binding with the NANNYcare® goat milk-based solution used for blocking the plate surface. Whereas the mouse anti-Bo IgG displayed high absorbance when the ELISA was performed with NANNYcare® and no target present.

### 2.3.2 Structural Characterisation of Microband Electrodes

Before use, devices were optically examined. Any devices displaying visual defects were discarded. The gold CE and platinum RE ran along the length of the six WEs as shown in Figure 2.2 (a). There were contact pads on both sides of the device to permit electrical

contact. On the right there were six pads to connect to each of the six WEs. On the left side there were eight pads, to connect to the RE and CE, as well as the six WEs. These pads were longer to allow connection through a microSD port. For lab use, an electrochemical cell as depicted in Figure 2.2 (c) was fabricated. For electrical connection, spring loaded pins were inserted into the Teflon lid and connect with the contact pads. This lid can make use of the contact pads on both sides of the sensor device. The cell was designed to facilitate sample volumes of 50  $\mu\text{L}$  to 8 ml.

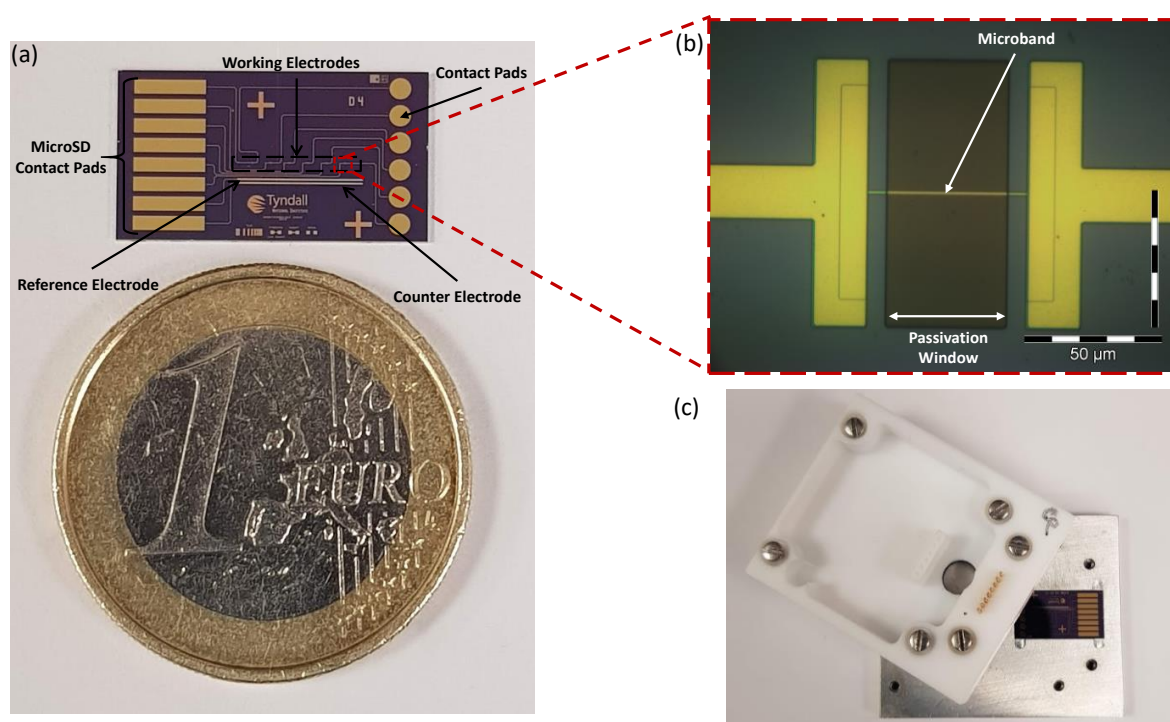


**Figure 2.2:** (a) Picture of fully integrated silicon sensor chip. (b) Optical micrograph of the single nanoband working electrode with dark passivation window. (c) Electrochemical cell consisting of an aluminium base to mount the fully fabricated device and a Teflon lid with gold spring-loaded pins to allow for electrical connection to contact pads. A well in the lid provides the electrolyte access to the working electrodes, reference electrode and counter electrode.

The optical micrograph in Figure 2.2 (b) shows an individual microband and the passivation window opened around it for electrical contact. Visual inspection ensures the passivation window is in the correct position and the connection tracks aren't exposed. The active electrode is better visualised using SEM. Figure 2.3 presents a single gold wire, 893 nm wide. This deviates from the expected width of 1  $\mu\text{m}$ . The dimensions of the microbands were also investigated using AFM. The electrode width, measured across five samples, was  $1.56 \mu\text{m} \pm 0.15 \mu\text{m}$ , with a corresponding height of  $79.76 \pm 17.52 \text{ nm}$ . These microbands are wider than the desired 1  $\mu\text{m}$  which was likely due to inconsistent

dimensions between the microband mask and the design. The height was expected to be 60 nm (10 nm of Ti and 50 nm of Au), however the passivation layer is slightly over-etched to ensure no SiN remained on the Au surface, leading the larger electrode heights as shown by the AFM measurements. The silicon dioxide layer is sufficiently thick to allow for this over-etching and maintain the insulation of the silicon wafer. Generally, the bands have a larger surface area than designed. This surface area is also seen to vary between wafers. However, these dimensions are still within the range of an ultramicroelectrode as desired.

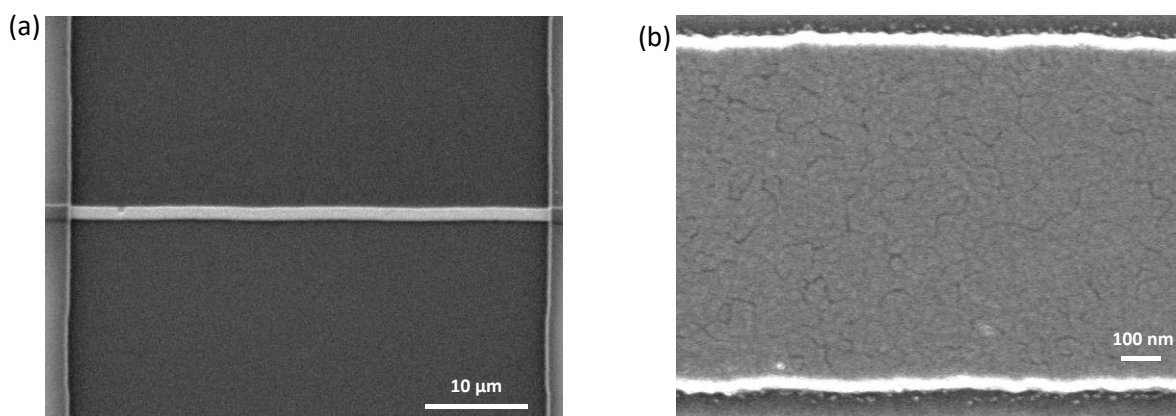


**Figure 2.3:** SEM image of (a) whole microband electrode and (b) a section of the microband at a high magnification.

### 2.3.3 Electrochemical Characterisation of Microband Electrodes

To ensure the microband devices are functioning as ultramicroband electrodes, they were potentiometrically cycled in 1 mM FcCOOH in 10 mM PBS. Figure 2.4 (a) shows a typical CV obtained using this electrochemical method. The steady state behaviour, with a typical current of  $\sim 1.8$  nA confirms the passivation layer has successfully prevented unwanted electrochemical processes along the interconnection tracks and activity is limited to the working electrode.

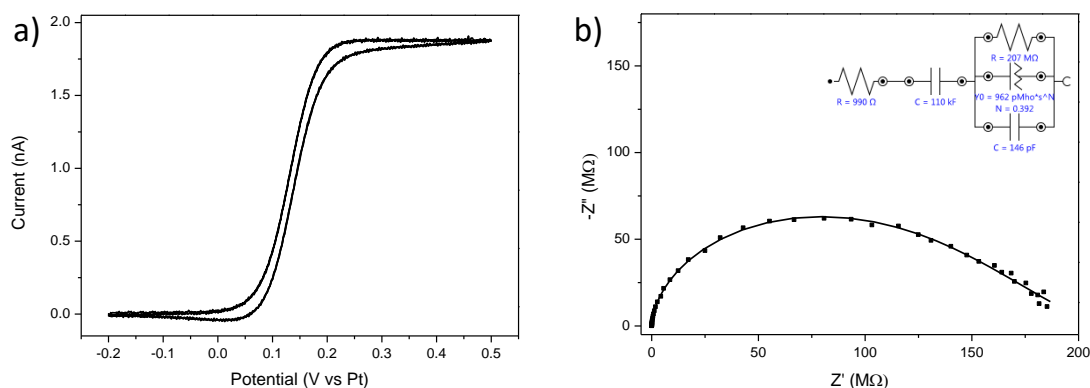


**Figure 2.4:** Electrochemical characterisation carried out in 1 mM FcCOOH in 10 mM PBS, pH 7.4. (a) Typical cyclic voltammogram of a gold microband electrode obtained in the potential range of -0.2 V to 0.5 V at 50 mV/s (versus on-chip platinum RE). (b) Typical Nyquist plot for a clean gold electrode 0.1 mHz to 100 kHz; excitation signal of 5 mV amplitude was applied at DC potential of 200 mV. Inset, the applied equivalent electrical circuit.

EIS was also performed as this technique is the basis for a label-free sensor. A typical Nyquist plot is presented in Figure 2.4 (b). The capacitive and resistive elements occurring in this plot are understood by fitting the data with an equivalent circuit (seen in the inset), similar to the Randles' circuit. The impedance of a resistor has no imaginary component, whereas the impedance of a capacitor has only imaginary components. Due to the semi-circle appearance of the plot, both resistive and capacitive elements must appear in the equivalent circuit. The double layer capacitance ( $C_{dl}$ ) can be approximated by calculating the height of the semi-circle on the imaginary axis,  $Z''$ . Similarly, the charge transfer resistance ( $R_{ct}$ ) can be surmised by measuring the diameter of the semi-circle along the real axis,  $Z'$ . As these are ultramicroelectrodes and not controlled by diffusion, the Warburg impedimetric component of the Randles' circuit is negligible. The constant phase element (CPE)  $Q$  accounts for any capacitance which is independent of frequency. These circuit components are commonly used to describe electrochemical reactions at a UME surface. A similar circuit has been previously published by our group for these microband electrodes.<sup>36</sup> As with the circuit seen in Figure 2.4 there was a slight overestimation of the circuit  $R_{ct}$  compared to the Nyquist curve. The dimensions of the microband as well as the elevated structure makes them unique, hence their circuit values were not compared to electrodes from other groups. The change in the surface properties of the electrode are mainly mirrored in changes to the  $R_{ct}$  as it represents the transfer electrons during the redox reaction of the FcCOOH probe. Therefore, it is the  $R_{ct}$  that is

monitored to during the electrode surface modification and final detection step of the sensor construction.

### 2.3.4 Characterisation of the Biocompatible Polymer

As detailed in the experimental Section 2.2.3.3, two electropolymers, o-ABA and PANI, were investigated as a surface modification for antibody immobilisation to the electrode. o-ABA is appropriate because its carboxylic functional group can be easily cross-linked to primary amines, which occur in proteins and many other biomolecules. However, o-ABA is an insulating polymer, which is not ideal for an electrochemical system. Subsequently, the conducting polymer PANI was employed to copolymerise with o-ABA, forming a semi-conductive polymer compound, poly (aniline-co-o-anthranilic acid).

This copolymer was deposited in two different acid concentrations. Initially, 0.5 H<sub>2</sub>SO<sub>4</sub> was chosen as this was used previously for the deposition of o-ABA.<sup>37</sup> The higher 1 M concentration was also investigated as this is commonly used for the deposition of PANI.<sup>38</sup> Electrodes were characterised before and after the polymer deposition using CV and EIS.

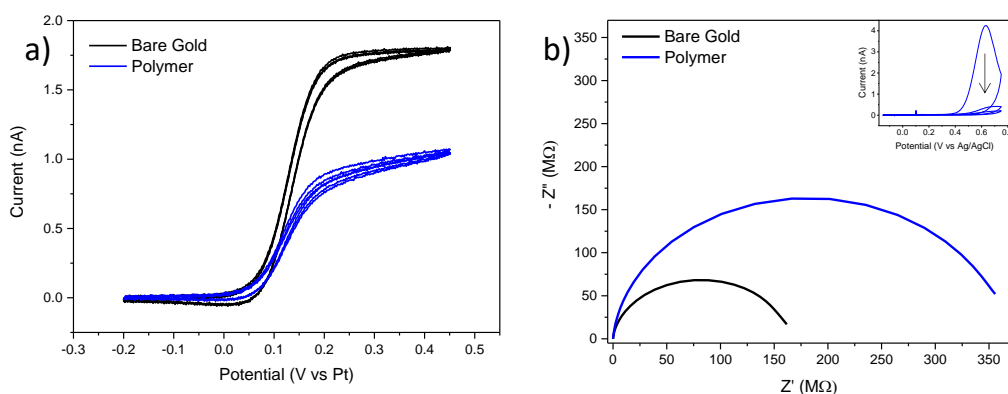


**Figure 2.5:** (a) CV at 50 mV s<sup>-1</sup> and (b) EIS with 5 mV amplitude applied to 200 mV in 1 mM FcCOOH in 10 mM PBS before (black) and after (blue) the deposition of poly (aniline-co-o-anthranilic acid) in 0.5 M H<sub>2</sub>SO<sub>4</sub>. Inset electropolymer deposition of poly (aniline-co-o-anthranilic acid) for 3 cycles at 50 mV s<sup>-1</sup>. Arrow indicates the reduction of the oxidation peak with increasing cycle number.

The lower acid concentration (0.5 M H<sub>2</sub>SO<sub>4</sub>) allowed fast deposition of only three scans, however it has created a mostly resistive layer on the surface. The current has almost halved and the R<sub>ct</sub> has increased by > 150 MΩ, as seen in Figure 2.5 (a) and (b) respectively. The large R<sub>ct</sub> seen in Figure 2.5 (b) after the polymer deposition (blue line) shows a considerable amount of the probing FcCOOH molecule was blocked from the surface. The additional resistance due to the insulative behaviour of the polymer is also manifested in the slight incline of the plateaus in the CV taken of the polymer deposition. This would be detrimental to the immunoassay sensitivity. As discussed in Chapter 1, Section 1.6.2.2, acid is a dopant for PANI<sup>39</sup> and deposition of the polymer in the higher acid concentration (1M H<sub>2</sub>SO<sub>4</sub>) permits the conductive characteristic of the PANI to contribute to the polymerisation on the electrode surface. This is demonstrated in Figure 2.6, where electrodeposition was undertaken in a 1 M H<sub>2</sub>SO<sub>4</sub> solution and exhibits semiconductor qualities. Charge transfer is much more favourable, therefore, and will considerably improve the sensitivity performance of the immunosensor.

Once an acid concentration was decided upon, different cycle numbers were tried to optimise the deposition layer. CV and EIS characterisation, shown in Figure 2.6, were used to investigate the effect of increasing the number of cycles during polymer deposition. The black data lines represent the clean electrode prior to electrodeposition, and the blue data lines represent the electrode post-polymerisation. The results presented in Figure 2.6 (a), (c) and (e), illustrate the CV current and potential response for 12, 20 and 25 cycles, respectively. There was little variation in current with increasing cycle number when compared to the bare gold electrode, however, there was a noticeable positive shift in potential. As the cycle number was increased, the potential shift also increased. This change in potential, where the steady-state region begins, is most likely due to slight absorption of the polymer onto the on-chip Pt pseudo-reference electrode. Going forward, the applied EIS potential was also increased to 220 – 250 V following electrode polymerisation, to ensure future impedance measurements were being performed at the optimal potential. The CV performed after polymerisation was used to determine the position of the peak current and therefore the optimal potential to apply to the system during EIS analysis.

The EIS Nyquist results, post-polymerisation, exhibited a similar response to the CV results. As the deposition cycles were increased, the charge transfer resistance at the



electrode also increased (blue data), see Figure 2.6 (b), (d) and (f). For 12 cycles (b) there was a slight increase in  $R_{CT}$  of  $19 \pm 9 \text{ M}\Omega$ , whereas for 25 cycles (f) there was a very large increase in  $R_{CT}$  of  $65 \pm 8 \text{ M}\Omega$ . The Nyquist curve for 20 cycles (d) has a delta of  $53 \pm 13 \text{ M}\Omega$  ( $n = 3$ ), which is larger than that seen after just 12 cycles but not too large as to quench the future signal. Moreover, the CV shift after 20 cycles is minimal, see Figure 2.6 (c). Based on CV and EIS characterisations therefore, 20 cycles were chosen for optimum polymerisation. This maximised the amount of -COOH binding sites available, while also limiting fouling to the RE.

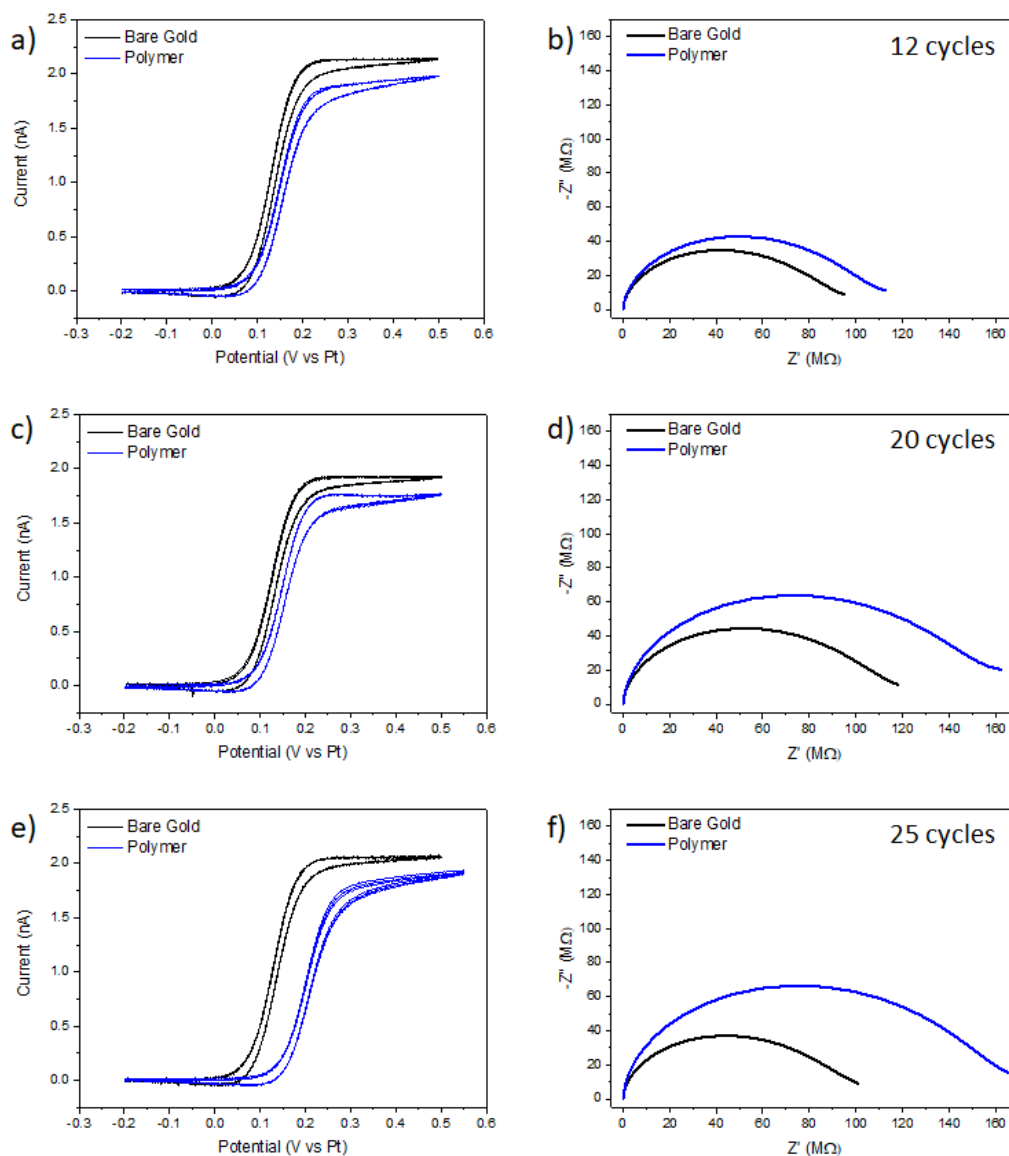


**Figure 2.6:** Comparison of CV and EIS in 1 mM FcCOOH in 10 mM PBS, before (black) and after (blue) poly (aniline-co-o-anthranilic acid) for (a) and (b) 12 cycles, (c) and (d) 20 cycles and (e) and (f) 25 cycles depositions.

AFMs were performed on a pristine gold electrode and a polymer modified electrode to demonstrate the structural change of the surface; see Figure 2.7 (a) and (b) respectively. The unmodified bare gold band has a Rms of 0.924 nm and mean Ra of 0.695 nm. The polymer coating increased the surface roughness to a Rms of 2.809 nm and mean Ra of 1.808 nm demonstrating that the polymer has become attached to the Au surface. Polyaniline films with thickness above 150 nm have shown loosely-packed fibrous structures.<sup>40</sup> The AFM of the polymer layer on the electrode in Figure 2.7 (b) shows a densely compact layer which is likely < 150 nm thick.

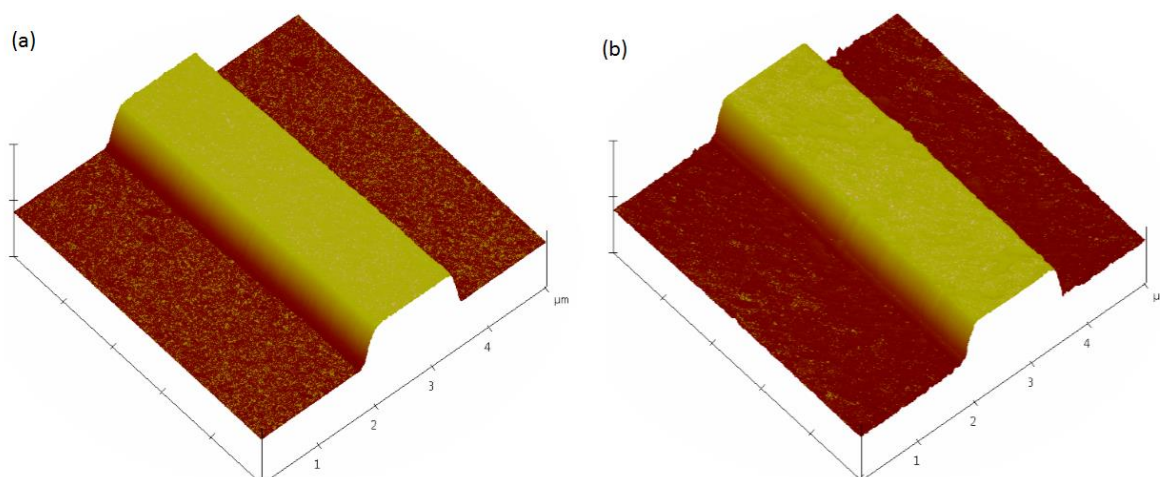


**Figure 2.7:** 3D AFM image of (a) bare gold microband and (b) microband with poly (aniline-co-o-anthranilic acid) electrodeposited onto surface.

### 2.3.5 Detection of Bovine IgG in Buffer

After the polymer was electrodeposited onto the electrode surface, crosslinking chemistry was used to attach the capture sheep anti-Bo IgG to the polymer. EDC was used to couple NHS to the carboxyl group and form a stable intermediate.<sup>41</sup> This allows for efficient conjugation to primary amines on the biomolecules, thereby covalently attaching these biomolecule to the polymer surface. Once the capture molecule was bound to the surface, ethanolamine was used to quench any remaining active sites, so the incoming Bo IgG target could only bind specifically to the capture anti-IgG protein. The immobilisation of antibodies to the electrode surface forms a partially insulating layer and hinders electron transfer occurring at the surface. Attachment of the target molecule further hinders the electron transfer. These layers are monitored using the redox probe, FcCOOH after they bind to the electrode surface.

The sensor was subjected to Bo IgG at a range of concentrations in PBS, pH 7.4. The manifestation of these concentrations can be seen in Figure 2.8 (a) CVs were taken after each concentration was incubated on the surface. The current magnitude is seen to decrease with the increase of Bo IgG concentration, due to the build-up of the biological layer at the electrode-electrolyte interface semi-blocking the redox reaction. Alternatively, EIS techniques allow for the monitoring of the increase of the  $R_{ct}$  signal as

the reduction in electron transfer of the redox probe causes an increase in the semi-circle feature seen in Figure 2.8 (b). The blank solution containing no Bo IgG (red) Nyquist curve shows a slightly smaller  $R_{ct}$  than the ethanolamine due to loosely bound biomolecules being removed from the surface during the washing steps. Preceding steps cause an increase in  $R_{ct}$  as the concentration of the target increases and the Bo IgG has bound to the capture molecules. An equivalent circuit for the modified electrode, Figure 2.8 (b) inset, was modelled off the Randles' circuit, as done previously in Section 2.3.3. This circuit varies from the equivalent circuit designed for the bare gold electrode. Additional resistive and capacitive elements were needed to describe the additional layers which have been immobilised on the electrode, causing an increase in both resistance and capacitance. The  $R_{ct}$  is explained by the addition of  $R_1$  and  $R_2$ . A semi-logarithmic relationship exists between the concentration of the target and the change in  $R_{ct}$ . This correlates well with the trend shown in the ELISA calibration plot (Figure 2.1). The Nyquist plot shows a much larger change in signal between each concentration of Bo IgG than the CV. Thus, EIS is widely used for evaluating immunosensors such as these.

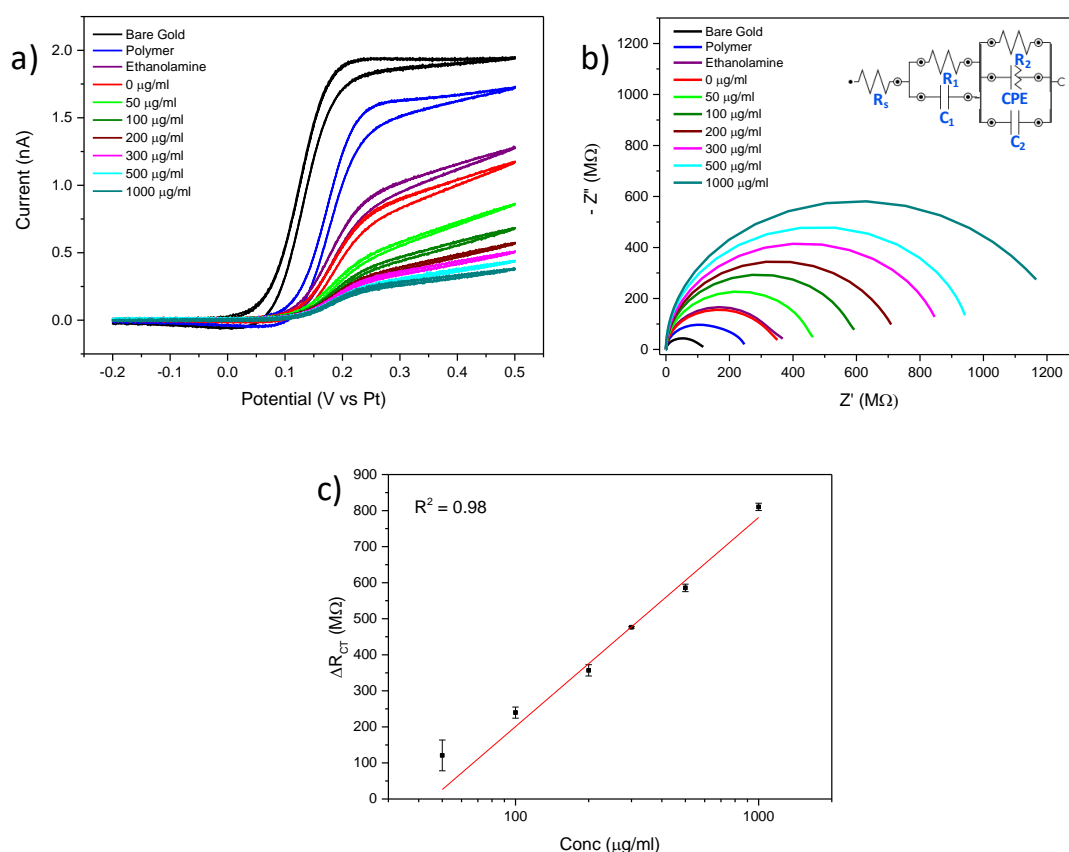


**Figure 2.8:** (a) CV at  $50 \text{ mV s}^{-1}$  and (b) Nyquist plot with  $5 \text{ mV}$  amplitude applied to  $250 \text{ mV}$  ( $200 \text{ mV}$  for bare gold) obtained of a poly (aniline-co-o-anthranilic acid) modified gold microband; immobilised anti-Bo IgG ( $1 \text{ } \mu\text{g/ml}$ ); ethanolamine quenching; and binding of the  $0 - 1000 \text{ } \mu\text{g/ml}$  (sequential addition) of target Bo IgG in  $10 \text{ mM PBS}$ ; recorded in  $1 \text{ mM FcCOOH}$  in  $10 \text{ mM PBS}$ . Inset, the applied equivalent circuit. (c) Semi-log relationship of the change in  $R_{ct}$  (ethanolamine baseline background subtracted) versus the antibody concentration,  $n = 3$  replications.

### 2.3.6 Detection of Bovine IgG in Serum

After the successful detection of IgG in buffer, the sensor was subjected to IgG in serum. Serum is a more complex matrix, and this experiment was necessary to determine the extent of non-specific binding from proteins present in the serum.

Microbands were modified as previously described. An additional blocking step was included when using serum as the sample matrix as we expected an increase in non-specific binding due to the increased number of proteins present in serum.<sup>42</sup> Casein is a protein found in mammalian milk and is often applied as a blocking agent in

immunosensors.<sup>43</sup> A goat's milk based powder was chosen as a casein source to eliminate any possible interference from bovine proteins which may bind to the anti-Bo IgG. This step now acts as the baseline for the sensor. Figure 2.9 (a) shows the Nyquist diagrams, in the presence of the probe molecule 1 mM FcCOOH, following modification of the electrode surface and exposure to increasing concentrations of the target antibody. The sensor was first exposed to this negative serum (red line). Some non-specific binding can be seen by the change in the  $R_{CT}$  of  $\sim 33 \text{ M}\Omega$  between the sensor baseline (purple) and the negative serum (red), which was expected. Setting of an appropriate positive cut-off point can be used to account for this background noise for an eventual on-farm application.<sup>44</sup> <sup>45</sup> The pooled serum was then spiked with known concentrations of Bo IgG and series of concentrations were incubated on the sensor surface and measured using EIS. An increase in the semicircle diameter, i.e.  $R_{ct}$ , was observed with increasing Bo IgG concentration. This proposes that the antibodies have bound to the immobilised capture anti-Bo IgG, further blocking the electron transfer at the electrode. A calibration curve was generated, Figure 2.9 (b), again showing a semi-logarithmic relationship between the change in charge transfer resistance and the concentration of Bo IgG.

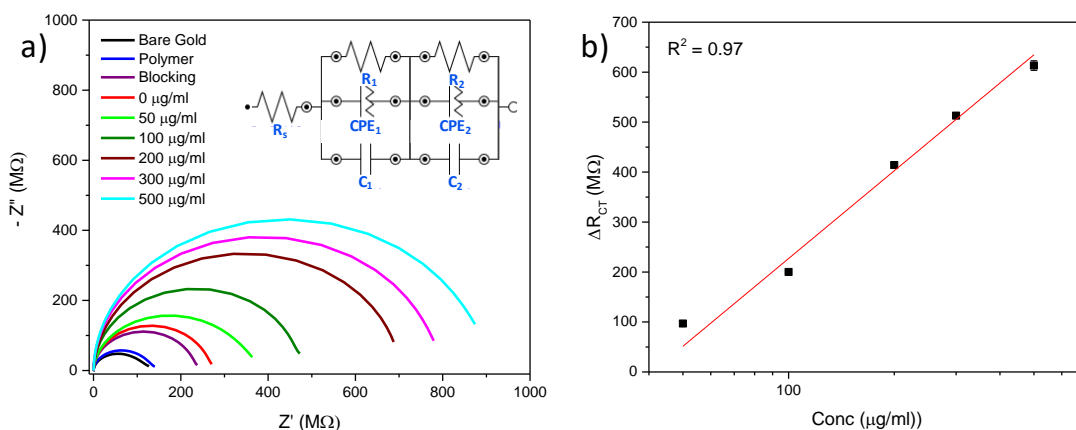


**Figure 2.9:** a) Nyquist plots plot with 5 mV amplitude applied to 220 mV (200 mV for bare gold) obtained of a poly (aniline-co-o-anthranilic acid) modified gold microband; immobilised anti-Bo IgG (1  $\mu\text{g/ml}$ ); ethanolamine quenching and NANNYcare<sup>®</sup> blocking; and binding of the target Bo IgG in pooled pre-colostral Bo serum; recorded in 1mM FcCOOH in 10 mM PBS. Inset, applied equivalent circuit. (b) Semi-log relationship of the change in  $R_{ct}$  (NANNYcare<sup>®</sup> baseline background subtracted) versus the antibody concentration,  $n = 3$  replications.

A number of chips were modified and tested with individual pre-colostral and post-colostral samples, using the spotting technique described in the experimental section (2.2.3.3). A typical EIS displaying the antibody response of the serum pre- and post-

feeding is seen in Figure 2.10. The IgG positive and negative samples are clearly distinguishable. The negative sample had a negligible change in impedance (red), whereas the positive sample showed a large impedimetric response, increasing by  $> 2500 \text{ M}\Omega$  (green) from the baseline. This is approaching the maximum signal output for the sensor. A sample dilution step was added to fit the calibration range in Figure 2.10. Going forward serum samples were diluted ten-fold in PBS.

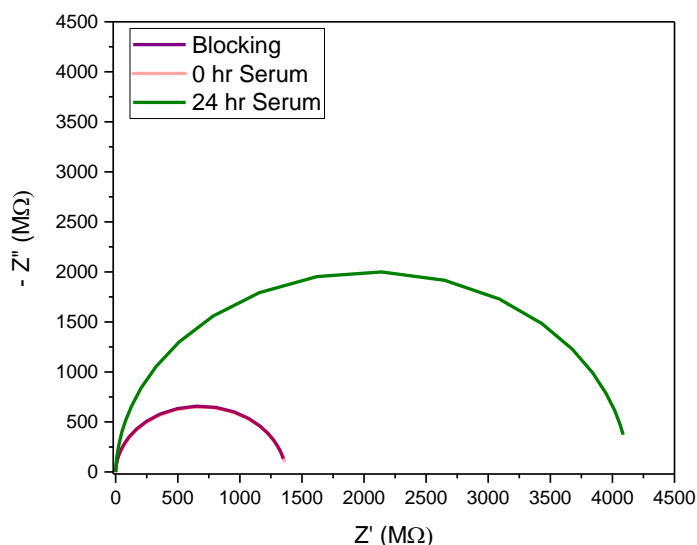


**Figure 2.10:** Nyquist plot for IgG negative (0 hr) and IgG positive (24 hr) whole serum samples incubated on anti-Bo IgG modified microrband electrodes with NANNYcare® blocking step, scanned in 1mM FcCOOH in 10 mM PBS, with a 5 mV amplitude applied to 200 mV.

In order to validate this theory several positive and negative serum samples were diluted and tested. In total, five calf samples taken at birth (red) were tested and then their respective samples taken 24 hrs later (green) after feeding; after antibody absorption should have occurred. The bar chart in Figure 2.11 represents the background subtracted  $\Delta R_{ct}$  of all ten sample assays. The negative samples minor delta ( $<150 \text{ M}\Omega$ ) is caused by non-specific binding as previously discussed. The positive samples show a much greater change ( $>450 \text{ M}\Omega$ ). These results strongly suggest that the uptake of maternal antibodies can be successfully monitored using the electrochemical microband sensors. As the analysis generated a result in less than 15 minutes, the sensors are ideal for on farm use. Their application would allow veterinarians and farmers to target calves with poor antibody absorption early, reducing the need for broad spectrum antibiotics and isolation costs.

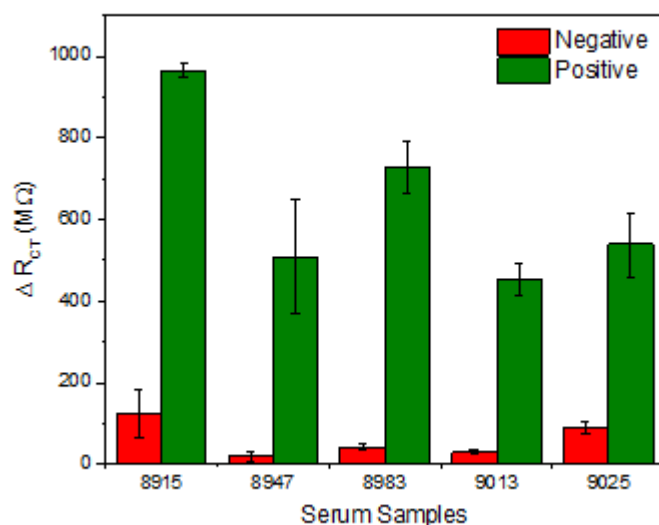


**Figure 2.11:** Bar chart comparison of  $R_{ct}$  for IgG negative serum samples with their respective IgG positive serum samples, with their respective NANNYcare® baseline subtracted. Samples were diluted 1:10 in 10 mM PBS pH 7.4.

All pre-colostral samples had an IgG concentration of below 150  $\mu\text{g/ml}$ . The post-colostral samples' IgG levels were between 3 and 8  $\text{mg/ml}$ . This highlights the considerable discriminatory power of our sensors. Although generating lower IgG concentrations than the cut-off point for successful passive transfer the samples employed in this study had sustained damage from undergoing several freeze thaw cycles.<sup>46-48</sup> These samples, provided by Teagasc, were frozen at  $-20^{\circ}\text{C}$  until a commercial ELISA was undertaken to determine the IgG concentration. The samples were then re-frozen at  $-20^{\circ}\text{C}$ , until transport to Tyndall National Institute where they were stored again stored at  $-20^{\circ}\text{C}$ , until testing with the impedimetric sensor. These freeze thaw cycles potentially reducing their detectable IgG levels due to denaturation. However, these samples still allowed for proof of concept, as the concentration of IgG detected was in the  $\text{mg/ml}$  range. Should future studies continue to highlight that our sensor reports lower concentrations of IgG than ELISA, this does not necessarily represent an issue. ELISA has been shown to report lower IgG results than RID and has an adjusted cut-off point to account for this.<sup>49</sup> The main concern of farmers and veterinarians is that successful passive transfer has occurred. Validation of an adjusted serum FPT cut-off for our sensor would allow decisions to be made in less than 15 minutes at farm level and eliminate the need for freezing samples. The data strongly suggest that use of the electrochemical



microband sensors developed in the current study can successfully monitor, uptake of maternal antibodies by neonatal calves. FPT cut-off point for ELISA is <10 mg/ml IgG, while the limit of detection of our label-free EIS method is in the  $\mu\text{g/ml}$  range. This detection range presents the opportunity for calves to be tested before they reach maximum IgG levels. Earlier monitoring would permit better regulation of the calves' feeding routines, taking advantage of the short window where IgG adsorption is unhindered by the intestinal lining. A new cut-off point for successful passive transfer could be established for antibody uptake during the first 6 hrs after birth. By testing at an earlier stage when high levels of colostrum IgG absorption are still occurring, using a POC device, improved treatment plans could be implemented. Validation of this device using whole blood is also required, as serum would not be an available sample matrix for an on-farm device.

## 2.4 Conclusion

In this chapter, a MicroSD device was characterised as an electrochemical sensor platform. This device was comprised of a fully integrated three electrode system including a platinum pseudo-reference electrode and a gold counter electrode. The six working electrodes allowed for monitoring of several samples on a single device. The architecture of these working electrodes was microband wires which function as ultramicroelectrodes. Thus, they experience the benefits of radial diffusion. The pinouts were designed to assimilate into handheld electronics with ease, making them an ideal disposable sensor.

The devices were successfully modified for the detection of Bo IgG. A biocompatible molecule poly (aniline-co-o-anthranilic acid) was found that could be crosslinked through EDC/NHS coupling to the capture biomolecule. Different electropolymerisation parameters were tested. The chosen optimal conditions were a 20-cycle deposition in a 1 M H<sub>2</sub>SO<sub>4</sub> medium. The anti-Bo IgG capture biomolecule remained on the surface through repeated cleaning steps without deterioration. The system was assessed with the target molecule, Bo IgG, and showed successful binding in the form of an increased  $R_{ct}$  of the microband. The sensor showed a semi-logarithmic relationship between the concentration of the target and the  $R_{ct}$  of the capture molecule. The system was tested in three different matrices: buffer, bovine serum and diluted bovine serum. An appropriate blocking solution was used to diminish non-specific binding in actual calf serum samples. The negative and positive samples were clearly distinguishable. The short analysis time (10 mins incubation and 5 mins scanning) makes this device optimal for on-farm use.

## 2.5 References

1. Weaver, D. M.; Tyler, J. W.; VanMetre, D. C.; Hostetler, D. E.; Barrington, G. M., Passive transfer of colostral immunoglobulins in calves. *J Vet Intern Med* **2000**, *14* (6), 569-77.
2. Hogan, I.; Doherty, M.; Fagan, J.; Kennedy, E.; Conneely, M.; Brady, P.; Ryan, C.; Lorenz, I., Comparison of rapid laboratory tests for failure of passive transfer in the bovine. *Ir Vet J* **2015**, *68* (1), 18.
3. Bush, L. J.; Staley, T. E., Absorption of Colostral Immunoglobulins in Newborn Calves1. *Journal of Dairy Science* **1980**, *63* (4), 672-680.
4. Bush, L. J.; Aguilera, M. A.; Adams, G. D.; Jones, E. W., Absorption of Colostral Immunoglobulins by Newborn Dairy Calves. *Journal of Dairy Science* **1971**, *54* (10), 1547-1549.
5. Stott, G. H.; Marx, D. B.; Menefee, B. E.; Nightengale, G. T., Colostral immunoglobulin transfer in calves I. Period of absorption. *J Dairy Sci* **1979**, *62* (10), 1632-8.
6. Bedenice, D. Failure of Passive Transfer. <https://www.msdtvetmanual.com/management-and-nutrition/management-of-the-neonate/failure-of-passive-transfer> (accessed 27/05/2020).
7. Elsohaby, I.; McClure, J. T.; Waite, L. A.; Cameron, M.; Heider, L. C.; Keefe, G. P., Using serum and plasma samples to assess failure of transfer of passive immunity in dairy calves. *Journal of Dairy Science* **2019**, *102* (1), 567-577.
8. Pfeiffer, N. E.; McGuire, T. C.; Bendel, R. B.; Weikel, J. M., Quantitation of bovine immunoglobulins: comparison of single radial immunodiffusion, zinc sulfate turbidity, serum electrophoresis, and refractometer methods. *American journal of veterinary research* **1977**, *38* (5), 693-698.
9. Dunn, A.; Duffy, C.; Gordon, A.; Morrison, S.; Argüello, A.; Welsh, M.; Earley, B., Comparison of single radial immunodiffusion and ELISA for the quantification of immunoglobulin G in bovine colostrum, milk and calf sera. *Journal of Applied Animal Research* **2018**, *46* (1), 758-765.
10. Lee, S. H.; Jaekal, J.; Bae, C. S.; Chung, B. H.; Yun, S. C.; Gwak, M. J.; Noh, G. J.; Lee, D. H., Enzyme-Linked Immunosorbent Assay, Single Radial Immunodiffusion, and Indirect Methods for the Detection of Failure of Transfer of Passive Immunity in Dairy Calves. *Journal of Veterinary Internal Medicine* **2008**, *22* (1), 212-218.
11. Tyler, J. W.; Hancock, D. D.; Parish, S. M.; Rea, D. E.; Besser, T. E.; Sanders, S. G.; Wilson, L. K., Evaluation of 3 assays for failure of passive transfer in calves. *Journal of Veterinary Internal Medicine* **1996**, *10* (5), 304-307.
12. Calloway, C. D.; Tyler, J. W.; Tessman, R. K.; Hostetler, D.; Holle, J., Comparison of refractometers and test endpoints in the measurement of serum protein concentration to assess passive transfer status in calves. *Journal of the American Veterinary Medical Association* **2002**, *221* (11), 1605-1608.
13. Tyler, J. W.; Parish, S. M.; Besser, T. E.; Van Metre, D. C.; Barrington, G. M.; Middleton, J. R., Detection of low serum immunoglobulin concentrations in clinically ill calves. *Journal of veterinary internal medicine / American College of Veterinary Internal Medicine* **1999**, *13* (1), 40-43.

14. Johnston, N. A.; Parish, S. M.; Tyler, J. W.; Tillman, C. B., Evaluation of serum  $\gamma$ -glutamyltransferase activity as a predictor of passive transfer status in crias. *Journal of the American Veterinary Medical Association* **1997**, *211* (9), 1165-1166.
15. Güngör, Ö.; Bastan, A.; Erbil, M. K., The usefulness of the  $\gamma$ -glutamyltransferase activity and total proteinemia in serum for detection of the failure of immune passive transfer in neonatal calves. *Revue de Medecine Veterinaire* **2004**, *155* (1), 27-30.
16. Tyler, J. W.; Besser, T. E.; Wilson, L.; Hancock, D. D.; Sanders, S.; Rea, D. E., Evaluation of a whole blood glutaraldehyde coagulation test for the detection of failure of passive transfer in calves. *Journal of Veterinary Internal Medicine* **1996**, *10* (2), 82-84.
17. Wilson, L. K.; Tyler, J. W.; Besser, T. E.; Parish, S. M.; Gant, R., Prediction of serum IgG1 concentration in beef calves based on age and serum gamma-glutamyl-transferase activity. *J Vet Intern Med* **1999**, *13* (2), 123-5.
18. Yang, L.; Guiseppi-Wilson, A.; Guiseppi-Elie, A., Design considerations in the use of interdigitated microsensor electrode arrays (IMEs) for impedimetric characterization of biomimetic hydrogels. *Biomedical Microdevices* **2011**, *13* (2), 279-289.
19. Cuttance, E. L.; Mason, W. A.; Denholm, K. S.; Laven, R. A., Comparison of diagnostic tests for determining the prevalence of failure of passive transfer in New Zealand dairy calves. *New Zealand Veterinary Journal* **2017**, *65* (1), 6-13.
20. Zakian, A.; Nouri, M.; Rasooli, A.; Ghorbanpour, M.; Constable, P. D.; Mohammad-Sadegh, M., Evaluation of 5 methods for diagnosing failure of passive transfer in 160 Holstein calves. *Veterinary clinical pathology* **2018**, *47* (2), 275-283.
21. Vetlab Supplies FASTest Bo IgG. <https://vetlabsupplies.co.uk/products/diagnostic-kits/fastest-igg-bovine/> (accessed 14/11/19).
22. Elsohaby, I.; Keefe, G. P., Preliminary validation of a calf-side test for diagnosis of failure of transfer of passive immunity in dairy calves. *Journal of Dairy Science* **2015**, *98* (7), 4754-4761.
23. VETLAB DVM Rapid Multi-Test II. <http://www.vetlab.com/RapidTestII.htm> (accessed 14/11/2019).
24. Kummer, L. L.; Govaere, J.; Egri, B., Comparison of the reliability of snap foal Ig test, Gamma-Check E test, refractometry and electrophoresis for determining the immune status of newborn foals in the first hours of life. *Acta veterinaria Hungarica* **2018**, *66* (4), 573-586.
25. Centaur Animal Health FOALCHEK® Equine IgG. <https://www.centauranimalhealth.com/foalchek-equine-igg/> (accessed 14/1/2019).
26. Wang, J., Electrochemical biosensors: Towards point-of-care cancer diagnostics. *Biosensors and Bioelectronics* **2006**, *21* (10), 1887-1892.
27. Luo, X.; Hsing, I. M., Electrochemical techniques on sequence-specific PCR amplicon detection for point-of-care applications. *Analyst* **2009**, *134* (10), 1957-1964.
28. Wan, Y.; Su, Y.; Zhu, X.; Liu, G.; Fan, C., Development of electrochemical immunosensors towards point of care diagnostics. *Biosensors and Bioelectronics* **2013**, *47*, 1-11.

29. Dungchai, W.; Chailapakul, O.; Henry, C. S., Electrochemical Detection for Paper-Based Microfluidics. *Anal. Chem.* **2009**, *81* (14), 5821-5826.
30. Wei, F.; Patel, P.; Liao, W.; Chaudhry, K.; Zhang, L.; Arellano-Garcia, M.; Hu, S.; Elashoff, D.; Zhou, H.; Shukla, S.; Shah, F.; Ho, C.-M.; Wong, D. T., Electrochemical Sensor for Multiplex Biomarkers Detection. *Clinical Cancer Research* **2009**, *15* (13), 4446.
31. Zhang, D.; Lu, Y.; Zhang, Q.; Liu, L.; Li, S.; Yao, Y.; Jiang, J.; Liu, G. L.; Liu, Q., Protein detecting with smartphone-controlled electrochemical impedance spectroscopy for point-of-care applications. *Sensors and Actuators B: Chemical* **2016**, *222*, 994-1002.
32. Hsieh, K.; Ferguson, B. S.; Eisenstein, M.; Plaxco, K. W.; Soh, H. T., Integrated Electrochemical Microsystems for Genetic Detection of Pathogens at the Point of Care. *Accounts of Chemical Research* **2015**, *48* (4), 911-920.
33. Rodrigues, L. P.; Ferreira, D. C.; Ferreira, L. F.; Cuadros-Orellana, S.; De Oliveira, G. C.; Brito-Madurro, A. G.; De Oliveira, R. J.; Abrahão, O.; Madurro, J. M., Electropolymerization of hydroxyphenylacetic acid isomers and the development of a bioelectrode for the diagnosis of bacterial meningitis. *Journal of Applied Electrochemistry* **2015**, *45* (12), 1277-1287.
34. Arrigan, D. W. M., Nanoelectrodes, nanoelectrode arrays and their applications. *Analyst* **2004**, *129* (12), 1157-1165.
35. Dawson, K.; Wahl, A.; Murphy, R.; O'Riordan, A., Electroanalysis at single gold nanowire electrodes. *J. Phys. Chem. C* **2012**, *116* (27), 14665-14673.
36. Creedon, N.; Sayers, R.; O'Sullivan, B.; Kennedy, E.; Pierre, L.; O'Riordan, A., *Label-Free Impedimetric Nanoband Sensor for Detection of Both Bovine Viral Diarrhoea Virus (BVDV) and Antibody (BVDAb) in Serum*. 2018.
37. Tsai, M.-Y.; Creedon, N.; Brightbill, E.; Pavlidis, S.; Brown, B.; Gray, D. W.; Shields, N.; Sayers, R.; Mooney, M. H.; O'Riordan, A.; Vogel, E. M., Direct correlation between potentiometric and impedance biosensing of antibody-antigen interactions using an integrated system. *Applied physics letters* **2017**, *111* (7), 073701.
38. Wang, Z.; Yuan, J.; Li, M.; Han, D.; Zhang, Y.; Shen, Y.; Niu, L.; Ivaska, A., Electropolymerization and catalysis of well-dispersed polyaniline/carbon nanotube/gold composite. *Journal of Electroanalytical Chemistry* **2007**, *599* (1), 121-126.
39. MacDiarmid, A. G., "Synthetic Metals": A Novel Role for Organic Polymers (Nobel Lecture). *Angewandte Chemie International Edition* **2001**, *40* (14), 2581-2590.
40. Carlin, C. M.; Kepley, L. J.; Bard, A. J., Polymer Films on Electrodes: XVI. In Situ Ellipsometric Measurements of Polybipyrazine, Polyaniline, and Polyvinylferrocene Films. *Journal of The Electrochemical Society* **1985**, *132* (2), 353-359.
41. Wang, C.; Yan, Q.; Liu, H.-B.; Zhou, X.-H.; Xiao, S.-J., Different EDC/NHS Activation Mechanisms between PAA and PMAA Brushes and the Following Amidation Reactions. *Langmuir* **2011**, *27* (19), 12058-12068.
42. Schneider, B. H.; Dickinson, E. L.; Vach, M. D.; Hoijer, J. V.; Howard, L. V., Highly sensitive optical chip immunoassays in human serum. *Biosensors and Bioelectronics* **2000**, *15* (1), 13-22.

43. Vogt, R. V.; Phillips, D. L.; Omar Henderson, L.; Whitfield, W.; Spierto, F. W., Quantitative differences among various proteins as blocking agents for ELISA microtiter plates. *J. Immunol. Methods* **1987**, *101* (1), 43-50.
44. Baughman, A. L.; Bisgard, K. M.; Edwards, K. M.; Guris, D.; Decker, M. D.; Holland, K.; Meade, B. D.; Lynn, F., Establishment of Diagnostic Cutoff Points for Levels of Serum Antibodies to Pertussis Toxin, Filamentous Hemagglutinin, and Fimbriae in Adolescents and Adults in the United States. *Clinical and Diagnostic Laboratory Immunology* **2004**, *11* (6), 1045-1053.
45. Gandhi, M.; Bacchetti, P.; Spinelli, M. A.; Okochi, H.; Baeten, J. M.; Siriprakaisil, O.; Klinbuayaem, V.; Rodrigues, W. C.; Wang, G.; Vincent, M.; Cressey, T. R.; Drain, P. K., Brief Report: Validation of a Urine Tenofovir Immunoassay for Adherence Monitoring to PrEP and ART and Establishing the Cutoff for a Point-of-Care Test. *J Acquir Immune Defic Syndr* **2019**, *81* (1), 72-77.
46. Petrakis, N. L., Biologic banking in cohort studies, with special reference to blood. *Natl Cancer Inst Monogr* **1985**, *67*, 193-198.
47. Jobe, D. A.; Lovrich, S. D.; Asp, K. E.; Mathiason, M. A.; Albrecht, S. E.; Schell, R. F.; Callister, S. M., Significantly Improved Accuracy of Diagnosis of Early Lyme Disease by Peptide Enzyme-Linked Immunosorbent Assay Based on the Borreliacidal Antibody Epitope of *Borrelia burgdorferi* OspC. *Clinical and Vaccine Immunology* **2008**, *15* (6), 981-985.
48. Wormser, G. P.; Schriefer, M.; Aguero-Rosenfeld, M. E.; Levin, A.; Steere, A. C.; Nadelman, R. B.; Nowakowski, J.; Marques, A.; Johnson, B. J. B.; Dumler, J. S., Single-tier testing with the C6 peptide ELISA kit compared with two-tier testing for Lyme disease. *Diagnostic Microbiology and Infectious Disease* **2013**, *75* (1), 9-15.
49. Gelsinger, S. L.; Smith, A. M.; Jones, C. M.; Heinrichs, A. J., Technical note: Comparison of radial immunodiffusion and ELISA for quantification of bovine immunoglobulin G in colostrum and plasma. *Journal of Dairy Science* **2015**, *98* (6), 4084-4089.

***Chapter 3***      **Fabrication of Polymer Microneedle Arrays**

### 3.1 Introduction

Microneedles are sharp, minimally invasive, microscopic structures (less than 1 mm in length) which allow for pain-free access to the body's interstitial fluid. The skin is made up of three main layers: (i) the epidermis, the outer layer, which contains the waterproof outermost barrier, the *stratum corneum*; (ii) the middle dermis layer, which contains nerve endings and hair follicles; and (iii) the deeper subcutaneous tissue, the hypodermis. Unlike conventional hypodermic needles which are injected into the dermis layer and deeper, microneedles pierce the *stratum corneum* and only enter the epidermis. Thus, they do not penetrate the nerve containing dermis layer, resulting in pain-free application.<sup>1-3</sup> Neither do they reach blood vessels and as such only interact with interstitial fluid, which along with plasma make up the skin's extracellular fluid, i.e. the fluid surrounding all the cells in the body.<sup>4</sup> Though they perforate the *stratum corneum*, they generally do not lead to bacterial contamination or skin irritation, and the skin is restored within 1-3 days of needle application.<sup>5-7</sup>

Microneedles have been employed for drug delivery, vaccine delivery, and analyte detection, as well as being popular in the cosmetic industry. Four forms of microneedles: solid, coated, hollow and dissolvable were originally explored.<sup>2,3,8-11</sup> All types have been popular for drug delivery applications; Figure 3.1. Solid microneedles are used to puncture the skin. Once the microneedles are removed transient pores remain causing skin permeability to small molecules and the drug or vaccine can be applied. Coated microneedles are covered with a layer of the drug molecules. These molecules are delivered directly into the epidermis layer of the skin upon insertion. Dissolvable microneedles are generally made from biodegradable polymers or sugars and will break down upon contact with the skin's interstitial fluid. Drug molecules are embedded in the microneedle structures and will be released upon dissolution of the structures. Hollow microneedles can transport the drug solution through the interior of the microneedle structures and directly into the interstitial fluid by diffusion or pressure driven flow. In recent years, research has expanded to include hydrogel-forming microneedles.<sup>3, 12-14</sup> Hydrogel microneedles are formed from cross-linking polymers which swell once inserted into the skin due to the aqueous media. The rear of the structures has a drug loaded adhesive patch. The swelling of the hydrogel facilitates a flux of the drug into the



skin. Solid microneedles rollers are employed in the cosmetic industry to reduce fine wrinkles, fine lines, and small stretch marks.<sup>15</sup> They are also utilised for the pre-treatment of skin to enable transdermal delivery of skin rejuvenating peptides and proteins via topical application<sup>5, 16</sup> Dissolvable microneedles are also gaining popularity within the cosmetics industry for the delivery of cosmetic drugs.<sup>5, 17, 18</sup>

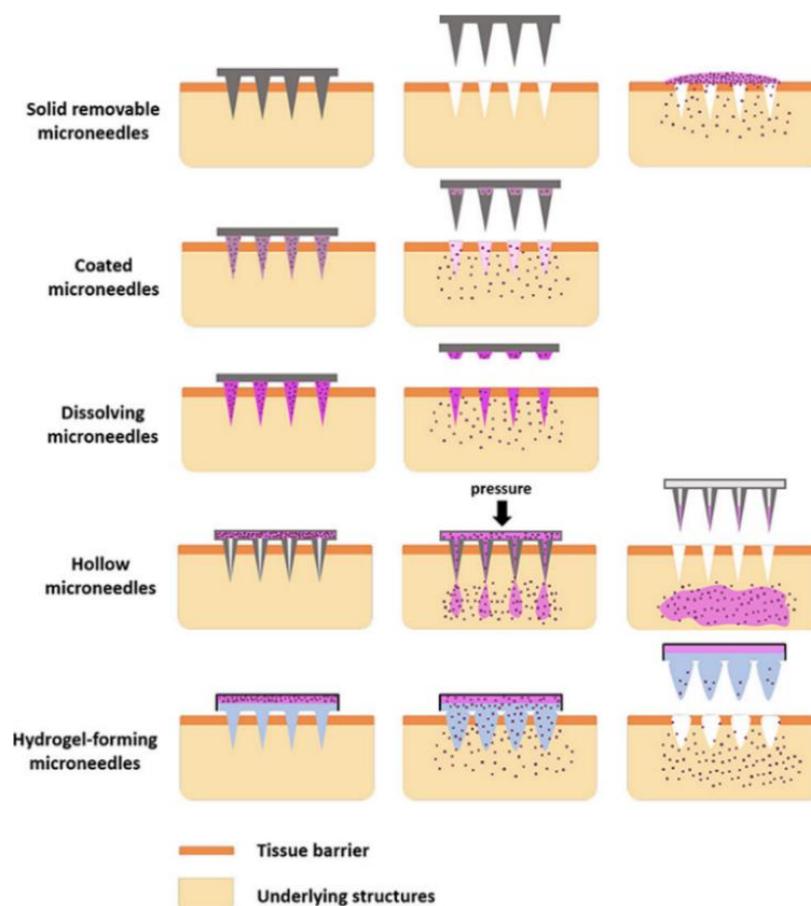


**Figure 3.1:** Different types of microneedles and their mechanisms for drug delivery. (Taken from <sup>8</sup>)

Microneedles are made from a variety of materials including, silicon, metal, ceramics, glass, polymers, sugars and hydrogels.<sup>19</sup> Silicon is a popular material for microneedles fabrication, as it has a relatively high hardness which is compatible with piercing the skin barrier.<sup>19, 20</sup> However, silicon has high manufacturing costs and has proven to be fragile during transportation and application. Often needle fragments have broken near the tip after insertion, and have remained within the skin.<sup>19, 21</sup> Consequently, more biocompatible materials, which are non-toxic to living tissue, have been favoured in recent years. Alternatively, metals such as stainless-steel, titanium, nickel, palladium, and

platinum are used to fabricate microneedles due to their mechanical properties which include high toughness, strength and hardness. An additional benefit is the low manufacturing cost compared to silicon and the variety of fabrication methods such as electroplating, photochemical etching, micro-milling, and laser cutting.<sup>1, 12</sup>

Some polymers also have a high strength, allowing them to pierce the skin without fracturing. Most polymers are biocompatible, making them an attractive material for microneedles. Furthermore, they may be biodegradable or water soluble, making them ideal for dissolvable, drug delivery devices. Polymers are suitable for fabrication through micro-moulding techniques, which is favourable as a low-cost mass production method. Other fabrication methods suitable for polymer microneedles include photolithography, 3D printing, casting, and injection moulding.<sup>1, 2</sup>

Commercial microneedle technologies are mainly aimed at drug delivery, including the Hollow Microstructured Transdermal System (3M™), Mactoflux® (Alza), h-Patch™ (Valeritas) and the MicronJet600™ (Nanopass Technologies). Similar to the h-Patch™, Valeritas has developed the V-Go® as a wearable device for insulin delivery. The beauty industry also has interest in microneedle devices for skin treatment, such as the MTS Roller™ (Clinical Resolutions) and the GloPro® (BeautyBio). Picofluidics have been undergoing research with the Cardiff MediCentre to produce cost effective microneedles for plasma treatment.<sup>22</sup>

Though no microneedles-based biosensors are commercially available, many research groups are trying to develop them for the detection of analytes such as glucose,<sup>23-31</sup> lactate,<sup>27, 32, 33</sup> lactic acid,<sup>25</sup> ascorbic acid,<sup>34</sup> cholesterol,<sup>26, 30</sup> uric acid,<sup>30, 35</sup> dopamine,<sup>35</sup> cancer biomarkers<sup>36</sup> and other biomarkers.<sup>37-44</sup> More recently, microneedle development has moved into the plant sector, to measure the salinity of a plant's stem<sup>45</sup> and for DNA extraction for disease diagnostic.<sup>46</sup> Applications towards farm animals are not currently seen. Coated and hollow microneedles have proven to be the most popular configurations used in diagnostic biosensors. Analytes interact with a coating on the solid microneedle structure, for example, an antibody binding to an antigen or a substrate reacting with an enzyme.<sup>24, 31, 37, 38, 47</sup> One of the most common analytes detected with coated microneedle sensors is glucose. The enzyme glucose oxidase is entrapped in a polymer layer onto a platinum (Pt) microneedle.<sup>24, 25</sup> Glucose oxidase produces hydrogen peroxide on

interacting with glucose, which Pt can electrochemically monitor. On the other hand, hollow microneedles are used to collect interstitial fluid through capillary action or negative pressure. Once the interstitial fluid has been withdrawn, other methods can be used to detect the analyte, including spectrometric<sup>48</sup> and colorimetric methods.<sup>27, 28</sup> A key limitation to hollow microneedles are that they are susceptible to blockages if the tip opening is too small, whereas larger tip openings require larger tip radii which then require larger insertion force.<sup>15</sup> This current study focuses on coated microneedles and our objective was to develop a wafer scale, low cost process for the fabrication of microneedle arrays designed for electrochemical monitoring of interstitial fluid for in vivo measurements.

Previous work was completed on constructing similar electrochemical polymer devices for glucose monitoring.<sup>31, 49</sup> In this work, a polymer replication method was employed to produce polymer microneedles from a Si master. After the replication, holes were drilled into the polymer for front to back connections and the wafer was cut into individual devices. This work moved towards scaling this process towards mass manufacturing, using a double-sided micro-moulding process to replicate the Si master.

Microneedles heights of 500  $\mu\text{m}$  were chosen to target bovine skin which has an epidermis layer of  $< 2$  mm, with thickness varying with breed.<sup>50</sup> As cows have a thick coat to protect them from the weather, these devices would target either the ear or udder where the coat is less dense. Blood sampling causes an animal discomfort, often causing them to kick and thus endangering the veterinarian taking the sample. A microneedle sensor removes the need for sampling, making the device user-friendly, and this pain-free method provides safer application.

These devices were designed to act as UMEs, by using a passivation layer to confine the electroactive area to the tip. As UMEs they would produce a steady-state response, providing faster response times and lower detection limits, as previously discussed in Section 1.5. The concentration of antibodies in interstitial fluid ranges from 9 to 28% of that in blood plasma,<sup>51</sup> making the sensitivity of the devices vital. The passivation layer also prevents biofouling at the base of the electrodes from contaminants on the skin, which would cause high levels of background noise.

## 3.2 Experimental

### 3.2.1 Materials and Reagents

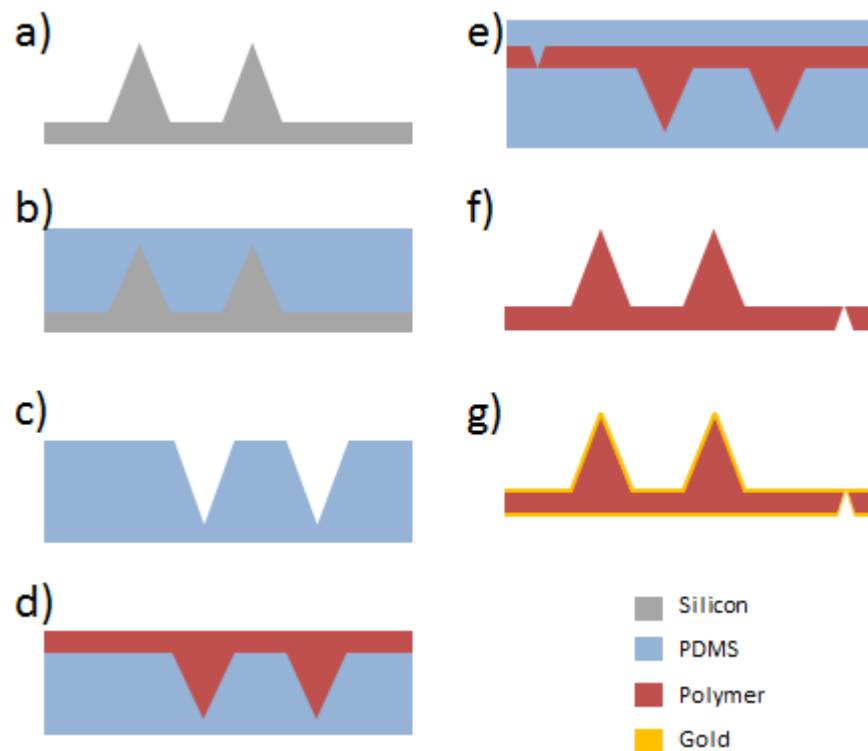
Gold, granular ~99.99% pure was obtained from PI-KEM Ltd., Staffordshire, UK. Sylgard 184 PDMS elastomer and curing agent were purchased from World Precision Ltd., Hertfordshire, UK. Norland optical adhesive NOA68 (polymer) was purchased from Tech Optics Ltd., Kent, UK. Epotek 430 and Epotek 353ND were purchased from John P Kummer Ltd., Marlborough, UK. All other reagents were purchased from Sigma Aldrich unless otherwise stated.

Deionised water (resistance  $18.2 \text{ M}\Omega \text{ cm}^{-1}$ ) was obtained using an ELGA Pure Lab Ultra system purchased from Alpha Diagnostic International.

### 3.2.2 Fabrication of Epoxy Microneedle Arrays

A polymer replication process allowed for a single silicon wafer to be repeatedly used to reproduce microneedles features in a polymer substrate as depicted in Schematic 3.1. A potassium hydroxide wet etch technique was used to create microneedle arrays in a 4 inch silicon wafer.<sup>52</sup> The silicon wafer was designed to have  $500 \mu\text{m}$  high microneedles, with a needle-to-needle pitch of  $1750 \mu\text{m}$  and an aspect ratio height-base of 3:2, Schematic 3.1(a). A PDMS mould with inverted features of the silicon master was provided by Dr. Conor O'Mahony and Mr Andrea Bocchino (Tyndall National Institute). PDMS elastomer was mixed in a 10:1 base:curing agent ratio, cast against the silicon microneedle master, degassed, and thermally cured at  $100^\circ\text{C}$  for 1 hour, Schematic 3.1(b). The rear mould was cast from a customised petri dish with features which were mechanically milled into the plastic petri dish, and the inverted structures were replicated into a PDMS mould in the same manner as the silicon microneedle wafer. This rear mould was designed to outline the individual sensors over a wafer, resulting in twelve  $15 \times 15 \text{ mm}$  sensors per wafer. The PDMS moulds were cleaned with washing up detergent and dried in the oven at  $80^\circ\text{C}$ . A layer of medical grade epoxy, Epotek 353 ND, was sandwiched between these PDMS moulds. Epotek 353 ND part A and part B were mixed in a ratio of 10:1 and poured into the warm front PDMS mould on removal from the oven. The heat from the PDMS mould reduces the viscosity of the epoxy and allows it to spread

easily, filling the mould. The epoxy filled mould was then placed in a vacuum chamber until the pressure reached  $< 200$  mTorr, to remove any air bubbles in the epoxy. The back PDMS mould was then placed on top, sandwiching the epoxy between both pieces of PDMS, as specified in Schematic 3.1 (e). Large bubbles were pushed towards the edge of the moulds and forced out. The combined moulds were placed on a vacuum table (with the microneedle structures faced down) with a large evenly distributed weight placed on top for one hour. The vacuum removed smaller bubbles, which if not removed, would cause defects in the wafer, while the weight dispersed the polymer evenly throughout the mould. The epoxy was cured in the oven at  $80^{\circ}\text{C}$  for one hour, the weight remaining in place to prevent movement of the moulds during curing. Once cooled, the wafer was carefully removed from the moulds. A tweezers was used to remove any thin films of epoxy that may have formed between the bridges and in the TWV features on the wafer.



**Schematic 3.1:** Schematic of fabrication process: (a) silicon master of MNs arrays; (b) PDMS mould of master, (c) cured and peeled; (d) The PDMS mould is filled with epoxy and (e) a second PDMS mould is placed on the back; (f) The epoxy is cured and peeled and (g) gold evaporated on each side of the structures.

Figure 3.2 represents the design for the rear mould. It incorporates features which permit arrays to be removed from the wafer without the need for a dicing step. These features

consist of partitioning walls which outline the sides of each sensor and trenches to create bridges which keep the die in place. Multiple TWV are also present on this mould, to facilitate an electrical connection from the front to the rear of each electrode. Four alignment marks are present to coordinate with the shadow mask during the evaporation step.

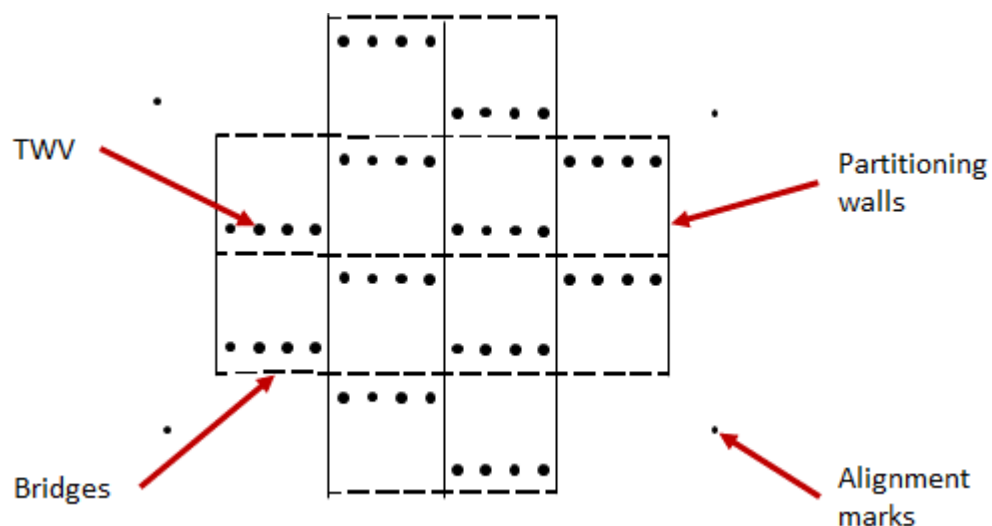
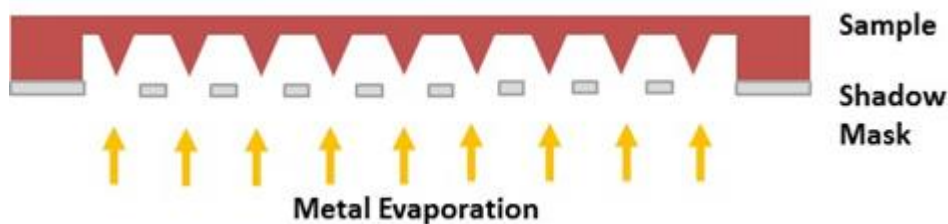


**Figure 3.2:** Outline of the design for the rear mould, with blackened areas representing the milled portions of the petri dish.

An aluminium (Al) shadow mask was designed to define the area of each electrode during evaporation of a metal. The mask acted as a physical barrier, allowing metal to only be evaporated onto the areas of the substrate where there is an opening as depicted in Schematic 3.2, producing four electrodes across each device. The shadow mask also generated metallized areas for the electrical connection of electrodes across devices. Each individual electrode on a device was connected to five other identical electrodes situated on surrounding devices and a contact pad located towards the edge of the wafer, as seen in Figure 3.6. This was to facilitate wafer scale processing of the electrodes using electrochemical techniques such as electrodeposition or cleaning through potentiodynamic cycling. This shadow mask was attached to the wafer face during evaporation using an e-beam evaporator (Moorfield E-Beam Evaporator). Titanium (Ti) was used as an adhesion layer to aid the Au layer adhere to the epoxy. A 20 nm layer was evaporated on both sides of the wafer followed by 100 nm of Au at a rate of  $1 \text{ \AA s}^{-1}$ . A tape test was carried out after the evaporation of Au, to confirm the adhesion of the metal layer and the need for the Ti layer. A piece of Kapton tape was firmly pressed into a section of Au on the back of the wafer, and repeatedly removed.



*Schematic 3.2: Diagram demonstrating how the Al shadow mask acts as a physical barrier, defining how the metal evaporates onto the substrate.*

### 3.2.3 Passivation of Microneedle Arrays

#### 3.2.3.1 COMSOL Simulations

Passivation was used to define the electrochemically active surface area of the electrode. An insulation layer covered the majority of the metallised area, limiting the conductive surface to the tips of the individual needles, creating UMEs. Diffusion profiles are no longer planar and if isolated to the discrete tip, currents produced will be small. However, if the diffusion profiles of adjacent tips overlap, the microelectrodes act as one large electrode, becoming diffusion-dependent and produce larger currents.

COMSOL simulations were performed by Mr. Benjamin O’Sullivan (Tyndall National Institute) to determine the acceptable exposed tip dimensions for these UMEs. A model was constructed using the commercial finite element software, COMSOL Multiphysics 5.3. The model’s experimental domain consisted of a 20 mm by 20 mm by 10 mm box, with the box sufficiently large that the edges of the domain were unaffected by the processes taking place at the electroactive surface in the centre of the domain. The model features a 3 x 2 array of 500  $\mu\text{m}$  microneedles with 3:2 height to base diameter ratio and 1750  $\mu\text{m}$  pitch. An insulation layer was added over the surface, leaving an exposed area at the tip. The active area of tip, defined as the electrode surface, was set as 20  $\mu\text{m}$  base radius x 60  $\mu\text{m}$  height, as shown in Figure 3.3. Larger active area dimensions were also considered. These simulations produced FcCOOH concentration profiles which allowed the prediction of the electrochemical behaviour.

Different scan rates were simulated to assess the effect of time on the diffusional mass transport of the redox molecule during CV. This was to provide insight into the diffusional independence of each tip in the microneedle array. Model parameters were set to reflect

common experimental conditions of a CV from 0 to 0.6 V with FcCOOH's  $E^0$  of 300 mV vs Ag/ AgCl reference electrode and the diffusion coefficient of oxidised and reduced species set as  $5.4 \times 10^{-6} \text{ cm}^2 \text{ s}^{-1}$ .

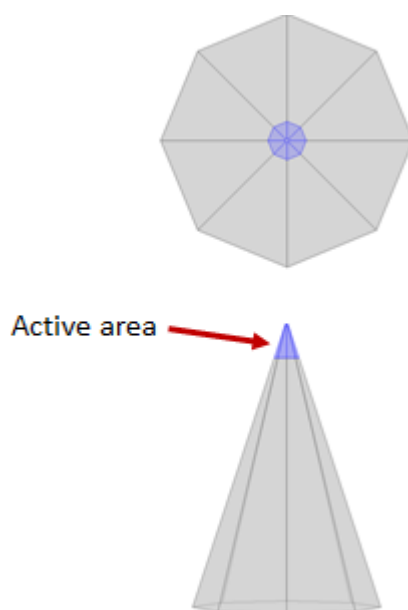


**Figure 3.3:** 3D microneedle geometry, generated in COMSOL, for 500  $\mu\text{m}$  MNs with 3:2 height to full base ratio. Active area of tip defined with 40  $\mu\text{m}$  diameter x 60  $\mu\text{m}$  height.

### 3.2.3.2 Spin Coating

Spin coating was used to entirely cover the gold area on the front of the sensor with a UV curing polymer, NOA68. Before curing, the sensor was put into the oven at 60°C for 2 hours to lower the viscosity of the polymer. Gravitational flow caused the polymer to recede from the microneedle tips. The polymer was then cured in a UV oven for 60 s (Bondmatic UV 1250).

Wires were then attached to the back of the devices to allow for electrochemical characterisation. The conductive copper epoxy, Epotek 430 was used to electrically connect the wire in place. Epotek 430 ND part A and part B were mixed in a ratio of 40:1 and was cured at 80°C for 1 hour. The entire back of the device was covered in NOA68 and cured for 120 s to allow for immersion in solution.



## 3.2.4 Characterisation of Structures

### 3.2.4.1 Scanning Electron Microscopy

SEM images were generated by Dr. Colm Barrett (Tyndall National Institute) during the fabrication process to establish if the microneedle features were structurally similar to the designs. A field emission SEM (JSM – 7500F, JEOL UK Ltd.) operating at a chamber pressure of 9.6  $\mu\text{Pa}$  and beam voltages between 5 and 10 kV was used to capture these images.

### 3.2.4.2 Electrochemical Characterisation

All electrochemical studies were performed using an Autolab Potentiostat/ Galvanostat PGSTAT128N (Metrohm Ltd, Utrecht, The Netherlands) controlled by Autolab NOVA software. All experiments were performed at room temperature in a Faraday cage. A three-electrode cell was adopted, using an array of microneedles as a working electrode versus an external Pt counter and Ag/AgCl reference electrodes. Electrode arrays were characterised in 1mM FcCOOH in 10 mM PBS (pH 7.4) using cyclic voltammetry (CV) performed at a potential window of 0 mV to 600 mV at 50  $\text{mV s}^{-1}$ .

## 3.3 Results and Discussion

### 3.3.1 Polymer Replication of Silicon MN Arrays

As described in Section 3.2.2, pairs of PDMS moulds were created for use in the replication process. The front mould, Figure 3.4 left, was a negative of the silicon master and created the microneedle structures during the polymer replication process. The rear mould, Figure 3.4 right, defined the twelve die present on a 4-inch wafer. Features included the partitioning walls, bridges, and conical protrusions to form the TWV.

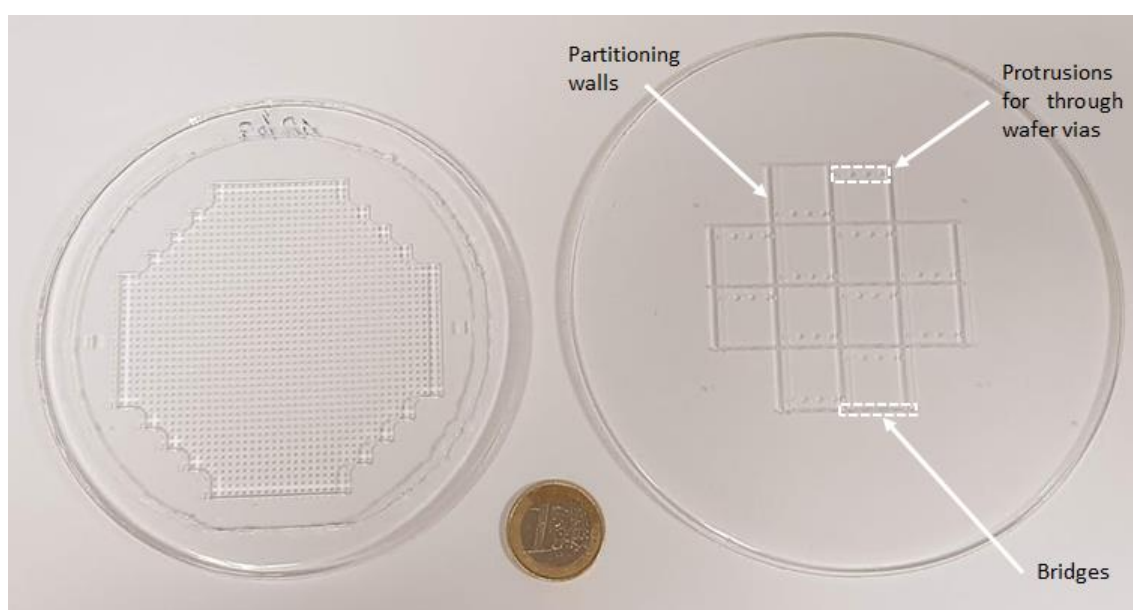


**Figure 3.4:** Image of the PDMS moulds for the fabrication of the epoxy wafer. The front mould (left) has inverted MNs structures. The rear mould (right) has protrusions to create TWV and bridges to hold each die in place but allow their removal with the application of pressure.

Generally, no visible defects were seen on the moulds, though occasionally a TWV cone would break. These defective moulds were discarded as the broken cone would produce a bubble at the back of the epoxy wafer, instead of a TWV. The presence of the microneedle arrays, partitioning walls, bridges, and TWV were all successfully transferred into the polymer. If no visible defects were seen, it implied the fabrication process sufficiently removed all major bubbles from the epoxy before curing. To further investigate the replication of the microneedle structures, SEM was employed and is discussed below.

The bridges designed the devices securely in place in the 4-inch wafer and were appropriately sized for the removal of the die with the application of finger pressure. Figure 3.5 demonstrates that a sample could be removed without damage to the surrounding die. This eliminated the need for a time-consuming dicing step. The presence of the TWV eliminated a drilling step which had been previously used in fabrication, thus reducing fabrication time. These features were more accurate and reproducible than drilled holes. The conical shape and smooth walls allowed for easier Au coating on the inside of the aperture, resulting in a more reliable electrical connection than previously seen. Previously, due to the unreliable electrical connections after evaporation when drilled holes were used, a tedious process of inserting conductive material into the opening to create a stable electrical connection was adopted. This has now been deemed unnecessary with the updated fabrication. Overall, the process produced defect free, wafer scale polymer moulds capable of replicating microneedle arrays into a set number of devices. The enhanced moulding process yielded more reproducible devices with consistent placing of TWV's, and bridges that allow easy removal of individual devices. The complexity of the fabrication process was reduced, and production time accelerated which moves it towards large scale manufacturing.

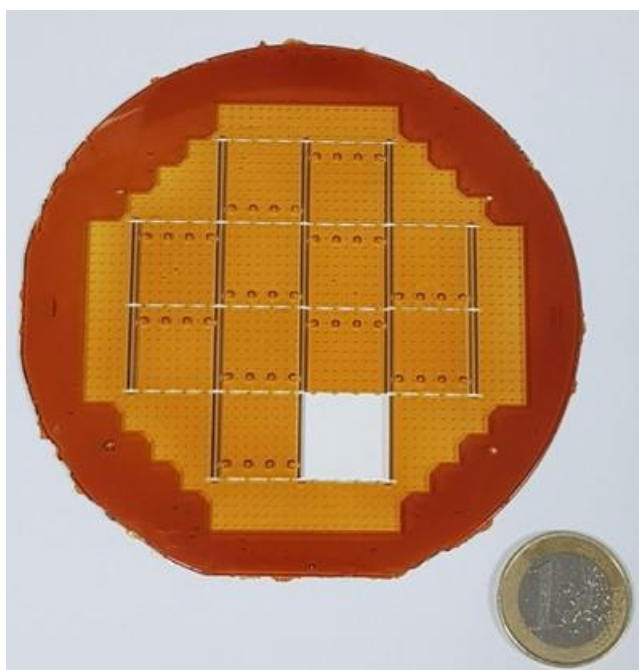


**Figure 3.5:** Image of the front of the polymer (Epotex 353 ND) replicated wafer with microneedle structures and features from the rear mould present.

After the epoxy wafer was removed from the PDMS moulds, the wafer was metalized to produce electrochemical devices. The Al shadow mask acted as a physical barrier during metal evaporation. Only the exposed areas were coated in Ti and Au, as seen in Figure 3.6. The Ti layer evaporated onto the wafer acted as an adhesive layer between the Au and the polymer. A tape test was carried out on a wafer without the Ti layer and a wafer with the Ti layer. On a wafer without a Ti adhesion layer, large specks of Au were removed from the epoxy surface on the first peeling of the tape. When this test was performed on a wafer with the Ti under-layer no gold residue was present after the tape had been secured and peeled off ten times. This clearly established the need for an adhesive layer.

Each device had four individual electrodes, each containing at least one row of microneedle structures. There was a variation in the number of microneedles present in each electrode due to the width of each electrode. Some electrodes contained two rows, or half rows where the needle structure was partially coated, as seen in Figure 3.7 (b). As current produced by these electrodes once passivated will be proportional to the amount of microneedle tips present, a variation of current would be expected. There were no electrical connections observed between electrodes on the same device, while the connection between electrodes on neighbouring devices existed due to connecting tracks. This was to accommodate electrochemical processing on a wafer scale, such as electrodeposition and sulphuric acid cleaning.

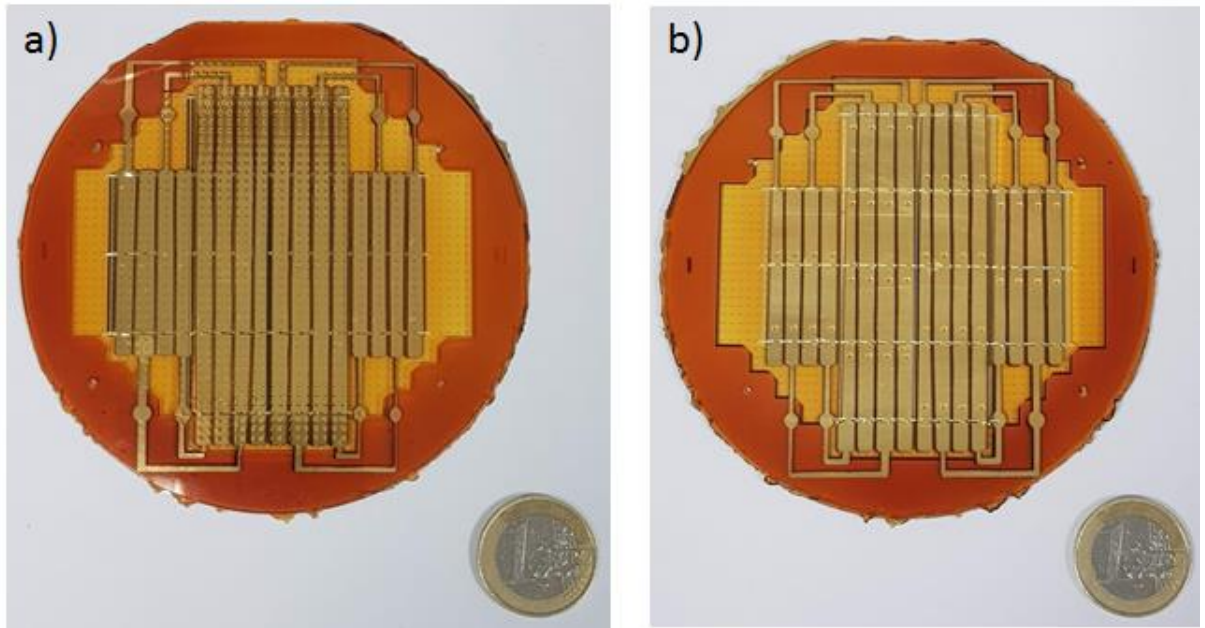


**Figure 3.6:** Image of (a) front of and (b) back of polymer wafer after evaporation of 20 nm Ti and 100 nm Au layer.

After evaporation, the devices were removed from the wafer. The back of a device was pushed causing the bridges on each side to snap. Once one device was free from the supporting structure, the rest could be removed by bending them, causing their bridges to snap. The device contained electrodes of dimensions 15 mm x 2.9 mm, with each electrode containing microneedle structures, as demonstrated in Figure 3.7. These 3D structures were easier to visualise at an angle, as in Figure 3.7 (b). From this visual inspection the structural integrity appeared to be intact.

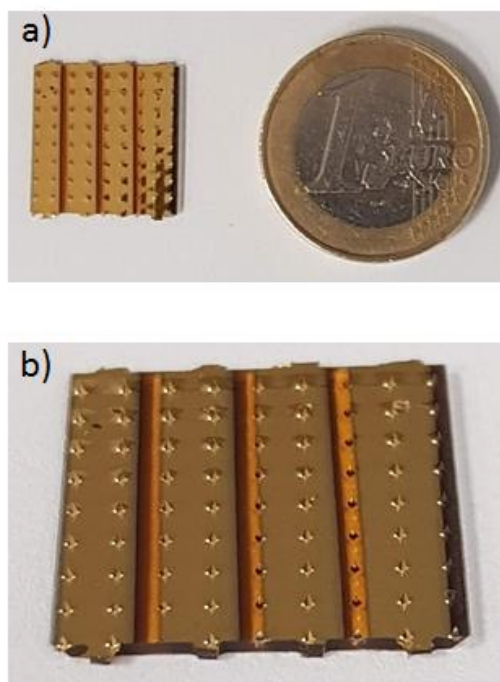


**Figure 3.7:** Image of device removed from wafer after metal evaporation, (a) taken directly overhead and (b) taken at an angle.

While no obvious defects in the epoxy devices were observed by visual inspection, SEM characterisation showed structural defects, especially at the tips. The eight-faced pyramidal structures were present, with each face clearly defined, as seen Figure 3.8 (a), which displays a pristine microneedle. Previous work using this process showed that polymer tips are not as sharp as the Si tips.<sup>53</sup> The tip radii of the Si are generally of the order of 50 - 100 nm, whereas the epoxy tips are typically 500 - 1000 nm in radius. This tip sharpness is still sufficient to allow insertion into human skin using finger pressure. The microneedle in Figure 3.8 (b) and (c) demonstrates how some of the tips were bowed, while Figure 3.8 (c) and (d) highlighted that the sides of the microneedles weren't always smooth. Using a hard polymer, such as Epotek 353 ND, ensures sharp structures that can withstand the pressure required to pierce the *stratum corneum*. However, these hard, sharp structures can cause damage to the PDMS mould during the peeling process. The needle tip tore sections of the inverted PDMS structures as it was being released from the mould. This damage was then transferred onto the epoxy structures as these tears were then filled with epoxy during the next replication step. The additional height of the structures is likely adding to the damage as a similar effect was seen when peeling the PDMS mould from the Si master. Therefore, the PDMS mould had already sustained damage before polymer replication step. However, these structures have successfully been utilised in

other work inserting into human skin,<sup>53</sup> proving they are capable of piercing the *stratum corneum*. Planned areas for bovine application are the ear and udder where there is minimal hair coating to allow comparable usage to human skin. The defects seen does not prevent the metallisation of the devices for the construction of an electrochemical cell.

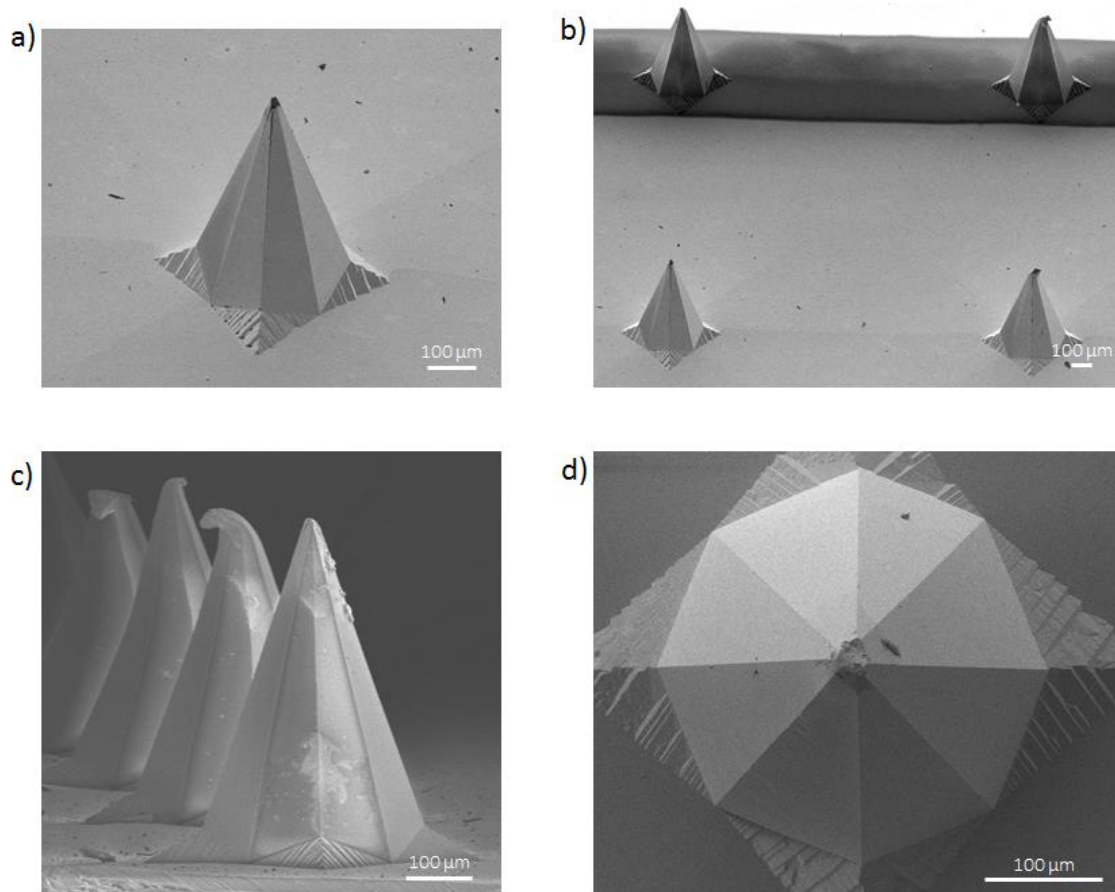


**Figure 3.8:** SEM images of epoxy microneedle structures coated with 100 nm of Au at (a, b) a 45° angle, (c) elevation view and (d) plan view.

### 3.3.2 Selective Passivation of Array Surface

#### 3.3.2.1 COMSOL Simulations

COMSOL simulations were run to predict the electrochemical behaviour of the microneedles arrays once they had been passivated, leaving only the tips as the exposed conductive area. In the model shown in Figure 3.9 the exposed tip is defined to have a base radius of 20  $\mu\text{m}$ , which would result in a 60  $\mu\text{m}$  high tip, as depicted in Figure 3.3. These dimensions are close to the tip dimensions produced in previous work.<sup>24</sup> The bulk concentration of the model shown in Figure 3.9 consists of 1 mM FcCOOH in its ground state (red). This concentration decreases near the microneedle tips, with the FcCOOH at the apex being completely oxidised (blue). The diffusion profiles were considered at a

variety of scan rates, as the slower the scan rate the larger the diffusion layer, as explained in Section 1.5. Even at the slowest scan rate of  $10 \text{ mV s}^{-1}$ , as illustrated in Figure 3.9 (a and b), there was no overlapping of the individual diffusion layers. Furthermore, this diffusional layer exhibits a circular profile, expected from UMEs, and can clearly be seen in the side-on view of the electrodes in Figure 3.9 (b). Similarly, radial diffusion is seen in Figure 3.9 (d) when the scan rate is increased to  $100 \text{ mV s}^{-1}$ . Though it is apparent in Figure 3.9 (c) that although the radius of the diffusion layer is smaller due to the faster scan rate, the radius is still large compared to the radius of the exposed area of the electrode, allowing radial diffusion to occur. However, when the scan rate increases sufficiently the diffusion layer becomes depleted such that the thickness is smaller than the electrode radius and mass transport becomes dominated by planar diffusion, causing it to be diffusionally-dependent. In Figure 3.9 (e), at the scan rate of  $1000 \text{ mV s}^{-1}$  the diffusion layer has become much smaller and Figure 3.9 (f) shows it is extremely constricted to the tip. From the plot depicted in Figure 3.10 (b), the maximum radius of the diffusion layer is approx.  $55 \text{ }\mu\text{m}$ , at this rate. However, at the periphery of this area, the concentration of FcCOOH is  $0.999 \text{ mM}$ . To allow for even 10 % of the species to be oxidised, the radius reduces to  $26 \text{ }\mu\text{m}$ , whereas, at  $100 \text{ mV s}^{-1}$  the radius is  $41 \text{ }\mu\text{m}$ .



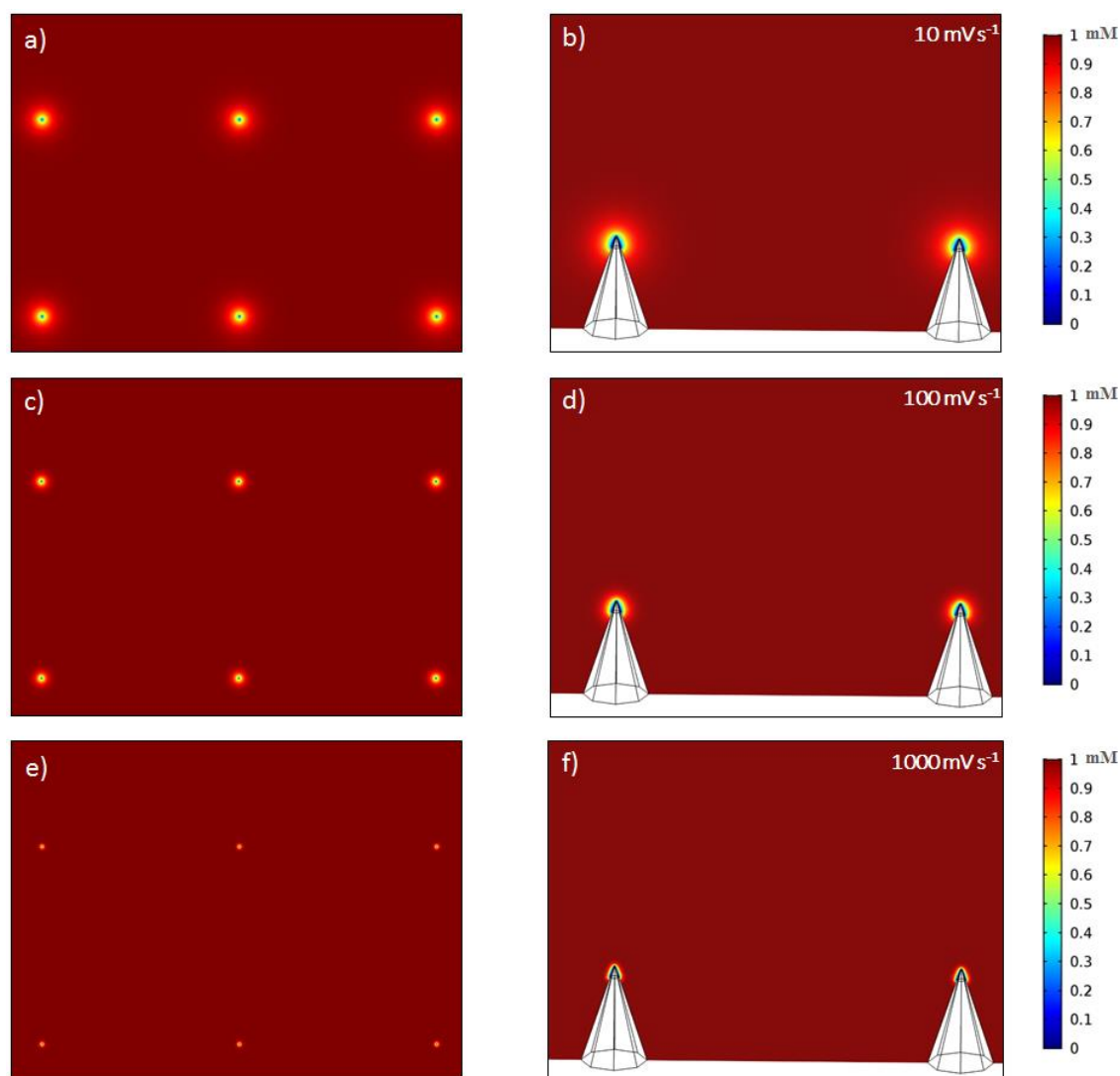


**Figure 3.9:** 1 mM  $\text{FcCOOH}$  concentration profile at 6.0 V for  $3 \times 2$  array of electroactive tips (radius  $20 \mu\text{m}$ ) with  $1750 \mu\text{m}$  pitch at, shown top down (left) and side on (right) at (a, b)  $10 \text{ mV s}^{-1}$ , (c, d)  $100$  and (e, f)  $1000 \text{ mV s}^{-1}$

Electrodes such as this would exhibit transient scans due to planar diffusion at fast scan rates such as  $1000 \text{ mV s}^{-1}$ , as seen in Figure 3.10 (red). Whereas, decreasing the scan rate ten-fold to  $100 \text{ mV s}^{-1}$  (Figure 3.10 green) resulted in a much larger diffusion layer, ensuring radial diffusion and steady-state behaviour. Reduction of the scan rate to  $10 \text{ mV s}^{-1}$  further increases the diffusion layer as seen in Figure 3.9 (a and b), again producing steady-state scans; Figure 3.10 (blue).

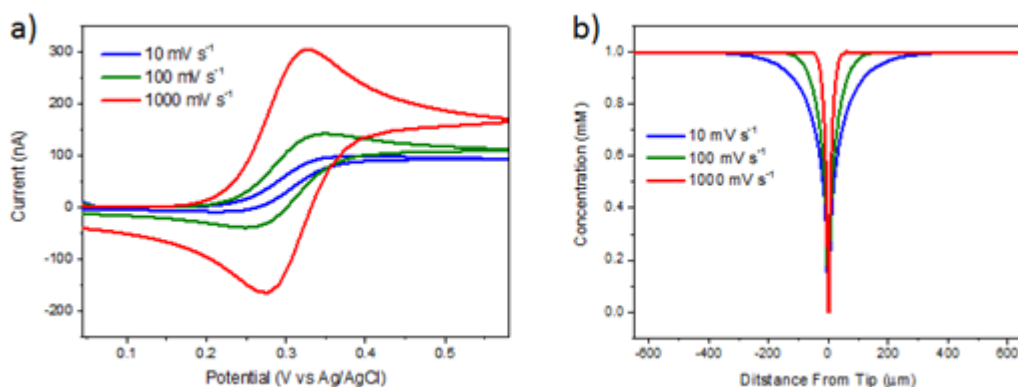


**Figure 3.10:** (a) Simulated CV for microneedle arrays (electroactive tips radius  $20\ \mu\text{m}$ ) in  $1\ \text{mM}$   $\text{FcCOOH}$  and (b) graph of the concentration of  $\text{FcCOOH}$  at  $0.6\ \text{V}$  vs distance from the tip for the simulated diffusion profile at  $10$ ,  $100$  and  $1000\ \text{mVs}^{-1}$ .

The exposed areas were varied in the model to establish a range of areas that could be used while still being diffusionally independent and displaying UME behaviour. As the diffusion profiles of each tip were extremely isolated with a radius of  $20\ \mu\text{m}$ , as seen in Figure 3.11 (a), larger exposed areas were also investigated. The top down view has the concentration profile taken at the base of the exposed area to clearly show the effect of the dimensions on the diffusion ring. A radius of  $30\ \mu\text{m}$ , which gave a height of  $90\ \mu\text{m}$  was considered in Figure 3.11 (c). Here each microneedle is seen to still have an isolated diffusion profile, though the radius is larger than previously seen. In Figure 3.11 (e) the electroactive area is larger again ( $50\ \mu\text{m} \times 150\ \mu\text{m}$ ), which has led to an even larger diffusion rings surrounding the exposed area. Still there is no overlapping seen between the tips.

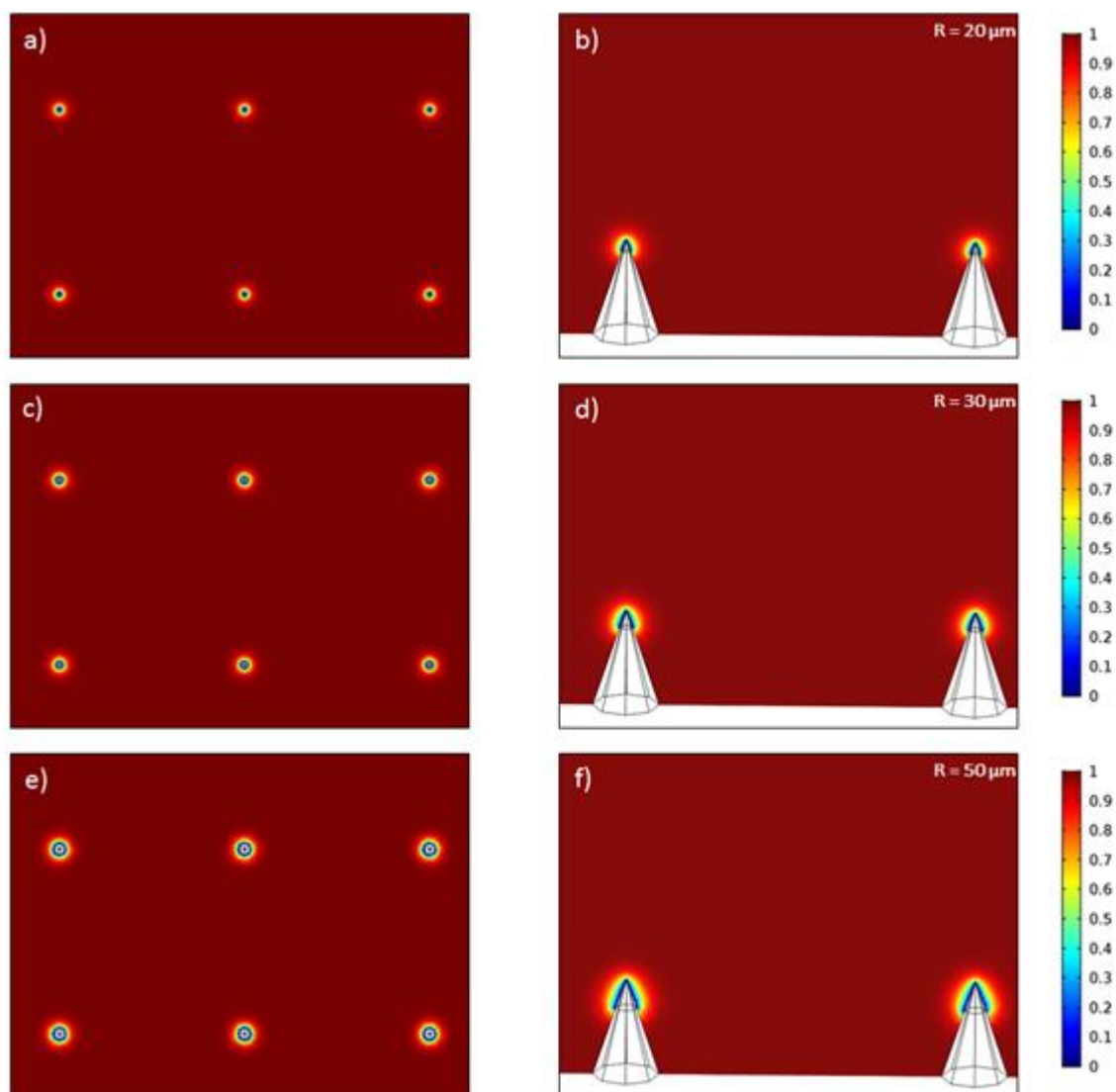


**Figure 3.11:** Concentration profiles for 3 x 2 array of electroactive tips in 1 mM FcCOOH at 6.0 V with 1750  $\mu\text{m}$  pitch at 50  $\text{mV s}^{-1}$  generated in COMSOL, shown top down (left) and side on (right). Electroactive area is defined to have a diameter of (a, b) 40  $\mu\text{m}$ , (c, d) 60  $\mu\text{m}$  and (e, f) 100  $\mu\text{m}$

A side-on view was also considered as depicted in Figure 3.11 (b), (d) and (f). Radial diffusion is simulated in Figure 3.11 (b) for which steady-state behaviour would be expected, as previously shown in Figure 3.10 (a). Figure 3.11 (d) also appears to have radial diffusion, however in Figure 3.11 (e), where the active area is largest, the circular shape of the diffusion profile is distorted, and has become less circular and more elongated. Due to the pyramidal shape of the area being investigated it is difficult to distinguish between radial and planar diffusion. CVs were simulated to determine the electrochemical response of these electrodes. The smallest exposed area with radius of 20  $\mu\text{m}$  generates a steady-state response at 50  $\text{mV s}^{-1}$ , Figure 3.12 (blue). When the radius is increased to the 30  $\mu\text{m}$  the current output almost doubles, Figure 3.12 (green). The

diffusion layer is not radial as previously thought but a hybridised form which shifts towards planar diffusion, exhibiting quasi-steady state characteristics. This is expected as UME's have a generally critical dimension  $\leq 25 \mu\text{m}$ ,<sup>54</sup> in this case the radius of the electroactive area. However, as the diffusion profiles remain completely isolated, and planar diffusion is still not dominant, a larger than recommended active area could be utilised by these devices, depending on the sensitivity required. Planar diffusion has taken over with a radius of  $50 \mu\text{m}$  and the electrochemical response becomes diffusionally-dependent, Figure 3.12 (red).

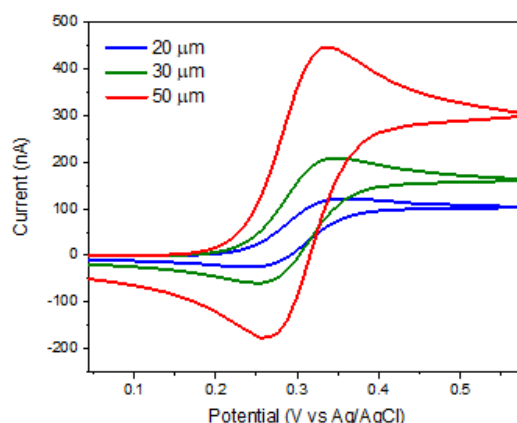


**Figure 3.12:** Simulated CV for  $3 \times 2$  microneedle arrays in  $1 \text{ mM FcCOOH}$  at  $50 \text{ mV s}^{-1}$  with exposed tip radius of  $20 \mu\text{m}$  (blue),  $30 \mu\text{m}$  (green) and  $50 \mu\text{m}$  (red) .

### 3.3.2.2 Passivation with Spin Coated Polymer

To form this UME array, a resistive layer must cover the gold surface, leaving just the tip exposed to ensure that was the only place electrochemical reactions can occur. Electrochemical characterisation in  $1 \text{ mM FcCOOH}$  in  $10 \text{ mM PBS}$  at  $50 \text{ mV s}^{-1}$  showed high discrepancies across all electrodes. Currents produced were typically a few hundred nanoamps and the voltammogram shape varied. Ferrocene characteristics were present, with a sharp increase in current at approx.  $0.2 \text{ V}$  as oxidation starts. Some electrodes displayed a steady-state quality though a plateau was not quite reached (Figure 3.13 (a)). Other electrodes, Figure 3.13 (b), displayed pseudo steady-state characteristics, suggesting a larger exposed area than desired. However, steady-state could be achieved by reducing the scan rate, allowing the diffusion layer to further grow.

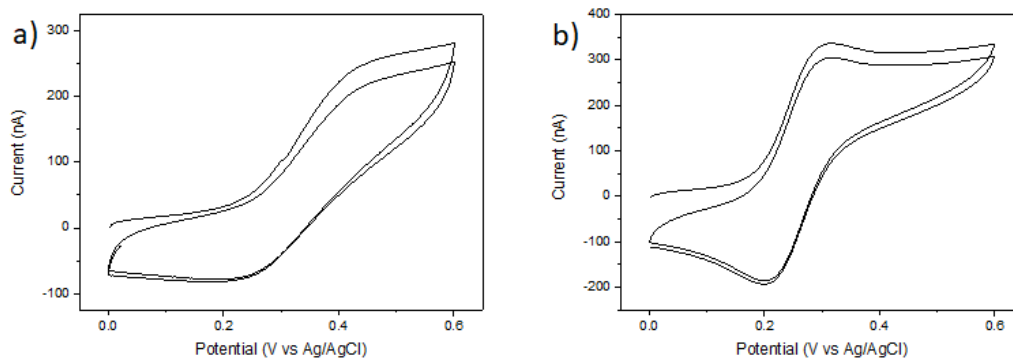


**Figure 3.13:** Examples of cyclic voltammograms of two microneedle devices after passivation in 1 mM FcCOOH in 10 mM PBS, pH 7.4 at  $50 \text{ mV s}^{-1}$ .

SEM was employed to investigate the polymer coverage on the gold surface and in Figure 3.14 the distinct areas of the exposed gold and passivating polymer were clearly visible. In Figure 3.14 (a), the polymer is seen to have coated most of the microneedle structure, leaving gaps along the edges of the faces on each side of the pyramidal structure. Here the exposed area of gold is relatively small and may produce steady-state or pseudo-state-state, such as seen in Figure 3.13 (a). The Epotek 353 ND chosen for this work has a Shore D Hardness of 85. The NOA68 polymer which was previously used to produce partial passivated needle tips<sup>24</sup> has a Shore D Hardness of 60. The softer polymer produced microneedles with smoother edges and after spin coating and curing of the passivation polymer only the needle tip was left exposed. This polymer was no longer used as it not certified as biocompatible. Therefore, a different polymer may need to be used with a reduce Shore D Hardness that would produce smoother features.

Another issue with this passivation layer the SEM highlighted related back to the structural defects discussed in Section 3.3.1. The flat faces of the microneedle structures are not always smooth and the polymer forms clumps around defects as evident in Figure 3.14 (b). This leaves the area under the defect partially uncovered and prevents consistency in the passivation layer. Large exposed such as those observed in Figure 3.14 (b) cause planar diffusion, resulting in transient CVs such as seen in Figure 3.13 (b). For this passivation method to be viable, shorter needles will have to be used to reduce the amount of damage on the PDMS moulds caused by the peeling the mould.

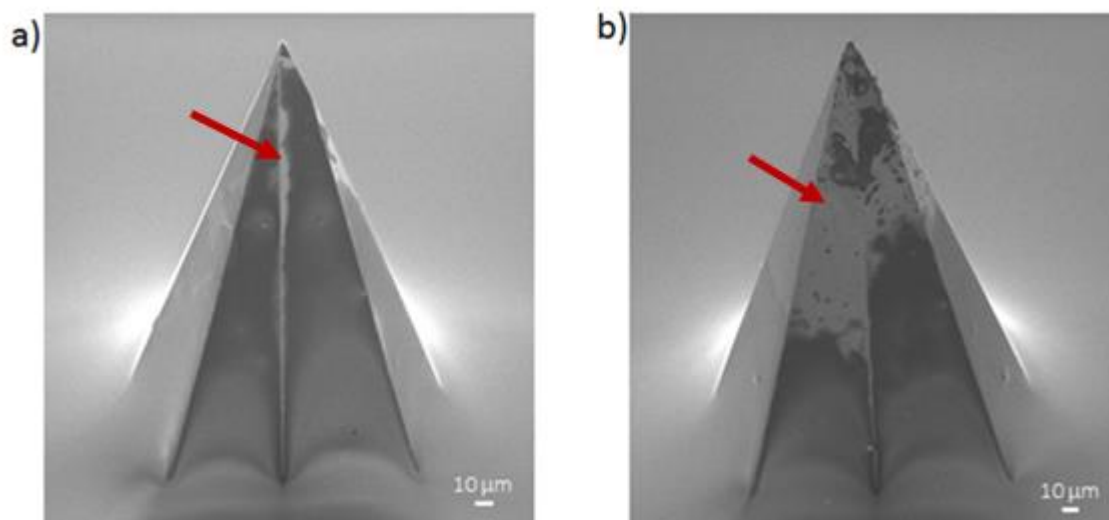


**Figure 3.14:** SEM images of a single microneedle after the spin coated passivation step. Lighter regions are the exposed gold as indicated by the red arrows.

An alternative coating method is needed for these structures such as dip coating, spray coating or some resists that can be electrodeposited. These methods would result in complete coverage of the surface. For future studies, either a mask could be used to selectively etch the microneedle tips, or the tips could be dipped into an etching reagent.

### 3.4 Conclusion

A simple, cost-effective method was devised for replicating silicon microneedle structures with a biocompatible polymer. This method allowed a four-inch wafer of microneedles to be converted into twelve electrochemical devices increasing the feasibility of mass production by the addition of a second mould. Each device included four electrodes to allow for a working electrode, a reference electrode, a counter electrode, and a second working electrode which would provide a control.

COMSOL highlighted that microneedles with a base radius of  $\leq 20 \mu\text{m}$  would satisfy the requirements of an UME. However, a slightly larger exposed area could be utilised of  $\leq 30 \mu\text{m}$  for analysis which does not require the sensitivity provided by steady-state behaviour while remaining more sensitive than diffusionally-dependent electrodes. Spin coating proved to be incompatible due to the material and dimensions of the structures. Although a suitable selective passivation method was not found in the current study these structures may still be used for drug or vaccine delivery. This application would not require the passivation layer. In order to generate successful electrochemical biosensors lending themselves to mass production and capable of use in bovine diagnostics, an alternative method for producing UMEs from these structures was devised and is presented in the following chapter.

### 3.5 References

1. Donnelly, R. F.; Raj Singh, T. R.; Woolfson, A. D., Microneedle-based drug delivery systems: Microfabrication, drug delivery, and safety. *Drug Delivery* **2010**, *17* (4), 187-207.
2. Indermun, S.; Luttge, R.; Choonara, Y. E.; Kumar, P.; Du Toit, L. C.; Modi, G.; Pillay, V., Current advances in the fabrication of microneedles for transdermal delivery. *Journal of Controlled Release* **2014**, *185* (1), 130-138.
3. Larrañeta, E.; McCrudden, M. T. C.; Courtenay, A. J.; Donnelly, R. F., Microneedles: A New Frontier in Nanomedicine Delivery. *Pharmaceutical Research* **2016**, *33* (5), 1055-1073.
4. Madden, J.; O'Mahony, C.; Thompson, M.; O'Riordan, A.; Galvin, P., Biosensing in dermal interstitial fluid using microneedle based electrochemical devices. *Sensing and Bio-Sensing Research* **2020**, 100348.
5. Rzhnevskiy, A. S.; Singh, T. R. R.; Donnelly, R. F.; Anissimov, Y. G., Microneedles as the technique of drug delivery enhancement in diverse organs and tissues. *Journal of controlled release : official journal of the Controlled Release Society* **2018**, *270*, 184-202.
6. Han, T. Y.; Park, K. Y.; Ahn, J. Y.; Kim, S. W.; Jung, H. J.; Kim, B. J., Facial Skin Barrier Function Recovery After Microneedle Transdermal Delivery Treatment. *Dermatologic Surgery* **2012**, *38* (11).
7. Bal, S. M.; Caussin, J.; Pavel, S.; Bouwstra, J. A., In vivo assessment of safety of microneedle arrays in human skin. *European Journal of Pharmaceutical Sciences* **2008**, *35* (3), 193-202.
8. Rzhnevskiy, A. S.; Singh, T. R. R.; Donnelly, R. F.; Anissimov, Y. G., Microneedles as the technique of drug delivery enhancement in diverse organs and tissues. *Journal of Controlled Release* **2018**, *270*, 184-202.
9. van der Maaden, K.; Jiskoot, W.; Bouwstra, J., Microneedle technologies for (trans)dermal drug and vaccine delivery. *Journal of Controlled Release* **2012**, *161* (2), 645-655.
10. Kim, Y. C.; Park, J. H.; Prausnitz, M. R., Microneedles for drug and vaccine delivery. *Adv. Drug Deliv. Rev.* **2012**, *64* (14), 1547-1568.
11. Prausnitz, M. R., Microneedles for transdermal drug delivery. *Adv. Drug Deliv. Rev.* **2004**, *56* (5), 581-587.
12. Ita, K., Transdermal delivery of drugs with microneedles: Strategies and outcomes. *Journal of Drug Delivery Science and Technology* **2015**, *29*, 16-23.
13. Ita, K., Transdermal delivery of drugs with microneedles—potential and challenges. *Pharmaceutics* **2015**, *7* (3), 90-105.
14. Donnelly, R. F.; Singh, T. R. R.; Garland, M. J.; Migalska, K.; Majithiya, R.; McCrudden, C. M.; Kole, P. L.; Mahmood, T. M. T.; McCarthy, H. O.; Woolfson, A. D., Hydrogel-Forming Microneedle Arrays for Enhanced Transdermal Drug Delivery. *Advanced Functional Materials* **2012**, *22* (23), 4879-4890.
15. Bhatnagar, S.; Dave, K.; Venuganti, V. V. K., Microneedles in the clinic. *Journal of Controlled Release* **2017**, *260*, 164-182.



16. Mohammed, Y.; Yamada, M.; Lin, L.; Grice, J.; Roberts, M.; Raphael, A.; Benson, H.; Prow, T., Microneedle Enhanced Delivery of Cosmeceutically Relevant Peptides in Human Skin. *PloS one* **2014**, *9*, e101956.
17. Kim, M.; Yang, H.; Kim, H.; Jung, H.; Jung, H., Novel cosmetic patches for wrinkle improvement: retinyl retinoate- and ascorbic acid-loaded dissolving microneedles. *International Journal of Cosmetic Science* **2014**, *36* (3), 207-212.
18. Park, Y.; Park, J.; Chu, G. S.; Kim, K. S.; Sung, J. H.; Kim, B., Transdermal delivery of cosmetic ingredients using dissolving polymer microneedle arrays. *Biotechnology and Bioprocess Engineering* **2015**, *20* (3), 543-549.
19. Ma, G.; Wu, C., Microneedle, bio-microneedle and bio-inspired microneedle: A review. *Journal of Controlled Release* **2017**, *251*, 11-23.
20. O'Mahony, C., Structural characterization and in-vivo reliability evaluation of silicon microneedles. *Biomed Microdevices* **2014**, *16* (3), 333-43.
21. Henry, S.; McAllister, D. V.; Allen, M. G.; Prausnitz, M. R., Microfabricated Microneedles: A Novel Approach to Transdermal Drug Delivery. *Journal of Pharmaceutical Sciences* **1998**, *87* (8), 922-925.
22. Picofluidics Picofluidics news. <http://www.picofluidics.com/6.html> (accessed 18th November).
23. Caffarel-Salvador, E.; Brady, A. J.; Eltayib, E.; Meng, T.; Alonso-Vicente, A.; Gonzalez-Vazquez, P.; Torrisi, B. M.; Vicente-Perez, E. M.; Mooney, K.; Jones, D. S.; Bell, S. E. J.; McCoy, C. P.; McCarthy, H. O.; McElnay, J. C.; Donnelly, R. F., Hydrogel-forming microneedle arrays allow detection of drugs and glucose in vivo: Potential for use in diagnosis and therapeutic drug monitoring. *PLoS ONE* **2015**, *10* (12).
24. Barrett, C.; Dawson, K.; O'Mahony, C.; O'Riordan, A., Development of low cost rapid fabrication of sharp polymer microneedles for in vivo glucose biosensing applications. *ECS Journal of Solid State Science and Technology* **2015**, *4* (10), S3053-S3058.
25. Caliò, A.; Dardano, P.; Di Palma, V.; Bevilacqua, M. F.; Di Matteo, A.; Iuele, H.; De Stefano, L., Polymeric microneedles based enzymatic electrodes for electrochemical biosensing of glucose and lactic acid. *Sensors and Actuators, B: Chemical* **2016**, *236*, 343-349.
26. Li, C. G.; Joung, H. A.; Noh, H.; Song, M. B.; Kim, M. G.; Jung, H., One-touch-activated blood multidagnostic system using a minimally invasive hollow microneedle integrated with a paper-based sensor. *Lab on a Chip - Miniaturisation for Chemistry and Biology* **2015**, *15* (16), 3286-3292.
27. Miller, P. R.; Skoog, S. A.; Edwards, T. L.; Lopez, D. M.; Wheeler, D. R.; Arango, D. C.; Xiao, X. Y.; Brozik, S. M.; Wang, J.; Polsky, R.; Narayan, R. J., Multiplexed microneedle-based biosensor array for characterization of metabolic acidosis. *Talanta* **2012**, *88*, 739-742.
28. Sharma, S.; Saeed, A.; Johnson, C.; Gadegaard, N.; Cass, A. E., Rapid, low cost prototyping of transdermal devices for personal healthcare monitoring. *Sensing and Bio-Sensing Research* **2017**, *13*, 104-108.
29. Sharma, S.; Huang, Z.; Rogers, M.; Boutelle, M.; Cass, A. E. G., Evaluation of a minimally invasive glucose biosensor for continuous tissue monitoring. *Analytical and Bioanalytical Chemistry* **2016**, *408* (29), 8427-8435.

30. Gao, J.; Huang, W.; Chen, Z.; Yi, C.; Jiang, L., Simultaneous detection of glucose, uric acid and cholesterol using flexible microneedle electrode array-based biosensor and multi-channel portable electrochemical analyzer. *Sensors and Actuators B: Chemical* **2019**, *287*, 102-110.
31. Barrett, C.; O'Sullivan, F.; Barry, S.; Grygoryev, K.; O'Gorman, D.; O'Mahony, C.; O'Riordan, A., *Novel Surface Modified Polymer Microneedle based Biosensors for Interstitial Fluid Glucose Detection*. 2019; p 1-4.
32. Anastasova, S.; Crewther, B.; Bembnowicz, P.; Curto, V.; Ip, H. M.; Rosa, B.; Yang, G. Z., A wearable multisensing patch for continuous sweat monitoring. *Biosensors and Bioelectronics* **2017**, *93*, 139-145.
33. Windmiller, J. R.; Zhou, N.; Chuang, M. C.; Valdés-Ramírez, G.; Santhosh, P.; Miller, P. R.; Narayan, R.; Wang, J., Microneedle array-based carbon paste amperometric sensors and biosensors. *Analyst* **2011**, *136* (9), 1846-1851.
34. Miller, P. R.; Gittard, S. D.; Edwards, T. L.; Lopez, D. M.; Xiao, X.; Wheeler, D. R.; Monteiro-Riviere, N. A.; Brozik, S. M.; Polsky, R.; Narayan, R. J., Integrated carbon fiber electrodes within hollow polymer microneedles for transdermal electrochemical sensing. *Biomicrofluidics* **2011**, *5* (1).
35. Skoog, S. A.; Miller, P. R.; Boehm, R. D.; Sumant, A. V.; Polsky, R.; Narayan, R. J., Nitrogen-incorporated ultrananocrystalline diamond microneedle arrays for electrochemical biosensing. *Diamond and Related Materials* **2015**, *54* (1), 39-46.
36. Keum, D. H.; Jung, H. S.; Wang, T.; Shin, M. H.; Kim, Y. E.; Kim, K. H.; Ahn, G. O.; Hahn, S. K., Microneedle Biosensor for Real-Time Electrical Detection of Nitric Oxide for In Situ Cancer Diagnosis During Endomicroscopy. *Advanced Healthcare Materials* **2015**, *4* (8), 1153-1158.
37. Coffey, J. W.; Meliga, S. C.; Corrie, S. R.; Kendall, M. A. F., Dynamic application of microprojection arrays to skin induces circulating protein extravasation for enhanced biomarker capture and detection. *Biomaterials* **2016**, *84*, 130-143.
38. Coffey, J. W.; Corrie, S. R.; Kendall, M. A. F., Early circulating biomarker detection using a wearable microprojection array skin patch. *Biomaterials* **2013**, *34* (37), 9572-9583.
39. Corrie, S. R.; Fernando, G. J. P.; Crichton, M. L.; Brunck, M. E. G.; Anderson, C. D.; Kendall, M. A. F., Surface-modified microprojection arrays for intradermal biomarker capture, with low non-specific protein binding. *Lab on a Chip - Miniaturisation for Chemistry and Biology* **2010**, *10* (20), 2655-2658.
40. Corrie, S. R.; Coffey, J. W.; Kendall, M. A. F. In *In vivo biomarker capture via the skin using surface-modified microprojection arrays*, ASME 2013 2nd Global Congress on NanoEngineering for Medicine and Biology, NEMB 2013, 2013.
41. Lee, K. T.; Muller, D. A.; Coffey, J. W.; Robinson, K. J.; McCarthy, J. S.; Kendall, M. A. F.; Corrie, S. R., Capture of the circulating Plasmodium falciparum biomarker HRP2 in a multiplexed format, via a wearable skin patch. *Anal. Chem.* **2014**, *86* (20), 10474-10483.
42. Miller, P.; Moorman, M.; Manginell, R.; Ashlee, C.; Brener, I.; Wheeler, D.; Narayan, R.; Polsky, R., Towards an Integrated Microneedle Total Analysis Chip for Protein Detection. *Electroanalysis* **2016**, *28* (6), 1305-1310.

43. Ng, K. W.; Lau, W. M.; Williams, A. C., Towards pain-free diagnosis of skin diseases through multiplexed microneedles: biomarker extraction and detection using a highly sensitive blotting method. *Drug Deliv. Transl. Res.* **2015**, *5* (4), 387-396.
44. Yeow, B.; Coffey, J. W.; Muller, D. A.; Grøndahl, L.; Kendall, M. A. F.; Corrie, S. R., Surface modification and characterization of polycarbonate microdevices for capture of circulating biomarkers, both in vitro and in vivo. *Anal. Chem.* **2013**, *85* (21), 10196-10204.
45. Jeon, E.; Choi, S.; Yeo, K.-H.; Park, K. S.; Rathod, M. L.; Lee, J., Development of electrical conductivity measurement technology for key plant physiological information using microneedle sensor. *J. Micromech. Microeng.* **2017**, *27* (8), 085009.
46. Paul, R.; Saville, A. C.; Hansel, J. C.; Ye, Y.; Ball, C.; Williams, A.; Chang, X.; Chen, G.; Gu, Z.; Ristaino, J. B.; Wei, Q., Extraction of Plant DNA by Microneedle Patch for Rapid Detection of Plant Diseases. *ACS Nano* **2019**, *13* (6), 6540-6549.
47. Li, B.; Wang, J.; Yang, S. Y.; Zhou, C.; Wu, M. X., Sample-free quantification of blood biomarkers via laser-treated skin. *Biomaterials* **2015**, *59*, 30-38.
48. Miller, P. R.; Taylor, R. M.; Tran, B. Q.; Boyd, G.; Glaros, T.; Chavez, V. H.; Krishnakumar, R.; Sinha, A.; Poorey, K.; Williams, K. P.; Branda, S. S.; Baca, J. T.; Polsky, R., Extraction and biomolecular analysis of dermal interstitial fluid collected with hollow microneedles. *Communications Biology* **2018**, *1* (1), 173.
49. Dawson, K.; Wahl, A.; Barry, S.; Barrett, C.; Sassi, N.; Quinn, A. J.; O’Riordan, A., Fully integrated on-chip nano-electrochemical devices for electroanalytical applications. *Electrochim. Acta* **2014**, *115*, 239-246.
50. Dowling, D., The thickness of cattle skin. *Australian Journal of Agricultural Research* **1955**, *6* (5), 776-785.
51. O’Connor, S. W.; Bale, W. F., Accessibility of circulating immunoglobulin G to the extravascular compartment of solid rat tumors. *Cancer research* **1984**, *44* (9), 3719-23.
52. O’Mahony, C.; Pini, F.; Blake, A.; Webster, C.; O’Brien, J.; McCarthy, K. G., Microneedle-based electrodes with integrated through-silicon via for biopotential recording. *Sensors and Actuators A: Physical* **2012**, *186*, 130-136.
53. O’Mahony, C.; Grygoryev, K.; Ciarlone, A.; Giannoni, G.; Kenthao, A.; Galvin, P., Design, fabrication and skin-electrode contact analysis of polymer microneedle-based ECG electrodes. *J. Micromech. Microeng.* **2016**, *26*, 084005.
54. Zoski, C. G., Ultramicroelectrodes: Design, Fabrication, and Characterization. *Electroanalysis* **2002**, *14* (15-16), 1041-1051.

***Chapter 4*      **Fabrication of Octagonal Nanoring Arrays****

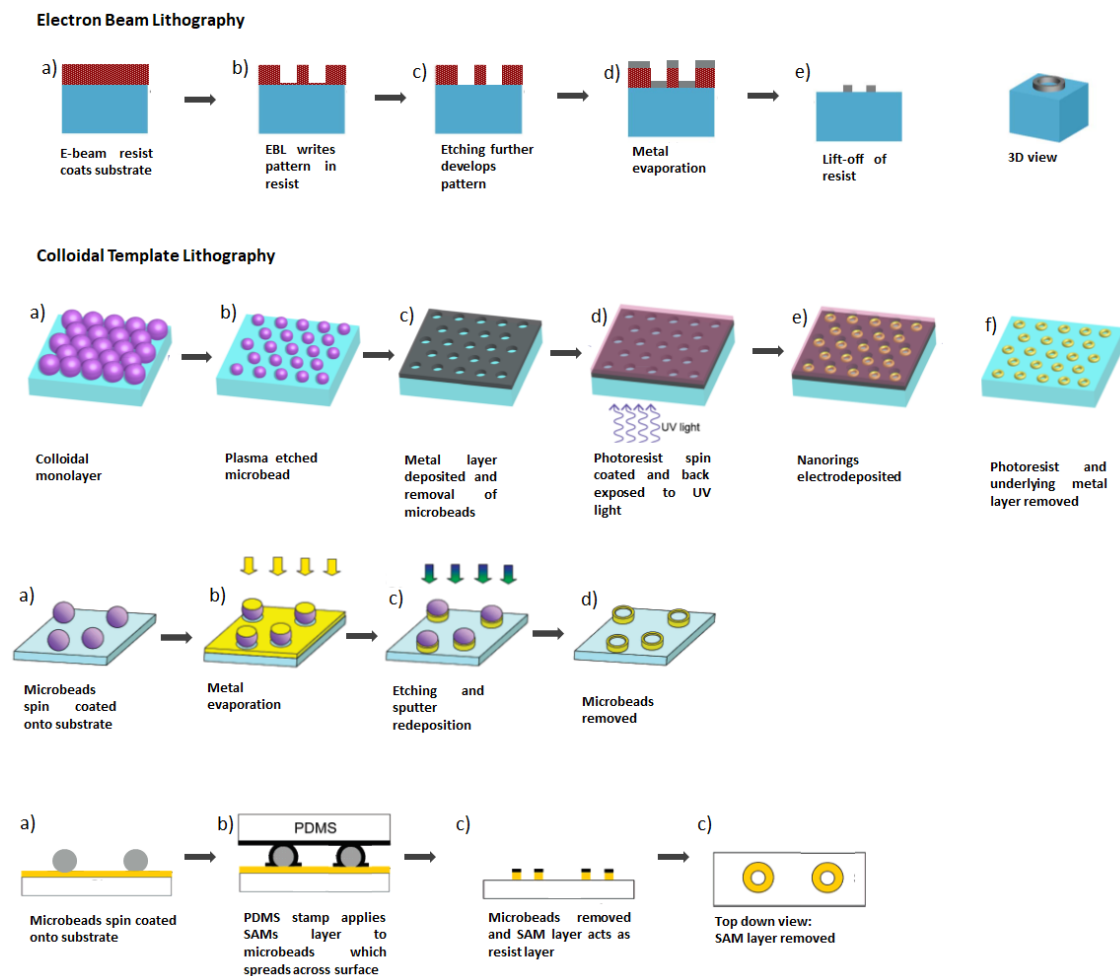
## 4.1 Introduction

Nanoring arrays have been implemented as transducers for label-free biosensors, with the successful detection of DNA,<sup>1, 2</sup> BSA<sup>3</sup> and cytosol<sup>4</sup> already achieved. Nanostructures have a critical dimension that is in the nanoscale.<sup>5, 6</sup> In the case of nanorings, the critical dimension is the width, allowing them to have much larger diameters. The nanoring arrays are most commonly utilised for their plasmonic resonance properties.<sup>2, 3, 7-10</sup> These structures show significantly higher detection sensitivities than nanodisk arrays.<sup>3</sup> Their resonance frequency can easily be tuned to the visible or near-infrared range by adjusting the nanoring geometry.<sup>3, 8, 10</sup> Meanwhile, magnetic materials have also been selected as potential magnetic nanoring devices.<sup>11, 12</sup> Nanoscale entities such as circular nanodisks can acquire the vortex state where the magnetic flux is confined within the magnetic structure without magnetic poles or stray fields. This vortex state creates an electron spin which can be used for low energy information storage in devices such as vertical magnetic random access memory (V-MRAM).<sup>13</sup> Nanorings can maintain a more stable vortex state than nanodisks and allow for even smaller radii allowing smaller device footprint.<sup>14, 15</sup> Nanoring structures are not commonly employed as electrochemical devices. However, nanoring arrays have been shown to have larger current densities over nanodisk arrays due to enhanced mass transport to the ring geometry.<sup>16</sup> This would result in higher current density outputs giving potential electrochemical nanoring devices higher sensitivity compared to nanodisks.

Typical fabrication processes for developing nanoring arrays include EBL<sup>10, 17-19</sup> or colloidal templates,<sup>3, 20-23</sup> as outlined in Schematic 4.1. EBL can write nanoring patterns directly into a resist using a focused beam of electrons. The patterned resist can then be removed selectively and the pattern can then be further developed using techniques such as RIE.<sup>24</sup> The resist patterning and removal is followed by evaporation of the nanoring material and resist lift-off techniques. While this method gives immense control over the ring shape, size, and periodicity, it also involves long processing time and high costs while also being incompatible with mass production requirements.

Alternatively, a colloidal template can be employed by spin-coating a solution of polystyrene microbeads onto a substrate. A dense monolayer is formed on the surface

through solvent evaporation. The periodicity of the final rings will be dictated by the original size of the microbeads. However, the diameter of the rings can be reduced by plasma etching the microbeads to reduce their diameters. Several processes have been adopted to form the nanorings on the substrate surface from this template. A metal layer can be evaporated over the template and sputter redeposition can be applied to form the ring pattern. Here, material is redeposited along the edges of the template after sputter etching.<sup>3, 14, 25</sup> Alternatively, evaporation can be undertaken at an angle deviating from the normal incident with a rotation to form nanorings instead of triangle shaped nanoparticles between the microbeads.<sup>26, 27</sup> If a conductive layer coats the substrate before the colloidal templates, a photoresist can be coated over the template to form a nanohole array. After resist etching, the nanorings can be electrochemically deposited which allows control of both the ring thickness and inner diameter.<sup>2, 7, 28</sup> Other methods employ self-assembling monolayers such as alkanethiols or APTES in an edge spreading lithography approach. SAM molecules will spread laterally along the surface of the microbead via reactive spreading so long as there is a continuous supply of molecules.<sup>29-31</sup> This results in full microbead coverage including the circular footprint, forming a nanoring pattern. This pattern can either be used as a resist<sup>18</sup> or Au NPs can be electrostatically attached to them.<sup>19</sup>



**Schematic 4.1:** Fabrication of nanoring arrays using EBL (adapted from <sup>8</sup>) and colloidal templates. Methods for forming nanorings from the templates involve: photoresist and electrodeposition (adapted from <sup>2</sup>); evaporation and sputter redeposition (adapted from <sup>3</sup>); and edge spreading lithography of SAM layer and etching (adapted from <sup>32</sup>).

Alternative templates to colloids can be used for many of these fabrication methods such as the nanopillar and nanohole arrays formed in anodised aluminium oxide (AAO) template.<sup>25, 33, 34</sup> The AAO templates can be fabricated to contain ordered, columnar pores. The template can act as a shadow mask for evaporation forming nanodots on the underlying substrate. RIE can be used to reform these nanodots as nanorings or nanotubes by redeposition the material around the pore walls. Alternatively, if the substrate is made from the desired material for the nanorings, the AAO template can act as a sputter mask. The substrate with a SiO<sub>2</sub> top layer is ion etched through the columnar pores. During the etching process, substrate material will be redeposited onto the pore walls resulting in nanorings on the SiO<sub>2</sub> layer.

Nanoimprint lithography (NIL), a technique previously employed for the fabrication of plasmonic arrays of nanodisks or nanoholes,<sup>35-37</sup> has also been used to produce nanoring arrays.<sup>11, 38</sup> This is a low-cost process, which will produce ordered arrays and is scalable to mass production. This is a mechanical lithography method which presses a stamp into an imprintable resist layer over the substrate. This stamp transfers contours of the template in the resist. To form nanorings a NIL mask consisting of nanopillars is used to transfer nanoholes into the resist on the substrate. Once the stamp is released etching or milling steps as used with other templates will complete the nanoring devices.

The microneedle array devices presented in Chapter 3, demonstrated a cost-effective approach for fabricating polymer electrodes on a wafer scale. These structures also present the opportunity for a novel approach to the fabrication of nanoring arrays towards electrochemical nanosensing. In this chapter, a novel method for transforming the microneedle structures into nanorings electrodes, while maintaining cost-effective manufacturing is presented. Once the gold surface at the front of the device is completely passivated, part of the protruding needle structure can be removed to expose a thin ring of exposed gold. Due to the eight-faced pyramidal structure of the microneedles, it is an octagonal shaped ring which is formed. In Chapter 3, Section 3.3.2.1 the diffusional overlap of redox species produced at the exposed electrode surface was investigated. The confinement of the diffusion profile to the microneedle surface strongly suggests nanorings with the same periodicity should not experience diffusional overlap. This would enable each ring in the array to act independently and have the mass transport enhancement of ultramicroelectrodes, similar to the microneedle structure with an isolated electroactive tip. Benefits of ultramicroelectrodes, such as lower detection limits and faster response times are further enhanced when dimensions are reduced to the nanoscale. The drawback to nanoelectrodes is their low current output, often in the pA range. However, this may be overcome by employing an array of nanoelectrodes thus magnifying their current output.



## 4.2 Experimental

### 4.2.1 Materials and Reagents

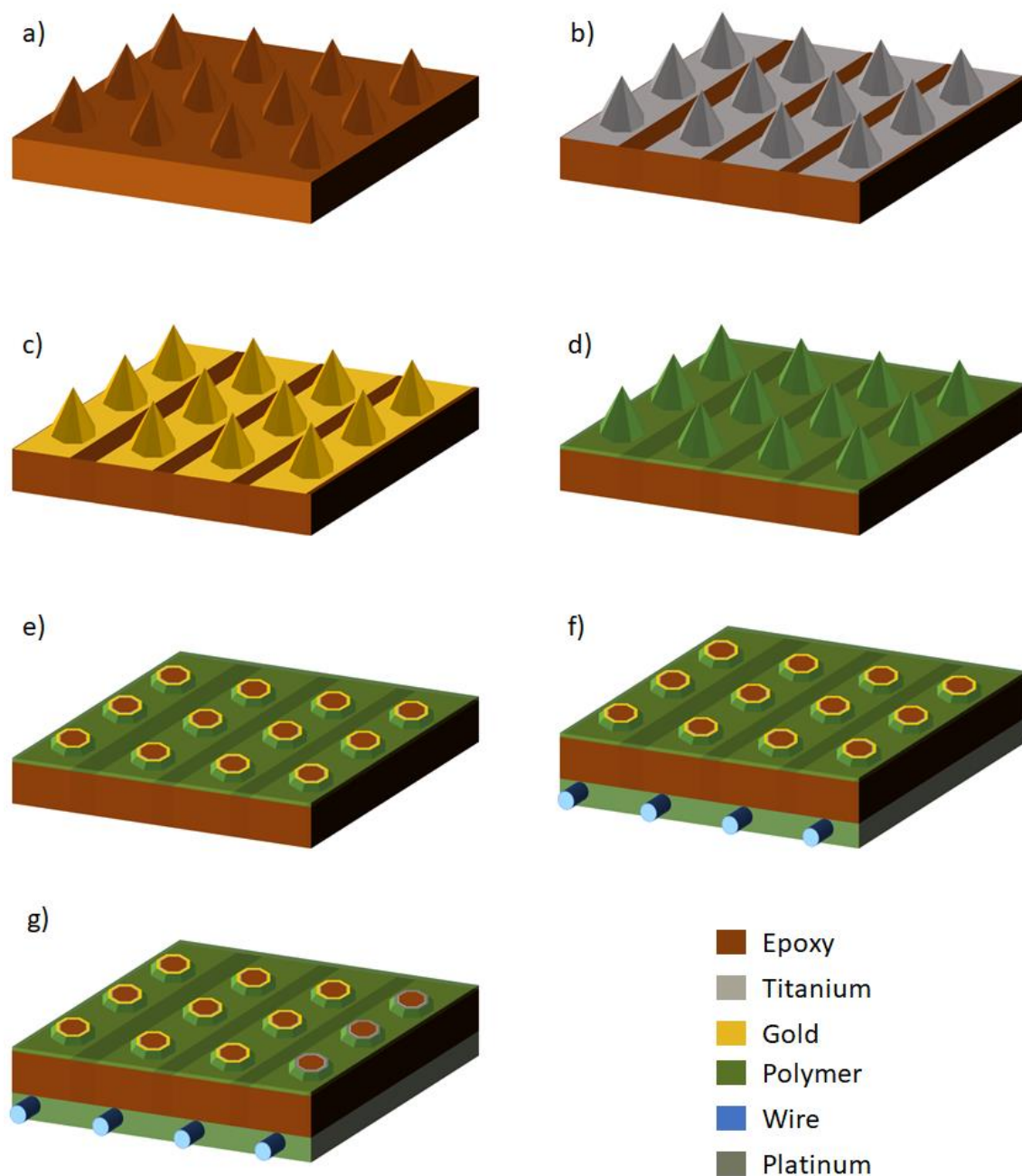
Gold, granular ~99.99% pure was obtained from PI-KEM Ltd., Staffordshire, UK. Sylgard 184 polydimethylsiloxane, PDMS elastomer and curing agent were purchased from World Precision Ltd., Hertfordshire, UK. Norland optical adhesive NOA68 (polymer) was purchased from Tech Optics Ltd., Kent, UK. Epotek 430 and Epotek 353ND were purchased from John P Kummer Ltd., Marlborough, UK. A dihydrogen dinitrosulphatoplatinum (DNS) bath was purchased from Johnson Matthey, London, UK. All other reagents were purchased from Sigma Aldrich unless stated. Deionised water (resistance  $18.2 \text{ M}\Omega \text{ cm}^{-1}$ ) was obtained using an ELGA Pure Lab Ultra system purchased from Alpha Diagnostic International.

### 4.2.2 Fabrication of Octagonal Nanoring Arrays

Microneedle array devices were fabricated using the polymer replication process described previously in Chapter 3, Section 3.4.2, resulting in epoxy structures as in Schematic 4.2 (a). Briefly, once the four-inch epoxy wafer was produced, evaporation of the metals was performed using the same shadow mask as constructed for the microneedle devices to form four metallised areas per device. For these devices, the Ti adhesion thickness of 15 nm was used (Schematic 4.2 (b)), followed by 100 nm Au layer (Schematic 4.2 (c)). After evaporation on both sides of the wafer, each device was removed, using finger pressure to press the device from the wafer support.

NOA68 was then spin-coated onto the microneedle structures and cured in a UV oven. These samples were cured immediately after spin-coating to ensure the whole front surface of the device was fully passivated, shown in Schematic 4.2 (d). Each metallised needle tip was then cut off with a scalpel, to form the octagonal nanorings shown in Schematic 4.2 (e). This was performed using samples stored at room temperature and samples stored in a  $-20^\circ\text{C}$  freezer. Reducing the temperature of the epoxy increased the brittleness, making it easier to cut once subjected to stress.

The back face of each electrode on a device was electrically connected to a wire with the conductive adhesive Epotek 430 which allowed for electrical connection to a potentiostat while the sensor was submerged in an electrolyte, completing the electrochemical cell. NOA68 was used to secure a wire to the back of each electrode and cured under UV light for 30 s. Epotek 430 ND part A and part B were mixed in a ratio of 40:1 and pasted between a stripped section of the wire and the gold strip on the back of each electrode. This cured for one hour at 80°C. The back of the device was then coated in NOA68 and cured under UV light for 120 s to passivate the exposed wire, Au, and Cu epoxy. Finally, to form a fully integrated three-electrode system, as shown in Schematic 4.2 (g), Pt was electrochemically deposited onto one of the electrodes, at -0.5 V vs Ag/AgCl for 5 s in the DNS bath.



**Schematic 4.2:** Fabrication of gold nanoring arrays: (a) epoxy microneedle arrays are fabricated using a polymer replication process; (b) a 15 nm adhesion layer of Ti is evaporated onto the electrode areas of the device; (c) the Ti is coated with 100 nm of Au; (d) an insulating polymer is spin coated onto the front surface of the device and UV cured; (e) the microneedle structures are cut to expose gold nanoring; (f) wires are attached to the back of each electrode on the device and the whole back of the device is passivated with the UV cured polymer and (g) Pt is electrodeposited onto one of the electrodes to generate a pseudo-reference electrode.

## 4.2.3 Characterisation of Structures

### 4.2.3.1 Scanning Electron Microscopy

SEM images were acquired by Dr. Colm Barrett and Dr Han Shao (Tyndall National Institute), to examine the structures after the cutting of the tips to form nanorings. A field emission SEM (JSM – 7500F, JEOL UK Ltd.) operating at a chamber pressure of 9.6  $\mu$ Pa and beam voltages between 5 and 10 kV or a field emission scanning electron microscope (FEI QUANTA 650 HRSEM) operating at 10 kV was used to capture these images.

### 4.2.3.2 Electrochemical Characterisation

All electrochemical studies were performed using an Autolab Potentiostat/ Galvanostat PGSTAT128N (Metrohm Ltd, Utrecht, The Netherlands) controlled by the Autolab NOVA software. All experiments were performed at room temperature in a Faraday cage. A three-electrode cell was adopted, using an array of Au octagonal nanorings as a working electrode versus an external Pt counter and Ag/AgCl reference electrodes. For experiments with the fully integrated device, the cell consisted of an electrode of Au nanorings as the working, an electrode of Au nanorings as the counter and an electrode of Pt nanorings as the pseudo-reference. Electrode arrays were characterised in 1 mM FcCOOH in 10mM PBS (pH 7.4) using cyclic voltammetry (CV) performed at a potential window of 0 mV to 600 mV at 50 mV s<sup>-1</sup>. Potentiodynamic cycling in 0.1 M H<sub>2</sub>SO<sub>4</sub> from -200 mV to 1600 mV at 100 mV s<sup>-1</sup> was performed to clean the surface.

## 4.3 Results and Discussion

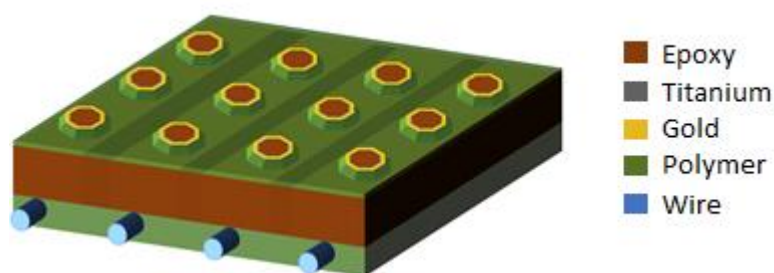
### 4.3.1 Electrochemical Characterisation of Nanoring Devices

As in Chapter 3, four-inch epoxy wafers were fabricated, containing twelve devices. Once more, a rear mould was employed to define each dice, leaving bridges to secure the die in place and vias for front to rear electrical connection. This electrical connect was established by the metallisation of both sides of the electrodes. Again, an Al mask was used specify the electrode area. After the evaporation of the Au, the devices were removed from the wafer. The polymer passivation layer was spin coated onto the surface of a device and immediately cured. The edges of the devices were examined for any exposed Au. Additional polymer was applied to any exposed areas on the front of the device and cured to fully passivate the device. Issues with the passivation of these devices, discussed in Section 3.3.2.2, were inconsequential as we were not trying to expose the tips. The incubation step in the oven was not required to reduce the viscosity and give time for gravitational flow, as the whole structure are was to be covered. The immediate curing of the polymer gave a thicker layer coating the structures. Structural defects observed which caused clumps in the passivation were generally confined to the tip of the microneedle structures. For this work it is the base of the structures which is of importance and must be fully passivated.

Once the microneedle tips were removed by cutting the protruding structures with a scalpel, the epoxy centre of the structures were uncovered with octagonal shaped rings of Au surrounding them. The remaining walls of the protruding structures were passivated by the polymer as seen in Schematic 4.3 thus the exposed Au layer on the top of the truncated microneedle was the only conductive media exposed. A thin Ti layer between the epoxy and Au was also uncovered. Ti is a poor electrical conductor,<sup>39, 40</sup> which quickly oxidises and has been shown to not interfere with the performance of the Au electrodes. However, to ensure any interferences this layer could potentially cause, it was made as thin as possible. As discussed in Section 3.3.1, an adhesion layer is necessary to ensure that the Au is fully adhered to the epoxy, and thus 20 nm of Ti previously proved to be sufficient to anchor the gold to the epoxy surface. However, for this work, thinner layers of Ti were assessed. A 10 nm layer proved to be an insufficient adhesion layer.

Using a tape test method, small specks of Au were observed on the tape following ten pull tests. A 15 nm layer showed no visible removal of gold visible on the tape being secured and removed from the surface ten times. Hence, the chosen Ti thickness was 15 nm, which is a 25% reduction from the previous work.

Reducing the adhesion layer will allow the Ti to re-oxidise faster rendering it electrochemically inactive if the oxide layer has been removed. This could occur if the electrode undergoes processes such as polishing or cycling in high concentration acids or bases.



*Schematic 4.3: Schematic of nanoring array electrochemical device.*

A completed nanoring device with wires attached is shown in Figure 4.1 (a). Four individual electrodes can be seen under the colourless passivation layer. Pyramidal structures are no longer visible as seen in chapter 2, Section 4.3.1. However, when viewed at an angle as in Figure 4.1 (b) shorter truncated microneedles are visible.

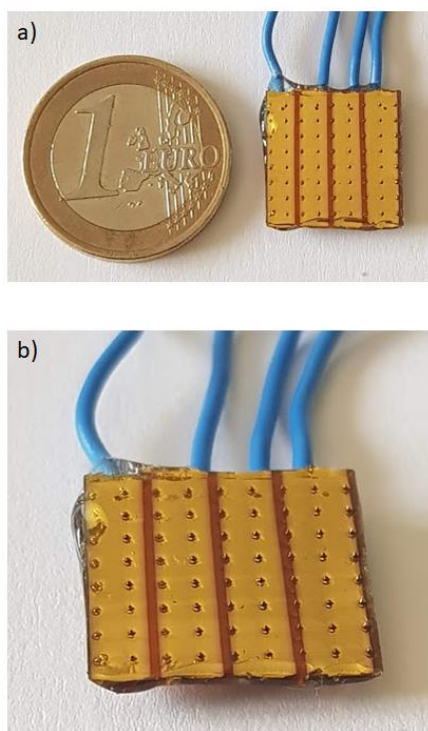


**Figure 4.1:** Image of device with wires attached to the back of each electrode, (a) taken directly overhead and (b) taken at an angle.

The octagonal nanoring arrays were electrochemically cleaned using a potentiodynamic cycling method in 0.1 M sulphuric acid. Characteristic peaks for a gold surface were seen as in Figure 4.2 (a). Gold oxide was formed at 1.4 V (vs Ag/AgCl). On the reverse sweep the gold oxide was reduced at 0.8 V. Initially the reduction peak area increased with each cycle. After ten cycles this peak had become reproducible with subsequent scans overlapping indicating the gold surface was clean Figure 4.2 (a). No other peaks were seen confirming that the Ti adhesion layer was electrochemically inactive.

Characterisation in 1 mM FcCOOH in 10 mM PBS showed steady-state behaviour as depicted in Figure 4.2 (b). This would strongly imply that the walls of the partial microneedle structure were sufficiently coated with an insulating layer, leaving only the top layer of gold exposed in a ring formation, as previously described. The average current output for these electrodes was  $166.38 \pm 59.63$  nA ( $n=10$ ), indicating these octagonal nanoring devices function as nanoelectrodes. This steady-state behaviour also signifies that the individual nanorings in the array exhibited diffusionally independent behaviour, as expected.

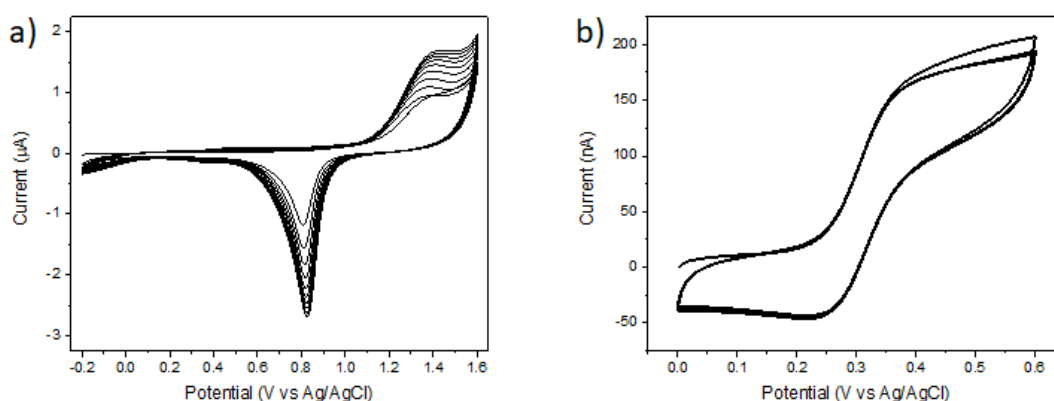


**Figure 4.2:** (a) Typical potentiodynamic cycling in 0.1 M H<sub>2</sub>SO<sub>4</sub> from -0.2 V to 1.6 V at 100 mV/s and (b) typical cyclic voltammogram 1 mM FcCOOH in 10 mM PBS, pH 7.4, in the potential range of -0.2 V to 0.5 V at 50 mV/s of an array of gold octagonal nanorings (versus external Ag/AgCl RE).

Although steady-state behaviour was achieved, the FcCOOH CVs show larger hysteresis than seen when working with microbands in Chapter 2, conveying a high capacitance in the nanorings. It has been shown that charging currents can occur due to high electric fields associated with metal interconnection tracks on silicon chip substrate.<sup>41-43</sup> Therefore, it is likely the high capacitance is due to the large area of planar gold on both sides of the substrate; under the passivation layer. CVs were performed in PBS to investigate contribution of the non-faradaic current, Figure 4.3. Again, large hysteresis was seen due to the planar gold's double layer. The charging current in a potential sweep is proportional to the scan rate according to the equation:

$$i_{cc} = AC_{dl}v \quad 4.1$$

where  $i_{cc}$  is the charging current,  $A$  is the area of the electrode, and  $C_{dl}$  is the double layer capacitance, and  $v$  is the scan rate. As seen from the inset of Figure 4.3 (b) there was a linear relationship between the scan rate and the charging current, as expected.



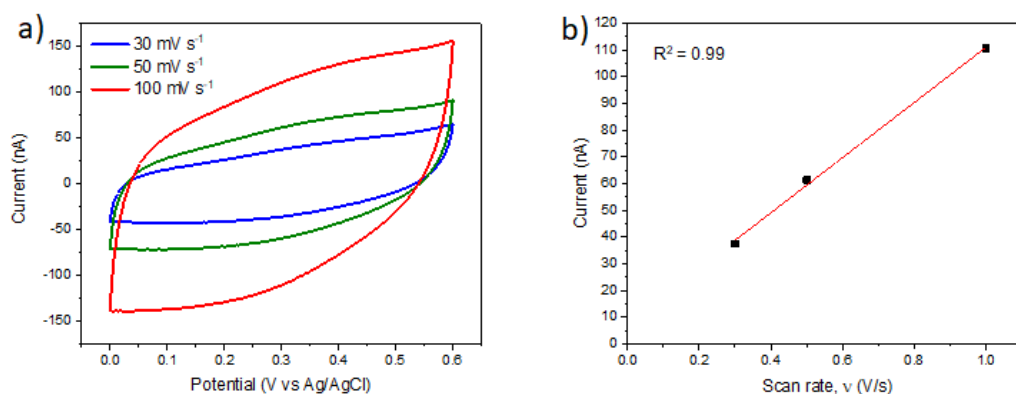


**Figure 4.3:** (a) CVs 10 mM PBS pH 7.4 at scan rates: 30 mV s<sup>-1</sup>, 50 mV s<sup>-1</sup> and 100 mV s<sup>-1</sup>. (b) Plot scan rate vs charging current.

The magnitude of the hysteresis seen in Figure 4.2 (b) is similar in size to the hysteresis produced by the charging current in Figure 4.3 (a) at 50 mV s<sup>-1</sup> (green). This charging current has swamped the faradaic current for CVs produced using the electroactive mediator FcCOOH. By reducing charging current the signal-to-noise ratio will be increased resulting in more sensitive analysis. In addition, fast scan rates can be used leading to faster analysis times, which is crucial for the development of POC sensors. The devices can be redesigned to reduce the surface area of the gold. By designing a holder compatible with a PCB board, the need for a conductive material on the reverse of the substrate would be eliminated. To further control the capacitance a shield layer can be adopted. Such a layer has been shown to greatly reduce the double layer capacitance for a nanowire electrode.<sup>41, 44</sup>

As this work aims to ultimately fabricate devices for impedimetric biosensors, EIS was performed and a typical Nyquist plot can be observed in Figure 4.4. The semi-circular feature representing the kinetic process of charge transfer was present. High capacitance is also presented in the Nyquist plot as the semi-circle is only partly moved down the y-axis at the lower frequencies. There appears to be only one time constant, implying the Ti layer is not affecting the electrochemical layer as it is believed that Ti rapidly forms a native oxide layer effectively passivating the metal.

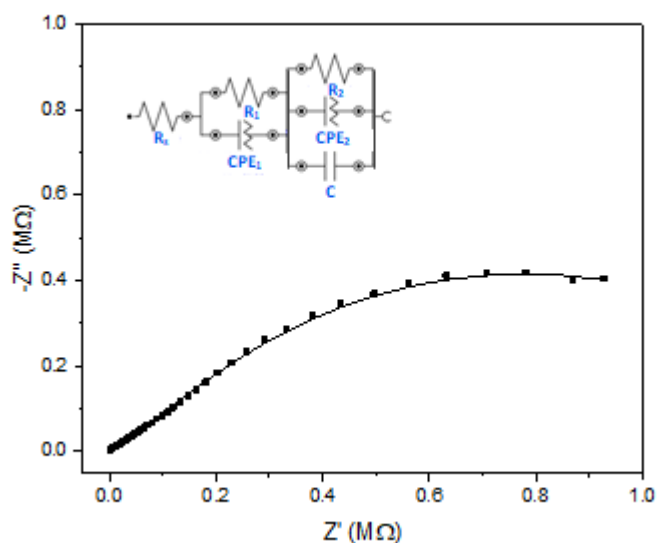


**Figure 4.4:** Typical Nyquist plot for a clean gold octagonal nanoring array from 0.1 Hz to 100 kHz with an amplitude of 5 mV applied to 350 mV in 1 mM FcCOOH in 10 mM PBS. Inset, the applied equivalent electrical circuit.

The equivalent circuit used to fit this data is a modified Randles' circuit. The resistors represent the  $R_s$  and  $R_{ct}$  contributions to the data and the capacitor for the double-layer capacitance. No Warburg component was included in the model, as only semi-circle features were observed, and these devices are not diffusionally-dependent. Instead CPEs were used to account for the additional capacitance.

### 4.3.2 Structural Characterisation of Nanoring Devices

SEM analysis was again used to assess the integrity of the nanoring structures. As seen in Figure 4.5 they consist of eight sides, however some sides were more defined than others. The direction of the cutting can be seen in Figure 4.5 (a) as east to west; and Figure 4.5 (b) NW to SE. The side, which the scalpel starts at has the clear edges, whereas the side that the structure breaks away from has suffered from plastic deformation and the metal structure are not so well defined. These sides have from defects and areas of the ring are obscured by epoxy.

SEM analysis was used to calculate the diameter of the rings as  $197.17 \pm 19.46$  nm ( $n = 22$ ). It can also be seen that the passivation layer does not evenly cover all sides of the

protruding structures. The quasi-steady state behaviour of the electrodes in Figure 4.2 (b) and Figure 4.4 suggests the passivation layer was sufficient to prevent faradaic behaviour of the planar gold but did not prevent the solvated molecules and ions from adsorbing onto the passivation layer and forming a double layer. Areas where the passivation layer was thinner would have contributed more unwanted capacitance once a potential is applied.

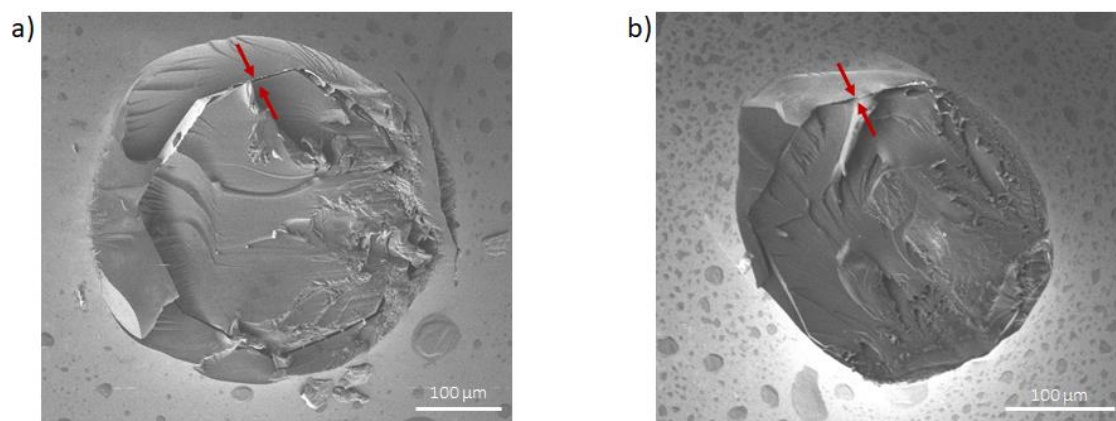


*Figure 4.5: : SEM images of octagonal nanoring structures, with red arrows indicating to the gap between polymer layers where the exposed gold sits.*

### 4.3.3 Three-Electrode System

These devices were designed to have four separate electrodes as defined by the shadow mask during the evaporation step of the fabrication. To form a fully integrated electrochemical device, a three-electrode system was employed consisting of a working, counter and reference electrodes. The remaining electrode was designed to be a second working electrode to operate as a control in a sensor device. To create the pseudo-reference electrode, Pt was electrochemically deposited onto the gold surface using a commercial DNS bath. A negative potential was adopted in this method to reduce the Pt ions present in the solution onto the gold surface. As described in Section 1.4.1, the initial current flow was due mainly to non-faradaic process associated with the charging of the double-layer, followed by a plateau where the faradaic electron-transfer was dominant. In Figure 4.6 (a) a current plateau was not observed as the deposition time was too short. However, a plateau was approached as the rate of current change was seen to slow.

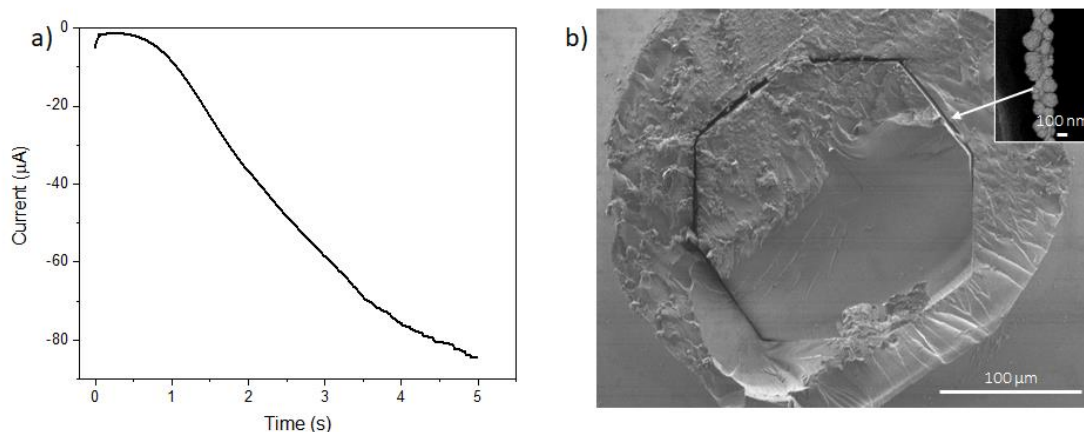


**Figure 4.6:** (a) Chronoamperometric deposition of Pt onto the gold electrodes done at  $-0.5$  V for 4 s. (b) SEM image of nanoring after Pt deposition. Inset high magnification section of the deposited Pt in the inset.

SEM analysis was used to visualise the Pt layer, which showed a compact cauliflower-like deposition. Pt is a popular pseudo-reference choice as it can perform in a variation of electrochemical systems such as aqueous, non-aqueous, gel or frozen electrolytes.<sup>45</sup> Electrodeposition of metals is a fast process and by electrodepositing a Pt post-production, one mask can be used for all the evaporation steps. The total coverage of the Pt layer seen in Figure 4.6 (b) inset, confirmed a longer deposition time was not required. Longer deposition would lead to large, unreproducible layers, creating large bulbous sections which could potentially break away from its anchor of the thin gold layer.

Electrochemical characterisation was repeated using this Pt electrode as the pseudo-reference as well as a gold nanoring array as the CE. The CV in Figure 4.7 (a) displays currents in the nA region as expected, however the shape is quasi-steady-state, as there is a slight peak at 250 mV. There is a slight overlap at slow scan rates, though not large enough to be completely diffusionally controlled. However, this is not the case in these devices as this behaviour was not seen in Figure 4.2 (b). Areas where the passivation is thin may tear when cut. This would leave small areas of gold along the wall of the nanoring exposed, increasing the electrode area and accounting for the quasi-steady-state shape of the CV. The Nyquist plot is similar to the one seen in Figure 4.4 and uses the same equivalent circuit.

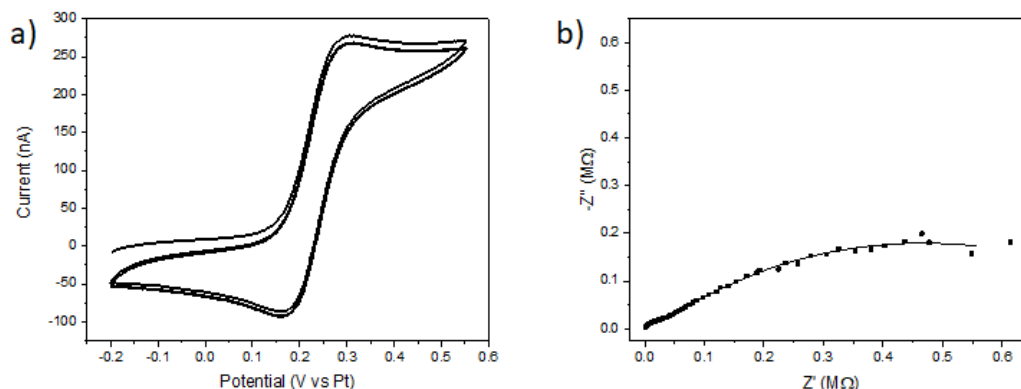


**Figure 4.7:** Typical (a) CV at  $50 \text{ mV s}^{-1}$  and (b) EIS from 0.1 Hz to 100 kHz with an amplitude of 5 mV applied to 270 mV in 1 mM FcCOOH in 10 mM PBS of nanoring array using on-chip Pt pseudo-reference and on-chip Au CE.

#### 4.3.4 Optimisation of Cutting Method

As seen in Figure 4.8, damage is sustained to the polymer structures when the microneedle tip is cut, causing the outline of the nanorings to appear ambiguous and clumps of polymer to be caught along the opening for the ring electrode. To create a cleaner cut the samples were stored in  $-20^\circ\text{C}$  for 30 mins prior to cutting. To establish if this effected the structures SEMs were taken of structures cut at room temperature (Figure 4.8 (a-c)) and those structures stored in a freezer prior to cutting (Figure 4.8 (d-f)).

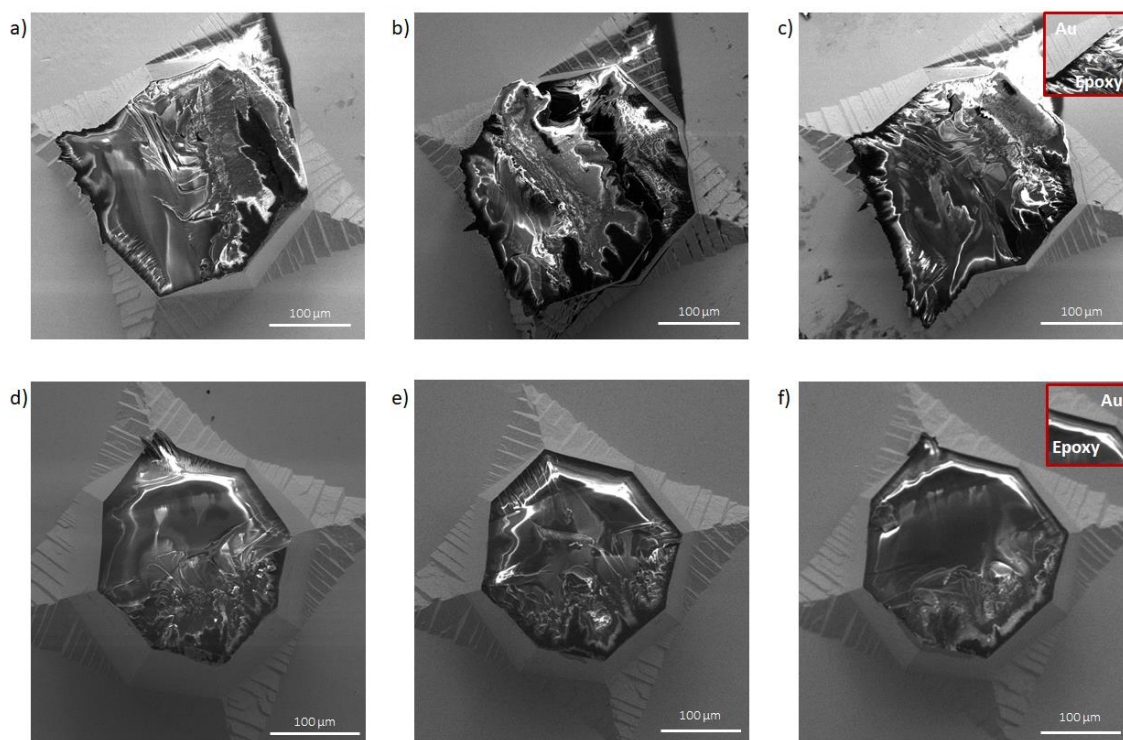


**Figure 4.8:** (a-c) SEM images of nanoring structures cut at room temperature. (d-f) SEM images of nanoring structures cut after storage at  $-20^{\circ}\text{C}$ . Insets show magnified region.

At low temperatures, polymers became brittle and there was a reduction in impact strength required to cut it. The plastic deformation was also reduced allowing the structures to instead fracture when cut. This resulted in more defined edges to the octagonal ring and less damage to the gold. As seen Figure 4.8 (a-c), when the polymer was at room temperature there was tearing of the gold coating and two of the edges were deformed, as seen in Section 4.3.2. Whereas when the polymer was first frozen, as in Figure 4.8 (d-f) all eight faces were distinguishable, the gold coating was intact, and little plastic deformation was seen. Not all these structures were completely pristine, evident in Figure 4.8 (d) and (e). One corner on each of these images' exhibited tearing, the tip has broken away from the underlying structure. However, the damage has been greatly reduced and confined to a single corner, signifying that reducing the temperature of the polymer before cutting notably improves the integrity of the structures. Further temperature reduction using a  $-80^{\circ}\text{C}$  freezer or liquid nitrogen should increase the brittleness of the epoxy substrate and reduce further damage due to cutting.

Current magnitudes from samples which were frozen, prior to cutting, were in the range of  $219.58 \pm 126.83$  nA ( $n=10$ ), with a typical CV depicted in Figure 4.9. The average

current is higher, than those fabricated at room temperature, as the smoother cut leaves less polymer to obstruct the electrode active area.

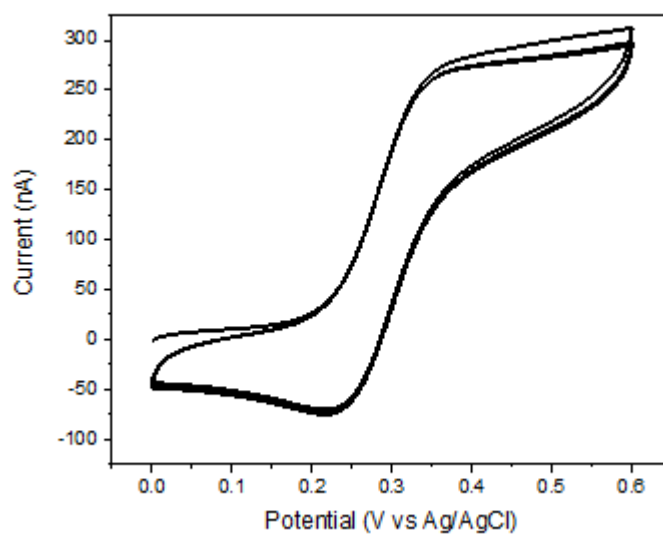


**Figure 4.9:** Typical CV in 1 mM FcCOOH in 10 mM PBS,  $50 \text{ mV s}^{-1}$  for a nanoring array cut after storage at  $-20^\circ\text{C}$ .

Variation in current magnitude is due to variation in height and number of individual electrodes per array. A new shadow mask must be designed to produce electrodes with the same number of nanorings, as discussed in chapter 5, Section 5.2.2. Polishing the protruding tips using a fine sandpaper could produce a more reproducible area than cutting, which would improve the reproducibility of the electrochemical output. This method was not investigated due to disruptions caused by COVID-19.

## 4.4 Conclusion

A novel, economical approach for fabricating Au nanoring arrays was presented and successfully transformed into an electrochemical device. Furthermore, these devices exhibited steady-state behaviour confirming a small defined electroactive area. Electrodeposition of Pt onto one of the electrodes allowed for an on-chip three electrode system, with a Pt pseudo-reference electrode, Au as the CE, and Au as the WE.

Examination of the electrode structure through SEM analysis showed octagonal-shaped rings. However, the epoxy has sustained damage during the cutting process and from Figure 4.8 (a-c) tearing of the gold was also evident. This tearing was remarkably reduced by decreasing the temperature of the epoxy before cutting the microneedle structures. Also, this gave the structure more defined edges, with all eight faces clearly visible. Devices cut under these conditions were successful at producing steady-state CVs, with current outputs of  $219.58 \pm 126.83$  nA.

This cost effective fabrication method also opens the possibility of creating concentric nanorings such as those produced by Halpern et al.<sup>7</sup> This would be achieved by performing second evaporation step after spin-coating followed by a second passivation layer. Previous concentric nanoring arrays have been produced to enhance plasmonic signals. These concentric nanorings could be utilised generator-collector mode. Enhanced sensitivity can be achieved by biasing both rings at different potentials inducing redox cycling. The species generated at one ring would be collected at the other, meaning that a redox species could undergo multiple redox cycles on the electrode surfaces before diffusing back into the bulk solution, thus amplifying the current output. The collector electrode should be held at a constant current to allow the faradaic current to be measured without the interference of the charging current.<sup>46</sup> This signal enhancement makes such device appealing for biosensor applications,<sup>47, 48</sup> including impedimetric biosensors.<sup>49</sup> Nanorings have been fabricated in conjunction with recessed disks to allow for this current amplification through generator-collector mode.<sup>50</sup> There are no devices currently in literature using concentric nanorings for this purpose. To achieve this, wires would have to be electrically connected to the second Au layer. A small area of the second



passivation layer can be removed from the front of each electrode using isopropyl alcohol or acetone. A wire can then be conductively attached the exposed gold and the area re-passivated. The inner ring would act as the generator and the outer as the collector. These devices have the potential to be highly sensitive biosensors.

## 4.5 References

1. Huang, C.; Ye, J.; Wang, S.; Stakenborg, T.; Lagae, L., Gold nanoring as a sensitive plasmonic biosensor for on-chip DNA detection. *Applied Physics Letters* **2012**, *100* (17), 173114.
2. Toma, M.; Cho, K.; Wood, J. B.; Corn, R. M., Gold Nanoring Arrays for Near Infrared Plasmonic Biosensing. *Plasmonics* **2014**, *9* (4), 765-772.
3. Larsson, E. M.; Alegret, J.; Käll, M.; Sutherland, D. S., Sensing Characteristics of NIR Localized Surface Plasmon Resonances in Gold Nanorings for Application as Ultrasensitive Biosensors. *Nano Letters* **2007**, *7* (5), 1256-1263.
4. Zhuang, L.; Zuo, H.; Wu, Z.; Wang, Y.; Fang, D.; Jiang, D., Enhanced Electrochemical Nanoring Electrode for Analysis of Cytosol in Single Cells. *Anal. Chem.* **2014**, *86* (23), 11517-11522.
5. Menon, V. P.; Martin, C. R., Fabrication and Evaluation of Nanoelectrode Ensembles. *Anal. Chem.* **1995**, *67* (13), 1920-1928.
6. Arrigan, D. W. M., Nanoelectrodes, nanoelectrode arrays and their applications. *Analyst* **2004**, *129* (12), 1157-1165.
7. Halpern, A. R.; Corn, R. M., Lithographically Patterned Electrodeposition of Gold, Silver, and Nickel Nanoring Arrays with Widely Tunable Near-Infrared Plasmonic Resonances. *ACS Nano* **2013**, *7* (2), 1755-1762.
8. Fouladi Mahani, F.; Mokhtari, A.; Mehran, M., Design and development of aluminum nanoring arrays for realization of dual-mode operation plasmonic color filters. *J. Opt. Soc. Am. B* **2018**, *35* (8), 1764-1771.
9. Kim, S.; Jung, J.-M.; Choi, D.-G.; Jung, H.-T.; Yang, S.-M., Patterned Arrays of Au Rings for Localized Surface Plasmon Resonance. *Langmuir* **2006**, *22* (17), 7109-7112.
10. Tsai, C.-Y.; Lu, S.-P.; Lin, J.-W.; Lee, P.-T., High sensitivity plasmonic index sensor using slablike gold nanoring arrays. *Applied Physics Letters* **2011**, *98* (15), 153108.
11. Kim, S.; Jung, J.-W.; Lee, T.-S.; Jeong, J.-H.; Lee, S. Y.; Yang, S.-M.; Jeong, J.-R., Large area asymmetric ferromagnetic nanoring arrays fabricated by capillary force lithography. *Electronic Materials Letters* **2012**, *8* (1), 71-74.
12. Zu, X.; Hu, X.; Lyon, L. A.; Deng, Y., In situ fabrication of ordered nanoring arrays via the reconstruction of patterned block copolymer thin films. *Chemical Communications* **2010**, *46* (42), 7927-7929.
13. Zhu, J.-G.; Zheng, Y.; Prinz, G. A., Ultrahigh density vertical magnetoresistive random access memory (invited). *Journal of Applied Physics* **2000**, *87* (9), 6668-6673.
14. Zhu, F. Q.; Fan, D.; Zhu, X.; Zhu, J.-G.; Cammarata, R. C.; Chien, C.-L., Ultrahigh-Density Arrays of Ferromagnetic Nanorings on Macroscopic Areas. *Advanced Materials* **2004**, *16* (23-24), 2155-2159.
15. Zhu, F. Q.; Chern, G. W.; Tchernyshyov, O.; Zhu, X. C.; Zhu, J. G.; Chien, C. L., Magnetic Bistability and Controllable Reversal of Asymmetric Ferromagnetic Nanorings. *Physical Review Letters* **2006**, *96* (2), 027205.

16. Atighilorestani, M.; Brolo, A. G., Comparing the Electrochemical Response of Nanostructured Electrode Arrays. *Anal. Chem.* **2017**, *89* (11), 6129-6135.
17. Banaee, M. G.; Crozier, K. B., Gold nanorings as substrates for surface-enhanced Raman scattering. *Opt Lett* **2010**, *35* (5), 760-2.
18. Near, R.; Tabor, C.; Duan, J.; Pachter, R.; El-Sayed, M., Pronounced Effects of Anisotropy on Plasmonic Properties of Nanorings Fabricated by Electron Beam Lithography. *Nano Letters* **2012**, *12* (4), 2158-2164.
19. Vaz, C. A. F.; Hayward, T. J.; Llandro, J.; Schackert, F.; Morecroft, D.; Bland, J. A. C.; Kläui, M.; Laufenberg, M.; Backes, D.; Rüdiger, U.; Castaño, F. J.; Ross, C. A.; Heyderman, L. J.; Nolting, F.; Locatelli, A.; Faini, G.; Cherifi, S.; Wernsdorfer, W., Ferromagnetic nanorings. *Journal of Physics: Condensed Matter* **2007**, *19* (25), 255207.
20. Sarkar, D. K.; Farzaneh, M., Fabrication of PECVD-grown fluorinated hydrocarbon nanoparticles and circular nanoring arrays using nanosphere lithography. *Applied Surface Science* **2008**, *254* (13), 3758-3761.
21. Winzer, M.; Kleiber, M.; Dix, N.; Wiesendanger, R., Fabrication of nano-dot- and nanoring-arrays by nanosphere lithography. *Applied Physics A* **1996**, *63* (6), 617-619.
22. Yu, X.; Zhang, H.; Oliverio, J. K.; Braun, P. V., Template-Assisted Three-Dimensional Nanolithography via Geometrically Irreversible Processing. *Nano Letters* **2009**, *9* (12), 4424-4427.
23. Liu, H.; Zhang, X.; Zhai, T., Plasmonic nano-ring arrays through patterning gold nanoparticles into interferograms. *Opt. Express* **2013**, *21* (13), 15314-15322.
24. Scheeler, S. P.; Lehr, D.; Kley, E. B.; Pacholski, C., Top-up fabrication of gold nanorings. *Chem Asian J* **2014**, *9* (8), 2072-6.
25. Hobbs, K. L.; Larson, P. R.; Lian, G. D.; Keay, J. C.; Johnson, M. B., Fabrication of Nanoring Arrays by Sputter Redeposition Using Porous Alumina Templates. *Nano Letters* **2004**, *4* (1), 167-171.
26. Jia, D.; Goonewardene, A., Two-dimensional nanotriangle and nanoring arrays on silicon wafer. *Applied Physics Letters* **2006**, *88* (5), 053105.
27. Li, Y.; Duan, G.; Liu, G.; Cai, W., Physical processes-aided periodic micro/nanostructured arrays by colloidal template technique: fabrication and applications. *Chemical Society Reviews* **2013**, *42* (8), 3614-3627.
28. Cho, K.; Loget, G.; Corn, R. M., Lithographically Patterned Nanoscale Electrodeposition of Plasmonic, Bimetallic, Semiconductor, Magnetic, and Polymer Nanoring Arrays. *The Journal of Physical Chemistry C* **2014**, *118* (50), 28993-29000.
29. Biebuyck, H. A.; Whitesides, G. M., Self-Organization of Organic Liquids on Patterned Self-Assembled Monolayers of Alkanethiolates on Gold. *Langmuir* **1994**, *10* (8), 2790-2793.
30. Saiz, E.; Cannon, R. M.; Tomsia, A. P., Reactive spreading: adsorption, ridging and compound formation. *Acta Materialia* **2000**, *48* (18), 4449-4462.
31. Xia, Y.; Whitesides, G. M., Extending Microcontact Printing as a Microlithographic Technique. *Langmuir* **1997**, *13* (7), 2059-2067.

32. McLellan, J. M.; Geissler, M.; Xia, Y., Edge Spreading Lithography and Its Application to the Fabrication of Mesoscopic Gold and Silver Rings. *Journal of the American Chemical Society* **2004**, *126* (35), 10830-10831.
33. Wang, Y.; Zang, K.; Chua, S.; Sander, M. S.; Tripathy, S.; Fonstad, C. G., High-Density Arrays of InGaN Nanorings, Nanodots, and Nanoarrows Fabricated by a Template-Assisted Approach. *The Journal of Physical Chemistry B* **2006**, *110* (23), 11081-11087.
34. Lovera, P.; Creedon, N.; Alatawi, H.; Mitchell, M.; Burke, M.; Quinn, A. J.; O’Riordan, A., Low-cost silver capped polystyrene nanotube arrays as super-hydrophobic substrates for SERS applications. *Nanotechnology* **2014**, *25* (17), 175502.
35. Robinson, C.; Justice, J.; Petäjä, J.; Karppinen, M.; Corbett, B.; O’Riordan, A.; Lovera, P., Nanoimprint Lithography–Based Fabrication of Plasmonic Array of Elliptical Nanoholes for Dual-Wavelength, Dual-Polarisation Refractive Index Sensing. *Plasmonics* **2019**, *14* (4), 951-959.
36. Nishiguchi, K.; Sueyoshi, K.; Hisamoto, H.; Endo, T., Fabrication of gold-deposited plasmonic crystal based on nanoimprint lithography for label-free biosensing application. *Japanese Journal of Applied Physics* **2016**, *55* (8S3), 08RE02.
37. Klein, M. J. K.; Guillaumée, M.; Wenger, B.; Andrea Dunbar, L.; Brugger, J.; Heinzelmann, H.; Pugin, R., Inexpensive and fast wafer-scale fabrication of nanohole arrays in thin gold films for plasmonics. *Nanotechnology* **2010**, *21* (20), 205301.
38. Cui, B.; Veres, T., Fabrication of metal nanoring array by nanoimprint lithography (NIL) and reactive ion etching. *Microelectronic Engineering* **2007**, *84* (5), 1544-1547.
39. Hass, G.; Bradford, A. P., Optical Properties and Oxidation of Evaporated Titanium Films\*. *J. Opt. Soc. Am.* **1957**, *47* (2), 125-129.
40. Pouilleau, J.; Devilliers, D.; Groult, H.; Marcus, P., Surface study of a titanium-based ceramic electrode material by X-ray photoelectron spectroscopy. *Journal of Materials Science* **1997**, *32* (21), 5645-5651.
41. Dawson, K.; Wahl, A.; Pescaglino, A.; Iacopino, D.; O’Riordan, A., Gold Nanowire Electrode Arrays: Investigations of Non-Faradaic Behavior. *Journal of The Electrochemical Society* **2013**, *161* (2), B3049-B3054.
42. Dawson, K.; Baudequin, M.; Sassi, N.; Quinn, A. J.; O’Riordan, A., Electroanalysis at discrete arrays of gold nanowire electrodes. *Electrochim. Acta* **2013**, *101*, 169-176.
43. Lanyon, Y. H.; De Marzi, G.; Watson, Y. E.; Quinn, A. J.; Gleeson, J. P.; Redmond, G.; Arrigan, D. W. M., Fabrication of Nanopore Array Electrodes by Focused Ion Beam Milling. *Anal. Chem.* **2007**, *79* (8), 3048-3055.
44. Barry, S.; Pescaglino, A.; Wahl, A.; Dawson, K.; O’Riordan, A. In *Reducing Charging Currents at Nanowire Sensors: Simulation, Fabrication and Evaluation*, 2019 IEEE SENSORS, 27-30 Oct. 2019; 2019; pp 1-4.
45. Kasem, K.; Jones, S., Platinum as a Reference Electrode in Electrochemical Measurements. *Platinum Metals Review* **2008**, *52*, 100-106.

46. Niwa, O.; Morita, M.; Tabei, H., Electrochemical behavior of reversible redox species at interdigitated array electrodes with different geometries: consideration of redox cycling and collection efficiency. *Anal. Chem.* **1990**, *62* (5), 447-452.
47. Sharma, D.; Lim, Y.; Lee, Y.; Shin, H., Glucose sensor based on redox-cycling between selectively modified and unmodified combs of carbon interdigitated array nanoelectrodes. *Analytica Chimica Acta* **2015**, *889*, 194-202.
48. Min, J.; Baeumner, A. J., Characterization and Optimization of Interdigitated Ultramicroelectrode Arrays as Electrochemical Biosensor Transducers. *Electroanalysis* **2004**, *16* (9), 724-729.
49. Varshney, M.; Li, Y., Interdigitated array microelectrodes based impedance biosensors for detection of bacterial cells. *Biosensors and Bioelectronics* **2009**, *24* (10), 2951-2960.
50. Ma, C.; Contento, N. M.; Gibson, L. R.; Bohn, P. W., Redox Cycling in Nanoscale-Recessed Ring-Disk Electrode Arrays for Enhanced Electrochemical Sensitivity. *ACS Nano* **2013**, *7* (6), 5483-5490.

***Chapter 5*      **Summary and Future Work****

## 5.1 Summary

The scope of this thesis was to develop a label-free, electrochemical based sensor to allow rapid, cost-effective, on-farm detection of desirable analytes such as protective immunoglobulins and pathogen biomarkers.

In Chapter 2, 1  $\mu\text{m}$  wide gold microband electrodes were fabricated on a silicon substrate using optical lithography. These microbands consisted of a 10 nm Ti and 50 nm Au metal stack. Characterisation using SEM and AFM found the dimensions of these microbands to be larger than designed, with a width of  $1.56 \mu\text{m} \pm 0.15 \mu\text{m}$ , and height of  $79.76 \pm 17.52 \text{ nm}$ . However, these dimensions did not affect the performance of the electrode as electrochemical characterisation in 1 mM FeCOOH in 10 mM PBS generated steady-state CVs. EIS produced semi-circle Nyquist curves with no diffusion-dependent characteristics, as expected of an UME.

The surface of these microbands was modified by the electropolymerisation of the copolymer, poly (aniline-co-o-anthranilic acid). The surface modification allowed the functionalisation of a bioreceptor. This sensor was successfully developed to detect Bovine IgG in calf serum to determine if successful passive transfer of the maternal antibodies from colostrum to the calf's bloodstream has occurred. Without sufficient antibody uptake, calves have a greater risk from infectious diseases and mortality. Anti-Bo IgG was functionalised to the surface via cross-linking between the carboxylic acid groups on the co-polymer and the amine groups on the anti-Bo IgG. EIS is a technique which is highly sensitive to changes on the electrode surface and was employed to monitor the binding of the Bo IgG target to the immobilised capture. Serum samples taken before colostrum feeding showed little or no change in the  $R_{CT}$  of the Nyquist plot. However, samples taken 24 hours after birth, where the calf has been feed colostrum and passive transfer has been successful, induced a large change in  $R_{CT}$ . This is due to the target binding and blocking the mediator molecules from interacting with the surface. The assay format enabled sample preparation to be kept to a simple 1:10 dilution of serum thereby easing future on-farm application. FPT determined by ELISA has established a cut-off of  $<10 \text{ mg/ml}$  IgG established for ELISA. However, EIS sensor presented in this work can detect antibody levels in the  $\mu\text{g/ml}$  range. This presents the opportunity to test

calves at an earlier stage and determine a new cut-off. This would improve treatment plans and reduce the need for broad-spectrum antibiotics.

Silicon fabrication is an expensive process. The silicon device in the first part of this thesis would offset these costs in a final product due to its multiplexing abilities. However, for a single test device, silicon is an unwise substrate choice. This work also endeavoured to fabricate a second sensor using a cost-effective epoxy substrate. Chapter 3 focused on fabricating cost-effective, scalable microneedle arrays for electrochemical sensors, through polymer replication of a silicon master. The intention of using microneedle structures for this device, was to eliminate the need for taking blood samples and instead apply and *in vivo* test in the interstitial fluid. Eliminating the sampling step not only reduces the amount of animal handling and restraint that is required, thereby improving animal welfare, but also improves the work environment of both farmer and vet from a health and safety point of view. A biocompatible epoxy was chosen for this work to allow for prospective *in vivo* applications. A back mould was designed to reduce the amount of fabrication steps thus reducing the fabrication time. It enabled easy removal the devices from the wafer, eradicating the need for a dicing step. Protrusions on the back mould created cone shaped holes in each electrode for the front to back electrical connection after metallisation of the wafer. Overall, the design of the back mould improves the fabrication process of MN electrodes for mass production. COMSOL simulations confirmed that the separation between the MNs in the arrays were adequate to ensure diffusional independence at a range of scan rates once the electroactive area was confined to the tip of the MNs. The selective passivation step of the process did not produce the desired results in that although electrochemical scans with steady-state behaviour were observed, a reproducible passivation was not observed. The SEM characterisation showed defects in the tips' structures that caused clumps in the passivation. Additionally, the sharp edges of the walls often showed no passivation. Despite this setback, the polymer replication process demonstrated its cost effectiveness. Not only is the epoxy a much cheaper alternative to silicon, the process doesn't require lithography and etching steps.

Chapter 4 presents an alternative method of creating nanoelectrodes from the microneedle structures by converting them into octagonal nanorings. This keeps the cost effective, scalable fabrication process of Chapter 3, but removes the defected microneedle tips. By



completely passivating the gold surface, a ring-shaped electroactive area can be exposed by cutting the microneedle structure. These nanorings produced steady-state CVs in 1 mM FcCOOH in 10 mM PBS. SEM characterisation showed damage to the epoxy from cutting with the scalpel. Reducing the temperature before cutting the structures showed an improvement in the ring structure and resulted in a higher current output. These devices show potential for POC biosensor applications due to their diffusionally independent behaviour which would provide fast and sensitive detection. Pt was deposited onto one electrode to create an on-chip three-electrode system, furthering its suitability as a POC device.

## 5.2 Future Work

### 5.2.1 Silicon Based Electrochemical Device

This work presented a proof-of-concept immunosensor for the detection of Bo IgG in Chapter 2. The ultimate goal is to develop a viable commercial product, aimed at on-farm diagnostics. To realise this goal, the electronic equipment required for data output must be converted into a portable format with a suitable interface to the sensor platform. The microSD pin-out on the sensor devices was chosen to be compatible with portable electronic platforms. One side of the device is compatible with a microSD port containing eight pins, one per electrode (CE, RE and six WE). This microSD port allows for electrical connections to a PCB board, which can act as a portable potentiostat, such as that previously developed by Mr. Aidan Murphy (MCCI). It is comprised of an Analog Devices ADuCM350 evaluation board, with an integrated Cortex M3 Core. This potentiostat is capable of performing CV scans but work is ongoing for EIS protocols.

A user-friendly interface will also be required to deliver immediate results to the veterinarian/farmer on-site. This system has Bluetooth capabilities which allow results to be delivered directly to a mobile phone, laptop, or tablet. Currently, this interface, shown in Figure 5.1 allows the user to adjust the parameters of the electrochemical measurement and records the graph produced. This suits the developmental stages of the overall device where data is being collected and analysed on the sensor performance. The final product will require a simple interface to log the sample number and inform the farmer whether the calf has absorbed sufficient levels of IgG or whether treatment is required.

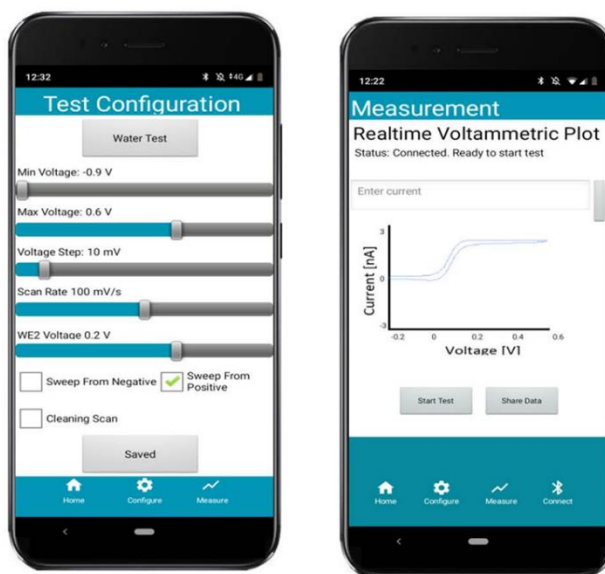


**Figure 5.1:** Mobile phone compatible interface to control the CV parameters, and the data output from the portable potentiostat.

Now that an electrode modification which supports the attachment of biomolecules to the surface has been demonstrated, this modification could be used for the attachment of other disease specific biorecognition elements. The available  $-COOH$  groups provide by the co-polymer can be cross-linked to a bioreceptor with an amine group (which are readily available when using whole antibodies). Developing a new immunosensor only requires a matching capture and target pair. Antibody and antigen pairs suitable for this development are often commercially available. The silicon electrochemical based sensor in this work was specifically designed to offer the opportunity for multiplexing. The six electrodes on the device would either allow for multiple samples to be tested simultaneously for the same analyte or for one sample to be tested simultaneously for multiple diseases, or a combination of both, making these sensors time and cost efficient. A spotting technique was adopted in Chapter 2 to address neighbouring sensor sites with microlitre volumes of sample. This technique allowed for multiple samples to be tested on a single device. However, it required the use of a micropipette and a steady hand, which would not be feasible for a point-of-care device. To rectify this a microfluidic flow cell is being developed to replace the Teflon and Pyrex cells currently being used. The integration of a microfluidic flow cell with the sensor devices allows for easy incubation of multiple samples, higher detection sensitivity, lower reagent volumes, and shorter incubation times. A multilayer microfluidic cell has been designed by Mr. Matthew Agnew (MCCI) and is depicted in Figure 5.2 (a).

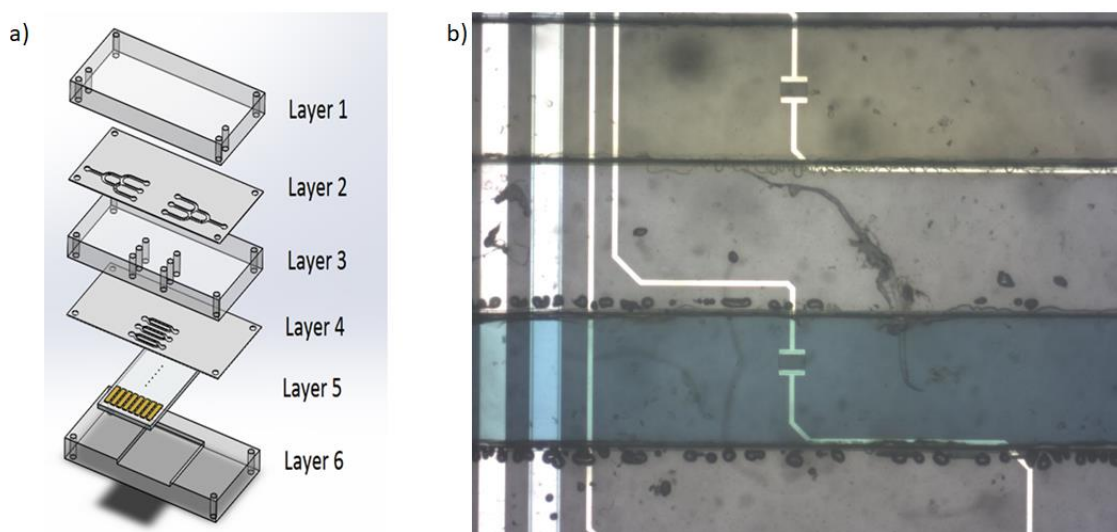


**Figure 5.2:** (a) Schematic of microfluidic flow cell and (b) optical micrograph of microfluidic ducts aligned over sensor sites on silicon sensor chips. Coloured dye fills each channel for better visualisation.

Employing such a microfluidic device with three channels would allow for three tests to be carried out simultaneously on one sample. Each channel splits ducts into two, with each duct designed to align with one of the WEs, as seen in Figure 5.2 (b). Each channel serves two sensor sites to allow samples to be tested for a specific disease on one site, with the second site acting as the control. While this design is ideal for the simultaneous measurement of all sensor sites, testing one sample for multiple disease. An updated design is required to allow for the application of multiple samples to the device. For this design it would be necessary for the three channels to remain separate and lead to separate inlets and outlets.

The integration of the Bo IgG sensor developed in this thesis, with the portable potentiostat, and the PMMA/PSA microfluidic flow cell, will lead to development of a device that can rapidly, and cost-effectively diagnosis diseases on-farm. With multiple samples being analysed on a single disposable sensor.

## 5.2.2 Epoxy Based Electrochemical Device

A two-mould polymer replication fabrication method was devised for the fabrication of microneedle arrays in Chapter 3. Future work should include a Parylene coating which would be selectively etched from the microneedle tip. Parylene has been chosen for the future passivation layer as it can be uniformly coated using chemical vapour deposition. This layer will be coated with photoresists and the area at the tip removed using lithography. The Parylene in this area will then be etched with RIE and the remaining photoresist moved.

Chapter 4 presented proof-of-concept of conversion of microneedles into nanoring electrodes. These nanostructures produced diffusionally independent CVs and Nyquist plots as expected for electrodes of their dimensions. High capacitance was evident in the electrochemical characterisation. The uneven coating of the passivation layer may have contributed to this. The Parylene passivation suggested to above complete the microneedle devices would also be suitable for the nanowire devices. As well as reducing the charging current produced by these nanoring arrays, it would remain cost-effective as no photoresist or additional etching steps would be required.

Although the structural integrity was improved for this cutting procedure by freezing prior to cutting, an alternative method of removing the microneedle structures could provide more reproducible structures. Polishing has been considered for this fabrication step and was to be undertaken but set aside due to the COVID pandemic. Figure 5.3 shows initial Au coated microneedle structures which have had their tips polished down. All eight sides of the ring are still intact and better defined than when the structures are cut with a scalpel. Debris from the polishing procedure remains on the Au surface. This should be removed by sonicating in DI water.

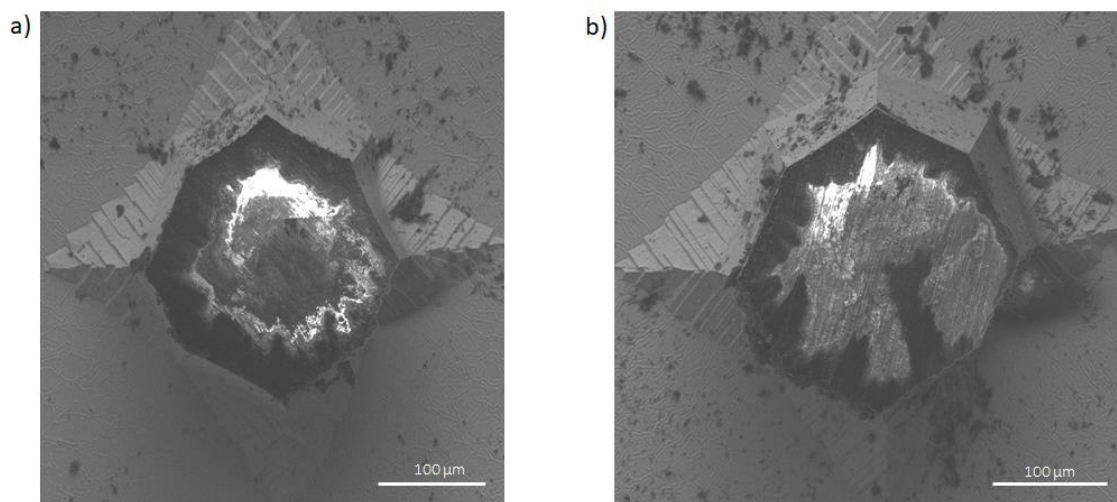
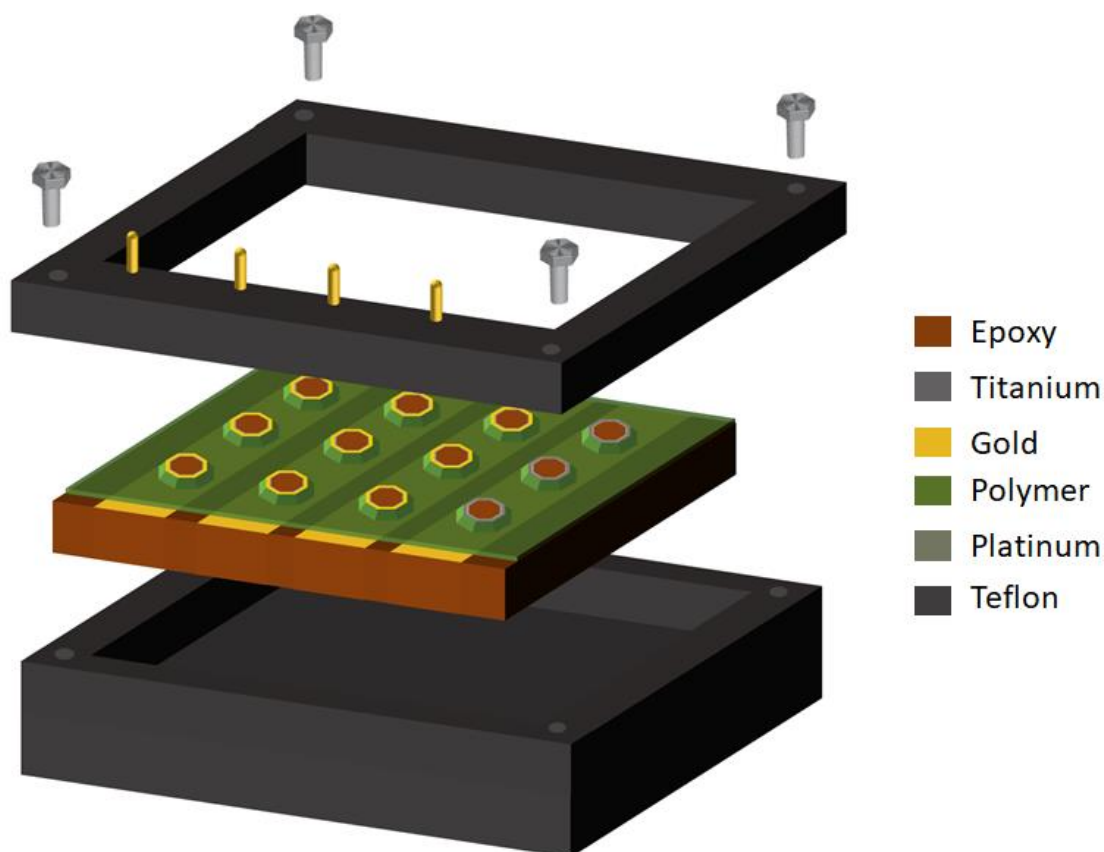


**Figure 5.3:** SEM images of epoxy microneedles coated with 100 nm of Au and the tips polished down.

Slight adjustments to the Si master creating planar border around each device, consisting of four rows of microneedles, would enable an electrochemical cell to be built for these devices. This would move the fabrication further towards a completely scalable process by eradicating the need for wires. It will also reduce the cost by halving the amount of metal required for each wafer, as evaporation will only take place on one side. The back mould would no longer need vias to connect the front and back of each electrode. A new shadow mask would also need to be designed to align with the new placement of the electrodes. This new design would standardise the number of structures in each electrode as it would be limited to a single row. This will affect the electrochemical performance of the electrode because there will be the same number of individual nanowires in each array and thus there will be less variation in the current output. Schematic 5.1 demonstrates how the electrochemical cell would hold these devices. The device would sit into a Teflon base. A Teflon lid would screw into the base, holding the device in place and creating a well for the solution to complete the electrochemical system. Square O-rings can be 3D printed to create a seal between the device and the cell lid. The top of each electrode would need to remain unpassivated. These areas of exposed gold would align with the pins (as in Chapter 2) in the Teflon lid, allowing for electrical connection to each electrode.



*Schematic 5.1: Design for electrochemical cell compatible with nanowire devices.*

These simple adjustments to the master would benefit both the microneedle and nanoring devices. A new shadow mask will improve the reproducibility of the electrode surface area and therefore electrochemical output. Fabrication time would be shortened as the wire attachment cannot be done on a wafer scale and is time consuming. Additionally, a holder rather than a beaker is required for POC devices. The holder would also make device more compatible with portable electronics as discussed in Section 5.2.1. Pre-terminated wires that attach to the pins in the holder electrically connect the electrodes to a PCB board.

## **Appendices**



## A.1 Abbreviations and Acronyms

AAO	Anodised aluminium oxide
AC	Alternating current
AFM	Atomic Force Spectroscopy
Ag/AgCl	Silver/silver chloride
APTES	3-aminopropyltrimethoxysilane
ATP	Aminothiophenol
Au	Gold
BMT	Benzenemethanethiol
Bo IgG	Bovine immunoglobulin G
BSA	Bovine Serum Albumin
BSE	Bovine spongiform encephalopathy
BT	Benzenethiol
BVD	Bovine viral diarrhoea
C	Capacitance
CCD	Charge-Coupled Detector
$C_{dl}$	Double layer capacitance
CE	Counter Electrode
CJD	Creutzfeldt-Jakob disease
CNT	Carbon nanotube
CPE	Constant phase element
Cu	Copper
CV	Cyclic Voltammetry
CVD	Chemical vapour deposition
DC	Direct current
DI	Deionised
DNS	Dihydrogen dinitrosulphatoplatinum
DSP	Dithiobis(succinimidyl propionate)
EBL	Electron beam lithography
EDC	N-(3-Dimethylaminopropyl)-N'-ethylcarbodiimide hydrochloride
EDP	Ethylene diamine pyrochatechol
EDTA	Ethylenediaminetetraacetic acid
EIS	Electrochemical Impedance Spectroscopy
ELISA	Enzyme-linked immunosorbent assay
Fc	Ferrocene
$Fc^+$	Ferrocenium
FcCOOH	Ferrocenemonocarboxylic Acid
FDA	Food and Drug Administration
FIB	Focused ion beam
FMD	Foot and mouth
FPT	Failure Passive Transfer
GGT	$\gamma$ -glutamyl transferase
GO	Graphene oxide
GPMS	3-glycidoxypropyldimethylethoxysilane
GPMS	3-glycidoxypropyltrimethoxysilane
$H_2SO_4$	Sulphuric acid
HEPES	4-(2-hydroxyethyl)-1-piperazineethanesulfonic acid

HOMO	Highest occupied molecular orbital
HRP	Horseradish Peroxidase
HSA	Human serum albumin
Ig	Immunoglobulin
IHP	Inner Helmholtz plane
KCl	Potassium chloride
KOH	Potassium hydroxide
LGS	Lignosulfonate
LUMO	Lowest unoccupied molecular orbital
MCH	Mercaptohexanol
MPA	3-mercaptopropionic acid
MWCNT	Multi-wall carbon nanotubes
N <sub>2</sub>	Nitrogen
NaCl	Sodium chloride
NaOH	Sodium Hydroxide
NHS	N-Hydroxysuccinimide
NIL	Nanoimprint lithography
NPs	Nanoparticles
o-ABA	ortho-aminobenzoic acid
OHP	Outer Helmholtz plane
OIE	World Organisation for Animal Health
PAMPS	Poly(2-acrylamido-2-methyl propanesulphonic acid)
PANI	Polyaniline
PBS	Phosphate buffer saline
PCB	Printed Circuit Board
PDMS	Polydimethylsiloxane
PECVD	Plasma enhanced chemical vapor deposition
PEDOT	Poly(3,4-ethylenedioxythiophene)
PGMA	Poly(glycidyl methacrylate)
PMMA	Poly(methyl methacrylate)
POC	Point-of-care
PPV	Poly(p-phenylenevinylene)
PPy	Polypyrrole
PSA	Pressure Sensitive Adhesive
PSSA	Polystyrene sulphonic acid
Pt	Platinum
PVP	Polyvinylpyrrolidone
PVS	Poly(vinyl sulfonate)
R	Resistance
R <sub>ct</sub>	Charge-transfer resistance
RE	Reference electrode
rGO	Reduced graphene oxide
RIE	Reactive ion etching
R <sub>s</sub>	Solution resistance
SAM	Self-assembled monolayer
SCE	Saturated Calomel Electrode
SEM	Scanning Electron Microscopy
SHE	Standard Hydrogen Electrode
SiN	Silicon Nitride
SWCNT	Single-wall carbon nanotubes

---

Ti	Titanium
TMAH	Tetramethyl ammonium hydroxide
TMB	3,3',5,5'-Tetramethylbenzidine
TWV	Through wafer via
UME	Ultramicroelectrode
W	Warburg element
WE	Working Electrode

## A.2 Peer Reviewed Publications

1. **Robinson, C.**; Creedon, N.; Sayers, R.; Kennedy, E.; O'Riordan, A., *Electrochemical detection of bovine immunoglobulins G to determine passive transfer of antibodies to calves*. Analytical Methods 2020, 12, 2655-2660.
2. Creedon, N.; **Robinson, C.**; Kennedy, E.; Riordan, A. O. *Agriculture 4.0: Development of Seriological on-Farm Immunosensor for Animal Health Applications*. In 2019 IEEE SENSORS, 27-30 Oct. 2019, 2019; 2019; pp 1-4.
3. Flynn, B. O.; Donno, M. D.; Barrett, C.; **Robinson, C.**; Riordan, A. O. *Smart microneedle sensing systems for security in agriculture, food and the environment (SAFE)*. In 2017 IEEE SENSORS, 29 Oct.-1 Nov. 2017, 2017; 2017; pp 1-3.

### A.3 Conference Attended

1. VistaMilk Annual Conference; 2020 June 3<sup>rd</sup>, Virtual Conference. “Monitoring IgG in Calves.” (*Oral Presentation*)
2. VistaMilk Annual Conference; 2019 November 12<sup>th</sup>, Carlow, Ireland. “Detection of Bo IgG in Calf Serum.” (*Oral Presentation*)
3. 25th Electrochem; 2019 August 26-28th; Glasgow, United Kingdom. “Label-free Electrochemical Immunosensor for the Detection of IgG in Calf Serum.” (*Oral Presentation*)
4. Analytical Research Forum; 2019 June 25th; London, United Kingdom. “Electrochemical Detection of Bovine IgG in Calf Serum.” (*Poster Presentation*)
5. 2nd ISE Electrochemistry in Graduate Research Student Meeting; 2018 November 9th; Limerick, Ireland. “Electrochemical Detection of Bovine IgG in Serum.” (*Oral Presentation*)
6. 1st ISE Electrochemistry in Graduate Research Student Meeting; 2017 October 27th; Cork, Ireland. “Implementation of Microneedle Devices as an Electrochemical Sensing Platform.” (*Oral Presentation*)
7. 70th Association for Veterinary Teaching and Research Work Annual Conference; 2016 October 7th; Dublin, Ireland. “Rapid Serological Detection of Bovine Herpesvirus-1 using Nanosensors” (*Oral Presentation*)
8. 29th World Buiatrics Congress; 2016 July 3-8th; Dublin, Ireland. “Rapid Serological Detection of Bovine Herpesvirus-1 using Nanosensors.” (*Poster Presentation*)
9. 8th Conference on Analytical Sciences Ireland, CASi; 2016 April 14-15th; Dublin, Ireland. “Microneedle Electrodes for Nitrate Detection in Water.” (*Poster Presentation*)
10. Tyndall Technology Days; 14-15 October 2015; Cork, Ireland. “Wireless-Interfaced Microneedle Electrochemical Sensors.” (*Oral Pitch Presentation*)

11. Tyndall Technology Days; 14-15 October 2015; Cork, Ireland “Detection of Nutrients in Soil and Water Run-off” (*Oral Pitch Presentation*)

## **A.4 Award**

Second Place, Student Poster Competition “Electrochemical Detection of Bovine IgG in Calf Serum.” Analytical Research Forum; 2019 June 25th; London, United Kingdom.